eman ta zabal zazu

Universidad del País Vasco
Euskal Herriko Unibertsitatea

Department of Analytical Chemistry

# Raman spectroscopy as a key technique for the interpretation of the geochemistry of Mars and other celestial bodies

Dissertation presented for the international PhD degree

**Imanol Torre Fernandez**

July 2021

Supervised by:

Juan Manuel Madariaga Mota

Kepa Castro Ortiz de Pinedo

# Acknowledgments

Imanol Torre Fernandez is grateful to the University of the Basque Country (UPV/EHU) and to the IBeA research group for his pre-doctoral contract (May 2017-May 2021) to afford the works included in this PhD thesis. Also, the economic support given by the University of the Basque Country (UPV/EHU) for the two research stays at Los Alamos National Laboratory (LANL, Los Alamos, New Mexico, USA) and Jet Propulsion Laboratory (JPL, Pasadena, California, USA) is gratefully acknowledged.

This PhD work has been developed thanks to the founding of several projects:

- Exomars-Raman project (ref. ESP2017-87690-C3-1-R) funded by Spanish Agency for Research (MINECO and the European Regional Development Fund).
- Project No. IT-742-13 for Consolidated Research Groups for the period 2013-2018, and by the project No. IT1213-19 for Research Groups of Excellence, for the period 2019-2021, both funded by the Basque Country Government.
- Strategic Project on Terrestrial and Planetary Weathering Processes (ref. PES 18/57) funded by the University of the Basque Country (UPV/EHU)

I would like to acknowledge to the Geominery Museum of the Spanish Geological and Miner Institute (IGME) for giving us the opportunity to create a database with their extensive collection of minerals and even allowing us to take some of these minerals for laboratory analyses.

Part of the analyses made during this work were carried out in the Coupled Multispectroscopy Singular Laboratory (Laspea) and in the General X-Ray Service of Rocks and Minerals of the Research General Services of the UPV/EHU (SGIker). I would like to thank Alfredo Sarmiento and Francisco Javier Sangüesa for all the support.

I would like to thank Los Alamos National Laboratory (LANL, Los Alamos, New Mexico, USA), where I did my first PhD student stay, especially Dr. Roger Wiens, Dr. Sylvestre Maurice, Dr. Ann Ollila and the *SuperCam* team in general for welcoming me in the group and allowing me to participate in some of the instrument development processes.

I would also like to acknowledge the Jet Propulsion Laboratory (JPL, Pasadena, California, USA) for receiving me for my second PhD student stay, especially Dr. Michael Tuite and Dr. Kenneth Williford, who helped me during my stay with them. In addition, I also want to thank Dr. George R. Rossman from the California Institute of Technology (Caltech, Pasadena, California, USA), who allowed me to use his laboratory for Raman analyses during that stay.

Finally, I would like to thank NASA, the Mars 2020 Project and the *SuperCam* team for inviting me to be a member of both the Mars 2020 and *SuperCam* science teams, allowing me to take the role of science payload uplink lead (sPUL) of the instrument. Especial thanks to Dr. Sylvestre Maurice and Dr. Olivier Gasnault for always being helpful while on shift in the Centre National d'Études Spatiales (CNES, Toulouse, France) and to all the *SuperCam* team for allowing me to take part in this incredible adventure about the exploration of Mars. I hope I will be able to keep contributing to both groups during my postdoctoral stage.

Tras los agradecimientos institucionales y formales, me gustaría plasmar aquí los personales, aclarando primero que no están escritos en orden de importancia, ni mucho menos.

Lo primero de todo, agradecer la compañía a todas las personas que han compartido laboratorio conmigo durante estos últimos años. Habéis hecho que Zamudio, Casiano, o donde estuvierais, no solo fuera un sitio de trabajo, sino también uno donde poder compartir experiencias, hablar de lo que sea, o divertirse. En definitiva, transformar un sitio de trabajo en algo más que eso, en donde poder llegar a considerar a la gente amig@s, es algo que se debe agradecer mucho durante un proceso tan largo como una tesis doctoral. En especial me gustaría nombrar a Jenni, Ilaria, Cris, Julene y Leti. Aunque algunas ya no estéis presentes en el día a día, todas habéis hecho que este proceso sea mucho más ameno, divertido y con grandes momentos para el recuerdo.

He querido dejar un pequeño hueco para poder mencionar en especial a Patri. Patri, al igual que tú me dijiste en su día, nada de lo que hay escrito en esta tesis podría haber sido posible sin tu ayuda. Me da mucha pena no verte a diario en el laboratorio y que no hayamos podido buscar marcianos a las cuatro de la madrugada delante de un ordenador en Toulouse. Aun así, sé que me llevo una muy buena amiga de esta etapa de mi vida y te deseo la mayor de las suertes en tu nueva andadura.

No podía dejar de lado tampoco a Fani. Muchas gracias por haber estado ahí para ayudar siempre que ha hecho falta desde que nos conocimos hace 11 años. Mucho ánimo también para tu recta final, en menos tiempo del que te des cuenta pasaremos a ser el trío doctor.

En el ámbito académico, me gustaría agradecer por último todo lo que me han aportado y toda la ayuda que me han brindado mis dos directores de tesis, especialmente en este último tramo. Sin su ayuda, este trabajo no hubiera sido posible.

Kepa, muchas gracias por todos los consejos, lecciones y enseñanzas, y también por las reprimendas. Aunque no te guste reconocerlo, ambos sabemos que eres como Gru, todo lo que me hayas podido decir o hacer

ha sido por mi bien, a pesar de que a veces pareciera lo contrario, y por ello te estoy muy agradecido.

Juanma, muchas gracias a ti también por toda la ayuda que me has dado estos últimos años. Estoy convencido que, de no ser por ti, no hubiese tenido la increíble suerte de poder realizar las dos estancias predoctorales que he hecho. Muchas gracias también por ser siempre esa parte positiva a la hora de analizar resultados y por hacerme ver que, muchas veces, subestimaba mi propio trabajo.

Pasando a un plano más personal, me gustaría agradecer la amistad y el apoyo a todas las personas que han estado a mi alrededor estos últimos años de mi vida, tanto a los que lleváis desde mi infancia, como a los que os he ido conociendo a lo largo de los años. Voy a evitar mencionar a personas concretas, porque si no esto se podría eternizar, pero muchas gracias a todos vosotros por haber estado presentes en todo este proceso, por aguantarme y por haber sido muchas veces una vía de escape.

También me gustaría agradecer a mis padres, Maite y Jose, y a mi hermano Gonzalo, haber estado ahí siempre para apoyarme. Vosotros sois los que más me habéis tenido que aguantar durante todo este proceso y los que me habéis apoyado siempre en todas mis decisiones. Ama, aita, muchas gracias por haberme enseñado a perseguir siempre aquello que te gusta e ilusiona, desde que era pequeño. Sin esas enseñanzas que me han hecho ser como soy hoy en día seguramente no estaría escribiendo ahora mismo estas líneas, gracias.

Por último, Maider, muchas gracias por todo en estos últimos años. Gracias por haberme hecho ser la persona que soy y por iluminarme todos los días en los que estoy ensombrecido. Me faltan las palabras para agradecer toda la comprensión y apoyo que me has brindado durante todo este tiempo, de modo que lo dejaré en eso: Gracias.

# Resumen

Debido al creciente interés sobre Marte por su posible habitabilidad, o presencia de vida, en el pasado del planeta, las misiones que se han realizado para su estudio en el pasado reciente o las que se están programando para el futuro son múltiples y numerosas. Entre las diferentes técnicas que están presentes en la carga científica de esas misiones se ha incorporado recientemente la espectroscopía Raman, tanto en la misión Mars 2020 (NASA) en los instrumentos SuperCam y SHERLOC, como en la misión ExoMars 2022 (ESA) en el instrumento RLS. Esta técnica no solo permite realizar una caracterización completa de la mineralogía de la superficie de Marte, sino que puede llegar a emplearse para determinar otras características del planeta. Esta capacidad de la espectroscopía Raman para caracterizar otros aspectos muy relevantes para el estudio de Marte está muy poco explotada y estudiada en la bibliografía. Por ello, en la presente tesis doctoral se ha empleado para el estudio y desarrollo de diferentes metodologías. Este desarrollo responde a la necesidad de tener unas buenas herramientas de análisis para interpretar los resultados Raman que llegan desde el rover Perseverance, (misión Mars 2020, NASA), y cualquier misión espacial futura que haga uso de esta técnica.

En ese sentido, el objetivo principal de la tesis doctoral es el desarrollo de metodologías innovadoras haciendo uso de la espectroscopía Raman aplicada al campo de la exploración espacial. Para cumplir este objetivo principal se han propuesto los siguientes objetivos parciales:

- La creación de una base de datos de espectroscopía Raman de minerales relevantes para el estudio de Marte, incluyendo ejemplares que no han sido estudiados aun en bibliografía, o cuyos espectros Raman no son de buena calidad.

- El desarrollo de modelos matemáticos para el estudio a través de la espectroscopía Raman no solo de la mineralogía de las muestras, sino de otras características relevantes de Marte. Concretamente:
    - El desarrollo de un modelo que permita dilucidar el contenido de forsterita y fayalita de los olivinos.
    - El estudio de las capacidades de la espectroscopía Raman para determinar eventos de alta presión sufridos por minerales.
    - El desarrollo de una metodología que permita identificar, clasificar y caracterizar compuestos orgánicos presentes en minerales, empleando para ellos la quimiometría.
- La evaluación de las capacidades de SuperCam para la identificación de fases minerales relevantes a Marte y compuestos orgánicos empleando la espectroscopía Raman.
- La realización de un estudio en profundidad de tres meteoritos para testear los modelos desarrollados en muestras provenientes de Marte, obtener información nueva del planeta y proponer una posible metodología para el estudio de las futuras muestras recogidas en Marte (Sample Sample Return mission, MSR).

Estos objetivos se han cumplido y la descripción, resultados obtenidos y discusión de los mismos figura en cada capítulo de la presente tesis doctoral.

Por un lado, se ha creado IMPAT Database, una base de datos espectral de patrones minerales relevantes al estudio del Planeta Rojo. En concreto, la base de datos cuenta con más de 100 muestras individuales de minerales que han sido analizadas para la correcta interpretación de los resultados Raman de Marte. Esta base de datos se ha creado con la colaboración del Museo Geominero de Madrid (IGME).

Además, empleando estos y otros resultados Raman, se han desarrollado una serie de modelos de caracterización a través de los cuales es posible obtener información adicional a la interpretación clásica mineralógica que se obtiene a través de la espectroscopía Raman.

Por un lado, a través de las bandas principales del olivino, se ha desarrollado un modelo de calibración con el que obtener su composición dada por la relación forsterita/fayalita, es decir, el contenido de magnesio y hierro del mineral. Este modelo puede llegar a ser de gran relevancia, puesto que el contenido metálico de este mineral está estrechamente relacionado con las características y evolución del magma del que el olivino procede. Además, las alteraciones que pueda sufrir y los productos derivados de ellas también dependen del contenido de magnesio y hierro del mineral, por lo que la capacidad de poder determinarlo en función de su espectro Raman es un gran avance para el estudio de la superficie de Marte.

Este modelo se ha desarrollado usando 64 espectros diferentes de olivinos con concentraciones metálicas conocidas. En concreto, durante la tesis se han propuesto tres modelos diferentes, usando la banda principal 1, banda principal 2 y la diferencia entre ambas bandas, frente a la posición de las mismas en el espectro. El proceso de validación de dichos calibrados se ha llevado a cabo empleando por un lado un patrón comercial de olivino de composición conocida, y por otro calculando las desviaciones de los resultados teóricos de las propias muestras de los calibrados. Tras la validación, se ha llegado a la conclusión de que el método más exacto y preciso de calcular el contenido metálico de los olivinos es empleando los dos modelos que emplean sus dos bandas principales y haciendo la media entre ellos. Empleando este método se han llegado a conseguir imprecisiones asociadas a las medidas de entre ± 2-3 %.

Estos modelos se han testeado además en muestras reales. Concretamente, en muestras de origen ígneo de la zona de Reykjanes

(Islandia), ya que es una zona considerada análoga a Marte. Los modelos dieron los resultados esperados y, además, se pudo ver cómo en una misma área puede llegar a haber una heterogeneidad grande en lo que respecta a la composición metálica de olivinos. Este hecho puede llegar a implicar temperaturas de formación dispares en el magma del que provienen estos minerales, lo cual es un hecho relevante para el estudio de Marte.

Otro de los parámetros que se ha podido calibrar a través de la espectroscopía Raman es la presión sufrida por un mineral. En concreto, se ha desarrollado un modelo que calcula la presión residual de las calcitas de choque, además de poder determinar si ha sufrido un cambio de fase debido a la presión o no. Gracias a este modelo, se ha podido concluir que una de las calcitas presentes en uno de los meteoritos marcianos estudiados (NWA 6148, una nakhlita) era de original de Marte, puesto que estaba presente como el polimorfo calcita II. Realizando un estudio bibliográfico de las diferentes zonas en las que se han encontrado carbonatos en Marte, se ha propuesto Syrtis Major Planum como el origen más probable de las nakhlitas en función de este hallazgo, ya que a día de hoy aun se desconoce dónde se formaron este grupo de meteoritos en Marte. En este sentido, se ha observado cómo el poder determinar otras características de las muestras analizadas por espectroscopía Raman, aparte de la mineralogía, como puede ser la presión residual que queda tras un impacto, puede llevar a conclusiones relevantes como la estimación de una región de formación para un grupo grande de meteoritos.

Además de en la calcita, se han estudiado los cambios espectrales causados por altas presiones que se producen tanto en los feldespatos como en la sílice, a través de muestras reales (Chesapeake Bay Crater en el caso de la sílica y en el meteorito EET 83227 en el caso del feldespato).

Independientemente del mineral estudiado, el poder determinar si un área ha sufrido cambios por alta presión y poder estimar la magnitud de esa presión es significativo para el estudio de la superficie de Marte, puesto que las últimas misiones a este planeta (tanto las activas como las futuras) están centradas en el estudio de cráteres de impacto, los cuales sufrieron en el pasado un evento de gran presión que pudo transformar su composición actual.

Por último, en lo que respecta al desarrollo de modelos, se han establecido varios para el estudio de posibles compuestos orgánicos en Marte a través de la espectroscopía Raman, ya que están estrechamente relacionados con la posible presencia de vida en el pasado del planeta, siendo su hallazgo uno de los objetivos principales de las misiones en Marte activas y futuras. En concreto, se ha elaborado por un lado un modelo que permite clasificar a qué familia de compuestos orgánicos pertenece el espectro Raman de un compuesto desconocido. Además, una vez determinada su familia, se ha elaborado un calibrado a través del cual poder caracterizar con precisión la largura y características de la cadena de carbonos de ciertos compuestos orgánicos. Todo este desarrollo metodológico ha permitido realizar la caracterización de un compuesto orgánico presente en una burbuja de un meteorito de Marte (NWA 6148), el ácido dodecanoico. La explicación más coherente para la presencia de este compuesto orgánico es que provenga de contaminación terrestre y que no sea original de Marte. Aun así, gracias a él se ha demostrado la capacidad de caracterizar este tipo de moléculas en inclusiones de material original de Marte, como lo es el meteorito NWA 6148.

Estos desarrollos descritos se han empleado para el estudio de meteoritos, tanto provenientes de Marte como de otros cuerpos celestes. Usando muestras de la colección de meteoritos de la UPV/EHU se han testeado los diferentes modelos de calibración desarrollados. Concretamente, se han analizado los meteoritos NWA 6148, DaG 735 y el EET 83227. Además, se ha elaborado una metodología para el análisis no destructivo

de este tipo de materiales extraterrestres, como preparación para la colección de muestras de Marte que van a ser muestreadas y se van a mandar a la tierra en la misión Mars Sample Return (NASA y ESA). Además de la espectroscopía Raman, se ha empleado SEM-EDS acoplado a dicha técnica a través de la interfaz SCA y ED-XRF como métodos para facilitar en mod mapeo el posterior análisis Raman.

Al margen de los estudios de meteoritos, durante la tesis el doctorando ha tenido la oportunidad de participar en la calibración científica de SuperCam, uno de los instrumentos del rover Perseverance, de la misión Mars 2020 de NASA, en el centro Los Alamos National Laboratory (LANL, New Mexico, EEUU). Durante este proceso, se ha evaluado la capacidad de SuperCam para el análisis de muestras de diferentes tipos y los diferentes parámetros de calidad del instrumento, como su repetitividad, reproducibilidad, estabilidad térmica, etc. Parte de estos resultados obtenidos en LANL se han incorporado a la memoria de la tesis doctoral. Por último, se ha estudiado la capacidad de la espectroscopía Raman para la detección de moléculas orgánicas. Este estudio se ha realizado empleando distintos compuestos de diferente naturaleza y distintos tamaños de partícula, aplicados en varias matrices diferentes, para poder así determinar la capacidad de SuperCam para el análisis de este tipo de compuestos en muestras reales.

Como conclusión general, el trabajo llevado a cabo durante esta tesis doctoral podría llegar a ser una valiosa fuente de información en lo que respecta al estudio de muestras de Marte a través de la espectroscopía Raman, a través tanto de la IMPAT-Database como de la metodología desarrollada, como se ha llegado a comprobar en el análisis geoquímico de los meteoritos marcianos estudiados. Por ello, la metodología desarrollada podría llegar a proporcionar información relevante relacionada con el área en la que se llevan a cabo análisis en Marte. En este sentido, esta tesis doctoral ha contribuido a la capacidad de

caracterizar la superficie de Marte, y cualquier muestra de la misma naturaleza, a través de la espectroscopía Raman.

# Chapter 1
# Introduction

*"Equipped with his five senses, man explores the universe around him and calls the adventure Science"*

Edwin Hubble, 1929

Since the beginning of human history, man has been fascinated by looking at the sky and trying to understand its mysteries. Long before the invention of writing, prehistoric human beings were already drawing in caves what in the future would be known as constellations and celestial maps (1, 2). In the beginning, these drawings and knowledge were mainly used in the spiritual and religious field and it was where our ancestors went to look for answers about the unknown. For example, the Mayan culture was one of the best known in making use of this knowledge to make predictions and organize their society around it (3).

However, over the years, humans realized that this knowledge could also be used for more practical purposes. Throughout time, before the existence

of the science called astronomy, man already used celestial bodies for things like marking the time, navigating knowing that the position of certain stars always marked a specific direction or organizing the sowing, since the position or appearance of certain constellations marked the change of seasons (1). All this new knowledge marked important advances in society, since by looking at the sky they were able to make predictions and perform tasks that would not have been possible in any other way at the time.

Although many cultures influenced the development of the study of the stars and the sky, it was the Ancient Greek culture that laid the foundations for what was to become Western astronomy. In addition to seeing their gods in them, or giving them the practical uses already known to date, Ancient Greek society also studied the sky for leisure and invented devices that became the seed of what in the future would be more complex instruments to study the firmament. Moreover, they were able to predict the next retrograde motion of Jupiter and invented the astrolabe and the equatorium. With these two instruments, they were capable of determining the position and height of the stars, the Sun, the Moon and the planets in the sky. They were used by navigators, astronomers and scientists in general to locate the stars and observe their movement, to determine the time from the latitude or, vice versa, to find out the latitude knowing the time. They were also used to measure distances by triangulation (1, 4). Over time, the first star maps were created using this technology (Figure 1.1).

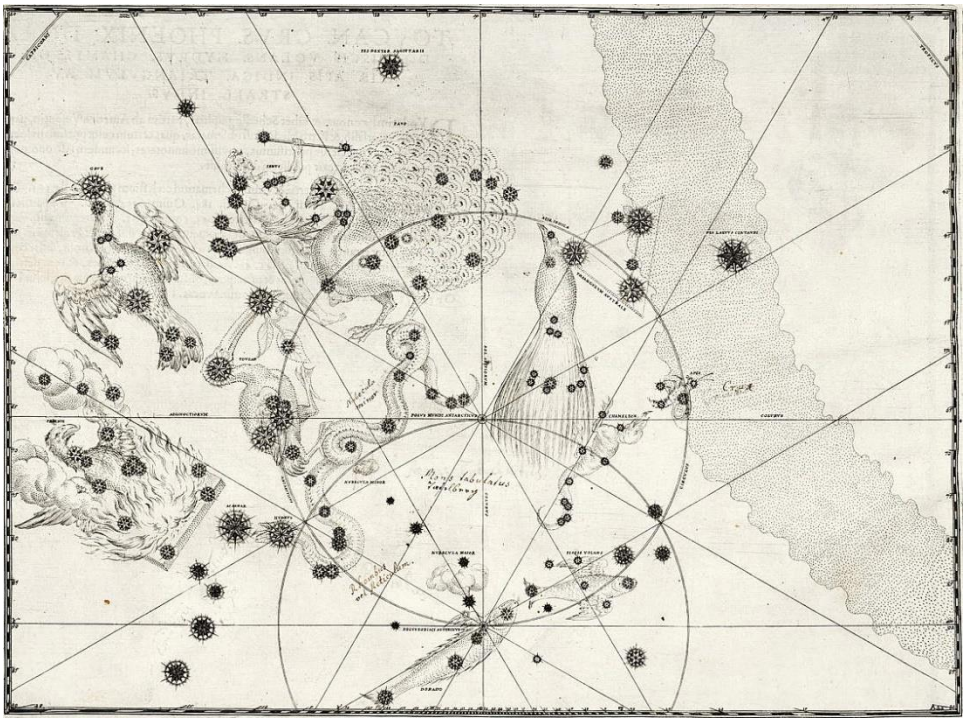

Figure 1.1. The first time that 12 new constellations around the south pole were registered in 1603. Figure extracted from (5)

Less than 2000 years have passed since those primitive instruments that revolutionized society in their time to those that do so today. The only difference is that today our capabilities are greater and we are able to obtain more information from celestial bodies. Even so, we must not forget that, nowadays, the purpose remains the same as thousands of years ago: to explore the unknown and to try to understand the universe around us.

## 1.1. Mars, the Red Planet

Among all the celestial bodies that were admired in ancient times, Mars has always been among the most important, due to its observable size from Earth and to its characteristic reddish color. In fact, its color and glow were the reasons why in different cultures it was associated with the god of war, fire or destruction, as in Roman culture (Mars), Babylonian culture (Nergal) or Sinosphere culture (火星, or the *Fire Star*) (6).

Interest in the planet never decreased over time and, at the end of the 19th century, the idea that Mars had been inhabited in the past by an intelligent and organized society emerged quite strongly. This thought was born out of the discovery of the Italian astronomer Giovanni Schiaparelli, who observed a series of canals on Mars through a telescope (Figure 1.2). The author Percival Lowell developed the theory that they were irrigation canals that were built by an advanced society no longer in existence (7). Although that theory was disproved, since then, the characteristics that have been discovered about Mars have led to believe that life may have existed on the planet in the past, but not in the way that authors from the 19th century thought.

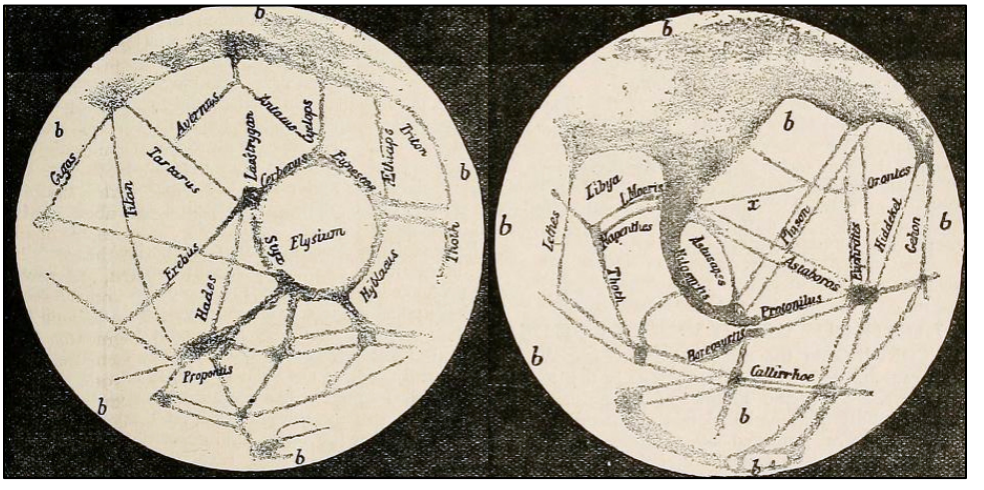


Figure 1.2. One of the first sketches based on the observations of the canals of Mars made by Giovanni Schiaparelli and Percival Lowell. Figure extracted from (8)

### 1.1.1. Geology of Mars

Mars is a rocky planet that suffered from a differentiation process during its formation, resulting in different geological layers inside the planet. Its history is similar to that of the Earth, having gone through geological changes and processes comparable to those of our planet. Although it is believed that Mars has undergone geological events similar to those on Earth, their study and understanding is much more complicated, since we have not yet been able to obtain unaltered samples from Mars.

For example, to determine the geological ages of the different layers of a planet or moon, the most common and best technique used is radiometric dating (9). However, this technique is hardly usable on Mars for this purpose, since samples from different areas of the planet and at different depths would be needed. The *Beagle 2* lander carried to Mars two instruments through which it was possible to do radiometric dating on Mars: The *X-ray Spectrometer* (*XRS*) and the *Gas Analysis Package* (*GAP*) (10). However, since the Beagle 2 unfortunately did not successfully land on Mars, those measurements were not performed.

As an alternative to radiometric dating, two other methods with different approximations have been tried.

On the one hand, the first method that stablished the different ages of Mars was the one that used crater density of the different impacts that cover all the planet's surface. The first attempts to calculate the crater density of the surface of Mars and to use this data to determine the geological ages of the planet were made in 1976 (11) and, since then, repeated attempts have been made to calculate the absolute ages of the planet (12, 13). In order to use the crater densities to estimate absolute ages this method needs to know precisely the rate of impact of crater formation by crater size per unit of area over geological time (also called production rate or flux) (14). However, there exists a lot of uncertainty both with calculating the flux and with the craters counting, especially with the smallest ones (15), which results in many difficulties to estimate absolute ages. This method stablished four different ages or periods in the geological history of Mars (16):

- Pre-Noachian. It starts with the accretion and differentiation of the planet about 4.5 billion years ago and ends with the formation of the Hellas impact basin, about 4.1 billion years ago.
- Noachian. It involves the formation of the oldest extant surfaces of Mars, which happened between 4.1 and 3.7 billion years ago.

- Hesperian. It took place between 3.7 and 3.0 billion years ago and during this period extensive lava plains were formed as well as several seas and lakes in the northern lowlands of the planet.
- Amazonian. It started around 3.0 billion years ago and is the current geological period of Mars. It was characterized by lava flows, glacial activity and minor releases of the liquid water formed during the Hesperian period.

On the other hand, an alternative timescale has been proposed recently using results from the instrument *Visible and Infrared Mineralogical Mapping Spectrometer* (*OMEGA*) onboard the *Mars Express* mission. This method was based on the study of the abundances of different types of weathered minerals present on Mars, which were the result of different weathering processes corresponding to different geological periods of the planet (17). This new timescale comprises three different ages and is especially emphasized around the mineralogical knowledge of the planet to, through it, explain the different periods:

- Phyllocian. It starts with the accretion and differentiation of the planet about 4.5 billion years ago and ends around 4.0 billion years ago. This period is characterized by the formation of phyllosilicates on the surface of Mars. This type of silicate requires alkaline conditions and the presence of water in order to form. In addition, this period is correlated with the formation of the valley network on Mars (Pre-Noachian – Noachian ages).
- Theiikian. It took place between 4.0 and 3.5 billion years ago. During this period there was a lot of volcanic activity throughout Mars, which released large amounts of $SO_2$ into the atmosphere. This gas reacted with water, primarily in its liquid form, to form sulfuric acid which, in the long term, formed hydrated sulfates in the surface of the planet.
- Siderikan. It started around 3.5 billion years ago and is the current geological period of Mars based on this timescale. This period is

> characterized by the decay of volcanism and liquid water on the surface. Due to that decline, the atmospheric peroxides started a slow oxidizing process of the different iron rich rocks of the planet's surface, which ended in the iron oxides that give the planet its characteristic color.

As just explained, throughout its history, Mars has undergone very distinct chemical and geological processes, resulting in a notable diversity and variety in both physiography and mineralogical composition. The planet is divided into two clearly differentiated parts, which coincide with its northern and southern hemispheres and which give name to this hemispheric dichotomy. The most visible distinction between these two sides is the difference in altitude between the two, since the northern part of the planet is a topographic depression that lies 3-6 km lower in elevation than the southern part (Figure 1.3) (18). This dichotomy is also observed by the impact crater density, which is very high in the southern hemisphere, while the northern side has fewer large craters and its surface is flatter. The last difference lies in their crustal thickness. Topographic and geophysical gravity data suggest that the northern hemisphere has a crust thickness of around 32 km, while in the southern side is of around 58 km (19, 20).

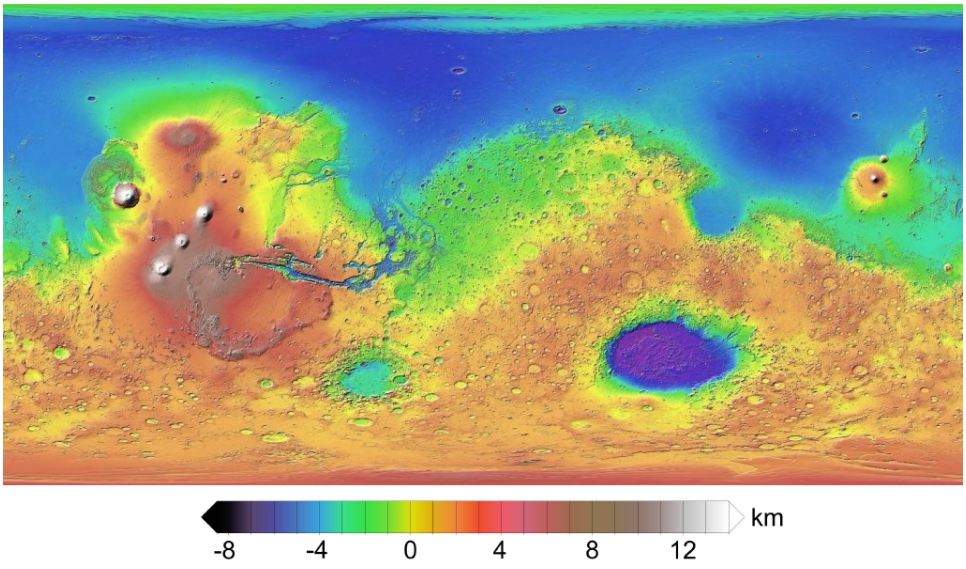


Figure 1.3. Mars Orbiter Laser Altimeter (MOLA) topographic map of Mars. Figure extracted from (21)

There are two theories to explain this dichotomy: an exogenic theory, which relies in external factors, and an endogenic theory, which is based on factors within the planet itself. The former one suggests that the planet suffered a huge single impact from an external celestial body or several large impacts, which caused the clear differences between the northern and southern part of Mars (22). In contrast, the endogenic theory proposes that the dichotomy was created by crustal thinning in the northern side of the planet caused by mantle convection, overturning and other chemical and thermal processes in the planet's interior (23).

Regardless of which of the two theories is correct, the fact is that, as already explained, Mars possesses an abundant diversity at a topological, physiographic, chemical and geological level. Moreover, as mentioned above, the geology and the chemical composition of the planet are often the basis for explaining other features; the characteristics of the planet for possible past life or its present habitability, the most recent theory on the geological absolute ages of the planet, the endogenic explanation of the planet's dichotomy, etc.

### 1.1.2. Mineralogy and Geochemistry

The study of Mars is of special interest for the search of the existence of life on Mars due to its similarities with ancient Earth. The fact that these characteristics are all present together let us consider Mars as a planet that could have supported life in the past. These Martian characteristics, which might be important for the understanding of possible past life on the planet, could be grouped into 4 groups of factors:

- *Energy*. If life ever existed on Mars as we know it on Earth, it needed a source of energy for its metabolic processes. On Mars, these sources could have been the Sun, oxidizing compounds, reducing compounds, redox gradients, and/or geochemical processes that might have taken place in the Martian subsurface (24).
- *Conducive physical conditions*. In the case of Mars, this would include factors such as a varying temperature during the day (in the case of Mars it is more extreme than the variations we have on Earth); low atmospheric pressure, which could imply that only microorganisms lived on the planet; strong ultraviolet irradiation, as well as galactic cosmic radiation and solar particle events (all of them being detrimental for life presence); climate variability, as Mars also has its axis of rotation inclined, it has seasons too; high $CO_2$ concentrations in its atmosphere; material transportation, which could have been possible due to the presence of ancient groundwater, surface water flows or aeolian processes (24-26).
- *Water*. Even though it is not a sufficient factor to confirm the existence of past life, its presence is so important that it is considered an independent factor. The presence of water implies the existence of partial vapor pressure, also called liquid water activity ($a_W$). In addition, liquid inventories have been observed in Mars in the form of ice which, combined with several conducive physical factors, could imply the movement of water over time throughout the planet, filling and emptying those inventories (27). In

addition, different salinity grades and compositions have been found in ancient lakes of the planet. This fact suggests that water on Mars had different pHs and redox potential conditions, which also have an important role in life (24, 28).

- *Chemical diversity*. The presence of the chemical elements C, H, N, O, P and S in the planet is very relevant, as they are considered nutrients (or an essential part of them) for the life as we know it on Earth. In addition, indigenous nitrogen has been found on Mars by the rover *Curiosity* (29), which suggests the possibility of nitrogen fixation processes in the past. However, some metals are at what on Earth are considered toxic levels, such as Zn, Ni, Cu, Cr, As or Cd (24, 30).

All these factors are relevant to life as we know it on Earth. Some support the theory of its past existence on Mars, while others indicate the opposite. However, many of them can be studied from the geological findings of the planet, since nowadays, being a dead planet (as far as we know), geology is one of the major sources of information about it. For example, the *Spirit* rover accidentally discovered a patch of ground made up of 90% silica, reminiscent of the effects and consequences of the contact on Earth between hot spring waters and volcanic rocks. This fact suggested the existence of an environment favorable for past microbial life (31). Another example would be the *Curiosity* rover's finding of complex organic compounds after analyzing two different zones of mudstone that were approximately 3.5 billion years old with the *Sample Analysis at Mars* (*SAM*) instrument (32). Lastly, all the discoveries related to hydrated minerals have helped in the understanding of the geological processes that have taken place on the surface of Mars for their formation. Most of these processes imply the existence in the past of the conditions necessary for the presence of life on the planet (33).

To sum it all up, to discover nowadays if Mars had life in the past, as we know it on Earth, or if it can be habitable in the future, the geological knowledge and discoveries of the planet are essential.

Although it is known that Mars has, and has had, many similarities with Earth, over time, and thanks to the different space missions sent there, it has been observed that it is also different in some aspects.

From an elemental composition point of view, Mars also has a molten core of heavy metals (iron and nickel), which is surrounded by a mantle and crust whose major element is silicon (34). However, the core of Mars is richer in sulfur than the terrestrial core, while the mantle is richer in potassium and phosphorus and about twice as rich in iron (35, 36). As for its surface, Mars has a greater abundance of volatile elements, such as sulfur and chlorine, which nowadays result in different chemical and atmospheric processes on the surface than those known on Earth (37).

Regardless of the knowledge that we have about the different geological layers of Mars, the most studied one is its surface, since it is the most accessible one. We have data from it thanks to the missions that have been sent, both to orbit the planet (orbiter) and to perform in-situ analyses on the surface (landers and rovers) (Table 1.1)

All these missions have given context to the elemental composition of the planet's surface. The most abundant elements of the planet's crust are silicon, oxygen, calcium, potassium, magnesium, iron and aluminum, while the minor ones are chromium, titanium, manganese, sulfur, chlorine, phosphorus and sodium (Figure 1.4) (37). This elemental distribution concurs with the composition of igneous rocks. As a remarkable element finding, the rover *Curiosity* found in 2017 the presence of boron, which is an essential element for life on Earth (38). Regarding the surface and atmosphere of Mars, hydrogen is mostly present in the form of water or hydrated minerals. Its atmosphere is mainly comprised of carbon dioxide

(95.9 %), argon (2.0 %), nitrogen (1.9 %), oxygen (0.14 %) and carbon monoxide (0.06 %) (37).

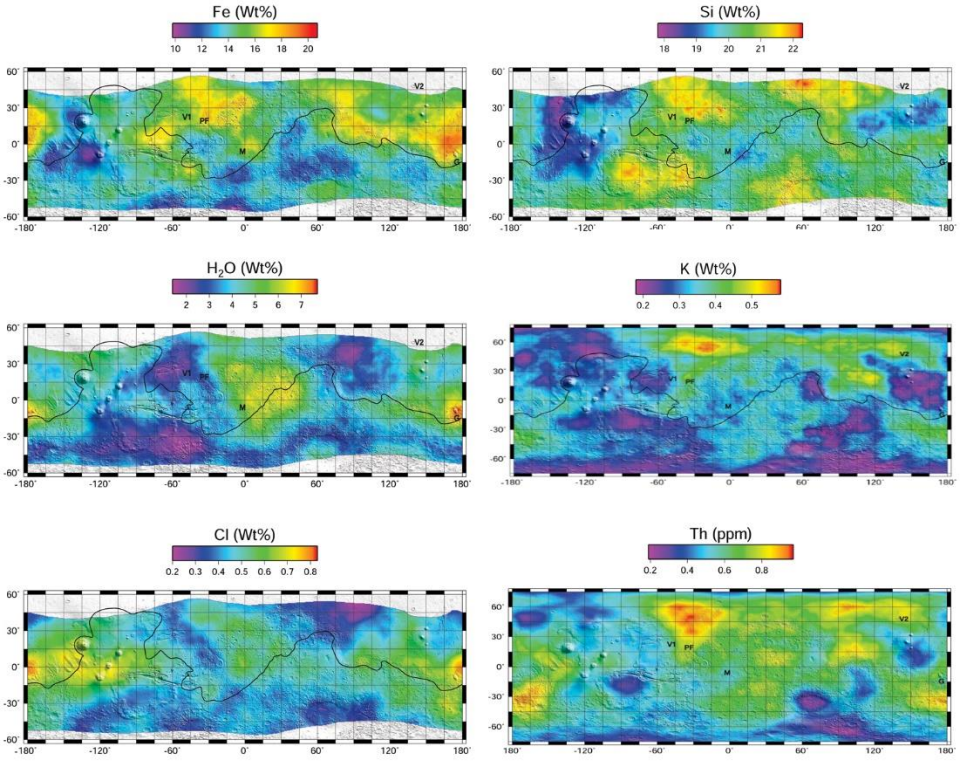


Figure 1.4. Elemental maps obtained from the Gamma Ray Spectrometer (GRS), from NASA's Mars Odyssey mission. The black line separates de northern and southern side of the Martian dichotomy. Figure extracted from (39)

As already mentioned, the elements are present mainly in the form of igneous rocks, as the most common rocks found on the surface of Mars are the ones that crystallized from magma. In other words, most of the rocks found on the planet's surface are primary rocks, not yet altered by weathering or other transformation processes. These rocks are mainly mafic and are formed primarily of olivines, pyroxenes and feldspars (mostly plagioclase), which give the planet's surface its darkest tonalities. These minerals are the main component of basalt, a dark volcanic rock.

Olivine is present throughout the entire surface of the planet, although it is not homogeneously distributed. The areas with the highest concentration

of this mineral are Nili Fossae and a zone of the Valles Marineris rift, which were formed in the Noachian period (40). The fact that these areas have a high abundance of olivines is relevant since it indicates that water activity or the presence of water has not been high historically in these regions. Olivine rapidly transforms into clay minerals in the presence of liquid water, thus, the existence of this primary mineral in high concentration is a good indicator that these areas of Mars have not had relevant aqueous activity since the formation of these rocks (41).

Regarding pyroxenes, they are also abundant throughout the surface of Mars, mainly in the form of orthopyroxenes, mainly enstatite, and clinopyroxenes (low-calcium and high-calcium, respectively). In literature the orthopyroxenes present on Mars are usually associated with older volcanic events occurred in the highland terrain, while the clinopyroxenes are associated with younger volcanic events. The latter minerals have a melting point higher than the former ones, thus, the older magmas of the highlands zones of Mars had higher temperatures than the younger ones that ended as clinopyroxenes (42).

With regard to the feldspars, the dichotomy of Mars once again is observed in its presence and abundance throughout the planet (Figure 1.5) (43). The *Thermal Emission Spectrometer* (*TES*) of the *Mars Global Surveyor* (*MGS*) mission observed that the southern part of the planet was characterized by Noachian aged highlands, which were formed mainly by primary plagioclase-rich basalts. However, it was observed that the northern part was more silica rich and their magmas were younger, being formed mainly by andesites. These magmas were originated from more chemically evolved and volatile-rich magmas (44).

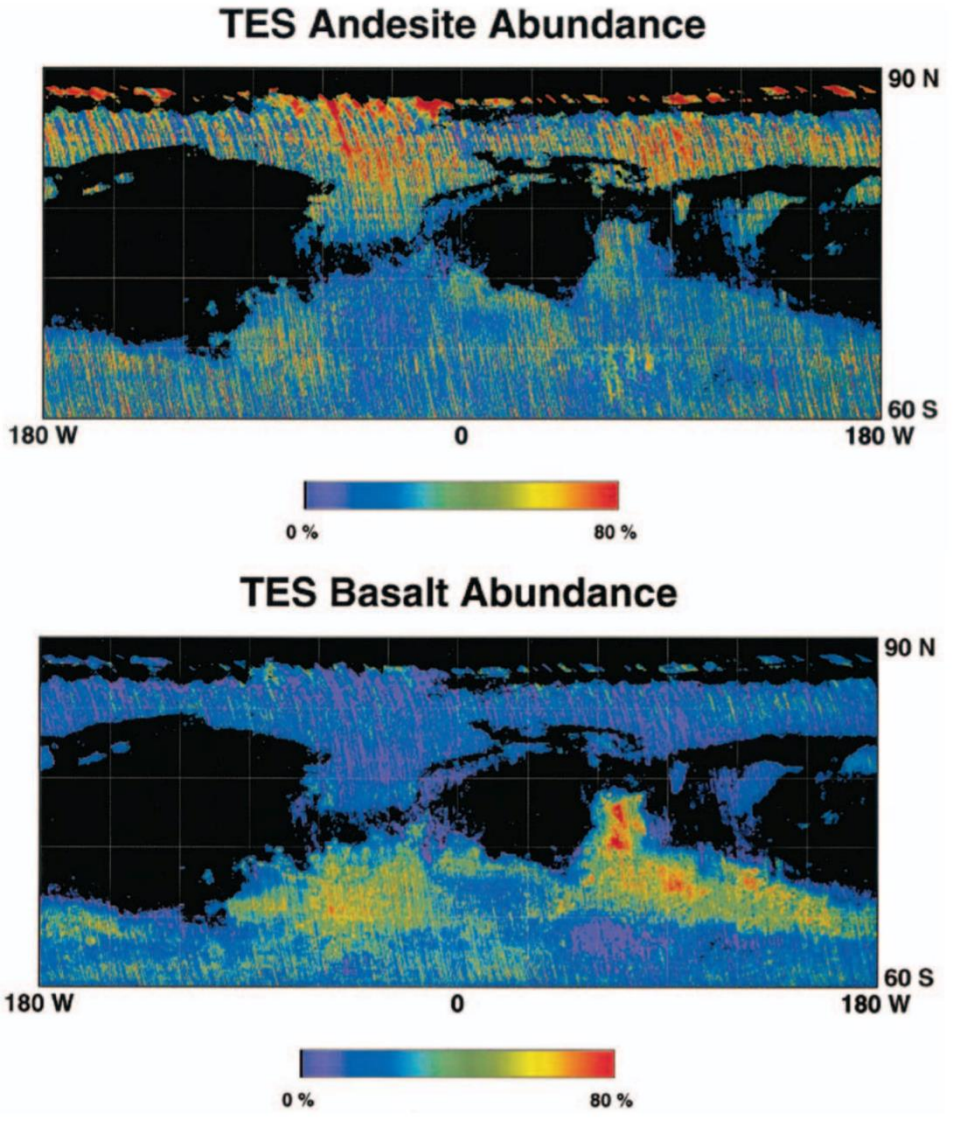


Figure 1.5. Global map of the abundance of andesite (top) and plagioclase-rich basalts (bottom). The regions with high dust content are blacked. Figure extracted from (43)

Besides the three main mineral families present in Mars (olivines, pyroxenes and feldspars), there are also other primary rocks that have been observed thanks to the different missions sent to the planet. For instance, both *TES* and the *Thermal Emission Imaging System* (*THEMIS*) of the *Mars Odyssey* mission identified felsic high silica rocks both in the Syrtis Major region and in one side of the Antoniadi crater. These rocks were characterized as quartz-rich dacites or granitoids (44).

At Gusev crater, the rover *Spirit* discovered several rocks very similar to those from Earth called komatiites, which are ultramafic volcanic rocks derived from the mantle. The ones found at Gusev crater were primitive or picritic basalts and, due to their amount of alkali elements compared to the amount of silica, they were classified as a mixture, or rock “in-between” a basalt, a picrobasalt and a tephrite (45).

In addition to the study of these magmatic primary rocks themselves, other minerals that could be considered as primary were also discovered around and between the basalts. For instance, the rover *Curiosity* observed, with the *Chemistry and Camera complex* (*ChemCam*) instrument, calcium sulfate in several rocks of Gale crater in their veins and nodules (46). This discovery promoted the use of the *Dynamic Albedo of Neutrons* (*DAN*) instrument, which suggested the presence of subsurface water at a depth of 0.6 m with a 4 % of water content in the soil (47).

Besides all these primary rocks and minerals mentioned above, which were the ones formed first in geological time, secondary or alteration minerals have also been found on Mars, which are the result of different alteration and weathering processes on the primary rocks. The minerals found to date have been formed mainly through hydrothermal alterations and weathering processes of the primary basaltic rocks. The ones observed so far have been mainly goethite, hematite, phyllosilicates (clays), iron sulfates, gypsum and opaline silica (48). Some of these minerals, such as opaline silica or the iron sulfate minerals, need to have an environment with low pH water to be formed. In addition, these minerals have been found in areas where fluvial landforms are present, suggesting that abundant water was once present in the region (49).

The formation of these secondary minerals had to have occurred with conditions that would have been suitable for the presence of life. However, if past life ever existed on the planet, its traces had to be conserved to this day on minerals and, in that sense, some types of rocks are better than

others for this purpose, which are the ones that should be investigated in active and future missions. For instance, both phyllosilicates and carbonates are good substrates for the preservation of organic matter (50). In addition, opaline silica and sulfates are good minerals to preserve chemical and morphological fossils, including those of microorganisms as evidence of microbes (51, 52).

Finally, besides the rocks present on the planet, regardless of whether they are primary or secondary, there is an important factor to take into account when studying the surface of Mars, that usually affects any other analysis; the regolith, or Martian dust. It is present almost throughout all the planet and is considered to be as fine as talcum powder. It usually covers the underlying bedrock, making analysis with spectroscopic techniques from both orbiters and rovers complicated or even impossible. This dust is mainly composed of different forms of iron (III) oxide, which, as mentioned above, was formed during the Siderikan period and gives to Mars its characteristic color (53). In addition to those iron oxides, the dust also contains some magnetite and Ti-magnetite, which confer it magnetic properties (54).

## 1.2. Martian Meteorites

Traditionally, meteorites have been defined as solid objects or bodies that come from the space and fall to Earth's surface through its atmosphere (55). However, as it is stated by A. E. Rubin and J. N. Grossman (56), this definition has several lacks. On the one hand, not all objects coming from space are meteorites. For example, the man-made objects, also known as space debris, may fall into Earth's surface. On the other hand, meteorites are not specific to Earth, as they have also been found in the Moon or Mars. Taking all this into account, a meteorite is re-defined as a solid object formed from a celestial body, which travels from the place on which it was formed to a region outside the gravitational field of that body, and that later collides with a body larger than itself (56).

Among all the meteorites found on Earth, the ones that come from Mars are one of the most relevant for several reasons. They are scarcer than other meteorites, only around 200 meteorites from Mars have been found out of a total of over 63000 discovered meteorites (57).

The reason for this scarcity is the high fortuitous series of events that must happen to them in order to reach the Earth's surface. There are several theories that explain these events, but the most extended one is that given by H. J. Melosh (58), who stated that all starts with a big impact event in the surface of Mars caused by a big celestial body. After this impact, which can generate a pressure up to 55 GPa and a temperature up to 1000 ºC in the shock (59), large quantities of Martian rocks are ejected from the planet at high speed (Figure 1.6), reaching a height where the gravity of Mars does not affect these materials any longer. After thousands of years travelling randomly through the Solar System, a small portion of the initial ejected materials reaches Earth's gravitational field and falls into its surface as a meteorite. As can be seen, the series of coincidences that these materials must experiment in order to reach Earth is quite large and, thus, this is the main reason for them to be scarcer than other types of meteorites, such as asteroids (where there is not a need of an impact in the original celestial body) or the ones that come from the Moon (which they need to travel a shorter distance).

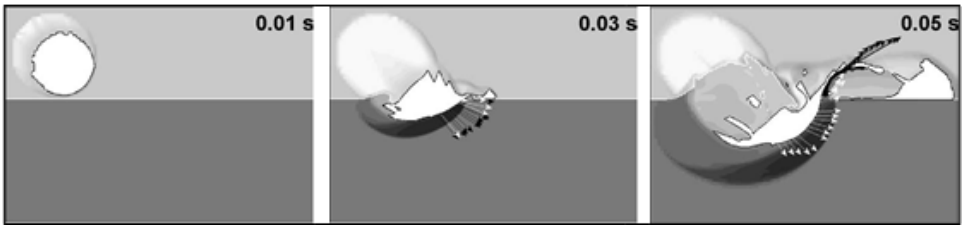


Figure 1.6. Impact of a celestial body (white) with the surface of Mars (dark grey) and the respective times after the contact. Arrows represent vectors of speed, some of them are related to the impact of the body (white) and others to the ejected materials (black). Figure extracted from (60)

When Martian meteorites were first studied, it was obvious that they had different characteristics from the other meteorites analyzed to date (61).

Their crystallization ages are fixed around 4.4 – 4.6 billion years ago and several known characteristics of Mars were ascertained in these meteorites, for example, the lack of a magnetic field in the planet or its magmatic activity along the years, which differentiated them from the rest of meteorites.

All the Martian meteorites had a similar origin of formation, as all of them are igneous rocks. Moreover, they all are achondrites with no chondrules in their structure and their geochemical composition is similar as they are unbrecciated augite to olivine cumulates rocks (61). However, it was observed that not every Martian meteorite was similar to each other, thus, it was concluded that they did not all have the same origin. The main subgroups in which they were divided were shergottites, nakhlites and chassignites (SNC meteorites).

- Shergottites. They were named after the discovery of the first meteorite that belonged to this group, the Shergotty meteorite, fallen in Bihar, India, in 1865. Their origin related to the Mojave crater, which is one of the youngest of Mars (62). Although they have similar characteristics, they can be subclassified into different groups attending to various properties, their rare-earth elements content, for instance (63).
- Nakhlites. The first nakhlite, Nakhla meteorite, fallen in Alexandria, Egypt, in 1911, gave the name to this Martian meteorite group. Their origin is still unknown, although they are thought to be related to one of the large volcanic zones of Tharsis, Elysium or Syrtis Major Planum (64).
- Chassignites. They were named after the discovery of Chassigny meteorite, which fell at Haute-Marne, France, in 1815. Their Martian origin is totally unknown nowadays, which could be due to the fact that there are very few meteorites in this category.

The SNC meteorites are one of the main ways to study the geology and chemical composition of Mars. Thanks to the analysis of Martian meteorites, among other discoveries, it has been possible to study the existence of water in the planet (65), its reservoir evolution (66) or even the possible existence of biological activity in the past (67). In addition, regarding the study of the mineralogy of Mars and the composition of its surface through the analysis of meteorites, questions like how was the magmatic activity during the formation of the planet (68), which was the origin of sulfates and sulfides in Martian surface (69) or what is the periodicity of resurfacing events and geological ages (70) have been addressed. As can be seen, the analysis of Martian meteorites allows the study of very diverse characteristics of the planet.

However, the study of this type of samples has an important and relevant drawback, as that not all the materials that form the meteorites are original from Mars, since, once they arrive to Earth's surface, the terrestrial weathering processes can alter them. This phenomenon alters and transforms the composition and mineralogy of the meteorites, which can cause misleading conclusions about Mars. In the literature there are works that study this type of alterations and the secondary products they form instead of the original materials from Mars, since it is of the same importance to know which are the original materials from the Red Planet and which are not (71-73). In fact, these studies usually help to correct errors, for example, the existence of biological activity in Mars (67), which was asserted because the alterations suffered by a meteorite on Earth were not taken into account.

## 1.3. Remote Exploration of Mars

As explained above, Martian meteorites can be a great source of information about the Red Planet, since they are currently the only source of material from Mars that we have on Earth. This fact makes the study of this type of samples of great relevance, since they can be analyzed by any

analytical technique that exists today. Even so, special caution must be taken, since terrestrial weathering can lead to misleading conclusions about Mars. To avoid such misleading conclusions, the best solution would be to obtain samples directly from the surface of the planet and return them to Earth, as has already been done on the Moon (74). Unfortunately, no mission to Mars has yet been developed for this purpose. Therefore, the best way to obtain data directly from Mars, making sure that the analyzed samples have not been altered at any time, is to analyze its surface through orbiter, lander and rover missions. Most of the missions launched to Mars have been focused on the analysis of the mineralogy, petrology and chemical composition of the planet, which provide great clues for a better understanding of the planet.

### 1.3.1. Previous Mars Missions

There have been many missions to Mars with a multitude of different objectives, both with scientific and technology testing purposes. Table 1.1 shows the successful Martian missions to date and their major objectives and/or payloads and achievements.

Table 1.1. Summary of all the successful Mars mission through history

| Mission name | Launch Year | Agency | Mission Type | Objectives / Major Discoveries |
|---|---|---|---|---|
| Mariner 4 | 1964 | NASA | Flyby | - First successful flyby of Mars in history<br>- First picture of a planet returned from deep space |
| Mariner 6 & 7 | 1669 | NASA | Flyby | - First atmospheric and surface results with a probe to prepare for future missions |
| Mars 2 (orbiter) | 1971 | Soviet Union | Orbiter | - Image the Martian surface and clouds and study its topography<br>- Determine temperatures of the planet and monitor atmospheric properties |
| Mars 3 (orbiter) | 1971 | Soviet Union | Orbiter | - Study the topography of the Martian surface<br>- Analyze the soil composition and study the possible Martian magnetic field |
| Mars 3 (lander) | 1971 | Soviet Union | Lander | - The first lander on Mars<br>- The first partial image of Mars was obtained. The lander lost contact while sending the image |

Table 1.1. Summary of all the successful Mars mission through history (continuation)

| Mission name | Launch Year | Agency | Mission Type | Major Results or Discoveries |
|---|---|---|---|---|
| Mariner 9 | 1971 | NASA | Orbiter | - The first orbiter of Mars<br>- Atmospheric studies and map the Martian surface closer and with higher quality |
| Mars 5 | 1973 | Soviet Union | Orbiter | - Keep mapping the surface<br>- Measurements of uranium, thorium and potassium content similar to those of terrestrial igneous rocks |
| Mars 6 & 7 | 1973 | Soviet Union | Flyby | - It carried a magnetometer to study Mars<br>- Intended to study cosmic rays and proton and electron fluxes from the Sun |
| Viking 1 (orbiter) | 1975 | NASA | Orbiter | - It carried two vidicon cameras to take better images<br>- It performed a surface thermal mapping<br>- It carried an IR spectrometer for a water vapor mapping |
| Viking 1 (lander) | 1975 | NASA | Lander | - It did the first clear image ever transmitted from Mars<br>- Performed the first experiment whose purpose was to look for evidence of life |

Table 1.1. Summary of all the successful Mars mission through history (continuation)

| Mission name | Launch Year | Agency | Mission Type | Major Results or Discoveries |
|---|---|---|---|---|
| Viking 2 (orbiter) | 1975 | NASA | Orbiter | - River valleys were found in many areas, which started the hypothesis about past liquid water on Mars |
| Viking 2 (lander) | 1975 | NASA | Lander | - Soil was analyzed and some weathering products of mafic igneous rocks were found<br>- Another biology experiment was carried out |
| Mars Global Surveyor | 1996 | NASA | Orbiter | - It performed a global mapping of Mars<br>- It carried out topographic mapping of the planet with MOLA<br>- It was used for atmospheric monitoring |
| Mars Pathfinder (lander) | 1996 | NASA | Lander | - It carried a magnetometer and an anemometer<br>- It performed atmospheric and meteorological measurements |
| Mars Pathfinder - Sojourner | 1996 | NASA | Rover | - It was the first rover to operate on another planet<br>- It carried several experiments to perform on the planet' s surface |

Table 1.1. Summary of all the successful Mars mission through history (continuation)

| Mission name | Launch Year | Agency | Mission Type | Major Results or Discoveries |
|---|---|---|---|---|
| Mars Odyssey | 2001 | NASA | Orbiter | - Mapping the levels of elements across the Martian surface<br>- Determine subsurface hydrogen<br>- Mapping of the mineral composition |
| Mars Express | 2003 | ESA | Orbiter | - Obtain high resolution photo-geology (10 m), mineralogical mapping (100 m) and atmospheric composition mapping<br>- Study the interaction between the atmosphere and the subsurface |
| Spirit | 2003 | NASA | Rover | - Study the geology of the surface, specially the one involving water processes<br>- Search for iron containing minerals |
| Opportunity | 2003 | NASA | Rover | - Study the geology of the surface, specially the one involving water processes<br>- Search for iron containing minerals |
| Mars Reconnaissance Orbiter | 2005 | NASA | Orbiter | - Study the geology and climate of Mars<br>- Provide reconnaissance of future landing sites<br>- Relay data from surface back to Earth |

Table 1.1. Summary of all the successful Mars mission through history (continuation)

| Mission name | Launch Year | Agency | Mission Type | Major Results or Discoveries |
|---|---|---|---|---|
| Phoenix | 2007 | NASA | Lander | - Study the geological history of water<br>- Study past or potential habitability of the planet |
| Curiosity | 2011 | NASA | Rover | - Determine the landing site habitability<br>- Study the climate and geology of Mars<br>- Serve as preparation for future human missions |
| Mars Orbiter Mission | 2013 | ISRO | Orbiter | - Develop technologies for future interplanetary missions<br>- Explore the Martian surface<br>- Study the atmosphere and its dynamics |
| MAVEN | 2013 | NASA | Orbiter | - Determine the history of the loss of atmospheric gases to space<br>- Provide answers about Martian climate evolution |
| ExoMars Trace Gas Orbiter | 2016 | ESA / Roscosmos | Orbiter | - Study the Martian atmosphere and its evolution<br>- Provide subsurface analyses of gases |

Table 1.1. Summary of all the successful Mars mission through history (continuation)

| Mission name | Launch Year | Agency | Mission Type | Major Results or Discoveries |
|---|---|---|---|---|
| InSight | 2018 | NASA | Lander | - Study the deep interior of Mars and the earliest evolutionary processes of the planet |
| MarCO A | 2018 | NASA | Flyby | - Test new miniaturized communication and navigation technologies |
| MarCO B | 2018 | NASA | Flyby | - Test new miniaturized communication and navigation technologies |
| Hope | 2020 | MBRSC | Orbiter | - Study the atmosphere of Mars and its layers globally from a supersynchronous orbit |
| Tianwen-1 (orbiter) | 2020 | CNSA | Orbiter | - Validate the communication and control technologies in deep space for future missions |

### 1.3.2. Mars 2020 Mission

Among the missions to Mars launched in the latest launch window there is NASA's Mars 2020 mission, which forms part of NASA's Mars Exploration Program (MEP). The spacecraft was launched from Cape Canaveral on the 30th of July of 2020 and arrived at its destination on the 18th of February of 2021. The main objectives of the mission follow those of the previous missions but, in this case, they will be carried out with a much more complete vehicle and instrument suite.

In addition, during the mission, the rover Perseverance will be able to sample from the surface of Mars and store the samples in 43 different tubes. These tubes form part of NASA's Mars sample-return mission efforts, as they will be part of a future mission, carried out by NASA and ESA, where the tubes will be picked up and carried back to Earth (75).

The main goal of Mars 2020 is to search for clues of past life on the planet, including biosignatures of past microbial life, water and an environment with past good habitability conditions. Regarding the latter, the mission will also test technology for future robotic and human exploration. These objectives will be reached by exploring and analyzing the geological diversity of the surroundings of the landing site (76).

In order to find the geological diversity needed to achieve all these objectives, the selected landing site for the mission was Jezero crater. This crater has a diameter of around 49.0 km and is located in the Syrtis Major quadrangle of Mars, whose mainly regions are Syrtis Major Planum, the impact basin Isidis Planitia and the grabens of Nili Fossae (Figure 1.7).

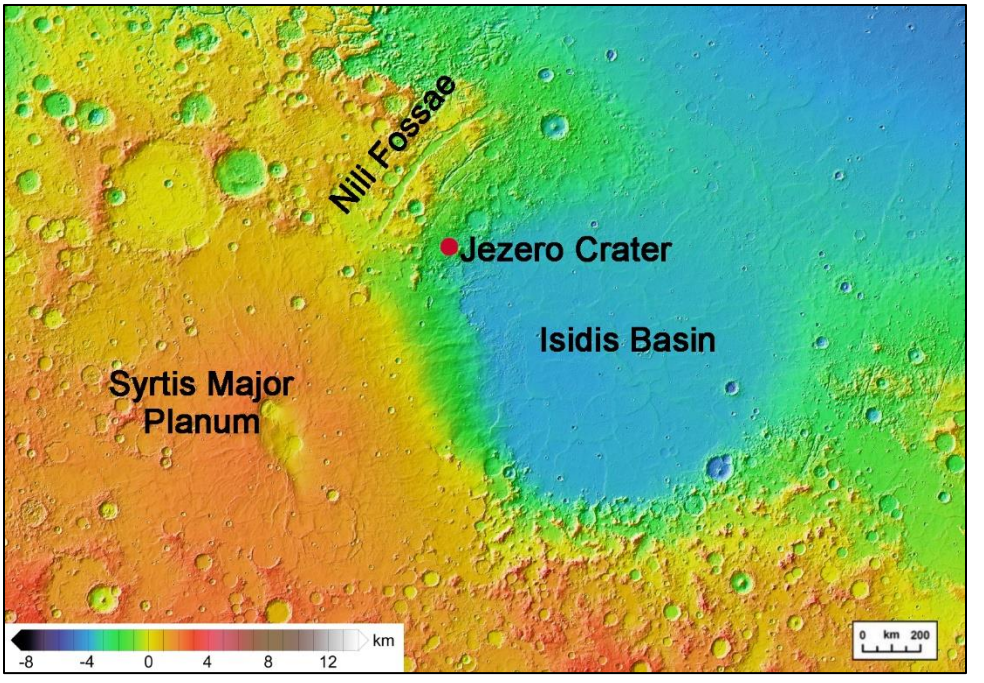


Figure 1.7. Jezero crater (red dot) represented in the Syrtis Major quadrangle, using a *Mars Orbiter Laser Altimeter* (*MOLA*) topographic map of Mars. Figure extracted from (21)

Through observations made of the crater, especially the geomorphic mapping and visible to near-infrared spectral analyses of the region, it was deduced that an ancient Martian lake system existed in Jezero (77). That study suggested the idea that the crater was filled with water at least in two different occasions. As observed in Figure 1.8, it has two channels that supplied liquid water to it, both in the northern and western side of the crater. Both channels have nowadays a geological formation similar to those of deltas on Earth, suggesting that the liquid water that flowed through those channels into the lake carried sediments that were deposited mainly in the crater entrance. This fact was demonstrated thanks to a study that correlated the diameter of a crater with its depth (78). When a crater is not deep enough depending on its diameter, it means that something entered and filled the crater, in this case, the sediments carried by the water. Some further calculations suggest that the crater has around 1 km of sediments depth (79).

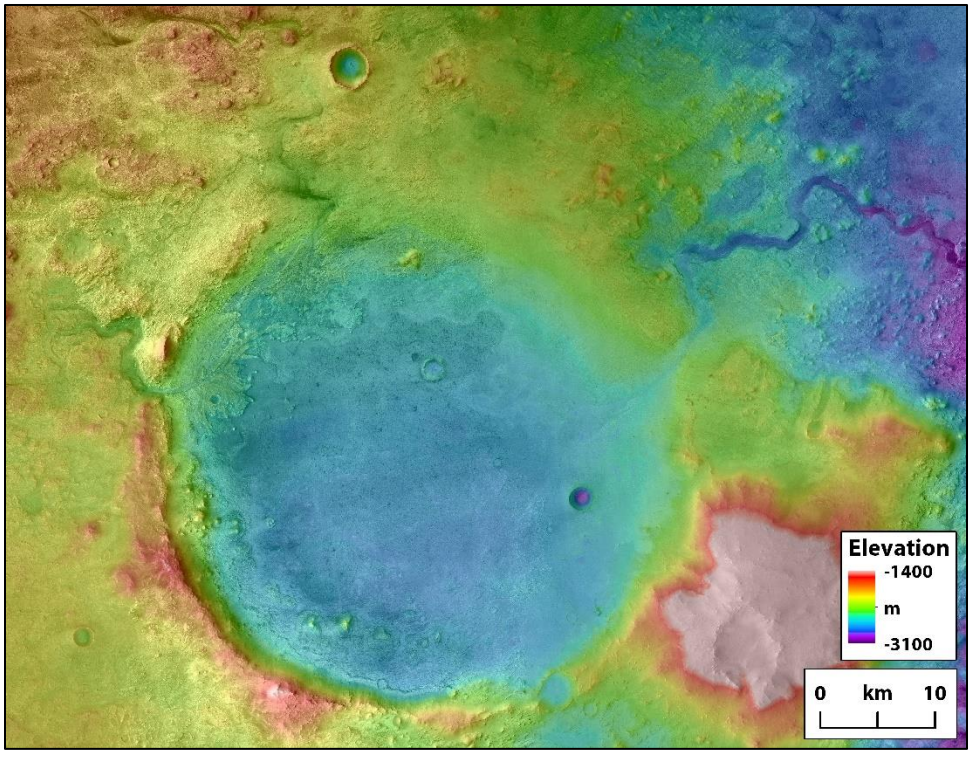


Figure 1.8. *MOLA* picture of the Jezero crater where both the northern and the western delta formations are observed. Their elevation compared with the crater bottom suggest large quantities of sedimentary material. Figure extracted from (21)

Due to its size and morphology, it is believed that the deltas needed around 10 million years to form (79). In addition, clay minerals have been found around the crater, some of them being identified as smectites (50, 80). These two factors make the chances that life could have existed in this area in the past higher than in other areas of Mars. Therefore, it is an ideal place to send a mission whose objective is to find traces of life or to search for areas that had habitability conditions in the past.

### 1.3.3. Perseverance Rover

In order to achieve all the goals and objectives outlined by NASA's Mars 2020 mission, all the scientific payload was set in the rover *Perseverance*. It landed on an area called Octavia E. Butler Landing (near the west delta of Jezero crater) and was later photographed, surrounded by different

mission landing elements, by the *ExoMars Trace Gas Orbiter* with its *CaSSIS* camera (Figure 1.9).

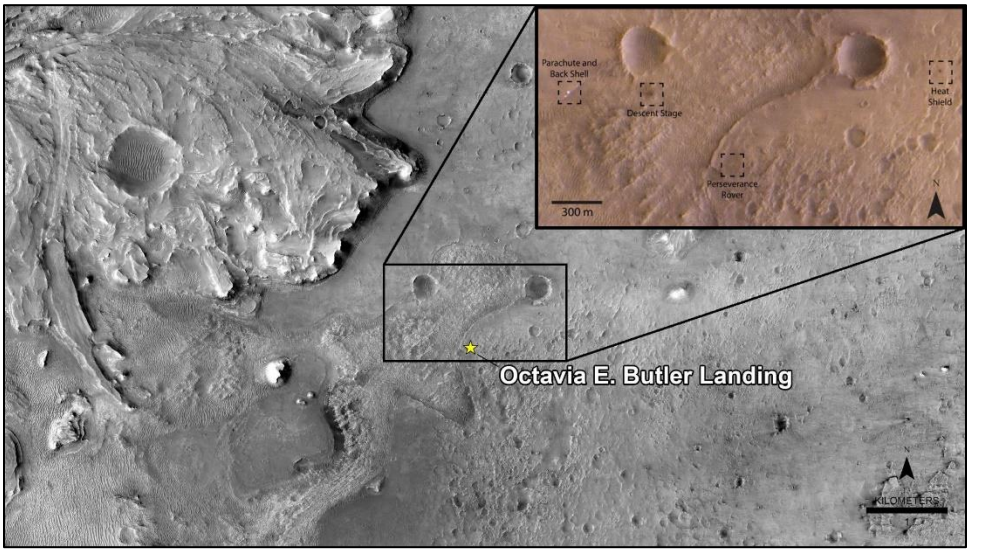


Figure 1.9. Octavia E. Butler Landing site of Perseverance rover, with a detailed picture where the rover, the parachute and back shell, the heat shield and the descent stage can be observed (Credit: NASA and ESA)

Perseverance has a similar design to *Curiosity*, its predecessor, both visually and regarding some instruments of its scientific payload. They both have similar body plan, landing system, cruise stage, and power system. However, *Perseverance* weighs 1025 kg, 126 more kilograms than *Curiosity*. This weigh increase is due carrying heavier instruments and several modifications and improvements that make the rover heavier. For instance, the wheels of the rover are more robust, since the ones from *Curiosity* were damaged while cruising the surface of Mars (81). Regarding its scientific payload, the rover carries 7 different instruments (Figure 1.10). In addition, it also carries a small helicopter, *Ingenuity*, as a flying on Mars technology test (82) and a system to drill, sample and store Martian soil and rocks.

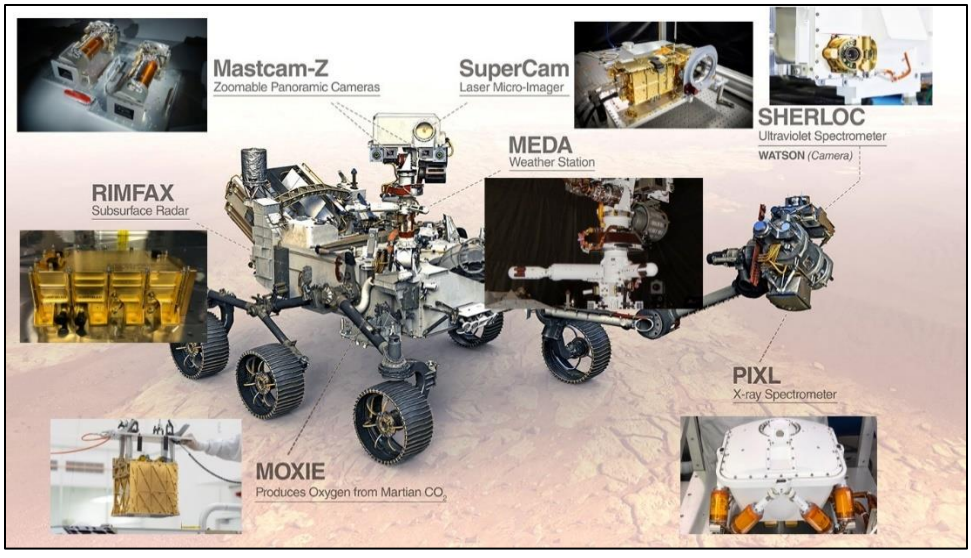


Figure 1.10. Perseverance's scientific instruments and their location in the rover. Small pictures of: the twin *Mastcam-Z* cameras, *MEDA* instrument, *MOXIE* box, *PIXL*'s sensor head, *RIMFAX* radar, *SHERLOC*'s engineering model and *SuperCam*'s mast unit (Credit: NASA)

*Mastcam-Z* consists of a twin set of cameras that will be able to take stereoscopic images of Mars. It is a camera system mounted in the mast of the rover, equipped with a zoom in function that will be able to focus and take 3D and panoramic color pictures and video at high speed and high definition of the surface of the planet (83). In fact, *Mastcam-Z* has already made its first 360 degrees high resolution panoramic picture of the Martian surface (Figure 1.11)

Figure 1.11. First 360 degrees panoramic picture of Mars taken by *Mastcam-Z* (Credit: NASA)

The *Mars Environmental Dynamics Analyzer* (*MEDA*) has a set of sensors that measure atmospheric parameters and monitors the Martian weather. It measures temperature, wind speed and direction, pressure, relative humidity, radiation and dust particle size and shape. Over time, it will be able to provide something similar to a "weather forecasts" (84).

The *Mars Oxygen In-Situ Resource Utilization Experiment* (*MOXIE*) is a technology test related with oxygen generation from the atmosphere. It will produce small quantities of oxygen using the carbon dioxide from Martian atmosphere. If successful, this technology could be scaled up in the future to sustain the oxygen required by a possible manned mission to Mars. This produced oxygen could also be used as propellant for the return of that manned mission (85).

The *Planetary Instrument for X-Ray Lithochemistry* (*PIXL*) is an X-ray fluorescence spectrometer mounted on the turret at the end of the robotic arm. It will be able to determine the fine scale elemental composition of the different Martian surface materials. It also has a camera that takes close-up pictures of rocks and soil textures (86).

The *Radar Imager for Mars' Subsurface Experiment* (*RIMFAX*) consist of a ground penetrating radar waves that analyzes and detects different ground densities. With this information, it will be possible to discern the presence of different geological and structural layers, buried rocks, meteorites and water (both as liquid and solid form). *RIMFAX* will be able to work to a depth of up to 10 m (87).

The *Scanning Habitable Environments with Raman & Luminescence for Organics & Chemicals* (*SHERLOC*) is an ultraviolet Raman spectrometer that will be able to characterize the fine-scale mineralogy of the surface of Mars, especially any organic compound thanks to its ultraviolet laser. This instrument is mounted on the rover's robotic arm. It also has cameras integrated in order to take close-up pictures and focus on the samples (its only color camera is called *WATSON*) (88).

Finally, last but not least, the *SuperCam* instrument will be able to perform imaging and chemical composition and mineralogy analysis from a distance thanks to its lasers and spectrometers. It is mounted in the rover mast and it will be able to analyze targets from a distance up to 7 m, providing with information about the composition of the Martian surface. It could be used as a way to analyze rocks far from *Perseverance* before the rover gets close enough to be able to analyze them with other instruments. *SuperCam* will be able to perform laser-induced breakdown spectroscopy (LIBS), Raman spectroscopy, time-resolved luminescence spectroscopy (TRLS), visible and near infrared spectroscopy (VISIR), remote micro-imaging (RMI) and microphone recordings (89-91).

### 1.3.4. SuperCam, a Multipurpose Instrument

As stated above, *SuperCam* is an instrument that will be able to assess the chemical and geological composition of the different features of the surface of Mars from afar. It is an upgraded version of the instrument *ChemCam* of the rover *Curiosity*, which is able to do Laser-induced breakdown spectroscopy (LIBS) and remote imaging. From a physical point of view, overall speaking *SuperCam* is less heavy than *ChemCam*, although its Mast Unit (MU) and calibration targets weight a little bit more (89, 90). Table 1.2 present some of its physical properties.

Table 1.2. Some physical properties of *SuperCam* (89)

| | **Mass (kg)** | **Dimensions (l x w x h; mm)** | **Maximum Power (W)** |
|---|---|---|---|
| **Mast Unit (MU)** | 6.11 | 383 x 201 x 163 | 27 |
| **Body Unit (BU)** | 4.44 | 221 x 157 x 205 | 43 |
| **Calibration Targets** | 0.24 | 110 x 85 x 11 | 0 |
| **Total** | 10.79 | - | 70 |

Another difference between *SuperCam* and *ChemCam* is the material of which the spectrometers of the instrument were made. Due to the instantaneous changes of temperature in the spectrometers on Mars, which might suffer changes of 20 ºC diurnally, the spectrometers were made of titanium instead of beryllium (*ChemCam*). This change helped to reduce the thermal expansion caused by the temperature changes, which affect the wavelength calibration, as titanium has a lower coefficient of thermal expansion than beryllium (89, 90).

Regarding its location in the rover, Figure 1.10 only shows the location of the most iconic part of *SuperCam*, its Mast Unit, which is placed at the top of the mast of the rover and it contains the laser, telescope, RMI, infrared spectrometer and the microphone. This part of the instrument was designed and built at the Centre National d'Etudes Spatiales (CNES, France). However, this is not the only part of *SuperCam*, as it also has another part called Body Unit (BU) integrated inside the body of the rover, which is as important as the Mast Unit. The Body Unit contains an optical demultiplexer, optical spectrometers for LIBS, Raman, and passive VIS spectroscopy and the electronics that control both the Body Unit and Mast Unit (89, 90). This part of the instrument was built and designed at Los Alamos National Laboratory (LANL, USA). Finally, the third part of the instrument, the calibration targets are placed close to the rear of the rover in an angle of 50º relative to horizontal and at a distance of 1.5 m from the Mast Unit. This part of the instrument was designed by the University of Valladolid (Spain) and built by the company AVS (Spain). The University of the Basque Country (Spain) took part in the testing and checking of all the targets. The calibration targets consist mostly of sintered pellets and will allow the calibration and health status checking of the different techniques of *SuperCam* (91). The instrument scheme and its different parts are depicted in Figure 1.12.

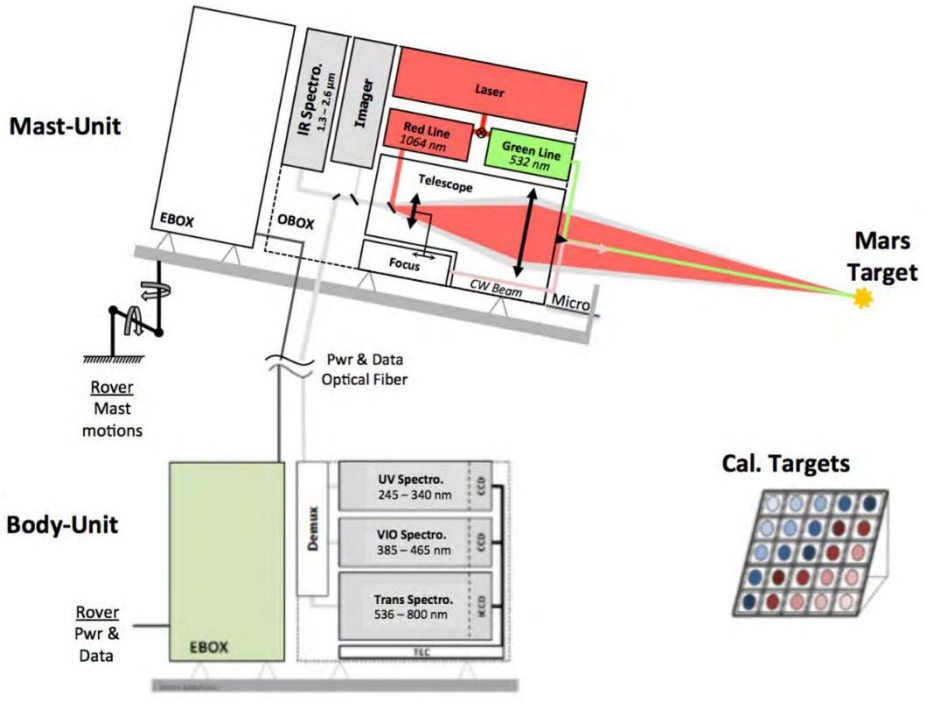


Figure 1.12. Schematic diagram showing the major components and subcomponents of the *SuperCam* instrument. Figure extracted from (89)

Using this setup, *SuperCam* will be able to perform different spectroscopic and imaging techniques. These techniques will allow the characterization of both the elemental and mineralogical composition of the surface of Mars. They are summarized in Table 1.3.

Table 1.3. Techniques that SuperCam is able to perform for Mars' surface analysis (89)

| Technique | Purpose | Maximum Distance | Footprint |
|---|---|---|---|
| **LIBS** | Quantitative elemental abundances | 7 m | 0.25-0.45 mm |
| **Raman** | Identification of Raman-bright minerals, organics | 7 m | 0.74 mrad |
| **TRLS** | Identification of organics, minerals, REEs | 7 m | 0.74 mrad |
| **VISIR** | Identification of minerals; atmospheric studies | To km | VIS: 0.74 mrad IR: 1.2 mrad |
| **RMI** | Rock textures, contexts | To km | 18.8 mrad |
| **Microphone** | Physical properties of rocks, atmospheric studies | 4 m | - |

LIBS is the technique responsible of the elemental characterization of the targets shot by *SuperCam*. This technique provides atomic emission spectra of the material ablated by the laser. It gives the quantitative elemental composition of major, minor and trace elements. Using this technique, *SuperCam* will be able to quantify the presence and abundancy of around 25 elements, which will give important information about both the main mineral composition and any trace element present in it. The laser used to ablate the target and create the plasma provides up to 14 mJ of 1064 nm photons. In addition, it will be possible to amplify weak emission signals in special cases, using time gating and intensification of the signal with the transmission spectrometer (green and red spectral range) (89, 90).

Thanks to the pulsed laser and time-gated spectrometer, *SuperCam* will also be able to perform TRLS. The laser produces fluorescence depending on the composition of the target hit. This fluorescence is emitted mainly by organic compounds and rare earth elements and generally has a decaying time of several picoseconds (92). This signal is detected by *SuperCam's*

spectrometers and can be used to discover organic materials from afar or characterize the rare earth elements present in minerals (89, 90).

*SuperCam* will also be able to do conventional VISIR measurements of the surface of Mars. This technique will use several spectrometers of the instruments. On the one hand, a wavelength-scanning spectrometer will be used for the near infrared range, as this spectral region provides clues for the identification and characterization of phyllosilicates. On the other hand, the visible range will be covered by the same spectrometers used for the LIBS, Raman and TRLS measurements, specifically, the violet (VIO) and the transmission spectrometer (89, 90).

The RMI technique of *SuperCam* will be able to obtain high resolution images of the analyzed areas for a contextualization and to help in the interpretation of the targets, thanks to the Bayer-filter color images with a resolution better than 80 microradians (89, 90).

Regarding the microphone, it can be used for several purposes during the missions. It will be able to record the sounds of Martian wind, which will help the instrument MEDA to determine the wind speed and even its direction. In addition, it can record the sound emitted by the LIBS shockwave when the plasma is created by the laser. The sound of this shockwave can be used to determine the hardness and density of the analyzed targets, which are relevant characteristics for a proper characterization of the studied rocks (89, 90, 93).

Finally, *SuperCam* will also be able to do measurements of distant targets using Raman spectroscopy, which is the main focus of this PhD thesis. Specifically, *SuperCam* will perform the first measurements of Raman spectroscopy using a green laser ever in space and it shares the distinction of the first planetary Raman spectrometer with SHERLOC. It uses the same pulsed laser as the one used for LIBS, but in this case its frequency is doubled to 532 nm. In order to obtain good signals, an intensifier is attached to the gated detector, which are coupled to a transmission

spectrometer. Instead of focused, the green Raman laser is collimated, and it overlaps with the 0.74 mrad field of view of the spectrometer. Thus, its footprint can range between 1.5 mm of diameter to 5 mm, depending on if the target is straight down at the ground or if it is at a distance of 7 m, respectively (89, 90).

## 1.4. Raman Spectroscopy, its Importance for Space Exploration

Raman spectroscopy is a technique that will be used for the first time in space exploration. Within the *Perseverance* rover, it is present on both the *SuperCam* remote analysis instrument and the *SHERLOC* contact analysis instrument. This spectroscopic technique provides the characterization of the molecular composition of the analyzed surface. In other words it will make it possible to determine the mineralogy and the compounds present on the surface of Mars. This fact is of great importance both for fulfilling the objectives of the Mars 2020 mission and for the study of other relevant features of the planet through these geological data, as has been explained in previous sections.

The Raman effect was discovered by the Indian physicist Chandrasekhara Venkata Raman, which gave name to the technique. As observed in Figure 1.13, Raman spectroscopy is based on a phenomenon that occurs when a source of light (usually a monochromatic laser, for intensity reasons) hits a surface. This laser light interacts with the molecular bonds and alters their vibrations. This results in electron jumps to a virtual state, which then return to their original ground electronic state. The resulting energy when that electron returns to its original state is called Rayleigh scattered light and is the most frequent scattered light that happens after this electron excitation. However, that electron might return to a different vibrational level than its original one, which might be of a higher energy or of lower energy. The light scattered when it returns from the virtual state to a vibrational level is called Stokes Raman scattering and Anti-Stokes Raman scattering, respectively. Raman spectroscopy is based on the collection and recording of that shift

in energy and usually the Stokes Raman scattering is the one used and recorded (94).

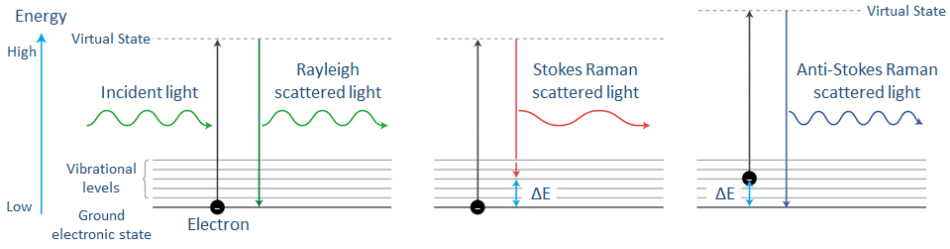


Figure 1.13. Depiction of the Raman phenomenon

As that shift in energy is related to the chemical molecular bond in a compound, the resulting signal is different depending on this bond and the elements and other bonds that surround it. In addition, different compounds have more, less or different bonds, as each compound is unique compared to others. This is translated in different amount, types and shapes or intensities of Raman signals, which means that each compound has a unique Raman spectrum that can be used to identify it. Therefore, using this technique, ideally, it will be possible to characterize the mineralogy of the analyzed surface by SuperCam unambiguously.

In addition to its traditional use, Raman spectroscopy can also be employed for other things. As many spectroscopic techniques, its signal intensities do vary depending on the concentration of the analyzed compound. For instance, this fact has been used for years by the pharmaceutical industry to quantify the amount of a given active ingredient or some excipient in medications (95). While this feature of Raman spectroscopy has been exploited by the pharmacological field, other fields have made almost no use of it. In geology, some similar methods have been proposed in literature (96), although this capability is almost not exploited as in the pharmaceutical industry. It would be very helpful to have more development around this use of the technique, as it would be of great use to determine the abundancy of a mineral in a rock, or to estimate the

weathering grade of a rock by measuring the amount of weathered product versus the primary minerals. As explained in previous sections, this knowledge would be of high relevance for the study of Mars.

In the geological field, Raman spectroscopy is also of great use, as a lot of geochemical information of a sample can be obtained from it. For instance, it is usually one of the go-to techniques for the characterization of meteorites. It has been proven in literature, using a meteorite as a testing sample, that this technique can be used in space exploration to characterize reliably the major, minor and trace mineral phases of a sample (97, 98). In addition, Raman spectroscopy can be used to distinguish different minerals of the same geological family that would be hard to differentiate with other spectroscopic molecular techniques, as it was done with the Fe, Ti and Cr oxides in the Elephant Moraine (EETA) 79001 meteorite (99). This technique not only allows to do a mineralogical characterization of a given sample, but it is also possible to assess the structural and compositional characteristics of certain minerals with it, such as in the case of quadrilateral pyroxenes, which are common on the surface of Mars (100). Besides the results directly related to the mineralogy of a sample and its structure, this technique also provides results in meteorite studies regarding other physical properties, such as the possible pressure shock that the sample endured, how intense was it, or if it suffered a progressive shock metamorphism or not (101-103).

In addition to all the information that is obtained through Raman spectroscopy in meteorite analyses, it is also employed in the study of terrestrial Martian analogs, both in-situ and in the laboratory to analyze sampled rocks. This technique has been used to characterize for the first time several Martian analogs in the Basque-Cantabrian basin (104, 105) and has been employed to study other Martian analog emplacements worldwide (106-108), since it is considered a very reliable technique to analyze surfaces similar to those of Mars. It has even been proven that it is able to characterize bio-geological signatures in analogs (109).

Raman spectroscopy also provides relevant information of the different minerals that are expected to be found on Mars, specifically, in Jezero crater. Regarding the volcanic rocks that *Perseverance* will encounter, Raman spectroscopy is able to determine the structural properties of pyroxenes and estimate the metallic composition of some of them (110, 111), characterize the feldspars present in the surface, their alkalinity grade, estimate the temperatures of the magmas from which they were formed or even assess if the feldspar suffered high-pressure in the past (112-114) and study the presence of olivine and its metallic composition (115). This spectroscopic technique is also suitable to study the different deposits formed in the delta of Jezero crater, as minerals of the sulfates and carbonates families give very good and strong Raman signals. They can be even used to determine the different hydration states of these compounds or the presence of some bacterial traces inside the deposits (116, 117).

Besides the study of the current mineralogic composition of a rock or the mineral properties, Raman spectroscopy has also been employed in literature to elucidate the formation processes of certain minerals that are present on Mars. For instance, the gypsum-syngenite-görgeyite system and the conditions needed for the transformation of one mineral to another have been studied by Raman spectroscopy (118). These minerals are very relevant because, as calcium sulfate polymorphs, they are potential reservoirs of organic compounds or traces of biosignatures on the Red Planet.

In addition to the results that can be obtained regarding the molecular characteristics of the sample (its mineralogy or the abundance of different compounds in the target), Raman spectroscopy can also be used to estimate certain elemental compositions of some minerals, even though it is a molecular technique. As stated above, the signal position and shape vary in function of the molecular chemical bonds and also of the different elements that surround the bond. In other words, depending of certain

elements relative composition that chemical bonds do vary, meaning that certain Raman signals might vary and, thus, could be calibrated to estimate that elemental relative composition of the analyzed surface. This feature is already used in the geological field with great results, although it still lacks of good accuracy and simplicity in its calibration models (94, 119).

All these ways of obtaining information from the analyzed samples through Raman spectroscopy can be of great relevance, especially when *SuperCam* is the only remote instrument for mineralogical analysis. This means that all the results that *SuperCam* can obtain have to be squeezed out as much as possible to get the maximum possible information from each spectrum. Therefore, a further deepening of the Raman methodologies for obtaining results would be necessary to not only characterize the minerals present on the surface of Mars, but also to use this technique combined with others and to develop new analytical strategies for the non-destructive analysis of the future returned Mars samples. This PhD thesis has been designed to contribute to that development of methodologies based on Raman spectroscopy.

## 1.5. Bibliography

1. Ruggles, C. L. N., Ancient Astronomy: An Encyclopedia of Cosmologies and Myth, 1st ed. **2005**, ABC-CLIO, Santa Barbara, California, USA.

2. Powell, J., From cave art to Hubble; Cave Paintings That Recorded the Night Sky (p.p. 9-16) **2019,** Springer, New York, USA.

3. Thompson, J. E. S., Maya astronomy, *Philosophical Transactions of the Royal Society of London. Series A, Mathematical and Physical Sciences,* **1974**, 276, 83-98.

4. James, E., The History and Practice of Ancient Astronomy, 1st ed. **1998**, Oxford University Press, Oxford, UK.

5. Bayer, J., Uranometria, omnium asterismorum continens schemata, nova methodo delineata aereis laminis expressa, **1603**, Christoph Mangle, Augsburg, Germany.

6. Sheehan, W., Bell, J., The Planet Mars: A History of Observation and Discovery, 1st ed. **1997**, The University of Arizona Press, Arizona, USA.

7. Lowell, P., Lockyer, J. N., First photographs of the canals of Mars, *Proceedings of the Royal Society A: Mathematical, Physical and Engineering Sciences,* **1906**, 77, 132-135.

8. Lowell, P., Mars and its Canals (reproduction of the original), **2020**, Outlook Verlag GmbH, Frankfurt, Germany.

9. Geyh, M. A., Schleicher, H., Absolute Age Determination: Physical and Chemical Dating Methods and Their Application, **1990**, Springer-Verlag, Berlin Heidelberg.

10. Talboys, D. L., Barber, S., Bridges, J. C., Kelley, S. P., Pullan, D., Verchovsky, A. B., Butcher, G., Fazel, A., Fraser, G. W., Pillinger, C. T., et al., In situ radiometric dating on Mars: Investigation of the feasibility of K-Ar dating using flight-type mass and X-ray spectrometers, *Planetary and Space Science,* **2009**, 57, 1237-1245.

11. Neukum, G., Wise, D. U., Mars: A Standard Crater Curve and Possible New Time Scale, *Science,* **1976**, 194, 1381-1387.

12. Neukum, G., Hiller, K., Martian ages, *Journal of Geophysical Research: Solid Earth,* **1981**, 86, 3097-3121.

13. Hartmann, W., Neukum, G., Cratering Chronology and the Evolution of Mars, *Space Science Reviews,* **2001**, 96, 165-194.

14. Hartmann, W. K., Martian cratering 8: Isochron refinement and the chronology of Mars, *Icarus,* **2005**, 174, 294-320.

15. Hartmann, W. K., Martian cratering 9: Toward resolution of the controversy about small craters, *Icarus,* **2007**, 189, 274-278.

16. Carr, M. H., Head, J. W., Geologic history of Mars, *Earth and Planetary Science Letters,* **2010**, 294, 185-203.

17. Bibring, J., Langevin, Y., Mustard, J. F., Poulet, F., Arvidson, R., Gendrin, A., Gondet, B., Mangold, N., Pinet, P., Forget, F., et al., Global Mineralogical and Aqueous Mars History Derived from OMEGA/Mars Express Data, *Science,* **2006**, 312, 400-404.

18. Watters, T. R., McGovern, P. J., Irwin, R. P., Hemispheres Apart: The Crustal Dichotomy on Mars, *Annual Review of Earth and Planetary Sciences,* **2007**, 35, 621-652.

19. Zuber, M. T., Solomon, S. C., Phillips, R. J., Smith, D. E., Tyler, G. L., Aharonson, O., Balmino, G., Banerdt, W. B., Head, J. W., Johnson, C. L., et al., Internal Structure and Early Thermal Evolution of Mars from Mars Global Surveyor Topography and Gravity, *Science,* **2000**, 287, 1788-1793.

20. Neumann, G. A., Zuber, M. T., Wieczorek, M. A., McGovern, P. J., Lemoine, F. G., Smith, D. E., Crustal structure of Mars from gravity and topography, *Journal of Geophysical Research: Planets,* **2004**, 109.

21. National Aeronautics and Space Administration, The Mars Orbiter Laser Altimeter [Internet]. Available from: https://attic.gsfc.nasa.gov/mola/images.html [accessed May 18, 2021].

22. Zuber, M. T., Banerdt, W. B., Andrews-Hanna, J. C., The Borealis basin and the origin of the Martian crustal dichotomy, *Nature (London),* **2008**, 453, 1212-1215.

23. Elkins-Tanton, L. T., hess, P. C., Parmentier, E. M., Possible formation of ancient crust on Mars through magma ocean processes, *Journal of Geophysical Research - Planets,* **2005**, 110, 1-11.

24. MEPAG Special Regions-Science Analysis Group, Findings of the Mars Special Regions Science Analysis Group, *Astrobiology,* **2006**, 6, 677-732.

25. Pettit, E., Nicholson, S. B., Radiation measures on the planet Mars, *Publications of the Astronomical Society of the Pacific,* **1924**, 36, 269-272.

26. Haberle, R. M., Clancy, R. T., Forget, F., Smith, M. D., Zurek, R. W., The atmosphere and climate of Mars, **2017**, Cambridge University Press, Cambridge, United Kingdom.

27. Tokano, T., Water on Mars and Life, **2004**, Springer, Berlin.

28. Rampe, E. B., Blake, D. F., Bristow, T. F., Ming, D. W., Vaniman, D. T., Morris, R. V., Achilles, C. N., Chipera, S. J., Morrison, S. M., Tu, V. M., et al., Mineralogy and geochemistry of sedimentary rocks and eolian sediments in Gale crater, Mars: A review after six Earth years of exploration with Curiosity, *Geochemistry,* **2020**, 80, 1-31.

29. Stern, J. C., Sutter, B., Freissinet, C., Navarro-González, R., McKay, C. P., Archer, P. D., Buch, A., Brunner, A. E., Coll, P., Eigenbrode, J. L., et al., Evidence for indigenous nitrogen in sedimentary and aeolian deposits from the Curiosity rover investigations at Gale crater, Mars, *Proceedings of the National Academy of Sciences,* **2015**, 112, 4245-4250.

30. Segura, A., Navarro-González, R., Nitrogen fixation on early Mars by volcanic lightning and other sources, *Geophysical Research Letters,* **2005**, 32, 1-4.

31. Nelson, M., Mars water discoveries - implications for finding ancient and current life, *Life Sciences in Space Research,* **2015**, 7, 1-5.

32. Voosen, P., NASA Curiosity rover hits organic pay dirt on Mars, *Science,* **2018**, 360, 1054-1055.

33. Mustard, J. F., Murchie, S. L., Pelkey, S. M., Ehlmann, B. L., Milliken, R. E., Grant, J. A., Bibring, J. P., Poulet, F., Bishop, J., Dobrea, E. N., et al., Hydrated silicate minerals on Mars observed by the Mars Reconnaissance Orbiter CRISM instrument, *Nature,* **2008**, 454, 305-309.

34. Nimmo, F., Tanaka, K., Early crustal evolution of mars, *Annual Review of Earth and Planetary Sciences,* **2005**, 33, 133-161.

35. Halliday, A. N., Wänke, H., Birck, J. L., Clayton, R. N., Chronology and Evolution of Mars; The Accretion, Composition and Early Differentiation of Mars (p.p. 197-230) **2001,** Springer, the Netherlands, Dordrecht.

36. Treiman, A. H., Drake, M. J., Janssens, M., Wolf, R., Ebihara, M., Core formation in the Earth and Shergottite Parent Body (SPB): Chemical evidence from basalts, *Geochimica Et Cosmochimica Acta,* **1986**, 50, 1071-1091.

37. Barlow, N., Mars: An Introduction to its Interior, Surface and Atmosphere, 1st ed. **2008**, Cambridge University Press, Cambridge, UK.

38. Gasda, P. J., Haldeman, E. B., Wiens, R. C., Rapin, W., Bristow, T. F., Bridges, J. C., Schwenzer, S. P., Clark, B., Herkenhoff, K., Frydenvang, J., et al., In situ detection of boron by ChemCam on Mars, *Geophysical Research Letters,* **2017**, 44, 8739-8748.

39. Lunar and Planetary Lab, University of Arizona, Gamma Ray Spectrometer (GRS), Mars Odyssey [Internet]. Available from: https://grs.lpl.arizona.edu/home.jsp [accessed May 18, 2021].

40. Hoefen, T. M., Clark, R. N., Bandfield, J. L., Smith, M. D., Pearl, J. C., Christensen, P. R., Discovery of Olivine in the Nili Fossae Region of Mars, *Science,* **2003**, 302, 627-630.

41. Gaudin, A., Dehouck, E., Grauby, O., Mangold, N., Formation of clay minerals on Mars: Insights from long-term experimental weathering of olivine, *Icarus,* **2018**, 311, 210-223.

42. Bell, J., The Martian Surface: Composition, Mineralogy and Physical Properties, Edited by Bell, J., **2008**, Cambridge University Press, Cambridge, UK.

43. Christensen, P. R., Bandfield, J. L., Rogers, A. D., Glotch, T. D. R., Hamilton, V. E., Ruff, S. W., Wyatt, M. B., The Martian Surface; Global mineralogy mapped from the Mars Global Surveyor Thermal Emission Spectrometer (p.p. 193-220) **2008,** Cambridge University Press, Cambridge, UK.

44. Bandfield, J. L., Hamilton, V. E., Christensen, P. R., A Global View of Martian Surface Compositions from MGS-TES, *Science,* **2000**, 287, 1626-1630.

45. Bost, N., Westall, F., Gaillard, F., Ramboz, C., Foucher, F., New Synthetic Martian Basalts from Spirit data, Gusev crater, *European Planetary Science Congress,* **October 2, 2011,** Nantes, France.

46. Nachon, M., Clegg, S. M., Mangold, N., Schröder, S., Kah, L. C., Dromart, G., Ollila, A., Johnson, J. R., Oehler, D. Z., Bridges, J. C., et al., Calcium sulfate veins characterized by ChemCam/Curiosity at Gale crater, Mars, *Journal of Geophysical Research. Planets,* **2014**, 119, 1991-2016.

47. Nikiforov, S. Y., Mitrofanov, I. G., Litvak, M. L., Lisov, D. I., Djachkova, M. V., Jun, I., Tate, C. G., Sanin, A. B., Assessment of water content in martian subsurface along the traverse of the Curiosity rover based on passive measurements of the DAN instrument, *Icarus,* **2020**, 346, 113818.

48. Rogers, A. D., Arvidson, R. E., Glotch, T. D., Wyatt, M. B., Bandfield, J. L., Blaney, D. L., Budney, C., Christensen, P. R., Anwar, S., Calvin, W. M., Mineral Composition and Abundance of the Rocks and Soils at Gusev and Meridiani from the Mars Exploration Rover Mini-TES Instruments, **2005**.

49. Weitz, C. M., Milliken, R. E., Grant, J. A., McEwen, A. S., Williams, R. M. E., Bishop, J. L., Thomson, B. J., Mars Reconnaissance Orbiter observations of light-toned layered deposits and associated fluvial landforms on the plateaus adjacent to Valles Marineris, *Icarus,* **2010**, 205, 73-102.

50. Murchie, S. L., Mustard, J. F., Ehlmann, B. L., Milliken, R. E., Bishop, J. L., McKeown, N. K., Noe Dobrea, E. Z., Seelos, F. P., Buczkowski, D. L., Wiseman, S. M., et al., A synthesis of Martian aqueous mineralogy after 1 Mars year of observations from the Mars Reconnaissance Orbiter, *Journal of Geophysical Research. Planets,* **2009**, 114, 1-30.

51. Squyres, S. W., Grotzinger, J. P., Arvidson, R. E., Bell, J. F., Calvin, W., Christensen, P. R., Clark, B. C., Crisp, J. A., Farrand, W. H., Herkenhoff, K. E., et al., In Situ Evidence for an Ancient Aqueous Environment at Meridiani Planum, Mars, *Science,* **2004**, 306, 1709-1714.

52. Squyres, S. W., Arvidson, R. E., Ruff, S., Gellert, R., Morris, R. V., Ming, D. W., Crumpler, L., Farmer, J. D., Des Marais, D. J., Yen, A., et al., Detection of Silica-Rich Deposits on Mars, *Science,* **2008**, 320, 1063-1067.

53. Peplow, M., How Mars got its rust, *Nature news,* **2004** May 3,.

54. Bertelsen, P., Goetz, W., Madsen, M. B., Kinch, K. M., Hviid, S. F., Knudsen, J. M., Gunnlaugsson, H. P., Merrison, J., Nornberg, P., Squyres, S. W., et al., Magnetic Properties Experiments on the Mars Exploration Rover Spirit at Gusev Crater, *Science,* **2004**, 305, 827-829.

55. Davis, A. M., Meteorites, comets and planets, 1st ed. **2005**, Elsevier, Amsterdam, the Netherlands.

56. Rubin, A. E., Grossman, J. N., Meteorite and meteoroid: New comprehensive definitions, *Meteoritics & Planetary Science,* **2010**, 45, 114-122.

57. Lunar and Planetary Institute, Meteoritical Bulletin Database [Internet]. Available from: https://www.lpi.usra.edu/meteor/ [accessed May 18, 2021].

58. Melosh, H. J., Impact ejection, spallation, and the origin of meteorites, *Icarus,* **1984**, 59, 234-260.

59. Fritz, J., Artemieva, N., Greshake, A., Ejection of Martian meteorites, *Meteoritics & Planetary Science,* **2005**, 40, 1393-1411.

60. Artemieva, N., Ivanov, B., Launch of martian meteorites in oblique impacts, *Icarus,* **2004**, 171, 84-101.

61. Ashwal, L. D., Wood, C. A., SNC meteorites - Igneous rocks from Mars, *13th Lunar and Planetary Science Conference,* **March 15, 1982,** Houston, Texas, USA.

62. Stephanie C. Werner, Anouck Ody, François Poulet, The Source Crater of Martian Shergottite Meteorites, *Science,* **2014**, 343, 1343-1346.

63. Bridges, J. C., Warren, P. H., The SNC meteorites; basaltic igneous processes on Mars, *Journal of the Geological Society,* **2006**, 163, 229-251.

64. Kereszturi, A., Chatzitheodoridis, E., Searching for the Source Crater of Nakhlite Meteorites, *Origins of Life and Evolution of Biospheres,* **2016**, 46, 455-471.

65. Leshin, L. A., Vicenzi, E., Aqueous processes recorded by Martian meteorites; analyzing Martian water on Earth, *Elements,* **2006**, 2, 157-162.

66. Kurokawa, H., Sato, M., Ushioda, M., Matsuyama, T., Moriwaki, R., Dohm, J. M., Usui, T., Evolution of water reservoirs on Mars: Constraints from hydrogen isotopes in martian meteorites, *Earth and Planetary Science Letters,* **2014**, 394, 179-185.

67. Becker, L., Glavin, D. P., Bada, J. L., Polycyclic aromatic hydrocarbons (PAHs) in Antarctic Martian meteorites, carbonaceous chondrites, and polar ice, *Geochimica Et Cosmochimica Acta,* **1997**, 61, 475-481.

68. Sautter, V., Toplis, M. J., Beck, P., Mangold, N., Wiens, R., Pinet, P., Cousin, A., Maurice, S., LeDeit, L., Hewins, R., et al., Magmatic complexity on early Mars as seen through a combination of orbital, in-situ and meteorite data, *Lithos,* **2016**, 254-255, 36-52.

69. Farquhar, J., Kim, S., Masterson, A., Implications from sulfur isotopes of the Nakhla meteorite for the origin of sulfate on Mars, *Earth and Planetary Science Letters,* **2007**, 264, 1-8.

70. Neukum, G., Basilevsky, A. T., Kneissl, T., Chapman, M. G., van Gasselt, S., Michael, G., Jaumann, R., Hoffmann, H., Lanz, J. K., The geologic evolution of Mars: Episodicity of resurfacing events and ages from cratering analysis of image data and correlation with radiometric ages of Martian meteorites, *Earth and Planetary Science Letters,* **2010**, 294, 204-222.

71. Sautter, V., Jambon, A., Boudouma, O., Cl-amphibole in the nakhlite MIL 03346: Evidence for sediment contamination in a Martian meteorite, *Earth and Planetary Science Letters,* **2006**, 252, 45-55.

72. Velbel, M. A., Aqueous corrosion of olivine in the Mars meteorite Miller Range (MIL) 03346 during Antarctic weathering: Implications for water on Mars, *Geochimica Et Cosmochimica Acta,* **2016**, 180, 126-145.

73. Jull, A. J. T., Courtney, C., Jeffrey, D. A., Beck, J. W., Isotopic Evidence for a Terrestrial Source of Organic Compounds Found in Martian Meteorites Allan Hills 84001 and Elephant Moraine 79001, *Science,* **1998**, 279, 366-369.

74. Chaikin, A., Hanks, T., A Man on the Moon: The Voyages of the Apollo Astronauts, 1st ed. **2007**, Penguin Books Limited, London, UK.

75. Muirhead, B. K., Nicholas, A. K., Umland, J., Sutherland, O., Vijendran, S., Mars Sample Return Campaign Concept Status, *Acta Astronautica,* **2020**, 176, 131-138.

76. Williford, K. H., Farley, K. A., Stack, K. M., Allwood, A. C., Beaty, D., Beegle, L. W., Bhartia, R., Brown, A. J., de la Torre Juarez, M., Hamran, S., et al., From Habitability to Life on Mars; The NASA Mars 2020 Rover Mission and the Search for Extraterrestrial Life (p.p. 275-308) Edited by Cabrol, N. A., Grin, E. A., **2018,** Elsevier, Amsterdam, the Netherlands.

77. Goudge, T. A., Mustard, J. F., Head, J. W., Fassett, C. I., Wiseman, S. M., Assessing the mineralogy of the watershed and fan deposits of the Jezero crater paleolake system, Mars, *Journal of Geophysical Research. Planets,* **2015**, 120, 775-808.

78. Garvin, J. B., Frawley, J. J., Sakimoto, S. E. H., Craters on Mars: Global Geometric Properties from Gridded MOLA Topography, *6th International Conference on Mars,* **July 20, 2003,** Pasadena, California, USA.

79. Schon, S. C., Head, J. W., Fassett, C. I., An overfilled lacustrine system and progradational delta in Jezero crater, Mars: Implications for Noachian climate, *Planetary and Space Science,* **2012**, 67, 28-45.

80. Mangold, N., Poulet, F., Mustard, J. F., Bibring, J. P., Gondet, B., Langevin, Y., Ansan, V., Masson, P. H., Fassett, C., Head, J. W., et al., Mineralogy of the Nili Fossae region with OMEGA/Mars Express data: 2. Aqueous alteration of the crust, *Journal of Geophysical Research. Planets,* **2007**, 112, 1-25.

81. Arvidson, R. E., DeGrosse, P., Grotzinger, J. P., Heverly, M. C., Shechet, J., Moreland, S. J., Newby, M. A., Stein, N., Steffy, A. C., Zhou, F., et al., Relating geologic units and mobility system kinematics contributing to Curiosity wheel damage at Gale Crater, Mars, *Journal of Terramechanics,* **2017**, 73, 73-93.

82. Schroeder, G., NASA's Ingenuity Mars Helicopter: The first attempt at powered flight on another world, *American Scientist,* **2020**, 108, 330.

83. Bell, J. F., Maki, J. N., Mehall, G. L., Ravine, M. A., Caplinger, M. A., Bailey, Z. J., Brylow, S., Schaffner, J. A., Kinch, K. M., Madsen, M. B., et al., The Mars 2020 Perseverance Rover Mast Camera Zoom (Mastcam-Z) Multispectral, Stereoscopic Imaging Investigation, *Space Science Reviews,* **2021**, 217, 24.

84. Pla-García, J., Rafkin, S. C. R., Martinez, G. M., Vicente-Retortillo, Á, Newman, C. E., Savijärvi, H., de la Torre, M., Rodriguez-Manfredi, J. A., Gómez, F., Molina, A., et al., Meteorological Predictions for Mars 2020

Perseverance Rover Landing Site at Jezero Crater, *Space Science Reviews,* **2020**, 216.

85. Hecht, M., Hoffman, J., Rapp, D., McClean, J., SooHoo, J., Schaefer, R., Aboobaker, A., Mellstrom, J., Hartvigsen, J., Meyen, F., et al., Mars Oxygen ISRU Experiment (MOXIE), *Space Science Reviews,* **2021**, 217.

86. Allwood, A. C., Hurowitz, J. A., Clark, B. C., Cinquini, L., Davidoff, S., Denise, R. W., Elam, W. T., Foote, M. C., Flannery, D. T., Gerhard, J. H., et al., The PIXL Instrument on the Mars 2020 Perseverance Rover, **2021**.

87. Hamran, S., Paige, D. A., Amundsen, H. E. F., Berger, T., Brovoll, S., Carter, L., Hanssen, L., Dypvik, H., Eide, J., Eide, S., et al., Radar imager for Mars' subsurface experiment—RIMFAX, *Space Science Reviews,* **2020**, 216.

88. Farley, K. A., Williford, K. H., Stack, K. M., Bhartia, R., Chen, A., de la Torre, M., Hand, K., Mars 2020 Mission Overview, *Space Science Reviews,* **2020**, 216.

89. Wiens, R. C., Maurice, S., Robinson, S. H., Nelson, A. E., Cais, P., Bernardi, P., Newell, R. T., Sharma, S. K., Deming, J., Beckman, D., et al., The SuperCam Instrument Suite on the NASA Mars 2020 Rover: Body Unit and Combined System Tests, *Space Science Reviews,* **2021**, 217, 4.

90. Maurice, S., Wiens, R. C., Bernardi, P., Caïs, P., Robinson, S., Nelson, T., Gasnault, O., Reess, J. M., Deleuze, M., Rull, F., et al., The SuperCam Instrument Suite on the Mars 2020 Rover: Science Objectives and Mast-Unit Description, *Space Science Reviews,* **2021**, 217, 47.

91. Manrique, J. A., Lopez-Reyes, G., Cousin, A., Rull, F., Maurice, S., Wiens, R. C., Madsen, M. B., SuperCam Calibration Targets: Design and Development, *Space Science Reviews,* **2020**, 216, 138.

92. Gaft, M., Reisfeld, R., Panczer, G., Modern Luminescence Spectroscopy of Minerals and Materials, **2015**, Springer International Publishing AG, Cham, Germany.

93. Chide, B., Maurice, S., Murdoch, N., Lasue, J., Bousquet, B., Jacob, X., Cousin, A., Forni, O., Gasnault, O., Meslin, P., et al., Listening to laser sparks: a link between Laser-Induced Breakdown Spectroscopy, acoustic measurements and crater morphology, *Spectrochimica Acta. Part B: Atomic Spectroscopy,* **2019**, 153, 50-60.

94. Hoffmann, G. G., Raman spectroscopy, **2019**, Momentum Press, New York, New York, USA.

95. Strachan, C. J., Rades, T., Gordon, K. C., Rantanen, J., Raman spectroscopy for quantitative analysis of pharmaceutical solids, *Journal of Pharmacy and Pharmacology,* **2007**, 59, 179-192.

96. Haskin, L. A., Korotev, R. L., Jolliff, B. L., Wang, A., Viskupic, K. M., Rockow, K. M., Raman Spectroscopy for Mineral Identification and Quantification for in situ Planetary Surface Analysis: A Point Count Method, *Journal of Geophysical Research,* **1997**, 102, 19293-19306.

97. Wang, A., Kuebler, K., Jolliff, B., Haskin, L. A., Mineralogy of a Martian meteorite as determined by Raman spectroscopy, *Journal of Raman Spectroscopy,* **2004**, 35, 504-514.

98. Mikouchi, T., Miyamoto, M., Micro Raman spectroscopy of amphiboles and pyroxenes in the Martian meteorites Zagami and Lewis Cliff 88516, *Meteoritics & Planetary Science,* **2000**, 35, 155-159.

99. Wang, A., Kuebler, K. E., Jolliff, B. L., Haskin, L. A., Raman spectroscopy of Fe-Ti-Cr-oxides, case study: Martian meteorite EETA79001, *The American Mineralogist,* **2004**, 89, 665-680.

100. Wang, A., Jolliff, B. L., Haskin, L. A., Kuebler, K. E., Viskupic, K. M., Characterization and comparison of structural and compositional features of planetary quadrilateral pyroxenes by Raman spectroscopy, *The American Mineralogist,* **2001**, 86, 790-806.

101. Xie, X., Minitti, M. E., Chen, M., Mao, H. o., Wang, D., Shu, J., Fei, Y., Natural high-pressure polymorph of merrillite in the shock veins of the Suizhou meteorite, *Geochimica Et Cosmochimica Acta,* **2002**, 66, 2439-2444.

102. Fritz, J., Greshake, A., Stoffler, D., Micro-Raman spectroscopy of plagioclase and maskelynite in Martian meteorites: Evidence of progressive shock metamorphism, *Antarctic Meteorite Research,* **2005**, 18, 96-116.

103. Farrell-Turner, S., Reimold, W. U., Nieuwoudt, M., Erasmus, R. M., Raman spectroscopy of olivine in dunite experimentally shocked to pressures between 5 and 59 GPa, *Meteoritics & Planetary Science,* **2005**, 40, 1311-1327.

104. Ruiz-Galende, P., Torre-Fdez, I., Aramendia, J., Gómez-Nubla, L., Castro, K., Arana, G., Madariaga, J. M., Study of a terrestrial Martian analogue: Geochemical characterization of the Meñakoz outcrops (Biscay, Spain), *Journal of Raman Spectroscopy,* **2020**, 51, 1603-1612.

105. Ruiz-Galende, P., Fernández, G., Torre-Fdez, I., Aramendia, J., Gomez-Nubla, L., García-Florentino, C., Castro, K., Arana, G., Madariaga, J. M., Characterization of sedimentary and volcanic rocks in Armintza outcrop (Biscay, Spain) and its implication for Oxia Planum (Mars) exploration, *Spectrochimica Acta. Part A, Molecular and Biomolecular Spectroscopy,* **2021**, 251, 119443.

106. Edwards, H. G. M., Vandenabeele, P., Jorge-Villar, S. E., Carter, E. A., Perez, F. R., Hargreaves, M. D., The Rio Tinto Mars Analogue site: An extremophilic Raman spectroscopic study, *Spectrochimica Acta. Part A, Molecular and Biomolecular Spectroscopy,* **2007**, 68, 1133-1137.

107. Veneranda, M., Manrique-Martinez, J. A., Lopez-Reyes, G., Medina, J., Torre-Fdez, I., Castro, K., Madariaga, J. M., Lantz, C., Poulet, F., Krzesińska, A. M., et al., Spectroscopic study of olivine-bearing rocks and its relevance to the ExoMars rover mission, *Spectrochimica Acta. Part A, Molecular and Biomolecular Spectroscopy,* **2019**, 223, 117360.

108. Edwards, H. G. M., Farwell, D. W., Grady, M. M., Wynn-Williams, D. D., Wright, I. P., Comparative Raman microscopy of a Martian meteorite and Antarctic lithic analogues, *Planetary and Space Science,* **1999**, 47, 353-362.

109. Hutchinson, I. B., Ingley, R., Edwards, H. G. M., Harris, L., McHugh, M., Malherbe, C., Parnell, J., Raman spectroscopy on Mars: identification of geological and bio-geological signatures in Martian analogues using miniaturized Raman spectrometers, *Philosophical Transactions of the Royal Society of London. Series A: Mathematical, Physical, and Engineering Sciences,* **2014**, 372, 20140204.

110. Huang, E., Chen, C. H., Huang, T., Lin, E. H., Xu, J., Raman spectroscopic characteristics of Mg-Fe-Ca pyroxenes, *The American Mineralogist,* **2000**, 85, 473-479.

111. Tribaudino, M., Mantovani, L., Bersani, D., Lottici, P. P., Raman spectroscopy of (Ca, Mg)$MgSi_2O_6$ clinopyroxenes, *The American Mineralogist,* **2012**, 97, 1339-1347.

112. Freeman, J. J., Wang, A., Kuebler, K. E., Jolliff, B. L., Haskin, L. A., Characterization of natural feldspars by Raman spectroscopy for future planetary exploration, *Canadian Mineralogist,* **2008**, 46, 1477-1500.

113. Befus, K. S., Lin, J., Cisneros, M., Fu, S., Feldspar Raman shift and application as a magmatic thermobarometer, *The American Mineralogist,* **2018**, 103, 600-609.

114. Sims, M., Jaret, S. J., Johnson, J. R., Whitaker, M. L., Glotch, T. D., Unconventional high-pressure Raman spectroscopy study of kinetic and peak pressure effects in plagioclase feldspars, *Physics and Chemistry of Minerals,* **2020**, 47.

115. Mouri, T., Enami, M., Raman spectroscopic study of olivine-group minerals, *Journal of Mineralogical and Petrological Sciences,* **2008**, 103, 100-104.

116. Wang, A., Freeman, J. J., Jolliff, B. L., Chou, I., Sulfates on Mars: A systematic Raman spectroscopic study of hydration states of magnesium sulfates, *Geochimica Et Cosmochimica Acta,* **2006**, 70, 6118-6135.

117. Edwards, H. G. M., Villar, S. E. J., Parnell, J., Cockell, C. S., Lee, P., Raman spectroscopic analysis of cyanobacterial gypsum halotrophs and relevance for sulfate deposits on Mars, *Analyst,* **2005**, 13, 917-923.

118. García-Florentino, C., Gomez-Nubla, L., Huidobro, J., Torre-Fdez, I., Ruíz-Galende, P., Aramendia, J., Hausrath, E. M., Castro, K., Arana, G., Madariaga, J. M., Interrelationships in the Gypsum–Syngenite–Görgeyite System and Their Possible Formation on Mars, *Astrobiology,* **2021**, 21, 332-344.

119. Kuebler, K. E., Jolliff, B. L., Wang, A., Haskin, L. A., Extracting olivine (Fo–Fa) compositions from Raman spectral peak positions, *Geochimica Et Cosmochimica Acta,* **2006**, 70, 6201-6222.

# Chapter 2
# Objectives

*"By failing to prepare, you are preparing to fail"*

Benjamin Franklin

Due to the increasing importance of Raman spectroscopy in the field of space exploration, it is necessary to have as many tools as possible to obtain information from the data obtained by this technique. In this sense, the main objective of this PhD thesis was the development of tools that provide useful knowledge about space exploration related samples, including in situ analyses of both geological terrestrial analogs and other celestial bodies, using Raman spectroscopy. For this PhD thesis, the main focus of study was the planet Mars.

To achieve that main objective, four different partial objectives (PO) were stablished.

**PO1.** To create a Raman spectral database of minerals relevant to the study of Mars and terrestrial analogs of the Red Planet, including mineral phases that are not currently contained in other Raman databases, and therefore, to increase the ability to interpret the spectroscopic results obtained from Mars.

**PO2.** To develop mathematical models to not only study by Raman spectroscopy the molecular or mineralogical composition of a sample, but also to determine different characteristics of it. This partial objective is divided into three different tasks.

*Task 1.* To develop a model able to quantify the forsterite and fayalite content of olivines with the highest possible accuracy and precision, since these minerals are of great relevance for the study of the past volcanic processes on Mars.

*Task 2.* To study the capabilities of Raman spectroscopy for the assessment of past high-pressure events suffered by relevant minerals for the study of Mars, such as calcite, silica and feldspar, and to test them with real samples that were subjected to high-pressure events in the past.

*Task 3.* To stablish a methodology to identify and characterize possible organic compounds found on Mars by Raman spectroscopy and chemometrics.

**PO3.** To assess the capabilities of *SuperCam* to identify mineral phases relevant to Mars and to detect organic compounds that might be present on its surface.

**PO4.** To make an in-depth study of different meteorites as representative samples of Mars, as a way to obtain relevant information of their corresponding parent body and to test the different developed models of Raman spectroscopy, stablishing part of a possible methodology to analyze in a non-destructive way the future samples from the Mars Return Sample mission,

combining Raman spectroscopy with other relevant spectroscopic techniques.

# Chapter 3
# Instrumentation and Experimental Procedure

*"The true method of knowledge is experiment"*

William Blake, 1788

## 3.1. Raman Spectroscopy

Throughout this PhD thesis different Raman spectroscopy instruments have been employed for different purposes. An Invia High Resolution micro-Raman spectrometer (Renishaw, UK) (Figure 3.1) was the go-to instrument for all the Raman analyses unless there were additional objectives or restrictions on the molecular and mineralogical analysis of the samples that would make the use of another instrument more convenient. The measurements were carried out using its 532 nm and 785 nm excitation continuous diode lasers with a Charge Couple Device (CCD) detector (Peltier cooled). The nominal laser power was 45 mW, although,

in order to avoid thermal alterations or decomposition of the surface of the samples, during the analyses only a maximum of 10 % of this power was used. The instrument was coupled to a microscope (Leica, Germany) and objectives of 50x (numerical aperture, N.A. of 0.75), 20x (N.A. of 0.40) and 5x (N.A. of 0.12) were used to make the measurements. Table 3.1 shows the different laser spot diameters depending on the objective and the laser wavelength used. The spectral resolution of the spectrometer was 1 $cm^{-1}$, which is enough to differentiate any slight shift of the position of the Raman features. The number of accumulations and the acquisition time was set in order to obtain the best possible spectra in terms of quality and signal-to-noise ratio.


Figure 3.1. Raman instruments used in the development of this PhD thesis: Invia (left) and one of the InnoRam instruments (right)

This instrument was used both to perform punctual analyses and Raman imaging analyses. Raman imaging was carried out whenever the surface of the sample was flat enough, since the samples with a steep slope were problematic. Although the stage for the sample allowed a spatial resolution of 1 µm, usually the maps were done with a separation of 10 µm between spectra in order to cover more surface of the sample. The instrument was calibrated prior to each set of analyses (usually two times per day) with the 520.5 $cm^{-1}$ Raman feature of a silicon chip.

Table 3.1. Laser diameter spot size depending on the laser wavelength and the objective augmentations

| Laser Wavelength | 5x Objective | 20x Objective | 50x Objective |
|---|---|---|---|
| 532 nm | 5.4 µm | 1.6 µm | 0.9 µm |
| 785 nm | 8.0 µm | 2.4 µm | 1.3 µm |

The Wire 4.2 software package (Renishaw, UK) was used for the spectral data analysis, treatment and interpretation. The Raman imaging spectral results were pre-processed by applying first a cosmic ray removal algorithm based on the nearest neighbor spectrum and width of the features. Then, an automatic baseline correction was performed when the spectra had too much fluorescence. This correction was performed by a polynomial fitting, usually with a polynomial of order 11 and a noise tolerance of 1.50. Afterwards, an automated Principal Component Analysis (PCA) noise removal procedure was used. Finally, in order to obtain the image, the main Raman band of the compound of interest was selected as a wavenumber range. Then, the area above the baseline for that band was calculated by the software for all the spectra. With that information, the software colored the image according to the values obtained.

In the cases where the analyses had to be carried out outside the laboratory, specifically, the analyses for the construction of the spectral database (see Chapter 4, *IMPAT Database*), two different Portable InnoRam spectrometers ($BWTEK_{INC}$, USA) (Figure 3.1) were employed. One of the instruments has a 785 nm excitation laser and the other one a 532 nm excitation laser. They both have a CCD detector with Peltier cooling. In order to do a proper focus, the spectrometers were coupled to a microscope, using a 50x objective (N.A. of 0.50). As with the Invia instrument, the laser power and the exposition times were modified depending on the studied sample's surface in order to avoid mineral alterations or thermodecomposition. The calibration of the equipment was performed before its use, using a silicon chip and its 520.5 $cm^{-1}$ feature as reference. The spectral results were acquired with the BWSpec™ 3.26

software ($BWTEK_{INC}$, USA), and for the data analysis and interpretation the Wire 4.2 software (Renishaw, UK) was employed.

The interpretation of the results acquired with both Raman instruments described above, as well as of any other Raman spectrum, was carried out by comparison of the obtained spectra with the ones of pure standards found in literature, in the RRUFF online database (1) and in the Raman spectral database developed during this PhD thesis (see Chapter 4, *IMPAT Database*). In order to develop the different classification and calibration models for organics (see Chapter 7, *Development of Classification and Characterization Models for Organics Analysis*) the software Unscrambler 9.7 (Camo Analytics, Norway) was employed.

## 3.2. SuperCam-Raman Spectrometer

During this PhD thesis the scientific calibration of the Raman system of *SuperCam* was carried out at Los Alamos National Laboratory (LANL, USA), along with the science and engineering team of the instrument. A more detailed description of this instrument, including its Raman capabilities, can be found in literature (2-5) and an overview can be found in Chapter 1, *Introduction*. For Raman, *SuperCam* uses the same pulsed laser as for LIBS but a Pockels cell is used to double its frequency, resulting in a 532 nm laser beam. In order to increase the Raman signals intensity, the spectral response of the samples go through an intensifier before they reach the gated detector.

The scientific calibration process was carried out using the Flight Model (FM) Body Unit (BU) and the Engineering Qualification Model (EQM) Mast Unit (MU) setup, FM-BU/EQM-MU. In order to optimize the laser performance, both units were put inside a thermal chamber at -10 ºC of temperature and with dry nitrogen at ambient pressure (Figure 3.2).

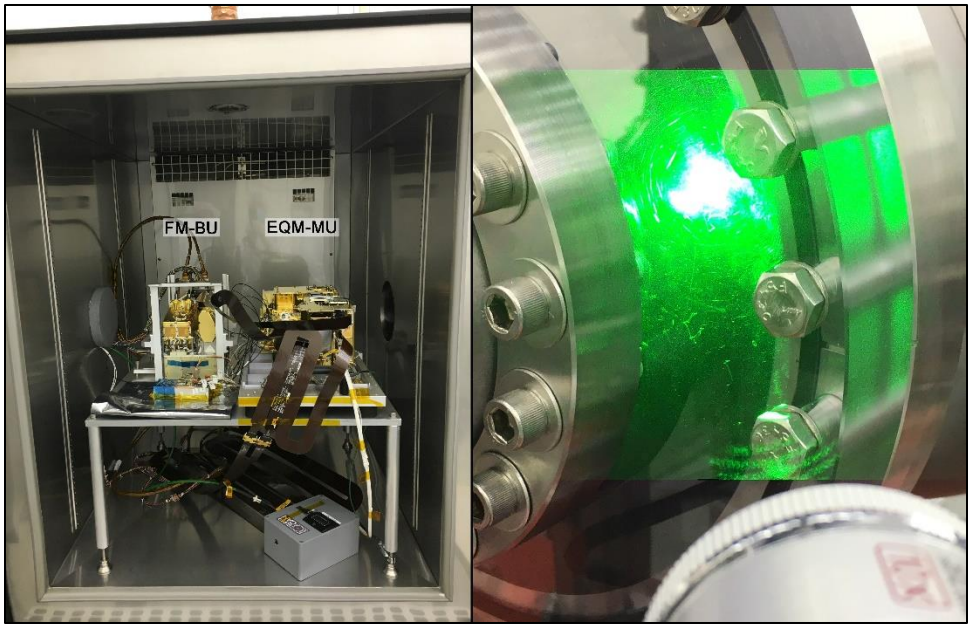


Figure 3.2. *SuperCam* setup used for the scientific calibration process at LANL inside the thermal chamber (left) and a Raman shot to a target using said setup (right)

The studied samples consisted mostly of natural minerals and rocks and pressed powder pellets. A total of 138 unique samples were tested with the Raman system of *SuperCam* during this calibration process. Most of them were set at a distance between 1.50 – 3.00 m. For each target, between 100 and 200 shots were recorded with their respective darks. In order to obtain a final spectrum, different combinations of coadds (addition of single shot spectra) and actives (average of different single shot spectra) between those 100-200 spectra were tested for the different targets. The integration time used was always of 5017 µs, with a delay between the shot and the gate opening of 650 ns, leaving the gate open for 100 ns. The gating and integration time parameters were optimized before the analyses of the samples using the main Raman signals of different mineral standards.

## 3.3. Raman spectroscopy coupled to a Scanning Electron Microscope

In cases where the sample was heterogeneous mineralogically and elementally and its surface and characteristics allowed it, as in the case of the meteorite NWA 6148 (see Chapter 9, *Methodology Development and Testing for the Mars Returning Samples*), a Raman spectrometer was used coupled to a Scanning Electron Microscope – Energy Dispersive X-Ray Spectroscopy (SEM-EDS, Carl Zeiss- Oxford Instruments) instrument through the Structural and Chemical Analyzer interface (SCA, Renishaw, UK) (Figure 3.3). This system is composed of three different units. The central unit is the SEM, which was an EVO 40 Scanning Electron Microscope (Carl Zeiss NTS GmbH, Germany). The image obtained with it were acquired using high vacuum and an acceleration voltage of 20 KV. Depending on the surface and the intent of the analysis, magnifications up to 10000x were reached using a secondary electron (SE) detector. An EDS was coupled to the SEM as the second unit, an X-Max Energy-Dispersive X-Ray spectroscopy equipment (Oxford Instruments, UK). With it, the elemental characterization in mapping mode was performed, using an 8.5 mm working distance, a 35° take-off angle and an acceleration voltage of 20 KV. Finally, the third unit is a Raman spectrometer that provided (through the SCA interface) the molecular information in the same micro-metric spot as the EDS inside the SEM chamber under vacuum. This Raman spectrometer is a Renishaw Invia micro-Raman (Renishaw, UK), with a Peltier-cooled (-70 ºC) detector. Punctual measurements were made using a 514 nm excitation laser in the areas of interest inside the SEM chamber. The mean spectral resolution was around 1 $cm^{-1}$ and the laser spot diameter was around 1-2 µm. The acquisition parameters used were 20 accumulations and 20 seconds of exposure for all the measurements carried out with this device. The applied power of the laser was set at the source at a maximum of 50 mW, while on the sample was always less than 10 mW. The software used for the data collection was the Renishaw Wire

3.2. This Raman spectrometer is coupled to the SEM chamber through the SCA interface using fiber optic cables.


Figure 3.3. SEM-EDS instruments (left) coupled to an Invia Raman through the SCA interface (right)

In order to avoid the common sample preparation for SEM-EDS, such a gold coating, which would result in a severe alteration of the sample, they were prepared attaching them with carbon adhesive tape to metallic pins. In this way, a similar effect to a coating was obtained to discharge the electrons from the sample.

## 3.4. X-Ray Fluorescence

In order to get a semi-quantitative elemental composition of the samples and to assess their elemental distribution throughout their surface, Energy Dispersive X-Ray Fluorescence (ED-XRF) was carried out. This technique was especially useful for the characterization of the meteorites studied in this PhD thesis, as it provided their elemental distribution that helped guide the subsequent analyses (see Chapter 9, *Methodology Development and Testing for the Mars Returning Samples*). The instrument used was a M4 Tornado (Bruker Nano GmbH, Germany) μ-Energy Dispersive X-ray Fluorescence spectrometer (μ-ED-XRF) (Figure 3.4), using both single point analysis and map imaging capabilities.

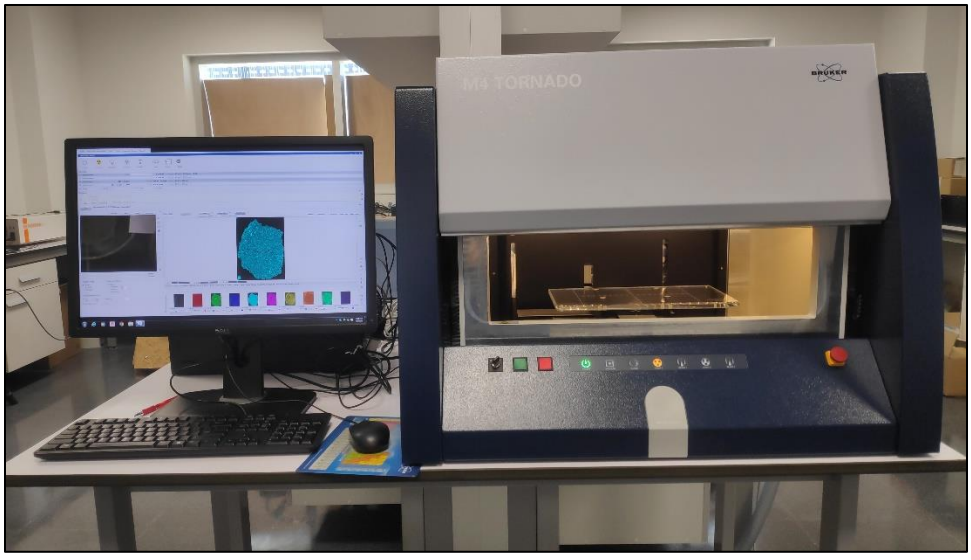


Figure 3.4. M4 Tornado for µ-Energy Dispersive X-ray Fluorescence

The instrument has a micro-focus side window Rh tube powered by a low-power HV generator and cooled by air that extends to a maximum voltage and current of 50 kV and 600 µA respectively. The micrometric lateral resolution of the instrument, 25 µm for the Mo $K_\alpha$-line, is achieved thanks to poly-cap optics. Its spot size varies as a function of the energy, being 17 µm at 2.3 KeV and 32 µm at 18.3 KeV. The map images were collected using a step of 20 µm with the 25 µm spot, where every single acquisition is represented by a pixel in the images obtained. The M4 Tornado implements an XFlash silicon drift detector with 30 $mm^2$ sensitive area and an energy resolution of 145eV for Mn-$K_\alpha$. To perform the focus of the samples two video microscopes are employed, the first one explores the sample under a low magnification (1 $cm^2$ area) while the second one performs the final focusing where the analysis will be carried out (1 $mm^2$ area). To improve the detection of the lightest elements (Z<16) all the ED-XRF measurements (both single points and mapping) were acquired always under vacuum conditions (20 mbar). Using this technique, the element distribution images of the sample can be obtained.

## 3.5. X-Ray Diffraction

In order to check the mineralogy and purity of commercial compounds or minerals used as standards for calibration purposes (see Chapter 5, *Forsterite and Fayalite Content in Olivines*) or for the Raman database (see Chapter 4, IMPAT Database), X-Ray Diffraction (XRD) of said samples was carried out by the Molecules and Material Unit of the Advanced Research Facilities of the University of the Basque Country (SGIker, UPV/EHU). The analyzed samples by XRD were first ground to fine powder using an agate mortar. The powder was analyzed by powder XRD on a PANalytical Xpert PRO diffractometer (Malvern, UK) (Figure 3.5).

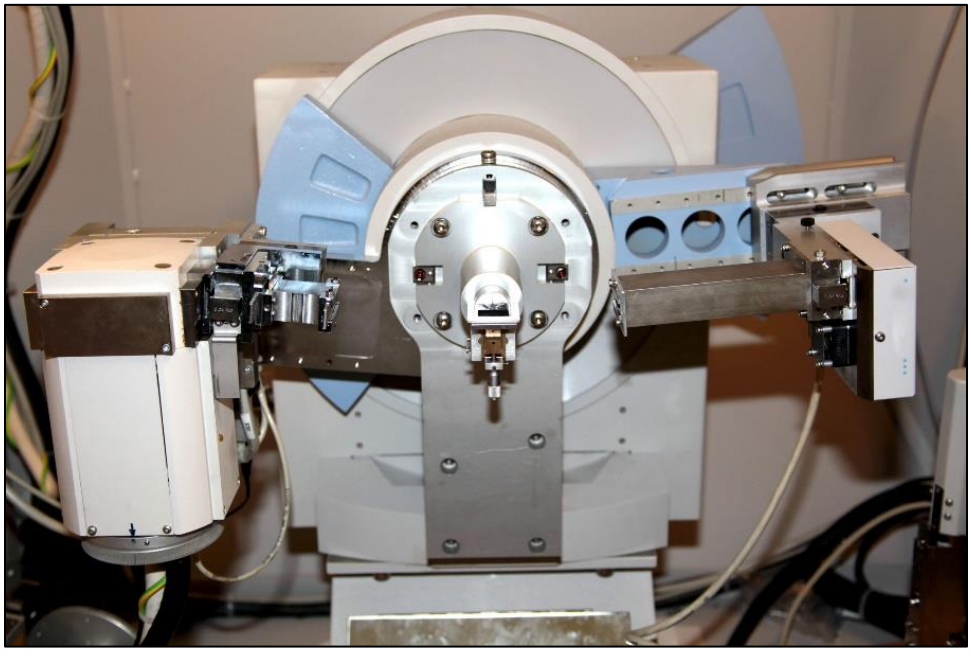

Figure 3.5. PANalytical Xpert PRO diffractometer for the X-Ray Diffraction of minerals

The instrument was equipped with a copper tube ($\lambda Cu_{K average \alpha}$=1.5418 Å, $\lambda Cu_{K\alpha 1}$=1.54060 Å, $\lambda Cu_{K\alpha 2}$=1.54439 Å), vertical goniometer (Bragg-Brentano geometry), a programmable divergence slit, a monochromator automatic sample exchanger, a secondary graphite monochromator and a PixCel detector. The conditions used for all the analyses were 40 KV and 40 mA, with a sweep between 5 and 70º2 theta. For the data processing of

the diffractograms obtained and the identification of the phases present, the software PANalytical X'pert HighScore was used in combination with the ICDD PDF2 database.

## 3.6. Time-of-Flight Secondary Ion Mass Spectrometry

In order to study the isotope ratio ($^{16}O/^{17}O$) and ($^{16}O/^{18}O$) for the study of the $Co_3O_4$ (see Chapter 9, *Methodology Development and Testing for the Mars Returning Samples*) a Time-of-Flight Secondary Ion Mass Spectrometry (ToF-SIMS) analysis was carried out by the laboratory of Nanotechnology and Surface Analysis of the Scientific-Technological Support Center for Research (CACTI) of the University of Vigo. The instrument used was an ToF-SIMS IV (Ion-ToF GmbH, Germany) (Figure 3.6). It was able to perform image analyses with a submicrometric lateral resolution of 100 nm and a with high sensitivity (<0.01 at. % in image mode and 0.0001 % as elemental results). The sample was bombarded with a pulsed Bismuth ($^{208}Bi_3^+$) ion beam at 25 keV at an angle of 45º of incidence. The Flood gun was employed to compensate the charge and the $Bi_3^+$ had a current of 0.23 Pa. The secondary ions generated were extracted with a 10 KV voltage and their time of flight from the sample to the detector was measured in a reflectron mass spectrometer. The spectra were recorded in the range of 0 – 800 m/e and with positive polarity. During all the measurements, the sample was confined inside a chamber with vacuum, 9 – 10 mbar. The positive ion spectra were calibrated to the $H^+$, $H_2^+$, $H_3^+$, $C^+$, $CH^+$, $CH_2^+$, $CH_3^+$, $C_2H_3^+$, $C_3H_5^+$, $C_4H_7^+$, $C_5H_9^+$, $C_6H_{11}^+$ peaks before data analysis. In order to prepare the sample, the fragment of the meteorite containing the $Co_3O_4$ was located and extracted from the meteorite and fixed to a piece of silicon wafer (Figure 3.6).

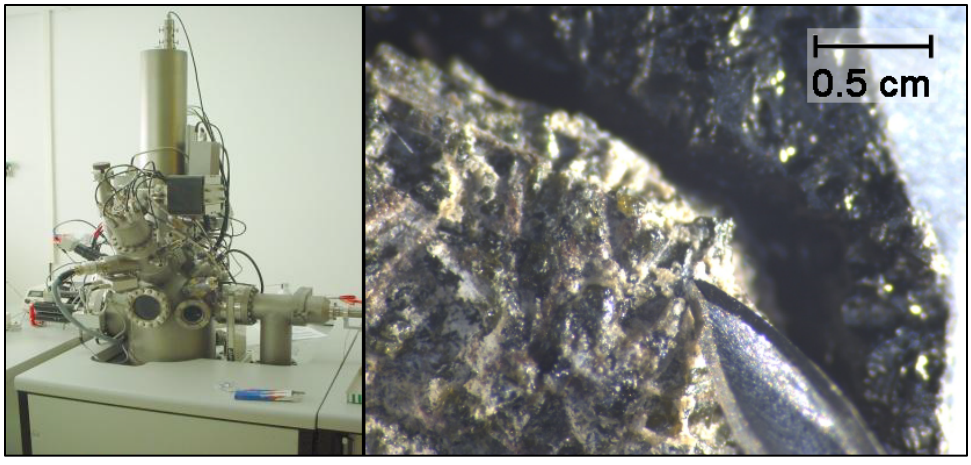


Figure 3.6. ToF-SIMS IV instrument (left) and a microscopic picture of the area from which the meteorite fragment containing $Co_3O_4$ was extracted (right)

## 3.7. Bibliography

1. Lafuente, B., Downs, R. T., Yang, H., Stone, N., Highlights in Mineralogical Crystallography; The power of databases: The RRUFF project (p.p. 1-30) **2015,** de Gruyter, Berlin, München, Boston.

2. Wiens, R. C., Maurice, S., Rull, F., The SuperCam remote sensing instrument suite for the mars 2020 rover: A preview, *Spectroscopy,* **2017**, 32, 50-55.

3. Wiens, R. C., Maurice, S., Robinson, S. H., Nelson, A. E., Cais, P., Bernardi, P., Newell, R. T., Sharma, S. K., Deming, J., Beckman, D., et al., The SuperCam Instrument Suite on the NASA Mars 2020 Rover: Body Unit and Combined System Tests, *Space Science Reviews,* **2021**, 217, 4.

4. Manrique, J. A., Lopez-Reyes, G., Cousin, A., Rull, F., Maurice, S., Wiens, R. C., Madsen, M. B., SuperCam Calibration Targets: Design and Development, *Space Science Reviews,* **2020**, 216, 138.

5. Maurice, S., Wiens, R. C., Bernardi, P., Caïs, P., Robinson, S., Nelson, T., Gasnault, O., Reess, J. M., Deleuze, M., Rull, F., et al., The SuperCam Instrument Suite on the Mars 2020 Rover: Science Objectives and Mast-Unit Description, *Space Science Reviews,* **2021**, 217, 47.

# Chapter 4
# IMPAT Database

*"I suggest that the best geologist is he who has seen most rocks"*

Herbert Harold Read, 1940

Nowadays some Raman databases are already available for public use. The most known and large one is the RRUFF database (1), where the spectra of hundreds of minerals can be found. However, not all the minerals are present in the RRUFF database and, in some cases, only one or two entries for some minerals are found or the spectra do not have enough quality to use them. There also exist some small databases in literature (2), but they are not freely available (they are not open access research articles) and the spectra are presented as images, which means that they cannot be straightforward handled by spectroscopic software.

In order to achieve a right interpretation of the Raman spectroscopy results obtained from the active and future space exploration missions a proper database with the spectra of standard minerals of interest is needed.

During this PhD thesis, the IMPAT database (Inorganic and Mineralogical Planetary And Terrestrial compounds database) was developed in order to collect as many Raman spectra as possible, not only of common mineral phases but also of uncommon ones.

In fact, the IMPAT database was created to fill some gaps of the most uncommon minerals in the freely available Raman databases. This database was created in collaboration with the Geominery Museum of the Spanish Geological and Miner Institute (IGME). Most of the minerals present in the IMPAT database belong to the permanent exhibition mineral collection of the museum. Due to that reason, the minerals were analyzed in situ with portable Raman instruments inside the museum.

In this sense, it must be pointed out that since the Raman analyses were carried out with portable instruments, using an optic fiber probe for the continuous excitation laser, the sunlight affected some of the measurements, which in some cases causing spectral features after the dark subtractions that did not correspond to the minerals. In addition, some of the analyzed silicates had strong fluorescence in their spectra. Due to these facts, in the presented spectra only those Raman signals corresponding to the analyzed minerals are indicated in the figures. The features not denoted with their wavenumber position are not related to the mineral. In addition, baseline correction or smoothing were not applied to any of the spectra in order to preserve the original signals and shape of the features present in the spectra. Luckily, instruments such as *SuperCam* use a pulsed excitation Raman laser, thus, neither of those problems should be an issue when it analyzes rocks on the surface of Mars.

Regarding the analyzed samples, the Raman spectra of 105 different specimens were collected. Since the IMPAT database is focused on providing support to the Mars exploration missions, it contains, mainly, the mineral groups most related to Mars. In this chapter, the spectra of some of the most relevant minerals from the IMPAT database are presented.

## 4.1. Phyllosilicates

Phyllosilicate minerals are one of the most important silicate groups regarding the study of Mars. They are one of the most abundant group of silicates that can be found throughout the surface of the planet (3). However, many of these minerals do not have their Raman spectrum reported in literature yet.

The importance of this group for the study of Mars is that they need the presence of water for its formation process. The finding of any mineral that belongs to the group of phyllosilicates is always related with the past presence of water in the Red Planet. Thus, the study of these minerals on Mars is directly related with the potential habitability of the planet. In fact, the study and presence of phyllosilicates on Mars have already provided information about the evolution of the Red Planet regarding its aqueous history in the different geochemical environments (4). In addition, phyllosilicates have allowed the study of the Noachian era in more detail, since it was on that geological era when they were mostly formed (5). It was a period characterized by rock alterations caused by weak acidic and alkaline aqueous solutions. These solutions originated from the mobilization of subsurface water and hydrothermal activity, which altered the different minerals they entered in contact with (6, 7). Due to the relevance of this family of minerals for the study of the aqueous events on Mars, it is important to have the most complete spectral database of these minerals collected by Raman spectroscopy. Eight of the phyllosilicates included in the IMPAT database can be observed in Figure 4.1.

Antigorite (Figure 4.1a), $(Mg, Fe)_3Si_2O_5OH_4$, is a monoclinic, lamellated mineral that belongs to the serpentine subgroup. It is a polymorph of serpentine that is formed at high-pressure, and it is usually found in metamorphosed serpentinites. Through this mineral, the subduction zone dynamics of a planet could be studied, since its high percent of hydration plays an important role in this phenomenon (8, 9). As is explained in

Chapter 6, *Mineral Alterations Caused by High-Pressure Events*, the high-pressure polymorphs of minerals are very relevant to the study of the surface of Mars. Regarding its Raman spectrum, antigorite presents its characteristic signals at 232, 376, 460, 685 and 1044 $cm^{-1}$.

As a member of the brittle micas, clintonite (Figure 4.1b), $Ca(Mg, Al)_3(Al_3Si)O_{10}(OH)_2$, is characterized by its divalent cations in the phyllosilicate interlayer. In the case of this mineral, those cations are $Ca^{2+}$ and $Ba^{2+}$, which usually substitutes the calcium in the crystal lattice (10). This mineral has Raman diagnostic signals at 127, 154, 192, 234, 344, 402, 655 and 893 $cm^{-1}$.

Fluorapophyllite-(K) (Figure 4.1c), $KCa_4(Si_8O_{22})F{\cdot}8H_2O$ is the most common member of the apophyllite phyllosilicates mineral group. They are formed as secondary minerals in basalts and cavities of granites and have similar properties to those of zeolites (11). This fact means that they are very relevant minerals regarding the aqueous processes that happened in the past on Mars. The Raman features of Fluorapophyllite-(K) can be observed at 90, 109, 141, 167, 209, 232, 322, 433, 486, 539, 584, 663, 792 and 1061 $cm^{-1}$.

Gyrolite (Figure 4.1d), $NaCa_{16}(Si_{23}Al)O_{60}(OH)_8{\cdot}14H_2O$, is a very uncommon phyllosilicate mineral. Even though its occurrence on Earth is quite rare, it is often associated with zeolites, thus, they are relevant for the study of Mars. In addition, it is usually found in hydrothermal altered basalt and basaltic tuffs, which are important geological features for study in Mars (12). Regarding its Raman spectrum, gyrolite presents signals at 212, 280, 355, 403, 458, 574, 603, 1037 and 1060 $cm^{-1}$.

The phyllosilicate hisingerite (Figure 4.1e), $Fe_2Si_2O_5(OH)_4{\cdot}2H_2O$, is usually regarded as a secondary mineral, since it is formed by weathering processes from a primary mineral. More specifically, it is formed from the weathering caused by hydrothermal alterations of other iron silicate and sulfide minerals (13). As stated above, any mineral related with

hydrothermal activity could be found on Mars and would be of great relevance. This mineral has Raman diagnostic signals at 223, 288, 402 and 607 $cm^{-1}$.

As a member of the mica mineral group, lepidolite (Figure 4.1f), $K(Li, Al)_3(Al, Si, Rb)_4O_{10}(F, OH)_2$, belongs to the polylithionite-trilithionite mineral series. It is usually found in nature in a wide variety of colors due to the high number of metals that can be part as substituents in its crystal lattice (14). The Raman features of lepidolite can be observed at 98, 184, 711, 1265 and 1496 $cm^{-1}$.

Muscovite (Figure 4.1g), $KAl_2(AlSi_3O_{10})(F,OH)_2$, is the most common member of the mica group of minerals. It is a hydrated phyllosilicate that is present in numerous types of rocks as a secondary mineral, formed from the weathering of minerals such as feldspars (15). Since it is related with both the presence of hydration and a weathering process that involves the presence of water, its study and identification is relevant for the study of the surface of Mars. Muscovite present Raman characteristic signals at 157, 190, 263, 416, 702, 745 and 907 $cm^{-1}$, with an additional broad feature around 1100 $cm^{-1}$.

Finally, raite (Figure 4.1h), $Na_4Mn_3Ti_{0.25}Si_8O_{20}(OH)_2 \cdot 10H_2O$, is an unusual mineral present in igneous intrusive rocks, along with alkali metals. Raite is considered a late stage hydrothermal mineral, formed in hydrothermal environments at the same time as minerals such as aegirine (16). Due to this reason, it could be an important mineral to study the late stage hydrothermalism of Mars. Regarding its Raman spectrum, it has signals at 150, 203, 275, 348, 389, 440, 535, 575, 668, 851 and 931 $cm^{-1}$.

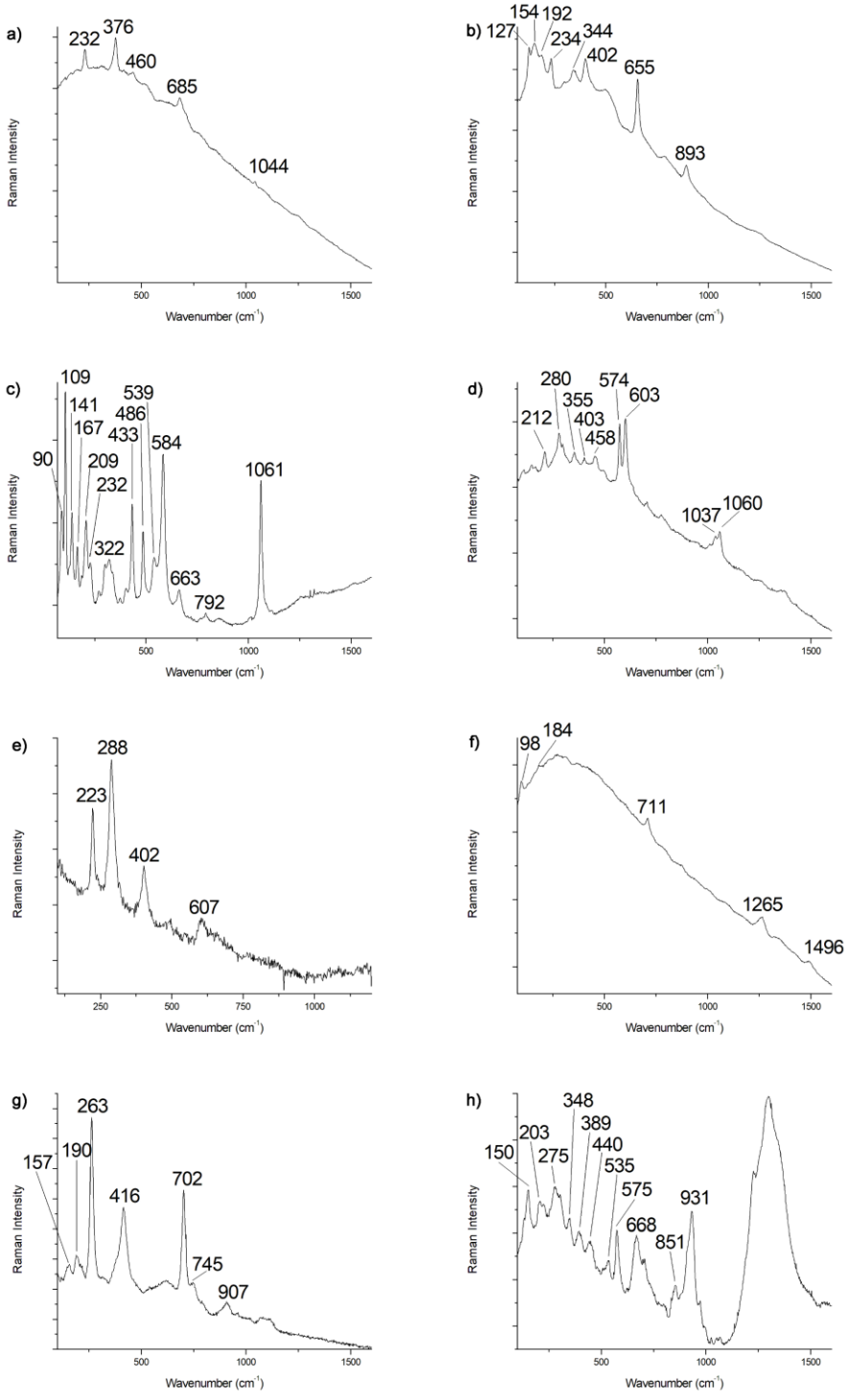


Figure 4.1. Raman spectra of the phyllosilicates a) antigorite, b) clintonite, c) fluorapophyllite-(K), d) gyrolite, e) hisingerite, f) lepidolite, g) muscovite and h) raite

## 4.2. Inosilicates

The inosilicates are a group of minerals that differ from other silicates by the distribution of their crystal lattice bonds. They can form single interlocking chains ($SiO_3$, 1:3 ratio) of silicate tetrahedra or double interlocking ones ($Si_4O_{11}$, 4:11 ratio) (14). Inosilicates are divided into two main groups: amphiboles and pyroxenes.

Amphiboles are minerals that crystallize into monoclinic and orthorhombic systems, as prisms or with needle-like shapes. They are the inosilicates that have the basic structure of double interlocking chain tetrahedra. In addition, they usually contain hydroxyl or halogen in their structure, which are relevant components on Mars, especially the hydroxyl group. Water is involved during their formation process in more evolved magmas with higher concentration of silica. This fact means that amphiboles are more abundant in intermediate to felsic igneous rocks, rather than in mafic ones (14). This family of minerals might provide relevant information for the study of Mars. For example, they can be used to study the volatile content of their parental magma (17).

Pyroxenes, the other inosilicate group, are usually found in igneous and metamorphic rocks. In this case, they are the inosilicate subgroup that form interlocking chains between the silicate tetrahedra in their crystal lattice (14). Their metallic composition is much more complex and wider than the one of other silicate, since the single chain silicate structure offers them more flexibility for the incorporations of other cations. Since pyroxenes are one of the most common minerals formed from magma in igneous rocks, they are commonly found on the surface of Mars and, thus, they are an important mineral group regarding the study of the Red Planet.

Some of the inosilicates that are included in the IMPAT database are shown in Figure 4.2.

Aegirine (Figure 4.2a), $NaFe(Si_2O_6)$, is the sodium endmember of the aegirine-augite series. It belongs to the clinopyroxene group of minerals and usually appears in alkalic igneous rocks. In some cases, aegirine can also be found in regionally metamorphosed schists, thus, in addition to be mineral directly related with the parent magma, it can also be formed after a metamorphism process, which involves heat and pressure (14). Regarding its Raman spectrum, aegirine presents Raman signals at 181, 215, 265, 295, 312, 346, 368, 386, 543, 561, 679, 867, 950, 974, 1043, 1142 and 1170 $cm^{-1}$.

Chkalovite (Figure 4.2b), $Na_2BeSi_2O_6$, is a rare mineral from the orthopyroxene family of minerals (18). In nature, this mineral is found in differentiated alkalic massifs and in the veins of pegmatite, an igneous rock. Chkalovite has a Raman spectrum that presents bands at 166, 262, 343, 389, 415, 457, 645, 938, 1012 and 1054 $cm^{-1}$.

The inosilicate edenite (Figure 4.2c), $NaCa_2Mg_5(Si_7Al)O_{22}(OH)_2$, belongs to the mineral group of the amphiboles. This mineral appears usually along with other magnesium rich minerals in metamorphic rocks. Regarding the study of Mars, its finding on the Red Planet would be a very relevant discovery, since it is one of the amphiboles that is best suited for fitting chloride anions into its chemical framework (19). The Raman features of edenite appear at 124, 162, 180, 224, 371, 396, 675, 931, 1029, 1061 and 1098 $cm^{-1}$.

Hillebrandite (Figure 4.2d), $Ca_2(SiO_3)(OH)_2$, is a rare pyroxene that crystallizes in the orthorhombic system. It is usually present in the contact zone of limestone and diorite (14), thus, it has high chances of being detected in areas of past volcanic activity where limestone was formed afterwards, which might be something that happened in some areas of Mars. Regarding the Raman spectrum of hillebrandite, it has signals at 118, 180, 314, 644, 961, 985 and 1016 $cm^{-1}$.

Pectolite (Figure 4.2e), $NaCa_2Si_3O_8(OH)$, is a mineral classified as part of the wollastonite group of minerals (see below). It crystallizes in the triclinic system and is usually found as radiated and fibrous crystalline masses. Pectolite is formed in the cavities of basalts, diabase and serpentinites when hydrothermal conditions are present (14). Due to this fact, it is a relevant mineral regarding the study of the surface of Mars. This mineral has a Raman spectrum that presents bands at 150, 276, 320, 358, 378, 414, 652, 973, 1002 and 1026 $cm^{-1}$.

Similar to pectolite, serandite (Figure 4.2f), $NaMn_2Si_3O_8(OH)$, is an inosilicate that is classified as part of the wollastonite group of minerals (see below). In nature, it is usually found as a solid solution with pectolite, with which it forms different minerals depending on the manganese and calcium substitution (14). It has a similar formation process as pectolite and, thus, is found in the same kind of environment. Regarding its Raman spectrum, it has bands at 110, 138, 164, 196, 225, 286, 366, 419, 668, 899, 978 and 1019 $cm^{-1}$.

The inosilicate sorensenite (Figure 4.2g), $Na_4SnBe_2Si_6O_{16}(OH)_4$, is a rare mineral that crystallizes in the monoclinic system. In nature, it is usually found along with nepheline syenite rocks, which are mainly composed of alkaline feldspar and nepheline (20). In other words, it is present in areas of rocks that needed a slow cooling of the magma. On Mars, if identified, it could be used to estimate the cooling rate and the depth of the parent magma of that area. The Raman features of this mineral appear at 139, 174, 210, 259, 302, 350, 383, 482, 499, 529, 579, 650 and 1023 $cm^{-1}$.

Finally, wollastonite (Figure 4.2h), $CaSiO_3$, crystallizes in the triclinic system and, despite being chemically very similar to the calcium pyroxene end member, they are very different structurally. In the case of wollastonite, it has a third tetrahedron in the linked chain in its crystal lattice (14). This mineral is formed when limestone or dolomite are subjected to high temperature and pressure, which can happen in the presence of silica

bearing fluids (21). Due to that reason, its presence in Mars would imply specific conditions of formation, which would help in the understanding of the surroundings in that area. Wollastonite has a Raman spectrum with signals at 109, 169, 337, 413, 583, 637, 970 and 1045 $cm^{-1}$.

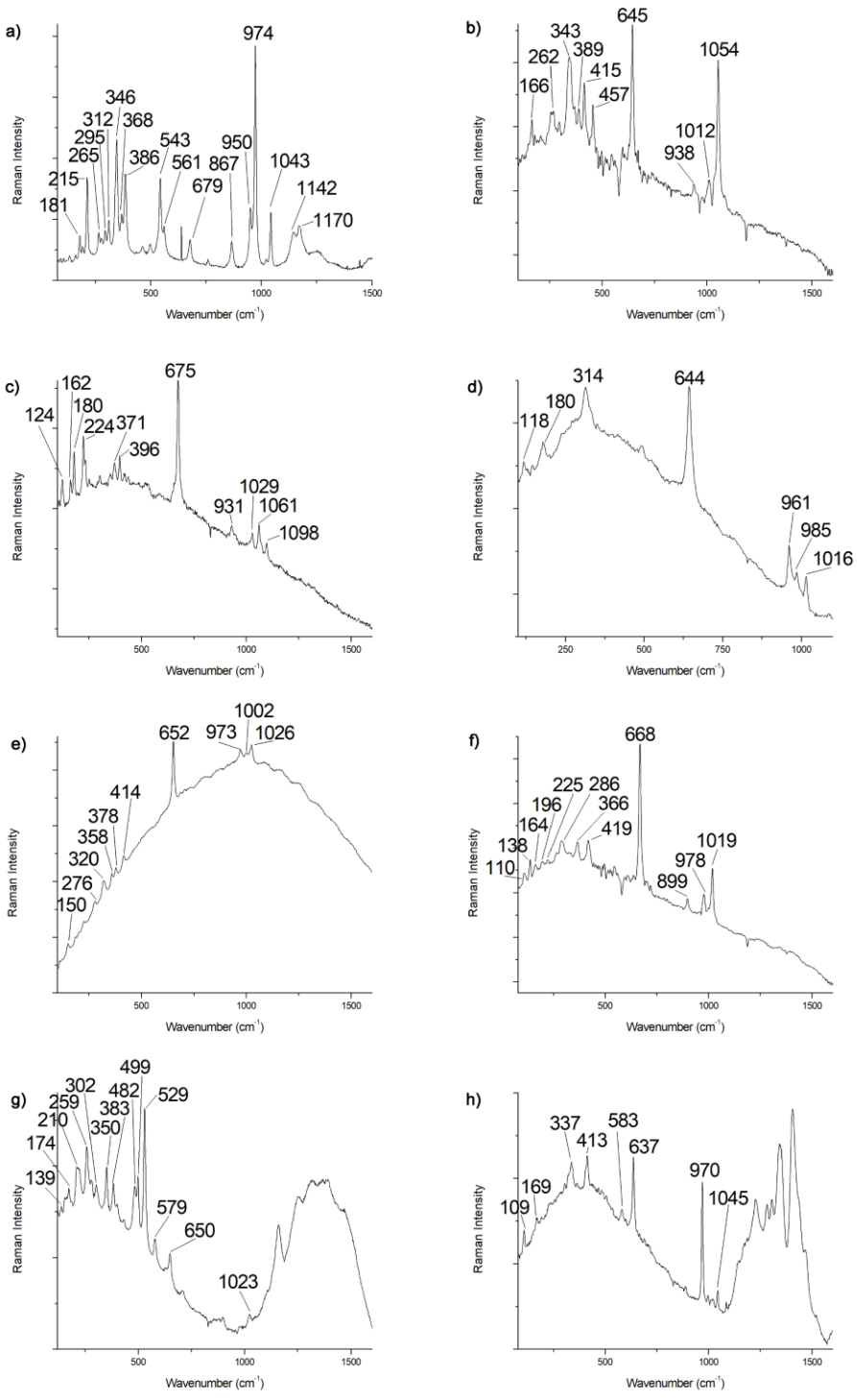


Figure 4.2. Raman spectra of the inosilicates a) aegirine, b) chkalovite, c) edenite, d) hillebrandite, e) pectolite, f) serandite, g) sorensenite and h) wollastonite

## 4.3. Other silicates

Besides phyllosilicates and inosilicates, other silicate groups were analyzed and included in the IMPAT database. More specifically, members of cyclosilicates, nesosilicates, sorosilicates and tectosilicates were analyzed. Some examples of each group can be observed in Figure 4.3.

Analcime (Figure 4.3a), $NaAlSi_2O_6 \cdot H2O$, is a mineral classified as a tectosilicate. It is a group of silicates also known as framework silicates, since their crystal lattice is formed of 3D framework of silicate tetrahedra as $SiO_2$ (1:2 ratio) (14). They are one of the most abundant family of silicates on Earth. Tectosilicates are divided into the silica, feldspars, feldspathoids, scapolites and zeolites subgroups. Regarding the study of Mars, they are very relevant since, for instance, are one of the main minerals that crystalize from magma (feldspars) (22). In addition to being one of the main constituents of igneous rocks, some minerals that belong to the tectosilicates group are also one of the most porous materials, such as zeolites (14). Analcime crystalizes in volcanic areas from aluminosilicates and sodium rich solutions (23), especially in pyroclastic sediments and saline solutions. Regarding its Raman spectrum, this mineral presents signatures at 142, 300, 388, 484, 580, 1025, 1105 and 1190 $cm^{-1}$.

Ilimaussite (Figure 4.3b), which is a cyclosilicate with a complex chemical formula, $(Na, K)_{7\text{-}8}(Ba, K)_{10}Ce_5(Nb, Ti)_6(Si_3O_9)_4(Si_9O_{18})O_6(O,OH)_{24}$, was also included in the IMPAT database. Cyclosilicates are minerals formed by linked rings composed of three or more tetrahedra (14). They are the less common group of silicates by abundance and, probably due to that fact, they are usually overlooked regarding the study of Mars. Even though they might not have properties as relevant to the study of the Red Planet as other silicates, they might also be present in its surface, thus, it is needed to have also Raman spectra of members from this family. In this case, the Raman spectrum of ilimaussite, a very rare cyclosilicate, can be

observed in Figure 4.3b. It is a mineral that crystallizes in the trigonal system and that is usually found in nature along with analcime, ussingite and pegmatite. This mineral has Raman signals at 164, 194, 215, 310, 344, 366, 384, 498, 543, 675, 867, 949, 972, 1042 and 1255 $cm^{-1}$, due to the diversity of chemical bonds in its basic structure.

Regarding the group of sorosilicates, the Raman spectra of epidote (Figure 4.3c), $Ca_2FeAl_2(Si_2O_7)(SiO_4)O(OH)$, and vesuvianite (Figure 4.3d), $Ca_{10}(Mg, Fe)_2Al_4(SiO_4)_5(Si_2O_7)_2(OH ,F)_4$, can be observed in the Figure 4.3. Sorosilicates consist of isolated pyrosilicate anions ($Si_2O_7^{6-}$), which are two tetrahedra that share an oxygen vertex in common (14). Regarding the two examples of sorosilicates presented, epidote crystallizes in the monoclinic system. Its formation process involves the presence of vapor of water in hydrothermal conditions at low and high temperatures (100 – 450 ºC) (14). This mineral constitutes igneous rocks that have undergone hydrothermal changes and some metamorphic rocks. As such, they are relevant for the study of Mars, since their presence would indicate hydrothermal conditions in the area at certain temperatures. The Raman spectrum of this mineral shows bands at 169, 245, 276, 351, 392, 454, 508, 568, 603, 687, 886, 918, 981, 1024 and 1087 $cm^{-1}$.

In the case of vesuvianite, it crystallizes in the tetragonal system due to isomorphic impurities. This mineral forms by contact metamorphism of clay limestone, dolomite and marlstone. These three rocks are relevant for the study of Mars, since they usually imply the presence of water for their formation. In addition, the identification of vesuvianite in a given area would mean that those minerals are also present and that in the past metamorphism conditions were present in that area. Regarding its Raman spectrum, vesuvianite presents signals at 182, 224, 255, 287, 325, 369, 407, 473, 544, 591, 638, 695, 753, 858, 933, 1022, 1109, 1169 and 1345 $cm^{-1}$.

Finally, several samples belonging to the silicate group of nesosilicates were analyzed to be included in the IMPAT database, among those, the Raman spectra of forsterite (Figure 4.3e), $MgSiO_4$, and monticellite (Figure 4.3f), $CaMgSiO_4$. This mineral group is also called orthosilicates, since they are composed by single orthosilicate tetrahedra ions ($SiO_4^{4-}$), that are connected only by interstitial cations (14). Forsterite, one of the two examples presented, belongs to the olivine solid solution along with fayalite, $FeSiO_4$, the other end member. It presents its Raman signals at 302, 431, 544, 605, 824, 856, 919 and 961 $cm^{-1}$. An explanation of the properties and characteristics of this mineral can be found in Chapter 5, *Forsterite and Fayalite Content in Olivines*, where olivines are studied in-depth by Raman spectroscopy.

Regarding monticellite, they belong to the olivine group of minerals, which means that they have the same crystalline structure as olivine but with different metallic content. In this case, the two end members that form the corresponding solid solution are monticellite, $CaMgSiO_4$, and kirschsteinite, $CaFeSiO_4$ (14). They are the equivalent to forsterite and fayalite, respectively. However, in this case one of the lattice positions occupied by either a magnesium or an iron atom in olivines, is occupied by a calcium in the case of monticellite/ kirschsteinite. Monticellite has a Raman spectrum that presents signals at 258, 361, 410, 638, 697, 818, 851 and 932 $cm^{-1}$.

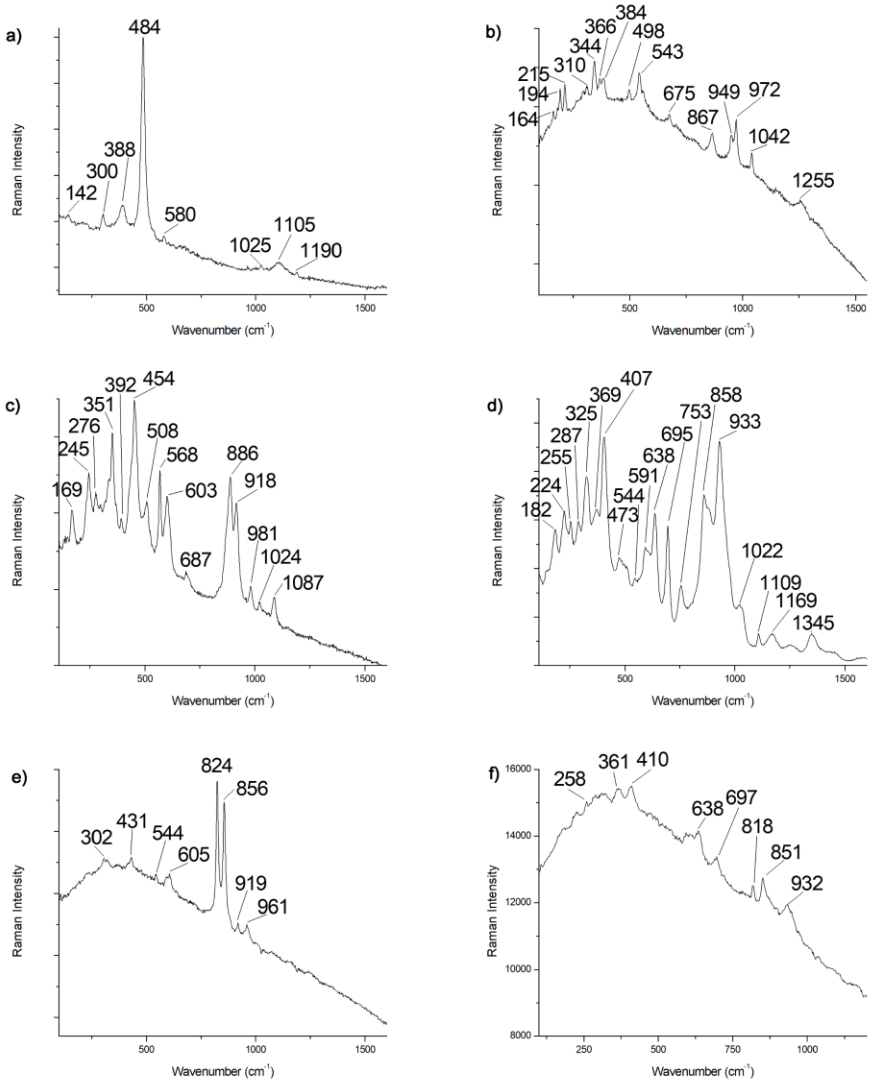


Figure 4.3. Raman spectra of the silicates a) analcime, b) ilimaussite, c) epidote, d) vesuvianite, e) forsterite and f) monticellite

## 4.4. Other minerals

Besides silicates, the Raman spectra of other minerals relevant to Mars were collected as part of the IMPAT database. An example of a carbonate, a sulfate and a sulfur are presented in Figure 4.4.

Calcites (Figure 4.4a), $CaCO_3$, and in a wider sense, carbonates, are a very relevant group of minerals for the study of Mars and the possible presence

of past life on the planet. Their formation process involves both to water and carbon, which are compounds directly related with the existence of life. In fact, it is one of the main mineral group that is widely studied as a possible indicative of the emergence of early life on Mars (24). An in depth analysis of the different carbonates already identified on Mars, their location and a more detailed description of calcite, can be found in Chapter 6, *Mineral Alterations Caused by High-Pressure Events*. Regarding its Raman spectrum, calcite presents its signal at 155, 280, 713 and 1085 $cm^{-1}$.

Regarding the sulfides and sulfates, they are mineral groups of high interest for exploration of the surface of Mars too. In fact, the hydrologic history of Mars might have been directly related with the presence of sulfur bearing materials. Most of these compounds were originated when Mars had volcanic activity, from the volcanic outgassing in the form of $H_2S$ and $SO_2$. These gases were the ones that formed the sulfates, hydrated sulfates and sulfurs that nowadays are found on Mars. The mentioned gases reacted with atmospheric components during a warm and wet era of Mars, dissolving in water to form acid solutions, which were neutralized when they entered in contact with the igneous rocks. As a result, the mentioned group of minerals would have formed (25).

Diaphorite (Figure 4.4b), $Ag_3Pb_2Sb_3S_8$, is a sulfur mineral that crystallizes into a monoclinic system. It is usually formed at medium temperatures in hydrothermal veins with other sulfides (14). It presents its Raman bands at 168 and 308 $cm^{-1}$.

Linarite (Figure 4.4c), $PbCu(OH)_2SO_2$, crystallizes into a monoclinic system and is found in nature as a secondary mineral in weathered areas that originally contained lead and copper sulfides (26). The Raman spectrum of linarite has features at 115, 368, 436, 511, 633 and 967 $cm^{-1}$.

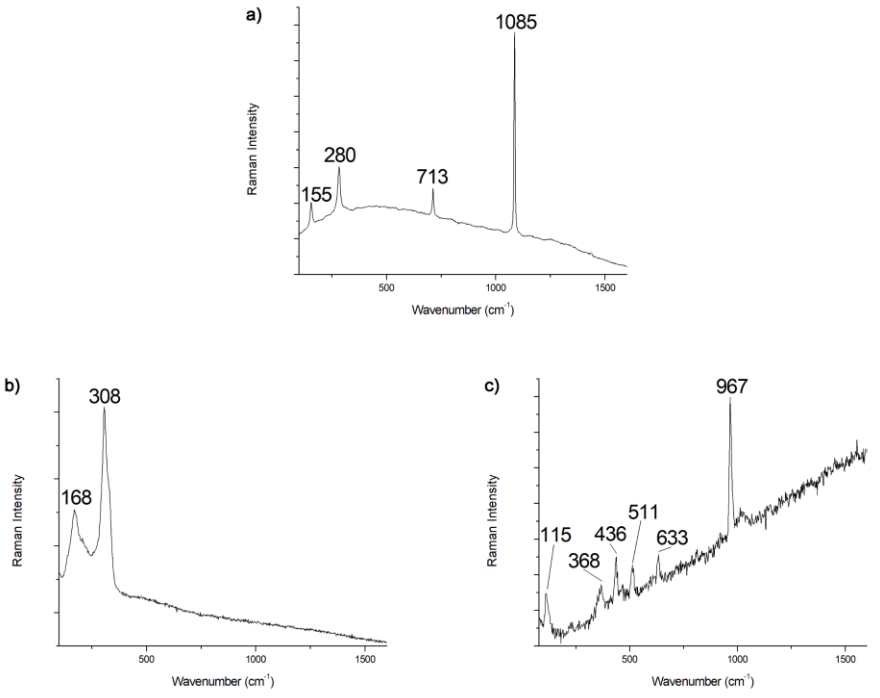


Figure 4.4. Raman spectra of the a) calcite, b) diaphorite and c) linarite

## 4.5. Conclusions

The development of a spectroscopic database of any kind is an arduous, complex and time consuming process. However, it is also an essential part to carry out an in-depth study of any unknown sample. During this PhD thesis, the Raman spectra of minerals relevant to the study of Mars have been collected in order to create the IMPAT database. In this sense, minerals whose Raman spectra were not present in the literature yet, were published with poor quality, or with scarce literature references, were selected and measured.

In addition to the expected or relevant mineral on Mars, several rare mineral samples have been included in the database. Although the presence of these minerals on Mars has never been considered, their geological formation processes could have taken place in the Red Planet and, thus, be present. In this sense, this database could play an important

role for the future interpretation of the results obtained from the surface of Mars.

Finally, it must be pointed out that the IMPAT database is not only a Raman spectroscopy set of spectra. In fact, the Raman spectra collection is the smallest part of the database. Nowadays, besides the Raman spectra of 105 mineral specimens relevant to Mars, the IMPAT database includes the visible and near-infrared (VISNIR) spectra of more than 400 minerals also related to the Red Planet. In addition, the elemental information obtained by ED-XRF of each sample analyzed is also collected.

## 4.6. Bibliography

1. Lafuente, B., Downs, R. T., Yang, H., Stone, N., Highlights in Mineralogical Crystallography; The power of databases: The RRUFF project (p.p. 1-30) **2015,** de Gruyter, Berlin, München, Boston.

2. Wang, A., Han, J., Guo, L., Yu, J., Zeng, P., Database of Standard Raman Spectra of Minerals and Related Inorganic Crystals, *Applied Spectroscopy,* **1994**, 48, 959-968.

3. Poulet, F., Mangold, N., Loizeau, D., Bibring, J. -., Langevin, Y., Michalski, J., Gondet, B., Abundance of minerals in the phyllosilicate-rich units on Mars, *Astronomy and Astrophysics (Berlin),* **2008**, 487, L41-L44.

4. Altheide, T. S., Chevrier, V. F., Noe Dobrea, E., Mineralogical characterization of acid weathered phyllosilicates with implications for secondary martian deposits, *Geochimica Et Cosmochimica Acta,* **2010**, 74, 6232-6248.

5. Craig, P. I., Ming, D. W., Rampe, E. B., Morris, R. V., Sulfate Mineral Formation from Acid-Weathered Phyllosilicates: Implications for the Aqueous History of Mars, .

6. Bibring, J., Langevin, Y., Mustard, J. F., Poulet, F., Arvidson, R., Gendrin, A., Gondet, B., Mangold, N., Pinet, P., Forget, F., et al., Global Mineralogical and Aqueous Mars History Derived from OMEGA/Mars Express Data, *Science,* **2006**, 312, 400-404.

7. Baldridge, A. M., Hook, S. J., Crowley, J. K., Marion, G. M., Kargel, J. S., Michalski, J. L., Thomson, B. J., de Souza Filho, C. R, Bridges, N. T.,

Brown, A. J., Contemporaneous deposition of phyllosilicates and sulfates: Using Australian acidic saline lake deposits to describe geochemical variability on Mars, *Geophysical Research Letters,* **2009**, 36, L19201-n/a.

8. Ulmer, P., Trommsdorff, V., Serpentine Stability to Mantle Depths and Subduction-Related Magmatism, *Science,* **1995**, 268, 858-861.

9. Dodony, I., Posfai, M., Buseck, P. R., Revised structure models for antigorite; an HRTEM study, *The American Mineralogist,* **2002**, 87, 1443-1457.

10. Tischendorf, G., Förster, H. J., Gottesmann, B., Rieder, M., True and brittle micas: composition and solid-solution series, *Mineralogical Magazine,* **2007**, 71, 285-320.

11. Frost, R. L., Xi, Y., Raman spectroscopic study of the minerals apophyllite-(KF) $KCa_4Si_8O_{20}F{\cdot}8H_2O$ and apophyllite-(KOH) $KCa_4Si_8O_{20}(F,OH){\cdot}8H_2O$, *Journal of Molecular Structure,* **2012**, 1028, 200-207.

12. Siauciunas, R., Baltakys, K., Formation of gyrolite during hydrothermal synthesis in the mixtures of CaO and amorphous SiO2 or quartz, *Cement and Concrete Research,* **2004**, 34, 2029-2036.

13. Eggleton, R. A., Tilley, D. B., Hisingerite: a ferric kaolin mineral with curved morphology, *Clays and Clay Minerals,* **1998**, 46, 400-413.

14. Klein, C., Hurlbut, C. S., Dana, J. D., Manual of mineralogy, 21st ed. **1999**, Wiley, New York, New York, USA.

15. Miller, C. F., Stoddard, E. F., Bradfish, L. J., Dollase, W. A., Composition of plutonic muscovite: genetic implications, *Canadian Mineralogist,* **1981**, 19, 25-34.

16. Mer'kov, A. N., Bussen, I. V., Goyko, Y. A., Kul'chitskaya, Y. A., Men'shikov, Y. P., Nedorezova, A. P., Raite and zorite, new minerals from the Lovozero Tundra, *International Geology Review,* **1973**, 15, 1087-1094.

17. Williams, K. B., Sonzogni, Y., Amphibole in the Tissint Martian Meteorite: Composition and Implication for Volatile Content of Parental Magma, *45th Lunar and Planetary Science Conference,* **March 17, 2014,** The Woodlands, Texas, USA.

18. Henderson, C. M. B., Taylor, D., Structural behaviour of chkalovite, Na2BeSi2O6: a member of the cristobalite family, *Mineralogical Magazine,* **1989**, 53, 117-119.

19. Oberti, R., Hawthorne, F. C., Cannillo, E., Camara, F., Long-range order in amphiboles, *Reviews in Mineralogy and Geochemistry,* **2007**, 67, 125-171.

20. Semenov, E. I., Sorensenite, a new sodium-beryllium-tin-silicate from the Ilimaussaq intrusion, South Greenland, **1965**, Reitzel, Kobenhavn.

21. Whitley, S., Halama, R., Gertisser, R., Preece, K., Deegan, F. M., Troll, V. R., Magmatic and Metasomatic Effects of Magma–Carbonate Interaction Recorded in Calc-silicate Xenoliths from Merapi Volcano (Indonesia), *Journal of Petrology,* **2020**, 61.

22. Freeman, J. J., Wang, A., Kuebler, K. E., Jolliff, B. L., Haskin, L. A., Characterization of natural feldspars by Raman spectroscopy for future planetary exploration, *Canadian Mineralogist,* **2008**, 46, 1477-1500.

23. English, P. M., Formation of analcime and moganite at Lake Lewis, central Australia: significance of groundwater evolution in diagenesis, *Sedimentary Geology,* **2001**, 143, 219-244.

24. Fernández-Remolar, D. C., Sánchez-Román, M., Amils, R., The case of the lacking carbonates and the emergence of early life on mars, *Sustainability (Basel, Switzerland),* **2010**, 2, 2541-2554.

25. Wang, A., Freeman, J. J., Jolliff, B. L., Chou, I., Sulfates on Mars: A systematic Raman spectroscopic study of hydration states of magnesium sulfates, *Geochimica Et Cosmochimica Acta,* **2006**, 70, 6118-6135.

26. Bloise, A., Dattola, L., Allegretta, I., Terzano, R., Miriello, D., Linarite and connellite dataset from Calabria region (Southern Italy): First evidence, *Data in Brief,* **2019**, 27, 104597.

# Chapter 5
# Forsterite and Fayalite Content in Olivines

*"Leave no stone unturned"*

Euripides, 428 BC

Olivine, $(Mg, Fe)_2SiO_4$, is a mineral composed of the two endmembers of its solid solution series: forsterite (Fo), $Mg_2SiO_4$, as the Mg endmember and fayalite (Fa), $Fe_2SiO_4$, as the Fe one (1). It is a silicate mineral that is usually found in igneous rocks alongside plagioclase and pyroxene, as they are all present in basalts and igneous formations. These minerals are commonly found in planets where the formation of the crust and upper mantle involved the solidification of a magma ocean, the density stratification and overturn, large-scale convection or volcanic activity (2). As such, olivine is an abundant mineral in planets such as Earth, especially in the subsurface, as

it is a mineral that suffers from weathering heavily in the surface, mainly in humid areas or in the presence of seawater.

Due to the similarities with our planet and, due to its formation process, olivine has been found on Mars, as it has been determined in numerous studies and analyses performed in Martian meteorites, as well as by orbiters in Mars and even in-situ by the *Spirit*, *Opportunity* and *Curiosity* rovers (3-5). Olivine is, therefore, one of the most abundant minerals on Mars, so it is and will be one of the most commonly found minerals on the planet's surface by rovers of the active and upcoming Martian missions. The fact that olivine weathers easily depending on the environmental conditions that surrounds it may prove to be more of an advantage than a disadvantage in space exploration.

The abundance of olivine in a given igneous formation, or the proportion of Mg/Fe that forms it, can be used to study the petrologic evolution of an area and to determine the origin and evolution of its parent magma, as it is one of the first minerals to crystallize from it (4). In addition, as it is described in literature (6), olivine can undergo different weathering processes depending on its location, especially if there is water present in the surroundings. Moreover, different weathering processes take place depending on which salts (if any) are present in said water and in which concentrations. All these facts lead to different weathering paths, resulting in different minerals formed at the end (6).

Considering that Mars 2020 and the upcoming Mars missions will study areas of ancient lakes and oceans, it is very likely that both primary olivine and its weathered products, along with other minerals such as carbonates, will be found on the surface. In fact, they have already been observed by the *Compact Reconnaissance Imaging Spectrometer for Mars* (*CRISM*) (7). Therefore, olivine may be the key to understand many of the geological processes occurred on the surface of the planet. This is the reason why it

is important to know as much as possible about olivine and its weathering processes and products, in order to be able to study Mars more effectively.

However, the thorough study of olivines requires reliable and sensitive techniques. In this sense, Raman spectroscopy is a technique present in both NASA's and ESA's rover payloads (8-10). As has been repeatedly proven in literature (11-14), Raman spectroscopy allows to know the Mg/Fe ratio of olivine through the position of its main Raman bands. Both end members of olivine have their main Raman signatures as a doublet in the 810-860 $cm^{-1}$ spectral range: 824 and 857 $cm^{-1}$ for the forsterite and 814 and 840 $cm^{-1}$ for fayalite. Depending on the Mg/Fe composition of a given olivine (given as $Fo_XFa_{(100-X)}$, where $Fo_X$ is related to the % molar content of forsterite, Mg, and $Fa_{(100-X)}$ is related to the % molar content of fayalite, Fe) the resulting combination of both Raman doublets (forsterite + fayalite) is a new doublet with its two main signals in varying positions, as the signal contribution from both fayalite and forsterite changes proportionally depending on the olivine metallic composition. Using this fact, it is possible to calibrate the Mg/Fe ratio as a function of the wavenumber position of the main Raman signals of olivine.

These types of calibration models have already been proposed in literature (12, 13). However, works carried out to date might not be precise enough to accurately determine the Mg/Fe ratio of olivine, which is a significant parameter for the characterization of the mineral. In some calibration models the uncertainty of the results obtained is of 10 % or even higher (12, 13), which could mislead the interpretation of Martian results. In addition, in this type of studies it is usual to obtain the data for the development of the models only with one or two different Raman instruments. This fact could lead to a significant bias in the proposed models, since parameters such as signal-to-noise ratio, bandwidth, spectral resolution, the baseline or the bands intensity are linked to each instrument. These factors could lead to significant variations in the Mg and

Fe content obtained through a given calibration model using different instruments.

Therefore, it is necessary to develop a model that bypasses these problems and provides results that are as accurate and precise as possible regardless of the Raman instrument with which the measurements are made. In order to bypass the possible bias generated by the use of only one instrument, a model that uses data acquired with several Raman spectrometers should be developed.

During this PhD thesis, such a model has been developed using both experimental Raman results of natural and commercial olivines obtained with two different instruments, and all the olivine Raman data that could be found in the literature. In this way, the proposed model avoids the bias mentioned above and can be used independently of the type and characteristics of the Raman instrument with which the spectra are obtained.

## 5.1. Olivine Data Set

As explained above, a collection of Raman spectra from olivines with a known composition was collected to develop a calibration model for the determination of the metallic content (Mg, Fe) of the mineral. This set of data is summarized in Table 5.1 with their corresponding metallic content and the position of their two main olivine bands (OB), OB1 (812-824 $cm^{-1}$) and OB2 (837-856 $cm^{-1}$), together with their difference, ΔOB (OB2–OB1). In order to increase the accuracy and precision of the models, the OB1 and OB2 values were collected to the tenth of $cm^{-1}$ of the wavenumbers.

In addition to the data set of olivines used for the calibration, a commercial pure olivine of known metallic concentration ($Fo_{89}Fa_{11}$, according to the supplier) was also employed as a standard to validate the proposed model. In order to check the purity of the commercial olivine, three different grains

were analyzed separately by means of X-ray diffraction (XRD). Figure 5.1 shows the XRD diffractogram of one of those measurements.

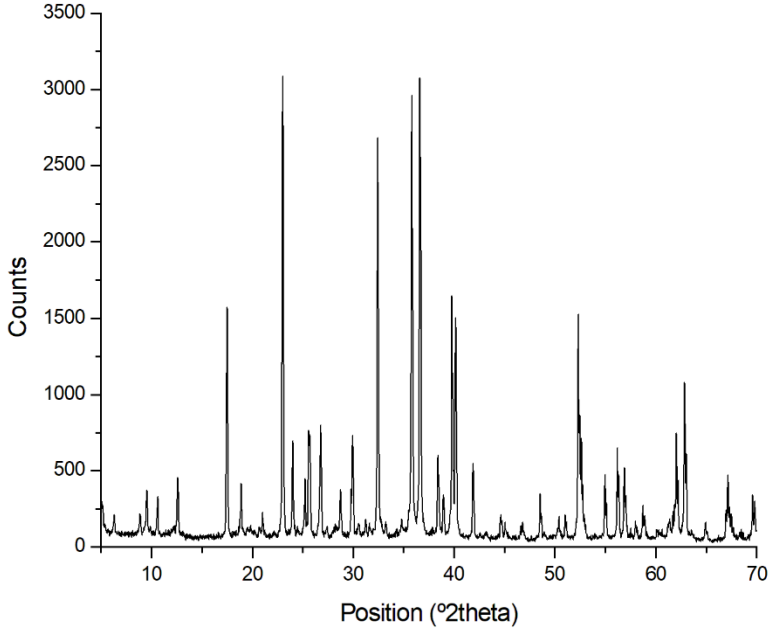


Figure 5.1. XRD diffractogram of one of the standard commercial olivine grains analyzed

Table 5.1. Metallic composition and main Raman signals position of the olivines used for the calibration model

| Composition | | Spectral information ($cm^{-1}$) | | | |
|---|---|---|---|---|---|
| $Fo_x$ (Mg %) | $Fa_x$ (Fe %) | OB1 | OB2 | ΔOB | Literature reference |
| 100 | 0 | 824.5 | 856.0 | 31.5 | (15) |
| 100 | 0 | 824.0 | 856.0 | 32.0 | (16) |
| 100 | 0 | 824.0 | 856.0 | 32.0 | (17) |
| 100 | 0 | 824.0 | 856.0 | 32.0 | (14) |
| 100 | 0 | 824.7 | 856.7 | 32.0 | (12) |
| 100 | 0 | 825.0 | 857.0 | 32.0 | (13) |
| 100 | 0 | 824.7 | 857.0 | 32.3 | (18) |
| 100 | 0 | 825.0 | 857.0 | 32.0 | (19) |
| 96 | 4 | 824.4 | 856.6 | 32.2 | (20) |
| 94 | 6 | 823.5 | 855.0 | 31.5 | (17) |
| 92.7 | 7.3 | 824.5 | 856.4 | 31.9 | (11) |
| 92 | 8 | 823.8 | 855.7 | 31.9 | (20) |
| 92 | 8 | 823.7 | 855.7 | 32.0 | (20) |
| 91 | 9 | 823.1 | 855.0 | 31.9 | (21) |
| 91 | 9 | 824.0 | 855.5 | 31.5 | (19) |
| 91 | 9 | 823.3 | 855.1 | 31.8 | (20) |
| 90 | 10 | 822.9 | 854.9 | 32.0 | (20) |
| 89.5 | 10.5 | 822.5 | 854.4 | 31.9 | (18) |
| 89 | 11 | 822.5 | 854.5 | 32.0 | (21) |
| 88 | 12 | 822.0 | 854.0 | 32.0 | (16) |
| 87.5 | 12.5 | 822.6 | 854.2 | 31.6 | (18) |
| 87.4 | 12.6 | 823.6 | 855.2 | 31.6 | (11) |
| 86.1 | 13.9 | 823.0 | 854.7 | 31.7 | (11) |
| 84.6 | 15.4 | 821.3 | 852.7 | 31.4 | (18) |
| 84.5 | 15.5 | 823.0 | 854.5 | 31.5 | (13) |
| 84 | 16 | 822.0 | 853.0 | 31.0 | (19) |
| 82.8 | 17.2 | 822.1 | 853.5 | 31.4 | (11) |
| 82.3 | 17.7 | 821.8 | 853.1 | 31.3 | (18) |
| 80.7 | 19.3 | 822.3 | 853.3 | 31.0 | (11) |
| 76.8 | 23.2 | 821.7 | 852.5 | 30.8 | (11) |
| 74.5 | 25.5 | 821.3 | 852.2 | 30.9 | (11) |
| 74 | 26 | 821.0 | 852.0 | 31.0 | (22) |

Table 5.1. Metallic composition and main Raman signals position of the olivines used for the calibration model (Continuation)

| Composition | | Spectral information ($cm^{-1}$) | | | |
|---|---|---|---|---|---|
| $Fo_x$ (Mg %) | $Fa_x$ (Fe %) | OB1 | OB2 | ΔOB | Literature reference |
| 72.2 | 27.8 | 820.9 | 851.8 | 30.9 | (11) |
| 71 | 29 | 821.6 | 851.6 | 30.0 | (20) |
| 70.6 | 29.4 | 820.4 | 851.2 | 30.8 | (11) |
| 70 | 30 | 820.4 | 851.1 | 30.7 | (20) |
| 69 | 31 | 819.6 | 849.9 | 30.3 | (21) |
| 66.9 | 33.1 | 820.5 | 850.4 | 29.9 | (11) |
| 65 | 34.7 | 820.1 | 849.7 | 29.6 | (11) |
| 65 | 35 | 819.0 | 849.2 | 30.2 | (21) |
| 62.8 | 37.2 | 819.8 | 849.4 | 29.6 | (11) |
| 62 | 38 | 819.0 | 848.7 | 29.7 | (21) |
| 56 | 34 | 818.2 | 847.6 | 29.4 | (21) |
| 52 | 48 | 819.6 | 848.8 | 29.2 | (20) |
| 50 | 50 | 818.9 | 848.1 | 29.2 | (20) |
| 49.6 | 50.4 | 818.1 | 846.5 | 28.4 | (17) |
| 45.4 | 54.6 | 817.0 | 846.0 | 29.0 | (17) |
| 45 | 55 | 818.0 | 846.5 | 28.5 | (19) |
| 41 | 59 | 818.0 | 846.0 | 28.0 | (23) |
| 40 | 60 | 817.0 | 844.8 | 27.8 | (20) |
| 39 | 61 | 816.5 | 844.4 | 27.9 | (21) |
| 34 | 66 | 818.1 | 845.6 | 27.5 | (20) |
| 30 | 70 | 817.1 | 844.8 | 27.7 | (20) |
| 23 | 77 | 817.2 | 843.9 | 26.7 | (20) |
| 20 | 80 | 816.4 | 843.4 | 27.0 | (20) |
| 11 | 89 | 814.9 | 842.8 | 27.9 | (20) |
| 10 | 90 | 815.2 | 841.7 | 26.5 | (20) |
| 8 | 92 | 815.3 | 838.9 | 23.6 | (21) |
| 1 | 99 | 814.5 | 841.1 | 26.6 | (20) |
| 0 | 100 | 814.4 | 839.7 | 25.3 | (16) |
| 0 | 100 | 813.8 | 839.0 | 25.2 | (24) |
| 0 | 100 | 814.2 | 839.6 | 25.4 | (17) |
| 0 | 100 | 813.6 | 839.7 | 26.1 | (14) |
| 0 | 100 | 812.7 | 837.7 | 25.0 | This work |

The signals of the diffractograms obtained from the three mineral grains were very similar to one another, showing all of them the features corresponding to the diffractogram of a high magnesian olivine (PDF 88-997 in the XRD ICDD PDF2 database). Fayalitic olivine was not found in any of the grains, which means that the grains were composed of the same type of olivine in a homogeneous way, without differences between the rims and the core of the grains. In addition to olivine, some minor and trace minerals were also observed in the different diffractograms: clinochlore (PDF 74-1137), tremolite (PDF 86-1318), phyllosilicates with talc structure (PDF 83-1768), muscovite (PDF 82-1852) and lizardite (PDF 83-1768). These trace minerals were probably the consequence of micro alterations of the olivine or the result of contamination of the commercial product. In any case, none of these minerals have Raman signals in the same region as the main Raman signals of olivine, thus, they did not interfere with the position of OB1 and OB2.

Additionally, wavelength dispersive X-ray fluorescence (WD-XRF) was carried out to double check the concentration of the commercial olivine and to compare the results with the ones proposed by the developed Raman model. Three different borate glass beads were prepared by melting in an induction microfurnace, mixing the grinded olivine grains with the Spectromelt A12 flux (Merck, Germany). The beads were then analyzed at vacuum with an AXIOS WD-XRF spectrometer (PANalytical, UK), using a Rh tube and three detectors (gas flux, sparkle and Xe sealing). The average result for the metallic composition of the commercial olivine obtained by WD-XRF was $Fo_{89.5\pm1.8}Fa_{10.5\pm0.5}$, where the confidence interval was calculated at a 95 % of confidence using the standard deviation of the three analyzed olivine grains. As observed, the composition declared by the supplier, $Fo_{89}Fa_{11}$, was within the composition obtained by WD-XRF, $Fo_{89.5\pm1.8}Fa_{10.5\pm0.5}$.

Finally, this olivine standard was analyzed by Raman spectroscopy. 10 different grains were analyzed obtaining the same Raman spectrum in all

of them (Figure 5.2). As can be observed, the Raman spectrum does not have any additional signal not related to olivine.

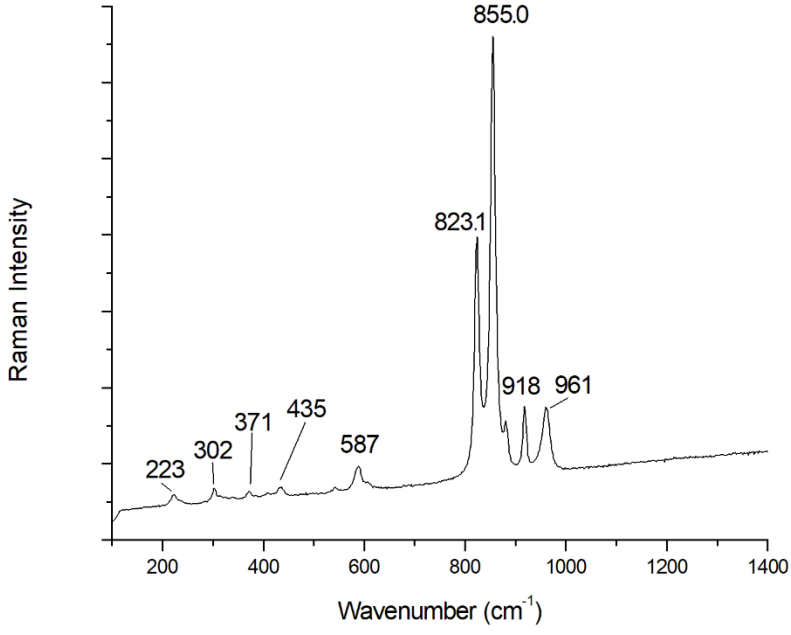


Figure 5.2. Raman spectrum of the standard commercial olivine obtained with the 532 nm excitation laser

The 223, 302 and 371 $cm^{-1}$ signals are assigned to lattice vibrational modes of the mineral, more specifically, to rotational and translational vibrations of the $SiO_4$ and to translational motions of the cations that occupy the octahedral spaces of the crystal lattice (16). The 435 and 587 $cm^{-1}$ Raman bands are associated with the internal bending vibrational modes of the $SiO_4$ ionic groups (16). Lastly, the 823, 855, 918 and 961 $cm^{-1}$ group of signals are assigned to the internal stretching vibrational modes of the $SiO_4$ ionic group (16). Regarding the main Raman bands of the spectrum of olivine, 823 and 855 $cm^{-1}$ in this particular case, they do usually present changes in their relative intensities as a function of the crystal orientation where the Raman laser hits (16, 25). However, this fact does not have any effect in the quantification of the metallic content of the olivines because

the proposed model uses the positions of the peaks, which are not affected by this fact, and not their intensities.

## 5.2. Olivine Calibration Models and Validation

Using the data of Table 5.1 three different calibration models were proposed, plotting the wavenumber position of OB1, OB2 and the difference between the two main bands (ΔOB = OB2 – OB1) versus the concentration of forsterite ($Fo_x$) of the olivines. Since the olivine only has two end members, the concentration of fayalite can be calculated by subtracting the $Fo_x$ from 100. The plots of the models together with their residuals graph are shown in Figure 5.3, 5.4 and 5.5, as well as the equations for the three models in Equation 5.1, 5.2 and 5.3, respectively. As can be observed, the calibration curve plots also have two red lines that represent the calculated confidence interval for all the curve at a 95 % level of confidence, using the overall standard deviation of the regression model to calculate it.

$$OB1\ (cm^{-1}) = 3.63 \cdot 10^{-4} \cdot Fo_X^2 + 0.0667 \cdot Fo_X + 814.2 \qquad \textit{Equation 5.1}$$

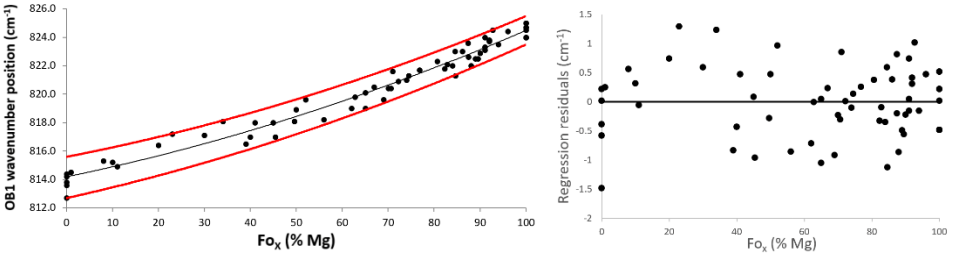


Figure 5.3. Forsterite content calibration curve created from the OB1 Raman band position and their forsterite values and the residuals plot of the regression model

As observed in Figure 5.3, when using the OB1 Raman signature of olivine to calibrate its metallic content, all the data fit inside the confidence interval depicted as two red lines for every olivine metallic composition, which implies that there are not outliers among the set of data used for the calibration model. Regarding its quality parameters, the determination

coefficient ($r^2$) obtained for the quadratic regression model expressed in Equation 5.1 is 0.970, and its overall standard deviation of the curve fit is ±0.61 $cm^{-1}$. In the residuals plot, it can be observed that they are scattered in a random way, as they do not follow a visible trend. In addition, all the points are equally distributed around the zero horizontal line and all of them in the same range of distance from it. All of these facts imply that the proposed model for the data set used (64 values published in literature) is the correct one and that the model's predictions should be accurate and precise on average, rather than systematically too high or too low.

$$OB2\ (cm^{-1}) = 3.00 \cdot 10^{-4} \cdot Fo_X^2 + 0.142 \cdot Fo_X + 839.6 \qquad \textit{Equation 5.2}$$

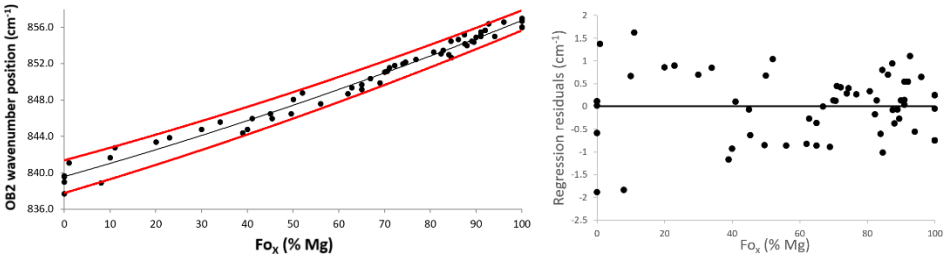


Figure 5.4. Forsterite content calibration curve created from the OB2 Raman band position and their forsterite values and the residuals plot of the regression model

In the case of the developed model using the OB2 olivine Raman signal (Figure 5.4), all the data points also fit inside the red confidence interval lines, supporting the same fact explained in the model with OB1, that is, there are not outliers in the set of data. For this model (Equation 5.2) a $r^2$ of 0.984 and an overall standard deviation of the curve fit of ±0.73 $cm^{-1}$ were obtained. Regarding the residuals model, in this case the points are also distributed in a random way and equally around the horizontal zero line. However, it must be pointed out that for this calibration model the residuals corresponding to the samples with a low magnesium concentration (the ones in the far left of the residuals plot of Figure 5.4) are slightly further apart from the zero than the rest of them. This could be due to a random factor that only affected a few points of the data set or that this range of points does not fit the calibration model as fine as the others,

implying that for olivine with low magnesium concentrations the uncertainty of the results would be higher.

$$\Delta OB\ (cm^{-1}) = 0.0685 \cdot Fo_X + 25.5 \qquad \textit{Equation 5.3}$$

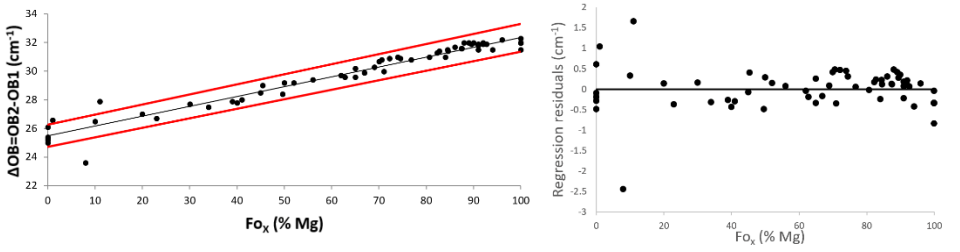


Figure 5.5. Forsterite content calibration curve created from the difference between OB2 and OB2 (ΔOB) and the forsterite values and the residuals plot of the regression model

Finally, the model developed using the difference between OB2 and OB1 olivine Raman signals can be seen in Figure 5.5, together with the regression curve (Equation 5.3), which had a $r^2$ of 0.951 and an overall standard deviation of the curve fit of ±0.50 $cm^{-1}$. Contrary to the previous two models, in this case the data points do not fit entirely inside the confidence interval curves plotted in red. More precisely, around half the points that correspond to olivines with low concentration of magnesium ($Fo_x$ < 20 %) are outside that interval. In addition, those same points are the ones that are further apart from the horizontal zero line in the residuals plot.

In order to check the accuracy of the three models, the standard commercial olivine described above was used ($Fo_{89.5\pm1.8}Fa_{10.5\pm0.5}$, by WD-XRF). The OB1 (832 $cm^{-1}$), OB2 (855 $cm^{-1}$) Raman signals (Figure 5.2) and the difference between the two (32 $cm^{-1}$) were used to calculate the metallic concentration of the mineral using the respective calibration models. The concentrations obtained were $Fo_{89.0\pm1.2}Fa_{11.0\pm0.2}$, $Fo_{91.2\pm1.5}Fa_{8.8\pm0.1}$ and $Fo_{95.0\pm1.0}Fa_{5.0\pm0.1}$ for the OB1, OB2 and ΔOB models, respectively (Table 5.2). The confidence intervals were calculated at a 95 % level of confidence using the overall standard deviation of the calibration curves.

Table 5.2. Forsterite and fayalite concentrations of the standard commercial olivine by WD-XRF and the calculated ones using the developed models by Raman spectroscopy

| Concentration by WD-XRF (%) | | Calculated concentration (%) by Raman | | | | | |
|---|---|---|---|---|---|---|---|
| | | OB1 model | | OB2 model | | ΔOB model | |
| $Fo_x$ | $Fa_x$ | $Fo_x$ | $Fa_x$ | $Fo_x$ | $Fa_x$ | $Fo_x$ | $Fa_x$ |
| 89.5±1.8 | 10.5±0.5 | 89.0 ±1.2 | 11.0 ±0.2 | 91.2 ±1.5 | 8.8 ±0.2 | 95.0 ±1.0 | 5.0 ±0.1 |

As observed, the forsterite confidence interval results obtained with the OB1 and OB2 models overlap perfectly with the WD-XRF concentration confidence interval, which means that the predicted concentrations with these two models were accurate. In contrast, the ΔOB model failed in the prediction of the Fo and Fa concentrations. Due to that reason, that model was discarded for further quality parameters assurance, since the resulting methodology for the olivine metallic content characterization had to be as accurately as possible.

In addition to the standard commercial olivine, the two remaining calibration models were validated using the 64 data values that were used for their development. The wavenumber position of OB1 and OB2 were introduced in the respective regression curves and the forsterite value corresponding to each data point was calculated. These values were then compared with the real ones summarized in Table 5.1. Table 5.3 summarizes this comparison, where the real $Fo_x$ values can be compared with the ones calculated for each calibration model.

Table 5.3. $Fo_x$ of the data set used to develop the calibration models and the calculated one using said models with the wavenumbers position

| Real composition | | Calculated composition with the models | |
|---|---|---|---|
| $Fo_x$ (Mg %) | Literature reference | OB1 – $Fo_x$ (Mg %) | OB2 – $Fo_x$ (Mg %) |
| 100 | (15) | 100.1 | 96.2 |
| 100 | (16) | 96.5 | 96.2 |
| 100 | (17) | 96.5 | 96.2 |
| 100 | (14) | 96.5 | 96.2 |
| 100 | (12) | 101.5 | 99.7 |
| 100 | (13) | 103.7 | 101.2 |
| 100 | (18) | 101.5 | 101.2 |
| 100 | (19) | 103.7 | 101.2 |
| 96 | (20) | 99.4 | 99.2 |
| 94 | (17) | 92.8 | 91.2 |
| 92.7 | (11) | 100.1 | 98.2 |
| 92 | (20) | 95.0 | 94.7 |
| 92 | (20) | 94.3 | 94.7 |
| 91 | (21) | 89.8 | 91.2 |
| 91 | (19) | 96.5 | 93.7 |
| 91 | (20) | 91.3 | 91.7 |
| 90 | (20) | 88.3 | 90.7 |
| 89.5 | (18) | 85.2 | 88.1 |
| 89 | (21) | 85.2 | 88.6 |
| 88 | (16) | 81.2 | 86.1 |
| 87.5 | (18) | 86.0 | 87.1 |
| 87.4 | (11) | 93.5 | 92.2 |
| 86.1 | (11) | 89.0 | 89.7 |
| 84.6 | (18) | 75.6 | 79.3 |
| 84.5 | (13) | 89.0 | 88.6 |
| 84 | (19) | 81.2 | 80.8 |
| 82.8 | (11) | 82.0 | 83.5 |
| 82.3 | (18) | 79.6 | 81.4 |
| 80.7 | (11) | 83.6 | 82.4 |
| 76.8 | (11) | 78.8 | 78.2 |
| 74.5 | (11) | 75.6 | 76.6 |
| 74 | (22) | 73.1 | 75.5 |

Table 5.3. $Fo_x$ of the data set used to develop the calibration models and the calculated one using said models with the wavenumbers position (Continuation)

| Real composition | | Calculated composition with the models | |
|---|---|---|---|
| $Fo_x$ (Mg %) | Literature reference | OB1 – $Fo_x$ (Mg %) | OB2 – $Fo_x$ (Mg %) |
| 72.2 | (11) | 72.3 | 74.5 |
| 71 | (20) | 78.0 | 73.4 |
| 70.6 | (11) | 68.0 | 71.2 |
| 70 | (20) | 68.0 | 70.7 |
| 69 | (21) | 61.0 | 64.1 |
| 66.9 | (11) | 68.9 | 66.9 |
| 65 | (11) | 65.4 | 63.0 |
| 65 | (21) | 55.4 | 60.2 |
| 62.8 | (11) | 62.7 | 61.3 |
| 62 | (21) | 55.4 | 57.4 |
| 56 | (21) | 47.8 | 51.0 |
| 52 | (20) | 61.0 | 57.9 |
| 50 | (20) | 54.5 | 53.9 |
| 49.6 | (17) | 46.8 | 44.6 |
| 45.4 | (17) | 35.4 | 41.6 |
| 45 | (19) | 45.8 | 44.6 |
| 41 | (23) | 45.8 | 41.6 |
| 40 | (20) | 35.4 | 34.3 |
| 39 | (21) | 29.8 | 31.8 |
| 34 | (20) | 46.8 | 39.2 |
| 30 | (20) | 36.5 | 34.3 |
| 23 | (20) | 37.5 | 28.7 |
| 20 | (20) | 28.7 | 25.5 |
| 11 | (20) | 10.1 | 21.7 |
| 10 | (20) | 14.1 | 14.5 |
| 8 | (21) | 15.4 | -4.9 |
| 1 | (20) | 4.6 | 10.4 |
| 0 | (16) | 3.1 | 0.8 |
| 0 | (24) | -6.0 | -4.2 |
| 0 | (17) | 0.2 | 0.1 |
| 0 | (14) | -9.3 | 0.8 |
| 0 | - | -25.9 | -13.7 |

In order to check if the results using the models were statistically the same as the ones provided by literature, a Student's t test of paired samples was carried for both models (Table 5.4), where the t values were calculated for a 95 % level of confidence. Since in the residuals plot there were differences between the data points of high and low forsterite content, the t test was also carried out for the $Fo_{0\text{-}50}$ and $Fo_{52\text{-}100}$ ranges separately. As observed, in all the cases the obtained t value was smaller than the t critical value for a 95 % level of confidence and, in addition, the ρ value was higher than 0.05. These facts mean that there are not statistical differences between the forsterite content provided by literature and the one calculated with both calibration models.

Table 5.4. t test of paired samples results for the $Fo_x$ from literature and the calculated ones using OB1 and OB2 calibration models

| | OB1 model | | | OB2 model | | |
|---|---|---|---|---|---|---|
| $Fo_x$ range (%) | 0-100 | 0-50 | 52-100 | 0-100 | 0-50 | 52-100 |
| Degrees of freedom | 63 | 19 | 43 | 63 | 19 | 43 |
| t value | 0.227 | 0.0551 | 0.464 | 0.0658 | 0.0529 | 0.0378 |
| t critical value (2 tails) | 2.00 | 2.09 | 2.02 | 2.00 | 2.09 | 2.02 |
| ρ value (2 tails) | 0.821 | 0.957 | 0.645 | 0.948 | 0.958 | 0.970 |

In addition, the t value calculated for the OB2 model in the $Fo_{52\text{-}100}$ range was smaller than the one for the OB1 model in the same range and the ρ value for the former model was higher than that one of the latter. These facts suggested that the OB2 model would work better for the fayalite rich olivines. However, the residuals plot of the OB2 model (Figure 5.4) suggested that this model would have more uncertainty in that forsterite concentration range. A good compromise solution for this problem would be to always use both models and to average their results, independently of the forsterite and fayalite concentrations of the mineral, which would provide good results for all the Fo-Fa concentrations range. For example, in the case of the commercial olivine, averaging the results of the OB1 and

OB2 models a concentration of $Fo_{90.1\pm1.9}Fa_{9.9\pm0.2}$ is obtained, where the confidence interval was calculated at a 95 % level of confidence using the overall standard deviation of both calibration curves and doing variance propagation. As observed, the concentration is still accurate. The only drawback of using this average method is that the uncertainty associated to the final result increases slightly due to the propagation of variances of the two overall standard deviations of the calibration curves. However, this uncertainty is still very low (±2.1 % for Fo and ±2.0 % for Fa) compared to the ones expressed in literature (around ±10 % as stated above), thus, the proposed method of averaging the results of the OB1 and OB2 models could be the recommended one.

## 5.3. Case Study: Olivine-Bearing Martian Analog

In order to test the capabilities of Raman spectroscopy to distinguish different olivine compositions, three different samples were studied, all of them being olivine-bearing rocks. The samples were collected in Reykjanes (Iceland), since the rocks of that region are considered optimal terrestrial analogs of Martian olivine-bearing rocks (26-28). The samples were prepared as coarse powder and analyzed by Raman spectroscopy. Due to their origin, they represent basaltic lavas from tissue-fed shield volcanos that were sourced from the Mid-Atlantic Ridge (29). The three rocks samples did contain a high amount of olivine phenocrysts or, in other words, olivine crystals that were formed early during the rock formation process and are usually larger than the other mineral grains. The samples were collected from areas where the rocks were not weathered or altered visually. More specifically, they were sampled from two different emplacements: two of them were collected at the geographic coordinates N63 49 01.7 W22 39 03.1 (IS16-0001 and IS16-0002) and the third one was collected at N63 48 58.3 W22 39 38.8 (IS16-0013).

Besides olivine, during the analysis of the samples the typical minerals present in this kind of samples were observed, such as different types of

pyroxenes (Raman bands observed around 325, 390, 665 and 1010 $cm^{-1}$) and feldspars (Raman bands observed around 285, 405, 482, 508 and 560 $cm^{-1}$). In addition to these main mineral phases, ilmenite, $FeTiO_2$ (its main Raman band was observed at 679 $cm^{-1}$), hematite, $Fe_2O_3$ (Raman bands observed at 225, 294, 409, 500, 609, 664 and 1318 $cm^{-1}$), and calcite ($CaCO_3$, its main Raman band was observed at 1086 $cm^{-1}$) were found very scarcely throughout the surface of the samples, which confirms that the rocks had a low degree of alteration and weathering.

Regarding the olivine, this mineral was found throughout all the surface of the three samples. In the case of the sample IS16-0001, several dozens of olivine spectra were found and their main olivine Raman signals varied from 816 and 848 $cm^{-1}$ to 823 and 855 $cm^{-1}$. Two of these olivine spectra can be observed in Figure 5.6, where it is clearly seen that there is a shift in the position of the two main Raman bands of the mineral. Using the method proposed above, the olivine metallic compositions were calculated using the OB1 and OB2 models and the results were averaged, calculating all the confidence intervals at a 95 % level of confidence using the overall standard deviation of both calibration curves and doing variance propagation. The IS16-0001 sample had olivine with a metallic concentration that ranged between $Fo_{38.7\pm0.8}Fa_{61.3\pm1.3}$ and $Fo_{90.1\pm1.9}Fa_{9.9\pm0.2}$.

As observed, the difference between the olivines found in this sample regarding their metallic content is very big. This fact is explained due the known differences between the core and the rim metallic composition of olivine grains, where the core is usually richer in magnesium than the rim of the mineral. This difference is created during the formation process of the rocks, within the cooling process of the magma, and it is caused by the difference of the melting point of forsterite (1890 ºC) and fayalite (1205 ºC) (30).

If the cooling process of the magma is slow, the forsterite solidifies first, while the fayalite remains in a magmatic state. While the temperature

keeps decreasing, the fayalite starts to solidify too, and it does it around the already solidified forsterite. As a result, when the rock is formed, the olivine grains end up with the highest amount of iron (fayalite) in their rims, while the forsterite usually concentrates in their cores. If the cooling process is fast and there is not enough time for this differentiation to happen, the final result is a more homogeneous olivine, where its core and rim have a similar metallic composition.

In the case of the sample IS16-0002 and IS16-0013, the olivine spectra collected always presented their two main Raman bands in the same positions, 822 and 854 $cm^{-1}$ and 818 and 847 $cm^{-1}$, respectively. Using the same method, the olivine metallic concentration calculated for IS16-0002 was $Fo_{83.6\pm1.8}Fa_{16.4\pm0.3}$ and for IS16-0013 it was $Fo_{46.7\pm1.0}Fa_{53.3\pm1.1}$. In the case of these two samples, the difference in metallic content between the rims and the cores of the olivine grains was not observed.

An explanation for this fact could be that, due to a faster cooling of the magma that formed these olivines, there was not enough time to create the differentiation explained above. However, it must be taken into account that IS16-0002 was sampled in the same location as IS16-0001, which means that they were formed from the same parent magma, but IS16-0001 presented the core versus rim differentiation. An explanation for this fact could be that the magma had different cooling rates in different areas and it had presence of cavities during its solidification processes. In these cavities, the magma could have had different cooling rates than the ones of the bulk.

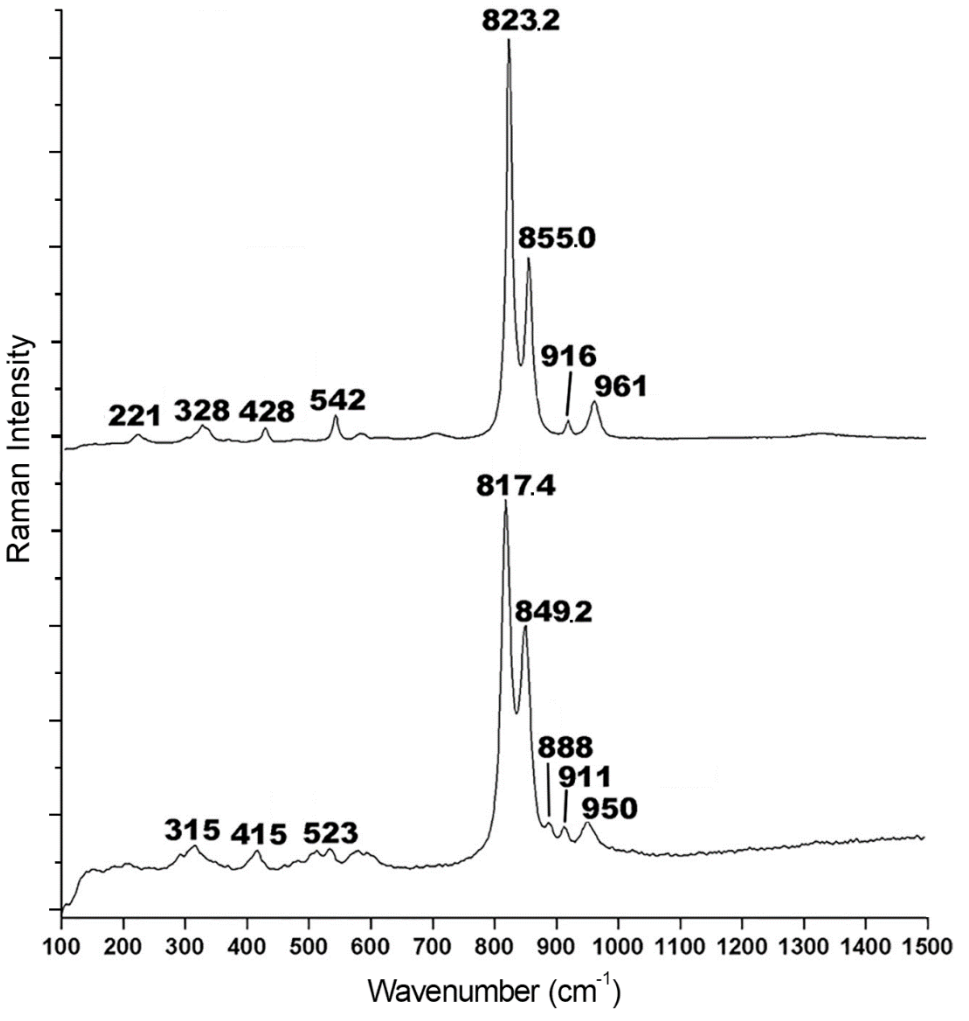


Figure 5.6. Two different olivines Raman spectra observed in the IS 16-0001 sample from Iceland. The spectra were obtained with the 532 nm excitation laser

## 5.4. Conclusions

In this chapter of the PhD thesis a new model was developed to calculate by Raman spectroscopy the magnesium and iron concentration of olivine, corresponding to the amount of forsterite and fayalite that forms it, respectively. Using the two main Raman bands of olivine and the difference between them, three different models were first tested. These models were developed using a set of 64 data from 14 different research papers, where different Raman instruments and acquisition parameters were used, which

eliminates any possible bias that the instrumentation could have introduced. The OB1 and OB2 values were used within a tenth of $cm^{-1}$ of the wavenumbers in order to increase the accuracy and precision of the models and their predicted results when applied to unknown samples.

The three developed models were validated with a standard commercial olivine, from which the mineralogical and metallic characterization was performed by XRD and WD-XRF. This ensured that any comparison with this standard to check the accuracy of the models was done properly. After studying the different quality parameters of the regression models, and comparing the results obtained for the standard olivine through them, it was determined that the most accurate models were the ones using OB1 and OB2 independently. However, it was observed that the model that used OB1 became more inaccurate than the one that used OB2 when analyzing iron rich olivines. In order to overcome this issue, it was stablished that the best way to study the metallic content of any olivine was to do it through both models and then average the results.

Despite these minor drawbacks, it was observed that the proposed models improve greatly the results obtained when compared to those of literature. In fact, using the averaging method, the uncertainty associated to the result is around ± 2-3 %, while the models found in literature have an uncertainty of ± 10 % or higher (12, 13).

The ability to differentiate among different types of olivines in real Martian analogs have also been tested during this PhD thesis. It was observed that for the IS16-0001 sample, Raman spectroscopy was able to differentiate a wide range of olivine compositions. In contrast, IS16-0002 and IS16-0013 did not show different olivine concentrations. These differences in the results, along with the fact that IS16-0001 and IS16-0002 were sampled in the same spot and IS16-0013 only 500 m away, implies that there could be rocks formed from the same parent magma that are heterogeneous between them. In this case, these differences observed by Raman

spectroscopy and the olivine calibration models helped to deduce other characteristics of the magma, such as the presence of cavities or the quickness of their cooling rate. On Mars a similar thing could happen, where two rocks might seem similar visually but have different formation processes. The finding of these differences could be the key to explain the evolution of the rocks of that area. Therefore, even if a rock looks similar to an already studied one, it should not be ignored and should be considered for studying too, since it could provide these differences needed to explain characteristics of their formation.

## 5.5. Bibliography

1. Papike, J. J., Chemistry of the rock-forming silicates: Ortho, ring, and single-chain structures, *Reviews of Geophysics,* **1987**, 25, 1483-1526.

2. Taylor, S. R., McLennan, S., Planetary Crusts: Their Composition, Origin and Evolution, **2008**, Cambridge University Press, Cambridge, UK.

3. Papike, J. J., Karner, J. M., Shearer, C. K., Burger, P. V., Silicate mineralogy of Martian meteorites, *Geochimica Et Cosmochimica Acta,* **2009**, 73, 7443-7485.

4. Ody, A., Poulet, F., Bibring, J. P., Loizeau, D., Carter, J., Gondet, B., Langevin, Y., Global investigation of olivine on Mars: Insights into crust and mantle compositions, *Journal of Geophysical Research. Planets,* **2013**, 118, 234-262.

5. Lane, M. D., Christensen, P. R., Determining olivine composition of basaltic dunes in Gale Crater, Mars, from orbit: Awaiting ground truth from Curiosity, *Geophysical Research Letters,* **2013**, 40, 3517-3521.

6. Ruiz-Galende, P., Torre-Fdez, I., Aramendia, J., Gómez-Nubla, L., Castro, K., Arana, G., Madariaga, J. M., Study of a terrestrial Martian analogue: Geochemical characterization of the Meñakoz outcrops (Biscay, Spain), *Journal of Raman Spectroscopy,* **2020**, 51, 1603-1612.

7. Brown, A. J., Viviano, C. E., Goudge, T. A., Olivine-Carbonate Mineralogy of the Jezero Crater Region, *Journal of Geophysical Research. Planets,* **2020**, 125, 1-30.

8. Wiens, R. C., Maurice, S., Rull, F., The SuperCam remote sensing instrument suite for the mars 2020 rover: A preview, *Spectroscopy,* **2017**, 32, 50-55.

9. Maurice, S., Wiens, R. C., Bernardi, P., Caïs, P., Robinson, S., Nelson, T., Gasnault, O., Reess, J. M., Deleuze, M., Rull, F., et al., The SuperCam Instrument Suite on the Mars 2020 Rover: Science Objectives and Mast-Unit Description, *Space Science Reviews,* **2021**, 217, 47.

10. Veneranda, M., Lopez-Reyes, G., Manrique, J. A., Medina, J., Ruiz-Galende, P., Torre-Fdez, I., Castro, K., Lantz, C., Poulet, F., Dypvik, H., et al., ExoMars Raman Laser Spectrometer: A Tool for the Potential Recognition of Wet-Target Craters on Mars, *Astrobiology,* **2020**, 20, 349-363.

11. Ishibashi, H., Arakawa, M., Yamamoto, J., Kagi, H., Precise determination of Mg/Fe ratios applicable to terrestrial olivine samples using Raman spectroscopy, *Journal of Raman Spectroscopy,* **2012**, 43, 331-337.

12. Kuebler, K. E., Jolliff, B. L., Wang, A., Haskin, L. A., Extracting olivine (Fo–Fa) compositions from Raman spectral peak positions, *Geochimica Et Cosmochimica Acta,* **2006**, 70, 6201-6222.

13. Mouri, T., Enami, M., Raman spectroscopic study of olivine-group minerals, *Journal of Mineralogical and Petrological Sciences,* **2008**, 103, 100-104.

14. Kolesov, B. A., Geiger, C. A., A Raman spectroscopic study of Fe–Mg olivines, *Physics and Chemistry of Minerals,* **2004**, 31, 142-154.

15. Servoin, J. L., Piriou, B., Infrared Reflectivity and Raman Scattering of $Mg_2SiO_4$ Single Crystal, *Physica Status Solidi (B),* **1973**, 55, 677-686.

16. Chopelas, A., Single crystal Raman spectra of forsterite, fayalite, and monticellite, *The American Mineralogist,* **1991**, 76, 1101-1109.

17. Kolesov, B. A., Tanskaya, J. V., Raman spectra and cation distribution in the lattice of olivines, *Materials Research Bulletin,* **1996**, 31, 1035-1044.

18. Yasuzuka, T., Ishibashi, H., Arakawa, M., Yamamoto, J., Kagi, H., Simultaneous determination of Mg# and residual pressure in olivine using micro-Raman spectroscopy, *Journal of Mineralogical and Petrological Sciences,* **2009**, 104, 395-400.

19. Lafuente, B., Downs, R. T., Yang, H., Stone, N., Highlights in Mineralogical Crystallography; The power of databases: The RRUFF project (p.p. 1-30) **2015,** de Gruyter, Berlin, München, Boston.

20. Breitenfeld, L. B., Dyar, M. D., Carey, C. J., Tague, T. J., Wang, P., Mullen, T., Parente, M., Predicting olivine composition using Raman spectroscopy through band shift and multivariate analyses, *The American Mineralogist,* **2018**, 103, 1827-1836.

21. Kuebler, K. E., Jolliff, B. L., Wang, A., Haskin, L. A., Extracting olivine (Fo–Fa) compositions from Raman spectral peak positions, *Geochimica Et Cosmochimica Acta,* **2006**, 70, 6201-6222.

22. Besson, J. M., Pinceaux, J. P., Anastopoulos, C., Velde, B., Raman spectra of olivine up to 65 kilobars, *Journal of Geophysical Research: Solid Earth,* **1982**, 87, 10773-10775.

23. Guyot, F., Boyer, H., Madon, M., Velde, B., Poirier, J. P., Comparison of the Raman microprobe spectra of $(Mg,Fe)_2SiO_4$ and $Mg_2GeO_4$ with olivine and spinel structures, *Physics and Chemistry of Minerals,* **1986**, 13, 91-95.

24. Liu, L., Mernagh, T. P., Raman spectra of forsterite and fayalite at high pressures and room temperature, *High Pressure Research,* **1993**, 11, 241-256.

25. Iishi, K., Lattice dynamics of forsterite, *The American Mineralogist,* **1978**, 63, 1198-1208.

26. Ehlmann, B. L., Bish, D. L., Ruff, S. W., Mustard, J. F., Mineralogy and chemistry of altered Icelandic basalts: Application to clay mineral detection and understanding aqueous environments on Mars, *Journal of Geophysical Research: Planets,* **2012**, 117, 1-27.

27. Black, S. R., Hynek, B. M., Mchenry, L. J., Mccollom, T., Cameron, B., Ludyan, J., Alteration Mineralogy and the Effect of Parent Lithology at Hydrothermal Mars Analog Sites: Initial Results from Hengill and Krafla Volcanoes, Iceland, *48th Lunar and Planetary Science Conference,* **March 20, 2017,** The Woodlands, Texas, USA.

28. Catalano, J. G., Thermodynamic and mass balance constraints on iron-bearing phyllosilicate formation and alteration pathways on early Mars, *Journal of Geophysical Research. Planets,* **2013**, 118, 2124-2136.

29. Jakobsson, S. P., Jónsson, J., Shido, F., Petrology of the Western Reykjanes Peninsula, Iceland, *Journal of Petrology,* **1978**, 19, 669-705.

30. King, R. J., Olivine Group, *Geology Today,* **2009**, 25, 193-197.

# Chapter 6

# Mineral Alterations Caused by High-Pressure Events

*"Geologist have a saying – rocks remember"*

Neil Armstrong

When studying a material that might have been subjected to high-pressures, as might be the case of the minerals present in meteorites, some alterations and transformations can be expected. These alterations can be permanent and can cause mineral phase transitions if the pressure at which the mineral is subjected to is high enough. This means that minerals transform into other ones due to a change in the structure of its crystal lattice caused by pressure. However, these transformations do not affect only meteorites. For example, they occur naturally when rocks move between the different layers of the Earth's mantle and crust (1).

In addition, pressure does not alter the internal structure of a mineral only when it is being applied. Even if the pressure is not high enough to produce a mineral phase transformation, the alterations that the crystal lattice suffers can remain after the applied pressure is gone. These remaining alterations can derive in small quantities of pressure, compared to the initial shock. This pressure, generated internally by the mineral due to the consequences of a past shock event, is called residual pressure or residual stress (2).

Whatever the origin is, these changes in the mineral phases can be studied by Raman spectroscopy, which can also determine the pressure at which these mineral alterations occur. For instance, anatase suffers an irreversible phase transition between 4.3 and 4.6 GPa of pressure (3). This mineral phase change does not alter the hardness nor the transparency of the original mineral, but its standard 197 $cm^{-1}$ Raman band shifts to lower frequencies (3). This fact means that by optical examination it would be hard to detect that an anatase suffered changes in its structure caused by high-pressure, but it is possible to detect it by Raman spectroscopy. Something similar occurs with other minerals, such as wurtzite, where changes in its mineral phase caused by high-pressure can be detected in the features of its Raman spectrum (4). These facts make Raman spectroscopy a valuable technique for the study of the pressure suffered by a mineral in the space exploration field, since high-pressure events are common.

Regarding the study of Mars, the analysis of past high-pressure events and their effects should always be taken into account, since the two main ways to study Mars are directly affected by this type of events.

On the one hand, when Mars is studied through the meteorites that hit the Earth, it is important to take into account that this type of samples have been subjected to a high-pressure event at least two times before they are collected. These rocks, original from the Red Planet, hit the Earth after a

fortuitous series of events, described in more detail in Chapter 1, *Introduction*. Two of those events are directly related with high-pressure: their ejection from Mars, usually caused by the impact of a celestial body, and their arrival to Earth, which ends with an impact against the surface of our planet (5).

This type of events usually produces different grades of shock metamorphism in the rocks, which go from mineral microstructure alterations, such as planar fractures, to complete transformations of the original mineral into a high-pressure polymorph (6). The shock metamorphism in meteorites is measured with a scale from 1 to 6 (S1–S6) to describe the meteorite as a whole, where S1 means that the rock is completely unshocked (impact of less than 5 GPa) and S6 means that it is heavily shocked (impact of 75–90 GPa) (7). It must be taken into account that these alterations and their degree can vary within a meteorite on a scale of centimeters, and can be very abundant (7, 8). When studying this type of samples, it is important to assess if they were altered by shock metamorphism and to what extent, so that altered minerals are not misinterpreted as original from Mars.

On the other hand, a similar fact occurs when the surface of Mars is directly studied. As was explained in Chapter 1, *Introduction*, due to the lack of a complex and thick atmosphere as we have on Earth, Mars has suffered more impacts from other celestial bodies on its surface throughout its history. The *Mars Orbiter Camera* (*MOC*) from the *Mars Global Surveyor* (*MGS*) NASA mission has determined that nowadays Mars still suffers from impacts of other celestial bodies. In fact, it received at least 20 impacts that created craters between 2 and 150 meters of diameter in an area of $21.5 \cdot 10^6$ $km^2$ between May 1999 and March 2006 (9). However, the rate at which Mars receives impacts has also changed through time.

This fact means that rocks on Mars could be altered and transformed by high-pressure events (depending on the magnitude of the impacts), which

must be taken into account when studying the surface of the planet (10). A clear example of this issue is the finding of silica in the surface of the planet, which can lead to different conclusions depending on the polymorph that is found. If coesite is observed on Mars, it would mean that it was probably formed from quartz due to a high-pressure event caused by an impact, since it is a high-pressure polymorph of silica (11, 12). However, when the rover *Curiosity* observed tridymite in Gale crater, it was deduced that the presence of this mineral on the surface implied possible past hydrothermal activity in the area, since tridymite is a low pressure and high temperature polymorph of silica (13, 14).

As we can see, high-pressure and shock events can determine the conclusions obtained from the analyses. This fact is even more relevant nowadays, since the *Perseverance* rover is in Jezero crater, which was formed by the impact of an external celestial body. Due to these reasons, it is important to have techniques capable of studying and discerning mineral phases that might had suffered high-pressure impacts in the past.

In this sense, as has been explained in Chapter 5, *Forsterite and Fayalite Content in Olivines*, Raman spectroscopy can be used not only to characterize the mineralogy of a sample, but also to study other parameters related to the samples, such as high-pressure events or the transformations caused by them. When a compound is subjected to high-pressure, their intramolecular bonds tend to destabilize and suffer alterations, since the compression caused by the pressure increases the kinetic energy of the electrons of the bond (15).

In some cases, these alterations are permanent and remain once the pressure is gone (after the impact), and in others they leave residual stress in the crystal lattice of the minerals (2), which can also be studied by Raman spectroscopy. As has already been explained throughout this PhD thesis, Raman spectroscopy is directly related to the vibrations of the bonds of molecules and, thus, these bond changes caused by pressure can be

observed in the Raman spectra. In fact, nowadays it is considered one of the best spectroscopic techniques to assess possible alterations in a mineral caused by pressure (16). For that reason, the capability of this technique to determine high-pressure events in mineral samples has been assessed in this PhD thesis.

## 6.1. Effects of High-Pressure in Calcites

Calcite, $CaCO_3$, is a carbonate mineral commonly found on Earth in sedimentary rocks such as limestone. It is the most stable polymorph of calcium carbonate, being aragonite the second most usual polymorph of this mineral and the vaterite the most unstable one. Calcite is easily dissolved by acidic dissolutions, including water that is slightly acid caused by the atmospheric $CO_2$ (17). This fact means that water can dissolve and transport calcite. Once the water evaporates, it leads to the calcite crystallization in a different location. This is the reason why calcite is usually found in places that water uses to flow, such as in rock veins, where the mineral is formed after the evaporation of the water that was passing through a crack of a rock. This same formation mechanism is the one by which stalactites and stalagmites are formed in caves.

The same mechanism occurs in meteorites once they arrive Earth. Until they are collected, water with dissolved calcium and bicarbonate ions passes through them and evaporate inside the meteorite cracks and cavities, causing the calcite to crystallize.

As a matter of fact, calcite is a common mineral present in Martian meteorites, having caused discussions in literature on whether calcites present in specific meteorites are original from Mars or not (18-21). In this sense, Raman spectroscopy and its capability to observe alterations caused by high-pressure in minerals can be a possible solution to assess if a calcite is original from the Red Planet or not, since, if a past high-pressure event is deducted from a calcite grain found in the core of a

meteorite, it would mean that the calcite was probably already there when the meteorite suffered the impact in Mars.

When talking about pressure and calcite, literature states that this mineral has several polymorphs. The most stable one, observed at atmospheric pressure, is calcite I. The pressure generated by an impact of a celestial body against the surface of a planet can be enough to transform calcite I into two other polymorphs, calcite II and calcite III. They are both a displacive modification of the crustal lattice of calcite I, which involves the softening of a phonon mode as a prelude to a symmetry breaking displacement of the lattice (22, 23). Calcite II starts forming when the pressure reaches a value of around 0.5 GPa, completing the transformation from calcite I to calcite II at around 1.5 GPa (24). In the case of calcite III, this polymorph is formed from calcite II at around 2 GPa and can go up to 90 GPa without further transformations (24).

Due to the alterations that they suffer in their crystal lattice, in other words, the chemical bonds of the mineral, they have different Raman spectra (Figure 6.1) (25). As observed, the main Raman feature of this mineral always appear in the same spectral range for the three polymorphs (1085–1099 $cm^{-1}$), which corresponds to the symmetric stretching of the $CO_3$ group. Calcite I and calcite II have this feature as a single Raman band at 1085 and 1090 $cm^{-1}$, respectively, while calcite III has it as a doublet at 1097 and 1099 $cm^{-1}$. The features around 715 $cm^{-1}$ are assigned to the symmetric deformation of the $CO_3$. In this case, the three polymorphs can be differentiated by this band, since calcite I has a single feature in that area (713 $cm^{-1}$), while calcite II has a doublet (715 and 721 $cm^{-1}$) and calcite III has a doublet (736 and 741 $cm^{-1}$) and a single band (695 $cm^{-1}$). Finally, the lower wavenumbers of the spectra present the highest variability regarding the number of signals. They are related to the external vibration of the $CO_3$ group that involves translatory of the group between the cation and the anion of the mineral.

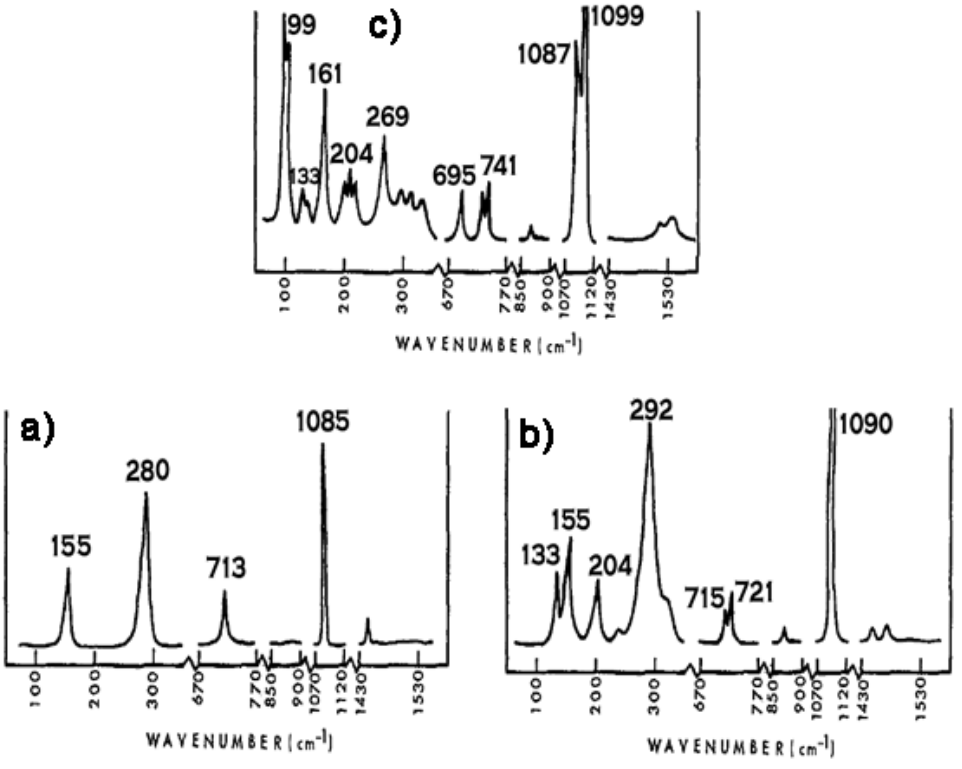


Figure 6.1. Raman spectrum of the calcium carbonate polymorphs a) calcite I, b) calcite II and c) calcite III. Extracted and modified from (25)

In order to check and verify the capability of Raman spectroscopy to detect past high-pressure events suffered by calcite, several samples of this mineral with different formation conditions were collected. Some small calcite stalactites were sampled from the Pozalagua cave (Carranza, Biscay, Spain), as representative calcite formed at room temperature and atmospheric pressure. As was expected, these samples presented the features corresponding to calcite I in their Raman spectrum (Figure 6.2). This fact means that they did not present any residual stress (see below) in their crystal lattice, which is consistent with their formation process, since they are formed by the recrystallization of calcium carbonate dissolved in water. Calcium and bicarbonate ions were filtered into the Pozalagua caves dissolved in water coming from the ground above. Once this water reached the cave, the calcite crystalized and formed, with the years, as a stalactite.

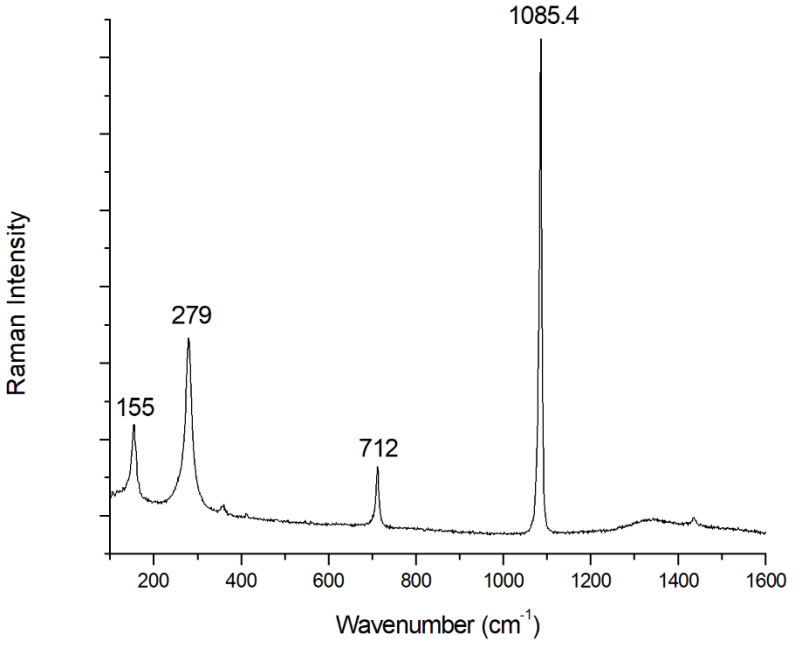


Figure 6.2. Calcite I polymorph Raman spectrum obtained from one stalactite formed in the Pozalagua cave (Carranza, Biscay, Spain). The spectrum was collected with the 532 nm excitation laser

In addition to the sets of stalactite samples, Macael White (Macael, Almeria, Spain) and Marquina Black (Marquina, Biscay, Spain) marbles were analyzed. In the case of Macael White, all of the spectra obtained from the calcite of these marbles corresponded to the calcite I polymorph. However, calcite II polymorph was observed in some of the measurements in the Marquina Black samples (Figure 6.3). The splitting of the 156 $cm^{-1}$ Raman band into a doublet with the new signal at 128 $cm^{-1}$, the new low intensity broad band at 204 $cm^{-1}$ and the shift to higher wavenumbers of the main Raman band (1088.2 $cm^{-1}$), are the spectral changes observed compared to a calcite I spectrum, indicating the presence of calcite II. Regarding the formation of these samples, marbles are formed from limestone when it is subjected to high-pressures and temperatures. Once these conditions are met, the calcite of the limestone recrystallizes and forms a denser rock. These pressures might remain in some areas as

residual stress inside the marble, which is what was observed in the Marquina Black measurements (Figure 6.3).

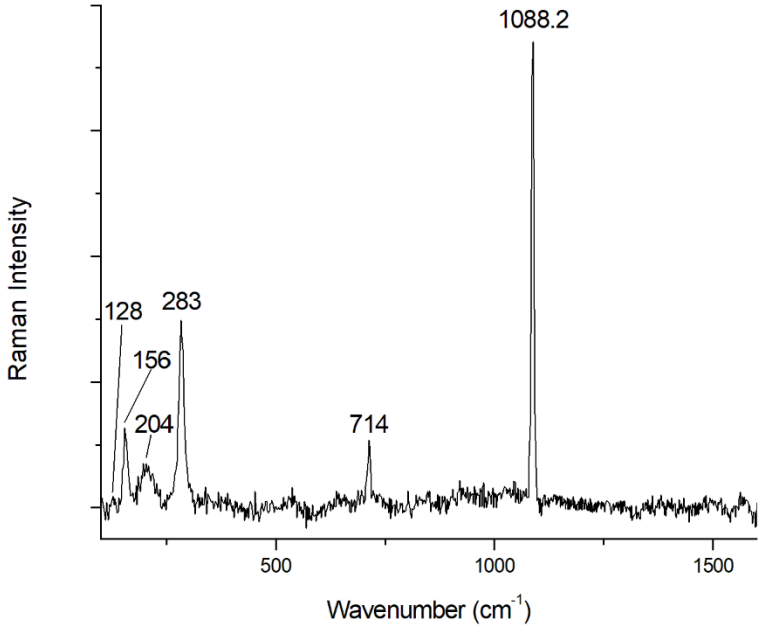


Figure 6.3. Calcite II polymorph Raman spectrum obtained from a Marquina Black marble sample (Marquina, Biscay, Spain). The spectrum was collected with the 532 nm excitation laser

Unfortunately, even though the formation process of marble from limestone generates enough pressure to obtain the calcite III polymorph (26), it was not identified in the analyzed marble samples. This fact means that even if calcite III was formed during that period, the marble did not retain enough residual stress to preserve the calcite as that polymorph. Due to this reason, it was not possible to test the Raman capabilities to detect calcite III.

Based on previous literature works and the calcite I and calcite II experimental results (Figure 6.2 and 6.3), it was observed that the main Raman signal of the three calcite polymorphs shifts to higher wavenumbers when the respective polymorph needs a higher pressure to be formed. In

order to check if that trend also occurred within each polymorph, data from different research papers on calcite I, calcite II and calcite III studied by Raman spectroscopy at different pressures were collected from literature (24, 25, 27-29). A summary of the collected data is presented in Table 6.1. When the pressure subjected to the calcite is plotted against the wavenumber position of its main Raman band, the data for each individual polymorph of calcite fit into a linear regression model (Figure 6.4), whose equations are presented in Equations 6.1, 6.2 and 6.3 for calcite I, calcite II and calcite III, respectively. C1B, C2B and C3B represent their main calcite Raman band position, respectively.

As observed in the residuals plot for each calibration model (Figure 6.5), all the residuals are scattered in a random way, as they do not follow a visible trend. In addition, all the data are equally distributed around the zero horizontal line and all of them in the same range of distance from it for each calibration model. All of these facts imply that the proposed models for the three data sets are the correct ones and that the model's predictions should be accurate on average, rather than systematically too high or too low. However, it must be pointed out that some points of the residuals of the model for calcite III are slightly further apart from the zero than the rest, which would imply a higher uncertainty for the results obtained with this model.

Regarding other quality parameters of the three calibration models, the determination coefficients ($r^2$) obtained for the calcite I, calcite II and calcite III linear regressions are 0.930, 0.934 and 0.916 and the overall standard deviations of the models are ±0.87, ±0.71 and ±1.52 $cm^{-1}$, respectively. As observed, the $r^2$ obtained for the three regression lines are not high enough for a good analytical quantification model, which means that the inaccuracy associated with the results obtained from them is going to be high. Due to these facts, the model should not be used as a quantitative model, but as an estimative model of the pressure that a calcite is being subjected to, or the one that remains as residual stress after a high-pressure event.

Table 6.1. Wavenumber position of the main Raman signal of different calcite I, calcite II and calcite III samples at different pressures. Data extracted from (24, 25, 27-29)

| Calcite I | | Calcite II | |
|---|---|---|---|
| Applied pressure (GPa) | Wavenumber ($cm^{-1}$) | Applied pressure (GPa) | Wavenumber ($cm^{-1}$) |
| 0.0001 | 1084.6 | 0.6 | 1090.0 |
| 0.0001 | 1085.0 | 1.05 | 1093.2 |
| 0.125 | 1085.5 | 1.05 | 1093.8 |
| 0.25 | 1086.5 | 1.35 | 1095.7 |
| 0.725 | 1090.0 | 1.525 | 1095.8 |
| 0.85 | 1090.0 | 1.6 | 1096.7 |
| 0.9 | 1090.5 | 1.75 | 1096.8 |
| 1.01 | 1091.6 | 1.875 | 1096.8 |
| 1.55 | 1091.6 | 1.825 | 1098.4 |
| 1.25 | 1092.5 | 2.125 | 1098.5 |
| 1.45 | 1092.5 | - | - |
| Calcite III | | | |
| Applied pressure (GPa) | Wavenumber ($cm^{-1}$) | Applied pressure (GPa) | Wavenumber ($cm^{-1}$) |
| 2.1 | 1101.8 | 4.17 | 1110.1 |
| 2.9 | 1103.3 | 4.5 | 1110.3 |
| 3.1 | 1104.4 | 4.77 | 1110.2 |
| 2.21 | 1105.2 | 5.2 | 1110 |
| 3.02 | 1105.2 | 5.23 | 1110.3 |
| 3.28 | 1105.3 | 5.24 | 1112.8 |
| 3.57 | 1105.4 | 6.95 | 1112.9 |
| 3.7 | 1105.3 | 5.24 | 1113.8 |
| 3.5 | 1107.8 | 5.94 | 1113.9 |
| 3.94 | 1107.8 | 5.95 | 1113.9 |
| 4.95 | 1108.7 | 7.4 | 1119.0 |
| 4.93 | 1109.5 | 9.18 | 1124.0 |

$$C1B\ (cm^{-1}) = 5.24 \cdot P(GPa) + 1085.3 \qquad \textit{Equation 6.1}$$

$$C2B\ (cm^{-1}) = 5.41 \cdot P(GPa) + 1087.6 \qquad \textit{Equation 6.2}$$

$$C3B\ (cm^{-1}) = 2.92 \cdot P(GPa) + 1096.1 \qquad \textit{Equation 6.3}$$

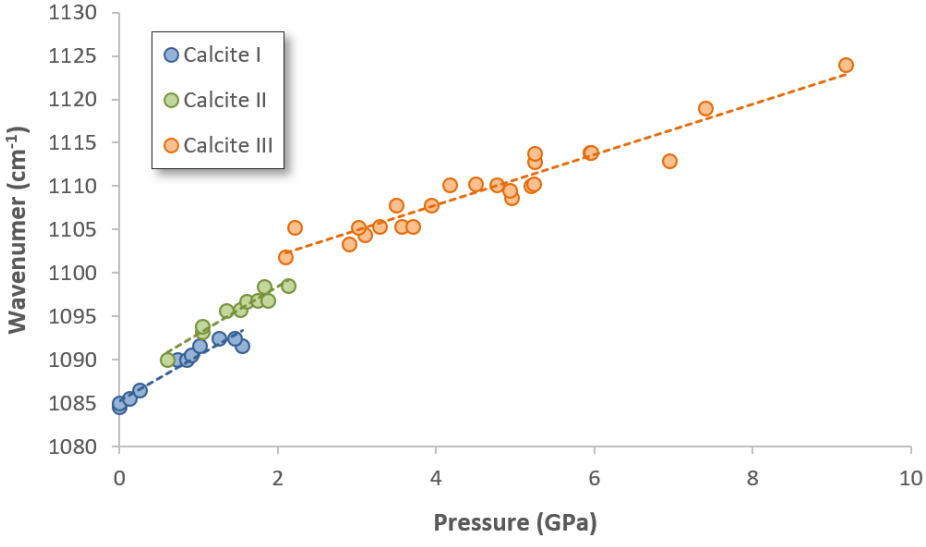


Figure 6.4. Regression lines of the wavenumber position of the main Raman signal of calcite I, calcite II and calcite III against the pressure applied to them

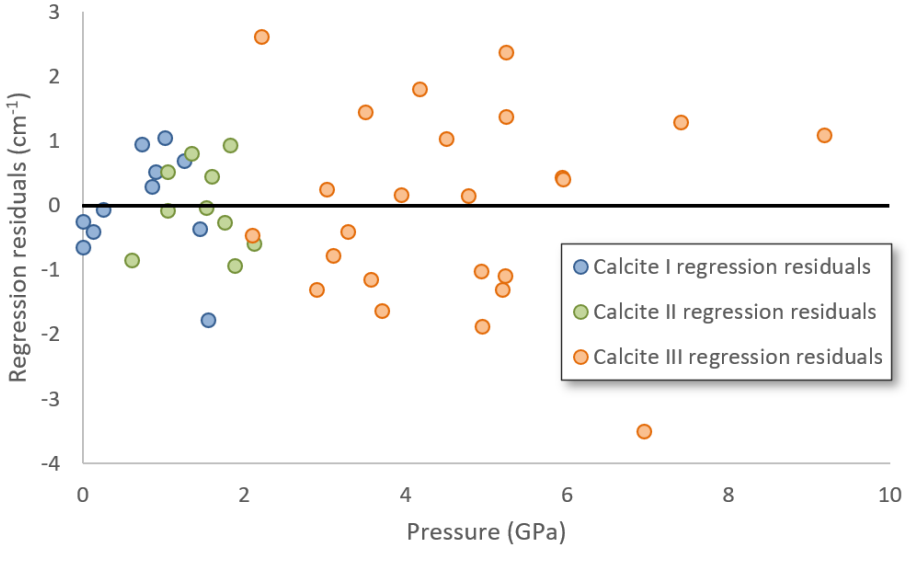


Figure 6.5. Residuals plot of the three regression models for calcite I, calcite II and calcite III

As is observed in Figure 6.4, the calibration lines for calcite I and calcite II overlap in the pressure range when one polymorph is transforming into the other (0.5–1.5 GPa). For Raman spectra where the calcite I features are observed, the calcite I model is the one that should be used. Otherwise, if the features of the Raman spectra correspond to calcite II (splitting of the signal at 155 $cm^{-1}$ into a doublet at 133 and 155 $cm^{-1}$, appearance of a new low intensity and broad band at 204 $cm^{-1}$, splitting of the signal at 713 $cm^{-1}$ into a doublet at 715 and 721 $cm^{-1}$ and shift of the main band to a higher wavenumber), then the calcite II model has to be used. In other words, first, a classification of the studied calcite has to be carried out and, once it is known which polymorph is being studied, then the model for that polymorph should be used.

The study of different calcites by Raman spectroscopy regarding high-pressure events was also tested with two Martian meteorites, the Dar al Gani (DaG) 735 shergottite and the Northwest Africa (NWA) 6148 nakhlite. A full geochemical characterization of these meteorites can be found in Chapter 9, *Methodology Development and Testing for the Mars Returning Samples*. As it is explained in that chapter, calcite was found throughout the surface of the samples as it is usual in meteorites. Its presence is usually related to terrestrial weathering processes that take place in desert areas (30, 31), when the calcite crystallizes as calcite I by the evaporation of water rich in carbonates and bicarbonates.

Regarding the DaG 735, the presence of mineral phases altered by pressure inside the meteorite were already reported (32). According to literature, these alterations were caused by the initial impact that originated the ejection of the rock fragments from Mars to the outer space. This is the case of perovskite, (Mg, Fe)$SiO_3$, and magnesiumwüstite, (Mg, Fe)O, identified as a shock induced dissociation of olivine, $(Mg, Fe)_2SiO_4$ (32). This transformation was observed in the olivine adjacent to or entrained in the shock melt vein and melt pockets of the DaG 735 Martian meteorite.

This dissociation of olivine implies that the pressure and temperature conditions were approximately 25 GPa and 700 °C at least (32).

When the sample was analyzed by Raman spectroscopy, some calcite spectra corresponding to shocked calcite I were detected, with signals at 1088, 714, 283 and 157 $cm^{-1}$ (Figure 6.6). As observed, the main band of the mineral is shifted to higher wavenumbers, which is indicative of residual stress. ED-XRF analyses were carried out in order to discard the presence of dolomite or magnesium substitution in the calcite, which typically occurs in nature, since that substitution also shifts the wavenumber of the main signal. The elemental results (described in Chapter 9, *Methodology Development and Testing for the Mars Returning Samples*) revealed only the presence of calcium in those spots. Since ED-XRF did not detect magnesium, it was confirmed the presence of pure calcite I affected by residual pressure.

This fact suggested that the calcite might be original from Mars and that it suffered the same pressure events described in literature for perovskite and magnesiumwüstite (32). Using the proposed calibration model for calcite I it was obtained that the calcite present in the DaG 735 meteorite had a residual stress of 0.5 ± 0.2 GPa in that area, where the confidence interval was calculated at a 95 % level of confidence using the overall standard deviation of the regression line. It must be pointed out that this value is the residual stress that remains in the calcite, not the pressure that the meteorite was subjected to, which was much higher.

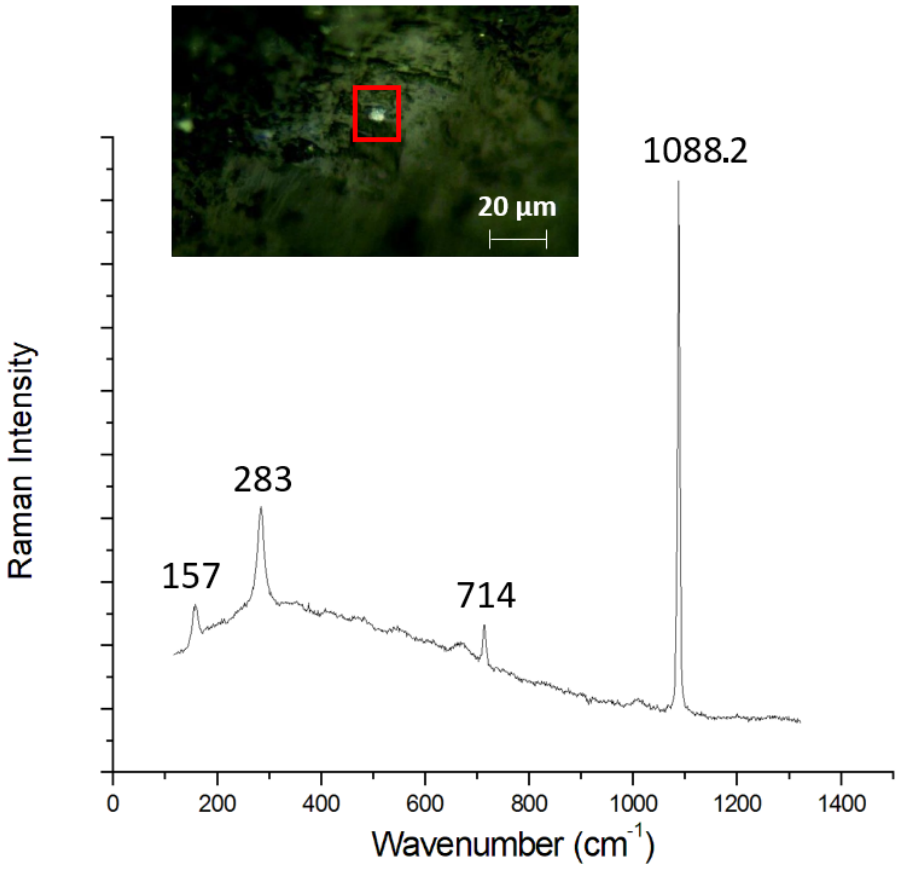


Figure 6.6. Calcite I spectrum observed in the DaG 735 Martian meteorite. A microscope image can be observed of the analyzed calcite crystal. The spectrum was collected with the 532 nm excitation laser

Regarding the NWA 6148, a calcite whose Raman spectrum corresponded to that of calcite II was identified in the inner part of the meteorite (Figure 6.7). As observed, the main Raman band is shifted to higher wavenumbers (1088.1 $cm^{-1}$) than the one of calcite I. Besides, a new low intensity broad feature is observed at 203 $cm^{-1}$, and the 155 $cm^{-1}$ signal is split into a doublet, having the new signal at 136 $cm^{-1}$. Regarding the doublet that should be present at 715 and 721 $cm^{-1}$, two small peaks can be observed at those wavenumbers. However, the signals do not have enough intensity to clearly stand out against the spectral noise, thus, it was decided not to include them as features. Using the calibration model developed above, it was obtained that the pressure of the calcite was of 0.1 ± 0.1 GPa, where

the confidence interval was calculated at a 95 % level of confidence using the overall standard deviation of the regression line. As explained above, the results of the calibration model have a high uncertainty, however, they are useful to estimate what is the pressure that the calcite was subjected to. It must be pointed out that the calculated pressure is not the initial pressure suffered by the mineral, but the current pressure that it is suffering at the moment of the analysis, in other words, the residual pressure. However, calcite II starts forming from calcite I at around 0.5 GPa (24), and in this case the observed calcite II had a residual stress of around 0.1 GPa. This fact could mean that, even though its phase transformation occurs at higher pressures, the polymorph might maintain its structure at lower ones, or at least its reversion is slow enough to be able to identify calcite II with that residual stress.

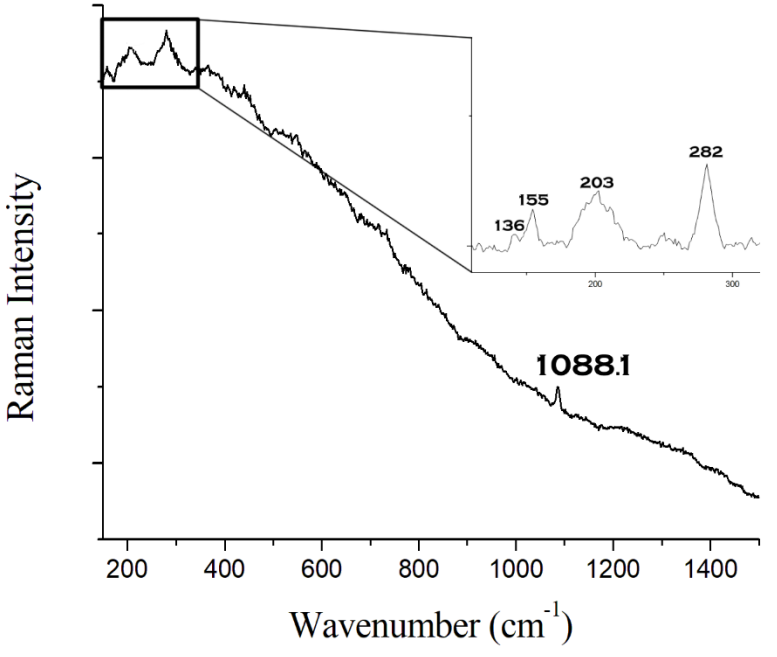


Figure 6.7. Calcite II spectrum observed in the inner part of the NWA 6148 Martian meteorite. The zoom in corresponds to the 100-300 $cm^{-1}$ spectra range, where a base line and spectral smoothing were carried out. The spectrum was collected with the 785 nm excitation laser

The finding of a Raman spectrum of calcite II in the NWA 6148 Martian meteorite meant that the calcite was not formed inside the sample by evaporation of water and crystallization of calcium carbonate in the Earth, since in that case all the spectra of calcite would have corresponded to calcite I. This means that the calcite was already formed when the meteorite entered and impacted the surface of our planet. Regarding the question of whether this calcite was original from the meteorite or it was incorporated to it in the impact, the most probable explanation is that it was original from the meteorite, because it was found in the inner part of the sample, not in the crust. This fact means that the calcite found in the NWA 6148 was probably original from Mars.

If the calcite found in the NWA 6148 meteorite is indeed original from Mars, it would be a new clue to elucidate the geographical origin of nakhlites. Currently, due to the comparison between the crystallization ages of nakhlites and the crater count chronology of different regions of Mars, it is suggested in literature that this group of meteorites formed on a large volcanic area in the region of Tharsis, Elysium or Syrtis Major Planum (33). If the calcite found in the NWA 6148 is original from Mars, it would mean that the area from where nakhlites were ejected had to have calcite in its surface. In Figure 6.8 the different emplacements where carbonates have been found on Mars can be observed. The carbonate minerals that have been found on Mars are those of iron, magnesium and calcium and the different combinations between those elements (34). These findings have been carried out both in situ, such as the finding of calcium carbonate in the Martian polar soil by the *Phoenix* lander (35) or the detection of iron rich carbonates in Gale crater by the *Curiosity* rover (36), and by remote observations from orbiters, such as the finding of various types of carbonates in Jezero crater by the *Mars Reconnaissance Orbiter* (*MRO*) (37). In total, carbonates have been found on Mars in 19 different emplacements, mainly inside impact craters (Figure 6.8) (35-42).

As can be observed, carbonates on Mars have been identified mainly inside and around Syrtis Major Planum. Regarding calcite in the Syrtis Major Planum area, this mineral has been identified within the central uplift peak of Leighton crater (white dot in Figure 6.8) (39) and in different craters in the region of Tyrrhena Terra (green dots in Figure 6.8) (40). Calcite was also detected in the Tharsis area, more specifically, in the Noachian Eridania region (yellow dot in Figure 6.8) (41). Finally, this mineral was identified in the Martian polar area too (red dot in Figure 6.8) (35), although this area is not of interest for the assessment of the possible formation area of nakhlites. Even though carbonates have been detected around the region of Elysium Planitia in two different emplacements, they were all magnesium and iron rich carbonates, which do not match with the presence of calcite in the NWA 6148 meteorite.

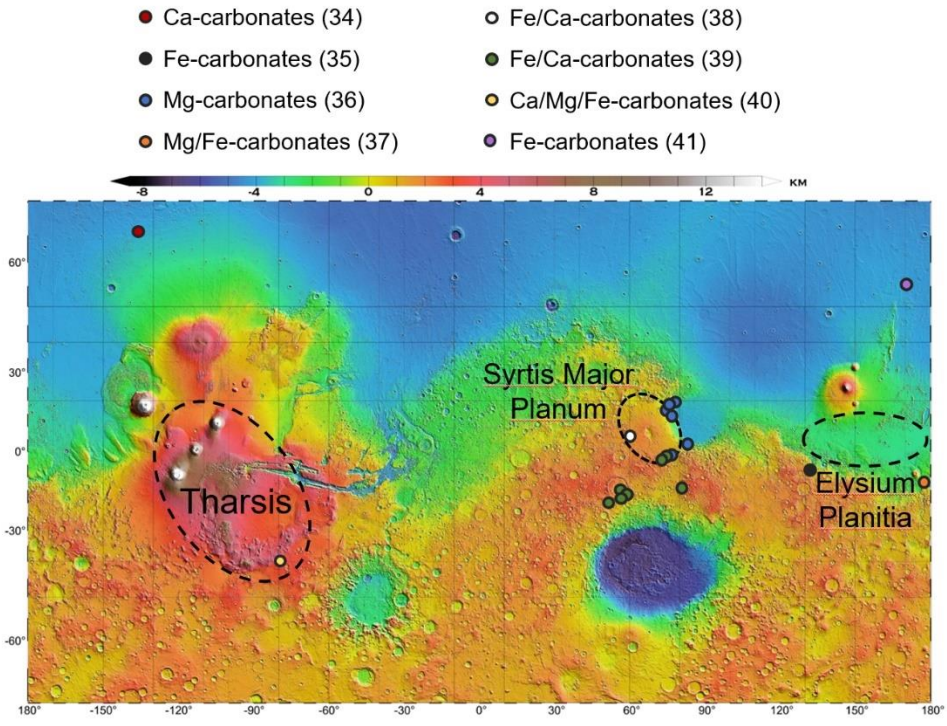


Figure 6.8. MOLA map (43) of the emplacements on Mars where carbonates have been identified either in situ with rovers and landers or with remote observation techniques with orbiters. The regions of Tharsis, Syrtis Major Planum and Elysium Planitia are highlighted

Overall, the Syrtis Major Planum region and its surroundings are the areas where most carbonates have been detected on Mars by far. In addition, calcite has been identified in two different zones in this area. Since calcite has also been detected in the region of Tharsis and iron and magnesium carbonates have been observed in Elysium Planitia, these two regions cannot be ruled out as possible formation areas of nakhlites. However, based on the data presented, the most probable area for the formation of nakhlites is Syrtis Major Planum.

## 6.2. Effects of High-Pressure in Silica and Feldspar

Similar to what occurs with calcite, high-pressure events also transform other mineral phases that can then be detected by Raman spectroscopy. As was explained above, the capability to detect past high-pressure events can be of great relevance when studying Mars.

Taking this into account, it was decided to study a Martian analog that would have undergone the same conditions as the craters that nowadays are being studied on Mars in situ, that is, Jezero (*Perseverance* rover) and Gale (*Curiosity* rover) craters. These craters were formed by a high-pressure impact of a celestial body and, afterwards, water filled the craters (44, 45).

On Earth, one of the best preserved wet-target craters is the Chesapeake Bay Crater (Virginia, USA). After it was discovered in the early 90s and dated back to 35.3 million of years ago, it was determined that the crater was formed due to the impact of an external celestial body (46). In order to study if that impact had led to mineral transformations caused by pressure, a sample from the ICDP-USGS Eyreville core, drilled between 2005 and 2006 to a total depth of 1766.3 m (47), was analyzed. More specifically, the WH16-014 sample was selected from the upper melt-rich section of the suevitic and lithic impact breccias ($5^{th}$ SU), which represents the stratigraphic unit conserving the clearest impact-related mineralogical

alterations. This unit is composed of autochthonous materials that were strongly altered during the impact event. The analyzed geological sample was obtained from a depth of 1407.2 m and weighted 21.4 g. The sample belongs to a sub unit located just below the upper suevite, which is characterized by a melt matrix containing a large number of mineral grains and lithic clasts. In order to have access to all the minerals contained in the sample, it was prepared as fine powder with a grain size lower than 150 µm by crushing the rock (previously grinded with an agate mortar) in an agate mill (McCrone Micronizer Mill) for 12 minutes.

Besides the minerals already described in literature (47), quartz altered by pressure was detected within the sample. This fact was observed due to the displacement of the main Raman signal of quartz (usually at 464 $cm^{-1}$). In the case of the analyzed sample, the main feature of quartz appeared in lower wavenumbers, shifting between 461.4-463.5 $cm^{-1}$. This phenomenon has been detected in other craters and is widely accepted as an alteration due to the pressure reached during impact event, which causes a shock-metamorphism of $SiO_2$ (48). In the Raman spectrum of quartz, its main band is assigned to the vibration of the oxygen atoms that are connected to two silica tetrahedra and its shift towards lower wavenumbers is related to the increase of the angle spanning those two tetrahedra (49). In addition, the high-pressure events produce alterations in the bond lengths and bond angles of the crystal structure of quartz, which lead to an increase of the main Raman band width, usually measured as its full width at half maximum (FWHM).

Taking into account this information, the signal shift observed in the main Raman band of the collected quartz spectra was plotted against its FWHM (Figure 6.9). In this case, the trend described in literature that relates wavenumber shift with an increase in its FWHM is not clearly observed. However, comparing the obtained values with the ones proposed in literature (48), it was possible to estimate that the pressure that this sample was subjected to during the impact event was between 21.7 and 25.8 GPa.

The fact that the impact that formed a crater can be studied by Raman spectroscopy is relevant to the study of Mars as it was stated above, since silica has been observed in the Red Planet. In fact, it is usually found in sedimentary deposits present inside and in the rims of craters in Mars (50, 51). Silica has been found in different emplacements, such as near the Antoniadi crater (52). Another crater where the finding of silica is very relevant is in Jezero crater (53) because with the Raman spectrometers that the rover *Perseverance* carries, it might be possible to find and use this silica to study the impact that formed Jezero.

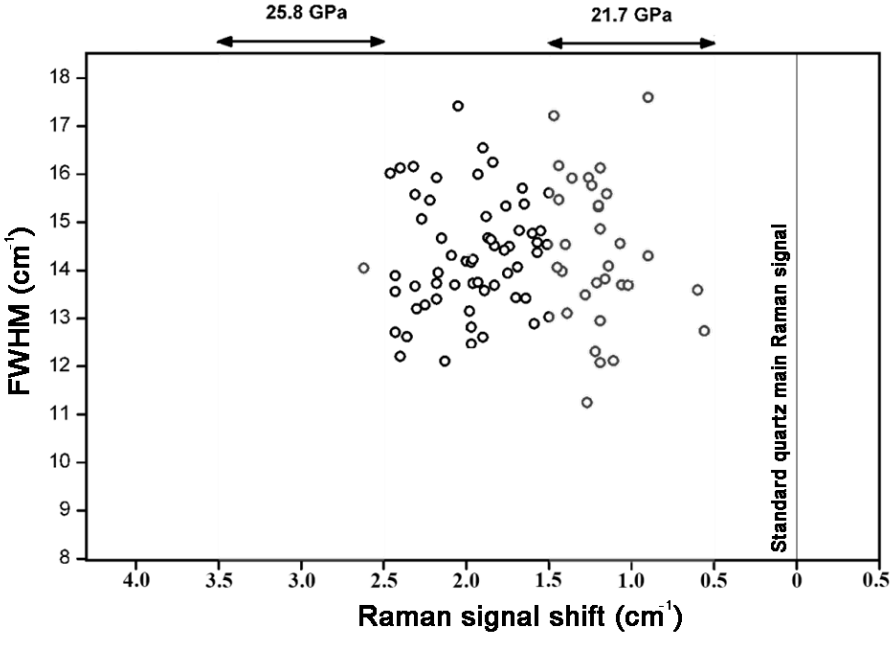


Figure 6.9. Graphical plot of the observed shift of the wavenumber position of the main Raman signal and its FWHM of the quartz of the Chesapeake Bay Crater. The spectra were collected with the 532 nm excitation laser. The values for the estimation of the pressure of the impact depending on the wavenumber position of the quartz band were obtained from (48) and added to the plot for clarity

As was explained above with the calcite found in the NWA 6148 meteorite, finding minerals altered by high-pressure events through Raman spectroscopy can help in the elucidation of other issues. In this sense, the Elephant Moraine (EET) 83227 meteorite was analyzed by Raman spectroscopy. A full description and geochemical characterization of this

meteorite can be found in Chapter 9, *Methodology Development and Testing for the Mars Returning Samples*. As it is described in that chapter, both Ca rich of high and low temperature feldspars were found in the EET 83227 meteorite.

In addition to the temperature effect on the feldspar mineral phase, an alteration caused by high-pressure was also observed in this mineral. As it can be observed in Figure 6.10, the signal-to-noise ratio of the obtained spectrum is worse than the one usually obtained with the Invia instrument for this mineral and the signals appear distorted, especially in the 600-1000 $cm^{-1}$ range (a comparison can be done with the normal feldspar Raman spectrum acquired from this meteorite described in Chapter 9, *Methodology Development and Testing for the Mars Returning Samples*). Besides, the features are wider than the ones observed in the other feldspars. In addition, the band at 980 $cm^{-1}$ is a bit wider than the ones mentioned previously. This fact was not due to an experimental reason, as the measurement was performed in the same conditions as the others. Besides, as the data was obtained by Raman mapping, it was observed that around 300 spectra of said Raman map had the same shapes and distorted features. This fact means that it was not a problem of a punctual analysis, but a zone of the sample with a slightly different feldspar spectrum than the others.

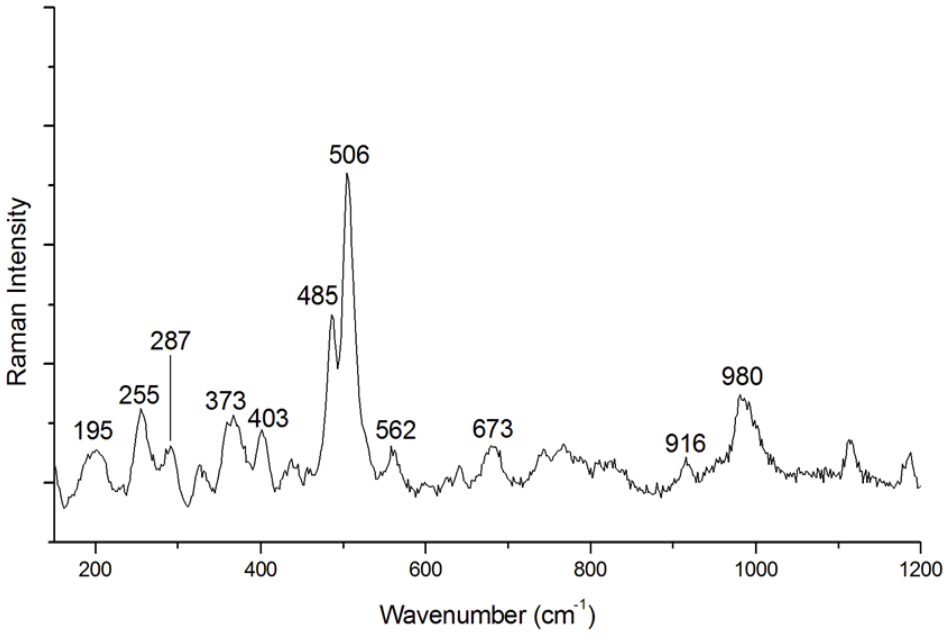


Figure 6.10. Shocked Ca rich feldspar identified in the EET 83227 sample by means of Raman spectroscopy. The spectrum was collected with the 532 nm excitation laser

As it is mentioned in the work of J. J. Freeman et al. (54), the worsening of the signal-to-noise ratio, the distortion of the features and the widening of the band at 980 $cm^{-1}$ are clear signs of a shocking event suffered by the feldspar. Unfortunately, in this case it was not possible to estimate the pressure that the meteorite was subjected to during the impact, since there are not research works in literature that relate the broadening of the 980 $cm^{-1}$ Raman band or the distortion of the signals with the pressure that the meteorite suffered. However, it is possible to detect if an area suffered from a high-pressure event thanks to these spectral features and changes.

## 6.3. Conclusions

In this chapter of the PhD thesis the capabilities of Raman spectroscopy to study certain minerals affected by past high-pressure events was assessed. In this sense, a model was developed to estimate by Raman

spectroscopy the pressure that a calcite can undergo. Rocks that are subjected to a punctual high-pressure event (such as an impact) retain part of that pressure as residual pressure, which can also be determined by the developed model. In other words, the calibration model could be used to determine the residual pressure that a calcite has after a pressure shock.

In order to test it, the calibration model was used to study the calcite present in the DaG 735 and NWA 6148 meteorites. In the case of the DaG 735, a calcite I affected by residual stress was identified. The presence of dolomite or magnesium substituting the calcium was discarded by ED-XRF, where only calcium was observed. This fact led to the conclusion that the mineral was original from Mars, as was also the case of perovskite and magnesiumwüstite, which were reported in literature as minerals present in the DaG 735 and affected by pressure. In this sense, Raman spectroscopy was proven to be capable of differentiating between a calcite affected by a high-pressure event and one that was not, even if the calcite was present as the polymorph calcite I.

Regarding the analysis of the NWA 6148 meteorite, calcite II was identified during its analysis, a fact that is indicative that calcite was present at the time of the impact of the meteorite against the Earth. The low residual pressure at which this calcite II was found, not only in this meteorite but also in the Marquina Black marble, suggests that the reversion process to calcite I is not fast or does not occur at the same pressure at which calcite II starts to form. This fact should be studied further, since nowadays literature only states that the transformation process occurs at around 0.5 GPa from calcite I to calcite II. Regarding its presence in the NWA 6148 meteorite, since the mineral was found in the inner part of the sample, the calcite was probably original from Mars. Using this information, it was tried to elucidate the Martian geographic origin of the nakhlites. Even thought it was not possible to confirm any of the emplacements cited by literature as the origin of nakhlites, we suggest Syrtis Major Planum as the most probable one based on the presence of calcite in the NWA 6148.

The determination of the geographical origin of a collection of meteorites, beyond knowing which celestial body they came from, is usually a hard task, since many factors and characteristics of the meteorites should be taken into account. However, any additional piece of information that helps in this matter is always useful. In this sense, it was proven that Raman spectroscopy can contribute to that discussion.

Besides the study on calcite in the DaG 735 and NWA 6148 meteorites, quartz and feldspar affected by a past high-pressure event were observed in a wet-target crater terrestrial analog (Chesapeake Bay Crater) and in the EET 83227 meteorite, respectively.

All these findings imply that high-pressure plays an important role in the space exploration field and should always be considered when studying extraterrestrial samples, either in situ in Mars or through meteorites. Raman spectroscopy can provide valuable information regarding alterations of minerals caused by high-pressure, which could help in the understanding of the surrounding area of the analyzed sample.

## 6.4. Bibliography

1. M. Akaogi, Phase transitions of minerals in the transition zone and upper part of the lower mantle, *Special Papers (Geological Society of America),* **2007**, 421, 1.

2. Holzhausen, G. R., Johnson, A. M., The concept of residual stress in rock, *Tectonophysics,* **1979**, 58, 237-267.

3. Sekiya, T., Ohta, S., Kamei, S., Hanakawa, M., Kurita, S., Raman spectroscopy and phase transition of anatase TiO2 under high pressure, *The Journal of Physics and Chemistry of Solids,* **2001**, 62, 717-721.

4. Decremps, F., Pellicer-Porres, J., Saitta, A. M., Chervin, J., Polian, A., High-pressure Raman spectroscopy study of wurtzite ZnO, *Physical Review. B, Condensed Matter,* **2002**, 65.

5. Melosh, H. J., Impact ejection, spallation, and the origin of meteorites, *Icarus,* **1984**, 59, 234-260.

6. Osinski, G. R., Pierazzo, E., Impact Cratering, 1st ed. **2012**, Wiley-Blackwell, Chicester, UK.

7. Weisberg, M. K., McCoy, T. J., Krot, A. N., Meteorites and the Early Solar System II; Systematics and evaluation of meteorite classification (p.p. 19-52) **2006,** Univ. of Arizona Press, Arizona, USA.

8. Fritz, J., Greshake, A., High-pressure phases in an ultramafic rock from Mars, *Earth and Planetary Science Letters,* **2009**, 288, 619-623.

9. Malin, M. C., Edgett, K. S., Posiolova, L. V., McColley, S. M., Dobrea, E. Z. N., Present-Day Impact Cratering Rate and Contemporary Gully Activity on Mars, *Science,* **2006**, 314, 1573-1577.

10. Michalski, J. R., Kraft, M. D., Diedrich, T., Sharp, T. G., Christensen, P. R., Thermal emission spectroscopy of the silica polymorphs and considerations for remote sensing of Mars, *Geophysical Research Letters,* **2003**, 30, 1-4.

11. Chen, M., Xiao, W., Xie, X., Coesite and quartz characteristic of crystallization from shock-produced silica melt in the Xiuyan crater, *Earth and Planetary Science Letters,* **2010**, 297, 306-314.

12. Bunch, T. E., Cohen, A. J., Coesite and Shocked Quartz from Holleford Crater, Ontario, Canada, *Science,* **1963**, 142, 379-381.

13. Yen, A. S., Morris, R. V., Ming, D. W., Schwenzer, S. P., Sutter, B., Vaniman, D. T., Treiman, A. H., Gellert, R., Achilles, C. N., Berger, J. A., et al., Formation of Tridymite and Evidence for a Hydrothermal History at Gale Crater, Mars, *Journal of Geophysical Research. Planets,* **2021**, 126, 1-16.

14. Morris, R. V., Vaniman, D. T., Blake, D. F., Gellert, R., Chipera, S. J., Rampe, E. B., Ming, D. W., Morrison, S. M., Downs, R. T., Treiman, A. H., et al., Silicic volcanism on Mars evidenced by tridymite in high-$SiO_2$ sedimentary rock at Gale crater, *Proceedings of the National Academy of Sciences,* **2016**, 113, 7071-7076.

15. Hemley, R. J., Effects of high pressure on molecules, *Annual Review of Physical Chemistry,* **2000**, 51, 763-800.

16. Goncharov, A. F., Raman Spectroscopy at High Pressures, *International Journal of Spectroscopy,* **2012**, 2012, 1-16.

17. Svensson, U., Dreybrodt, W., Dissolution kinetics of natural calcite minerals in $CO^{2-}$ water systems approaching calcite equilibrium, *Chemical Geology,* **1992**, 100, 129-145.

18. Benzerara, K., Menguy, N., Guyot, F., Dominici, C., Gillet, P., Nanobacteria-like calcite single crystals at the surface of the Tataouine meteorite, *Proceedings of the National Academy of Sciences,* **2003**, 100, 7438-7442.

19. Kirkland, B. L., Lynch, F. L., Rahnis, M. A., Folk, R. L., Molineux, I. J., McLean, R. J. C., Alternative origins for nannobacteria-like objects in calcite, *Geology,* **1999**, 27, 347-350.

20. McSween, H. Y., Harvey, R. P., A possible high-temperature origin for the carbonates in the martian meteorite ALH84001, *Nature,* **1996**, 382, 49-51.

21. Wang, A., Kuebler, K., Jolliff, B., Haskin, L. A., Mineralogy of a Martian meteorite as determined by Raman spectroscopy, *Journal of Raman Spectroscopy,* **2004**, 35, 504-514.

22. Carrasco-Busturia, D., The temperature - pressure phase diagram of the calcite I - calcite II phase transition: A first-principles investigation, *The Journal of Physics and Chemistry of Solids,* **2021**, 154, 110045.

23. Smyth, J. R., Ahrens, T. J., The crystal structure of calcite III, *Geophysical Research Letters,* **1997**, 24, 1595-1598.

24. Liu, L., Mernagh, T. P., Phase transitions and Raman spectra of calcite at high pressures and room temperature, *The American Mineralogist,* **1990**, 75, 801-806.

25. Fong, M. Y., Nicol, M., Raman spectrum of calcium carbonate at high pressures, *The Journal of Chemical Physics,* **1971**, 54, 579-585.

26. Zhang, L., Meng, Y., Yang, W., Wang, L., Mao, W. L., Zeng, Q., Jeong, J. S., Wagner, A. J., Mkhoyan, K. A., Liu, W., et al., Disproportionation of (Mg,Fe)$SiO_3$ perovskite in Earth's deep lower mantle, *Science,* **2014**, 344, 877-882.

27. Gillet, P., Biellmann, C., Reynard, B., McMillan, P., Raman spectroscopic studies of carbonates part I: High-pressure and high-temperature behaviour of calcite, magnesite, dolomite and aragonite, *Physics and Chemistry of Minerals,* **1993**, 20.

28. Suito, K., Namba, J., Horikawa, T., Taniguchi, Y., Sakurai, N., Kobayashi, M., Onodera, A., Shimomura, O., Kikegawa, T., Phase relations of $CaCO_3$ at high pressure and high temperature, *The American Mineralogist,* **2001**, 86, 997-1002.

29. Liu, C., Zheng, H., Wang, D., Raman spectroscopic study of calcite III to aragonite transformation under high pressure and high temperature, *High Pressure Research,* **2017**, 37, 545-557.

30. Rull, F., Martinez-Frias, J., Sansano, A., Medina, J., Edwards, H. G. M., Comparative micro-Raman study of the Nakhla and Vaca Muerta meteorites, *Journal of Raman Spectroscopy,* **2004**, 35, 497-503.

31. Tomkinson, T., Lee, M. R., Mark, D. F., Dobson, K. J., Franchi, I. A., The Northwest Africa (NWA) 5790 meteorite: A mesostasis-rich nakhlite with little or no Martian aqueous alteration, *Meteoritics & Planetary Science,* **2015**, 50, 287-304.

32. Kenji Hiraga, Eiji Ohtani, Toshiro Nagase, Henry J. Melosh, Masaaki Miyahara, Shin Ozawa, Naohisa Hirao, Ahmed El Goresy, Makoto Kimura, Takeshi Sakai, et al., Natural dissociation of olivine to (Mg,Fe) $SiO_3$ perovskite and magnesiowüstite in a shocked Martian meteorite, *Proceedings of the National Academy of Sciences - PNAS,* **2011**, 108, 5999-6003.

33. Treiman, A. H., The nakhlite meteorites: Augite-rich igneous rocks from Mars, *Chemie Der Erde,* **2005**, 65, 203-270.

34. Filiberto, J., Schwenzer, S. P., Volatiles in the Martian Crust, **2018**, Elsevier, Saint Louis, Missouri, USA.

35. Boynton, W. V., Ming, D. W., Kounaves, S. P., Young, S. M. M., Arvidson, R. E., Hecht, M. H., Hoffman, J., Niles, P. B., Hamara, D. K., Quinn, R. C., et al., Evidence for Calcium Carbonate at the Mars Phoenix Landing Site, *Science,* **2009**, 325, 61-64.

36. Sutter, B., Heil, E., Navarro-Gonzalez, R., Niles, P. B., Mahaffy, P. R., Stern, J. C., Mertzman, S., Rampe, E. B., Morris, R. V., Ming, D. W., et al., Iron-Rich Carbonates as the Potential Source of Evolved CO2 Detected by the Sample Analysis at Mars (SAM) Instrument in Gale Crater, *American Geophysical Union,* **December 14, 2015,** San Francisco, California, USA.

37. Ehlmann, B. L., Mustard, J. F., Murchie, S. L., Poulet, F., Bishop, J. L., Brown, A. J., Calvin, W. M., Clark, R. N., Marais, D. J. D., Milliken, R. E., et al., Orbital Identification of Carbonate-Bearing Rocks on Mars, *Science,* **2008**, 322, 1828-1832.

38. Morris, R. V., Ruff, S. W., Gellert, R., Ming, D. W., Arvidson, R. E., Clark, B. C., Golden, D. C., Siebach, K., Klingelhöfer, G., Schröder, C., et al., Identification of Carbonate-Rich Outcrops on Mars by the Spirit Rover, *Science,* **2010**, 329, 421-424.

39. Michalski, J. R., Niles, P. B., Deep crustal carbonate rocks exposed by meteor impact on Mars, *Nature Geoscience,* **2010**, 3, 751-755.

40. Wray, J. J., Murchie, S. L., Bishop, J. L., Ehlmann, B. L., Milliken, R. E., Wilhelm, M. B., Seelos, K. D., Chojnacki, M., Orbital evidence for more widespread carbonate-bearing rocks on Mars, *Journal of Geophysical Research. Planets,* **2016**, 121, 652-677.

41. Gilmore, M. S., Golder, K. B., Korn, L., Aaron, L. M., Carbonate Associated with Gullies in the Eridania Region of Mars, *Eighth International Conference on Mars,* **July 14, 2014,** Pasadena, California, USA.

42. Turner, S. M. R., Bridges, J. C., Grebby, S., Ehlmann, B. L., Hydrothermal activity recorded in post Noachian-aged impact craters on Mars, *Journal of Geophysical Research. Planets,* **2016**, 121, 608-625.

43. National Aeronautics and Space Administration, The Mars Orbiter Laser Altimeter [Internet]. Available from: https://attic.gsfc.nasa.gov/mola/images.html [accessed May 18, 2021].

44. Schon, S. C., Head, J. W., Fassett, C. I., An overfilled lacustrine system and progradational delta in Jezero crater, Mars: Implications for Noachian climate, *Planetary and Space Science,* **2012**, 67, 28-45.

45. Martín-Torres, F. J., Zorzano, M., Valentín-Serrano, P., Harri, A., Genzer, M., Kemppinen, O., Rivera-Valentin, E. G., Jun, I., Wray, J., Bo Madsen, M., et al., Transient liquid water and water activity at Gale Crater on Mars, *Nature Geoscience,* **2015**, 8, 357-361.

46. Collins, G. S., Wünnemann, K., How big was the Chesapeake Bay impact? Insight from numerical modeling, *Geology,* **2005**, 33, 925-928.

47. J. Wright Horton, J., Michael J. Kunk, Harvey E. Belkin, John N. Aleinikoff, John C. Jackson, I-Ming Chou, Evolution of crystalline target rocks and impactites in the Chesapeake Bay impact structure, ICDP-USGS Eyreville B core, *Special Papers (Geological Society of America),* **2009**, 458, 277.

48. Mcmillan, P. F., Wolf, G. H., Lambert, P., A Raman spectroscopic study of shocked single crystalline quartz, *Physics and Chemistry of Minerals,* **1992**, 19, 71-79.

49. Fritz, J., Wünnemann, K., Reimold, W. U., Meyer, C., Hornemann, U., Shock experiments on quartz targets pre-cooled to 77 K, *International Journal of Impact Engineering,* **2011**, 38, 440-445.

50. Squyres, S. W., Arvidson, R. E., Ruff, S., Gellert, R., Morris, R. V., Ming, D. W., Crumpler, L., Farmer, J. D., Des Marais, D. J., Yen, A., et al., Detection of Silica-Rich Deposits on Mars, *Science,* **2008**, 320, 1063-1067.

51. McLennan, S. M., Sedimentary silica on Mars, *Geology,* **2003**, 31, 315-318.

52. Smith, M. R., Bandfield, J. L., Geology of quartz and hydrated silica-bearing deposits near Antoniadi Crater, Mars, *Journal of Geophysical Research. Planets,* **2012**, 117, 1-24.

53. Tarnas, J. D., Mustard, J. F., Lin, H., Goudge, T. A., Amador, E. S., Bramble, M. S., Kremer, C. H., Zhang, X., Itoh, Y., Parente, M., Orbital Identification of Hydrated Silica in Jezero Crater, Mars, *Geophysical Research Letters,* **2019**, 46, 12771-12782.

54. Freeman, J. J., Wang, A., Kuebler, K. E., Jolliff, B. L., Haskin, L. A., Characterization of natural feldspars by Raman spectroscopy for future planetary exploration, *Canadian Mineralogist,* **2008**, 46, 1477-1500.

# Chapter 7

# Development of Classification and Characterization Models for Organics Analysis

*"If you torture the data long enough, it will confess"*

Ronald Coase, 1972

As was explained in the *Chapter 1, Introduction*, one of the main goals of the Mars 2020 mission is to search for evidences of past life in Mars, for example, by the finding of biosignatures. A biosignature is any substance, phenomenon or chemical-physical property that indicates past or present life on an area and that can be found in multiple ways and forms.

For instance, the morphology of a surface can be indicative of past life, since some bacteria alter the surface that they inhabit, leaving

characteristic shapes on it (1). The atmospheric characteristics are also very important, as they might provide observable biosignatures, such as its composition (e.g. the presence of methane) (2, 3) or even the reflectance spectrum of a planet taken from orbit, since some pigments that are only related to a biologic origin present characteristic spectral signals due to their color (4, 5).

Finally, there are some biosignatures directly related to chemical factors. For example, a chemical disequilibrium of a compound could be interpreted as a biosignature, since it would mean that a chemical equilibrium is being pushed in a direction due to external factors (e.g., the amount of methane on Earth's atmosphere is orders of magnitude above the equilibrium value due to the constant influx of this gas emitted by life forms) (6). Another biosignature related to a chemical factor would be the finding of organic molecules that are related to life processes. In this sense, Mars is not the best planet to look for this type of molecules, since the high amount of oxidant compounds of its surface and atmosphere and the ultraviolet radiation from the Sun do alter and destroy organic molecules at or near the Martian surface (7). However, these organic compounds could have been trapped inside mineral structures, especially inside clays, and endure these alteration processes, since clays can protect organic molecules from the effects of both the radiation and the strong oxidant compounds (7).

The fact that organic compounds have had more chances to be preserved trapped inside clays is of special relevance in Jezero crater, where the rover Perseverance landed, since clays have been detected both inside and around the crater (8). This fact makes Jezero crater one of the best places of Mars for the preservation of organic compounds related to life, in the case they existed in the past. Regarding Raman spectroscopy, it is usually not a good technique to analyze clays, since they provide a very weak signal and high fluorescence (9). However, this fact is in this case an advantage rather than a disadvantage, because organic Raman signals would not be hidden by the mineral spectral features and would be clearly

visible in the spectrum. Regarding the problem of the fluorescence caused by the clays, it is solved by using the Raman spectrometer of *SuperCam*, since it has a pulsed laser (10, 11). This fact means that the fluorescence coming from the mineral would not appear in the spectrum, since it is emitted at a different time than the delay and gating used for the Raman measurements of *SuperCam*. In addition, the fluorescence coming from the organic compounds would be visible in the Raman spectra, as its delay and gating times match with the ones used for the Raman spectral collection.

Even if *SuperCam* is able to detect and collect the spectrum of an organic compound, their analysis and characterization through Raman spectroscopy is complex, because the variety and similitudes of organic molecules is much higher than those of inorganic minerals, making the Raman spectra very similar from one to the other among the organic compounds of the same family. In addition, organic compounds usually present more than one dozen of Raman signatures in their spectrum, making its interpretation harder than in the case of minerals.

In this PhD thesis some carboxylic acids and amino acids have been studied in order to develop classification and characterization models to identify and study them by Raman spectroscopy. These organic compounds are directly related with the presence of life and take part in many biological processes (12). In addition, they are important alteration subproducts that occur during the decay of certain life forms (13). The developed models were then tested with two inclusions found in the Northwest Africa (NWA) 6148 Martian meteorite that had presence of organic compounds.

## 7.1. Organic Compounds Database

In order to develop the classification and characterization models presented in this chapter, a set of pure organic compounds was selected and analyzed by Raman spectroscopy. The selected compounds, as well

as their Raman features observed in the 1400-3000 $cm^{-1}$ wavenumber range and their band assignations, can be found in Table 7.1. The 1400-3000 $cm^{-1}$ Raman spectral region of an organic compound is the range where the different functional groups of the organic molecules usually have their characteristic bands.

Table 7.1. Main Raman bands in the 1400-3000 $cm^{-1}$ range of the analyzed organic compounds. The spectra were collected with the 532 nm laser. Relative intensities indicated by s=strong, m=medium, w=weak; vibration type indicated by v=stretching, δ=bending, ρ=rocking, sc=scissoring

| Organic Compound | δ($CH_2$) | δ($CH_2$) | ρ(NH) | ρ(NH) | sc($NH_2$) | ν(C=O) | ν(C=O) | ν(CH) | ν(CH) | ν(CH) | ν(CH) |
|---|---|---|---|---|---|---|---|---|---|---|---|
| L-Glutamic acid monosodium salt | 1401 (m) | 1434 (m) | 1532 (w) | 1570 (w) | 1605 (w) | | | 2849 (m) | 2890 (s) | 2937 (s) | 2974 (s) |
| L-Aspartic acid potassium salt | 1414 (m) | | | | 1598 (w) | | | | | 2939 (s) | |
| Succinic acid | | 1421 (m) | | | | | 1656 (m) | 2828 (w) | | 2928 (s) | 2970 (s) |
| L-Aspartic acid | 1417 (m) | 1461 (w) | 1504 (w) | 1546 (w) | 1617 (w) | | 1691 (m) | | | 2956 (s) | 2997 (s) |
| Glycine | 1411 (m) | 1440 (m) | 1511 (w) | 1569 (m) | 1631 (w) | | 1670 (m) | | | 2973 (s) | 3008 (s) |
| DL-Malic acid | 1423 (m) | 1453 (m) | | | | 1634 (m) | 1675 (m) | | | 2946 (s) | 2991 (m) |
| L-Alanine | 1409 (m) | 1462 (m) | 1500 (w) | | 1596 (m) | | | | 2889 (m) | 2932 (s) | 2968 (s) |
| L-Ornithine | 1418 (w) | 1462 (m) | 1488 (w) | 1540 (w) | 1609 (w) | 1634 (w) | | | 2887 (m) | 2941 (s) | 2972 (s) |
| L-Valine | 1427 (w) | 1453 (m) | 1510 (w) | | | 1628 (w) | | | 2880 (s) | 2910 (s) | 2970 (s) |

Table 7.1. Main Raman bands in the 1400-3000 $cm^{-1}$ range of the analyzed organic compounds. Spectra collected with the 532 nm laser. Relative intensities indicated by s=strong, m=medium, w=weak; vibration type indicated by v=stretching, δ=bending, ρ=rocking, sc=scissoring (continuation)

| Organic Compound | δ($CH_2$) | δ($CH_2$) | ρ(NH) | ρ(NH) | sc($NH_2$) | ν(C=O) | ν(C=O) | ν(SH) | ν(CH) | ν(CH) | ν(CH) | ν(CH) |
|---|---|---|---|---|---|---|---|---|---|---|---|---|
| B-Alanine | 1429 (m) | 1447 (m) | | | | | 1682 (w) | | | 2913 (s) | 2932 (s) | 2975 (s) |
| L-Cysteine | 1425 (w) | | | | | 1617 (w) | | 2546 (s) | | | 2957 (s) | 2999 (s) |
| L-Leucine | 1409 (m) | 1456 (m) | 1517 (w) | 1583 (w) | 1626 (w) | | | | 2870 (s) | 2901 (s) | 2937 (s) | 2988 (s) |
| γ-Aminobutyric acid | 1400 (m) | 1424 (m) | 1539 (w) | 1579 (w) | | | | | 2865 (m) | 2910 (s) | 2937 (s) | 2985 (m) |
| L-Threonine | 1418 (m) | 1452 (w) | 1548 (w) | 1598 (w) | | | 1645 (w) | | 2876 (s) | | 2941 (s) | 2997 (s) |
| Fumaric acid | | | | | | 1604 (w) | 1686 (s) | | | | | |
| L-Isoleucine | 1421 (w) | 1449 (m) | 1514 (m) | 1582 (w) | 1624 (w) | | | | 2892 (s) | | 2951 (s) | 2994 (s) |
| L-Lysine | 1400 (m) | 1442 (m) | | | 1608 (m) | | | | 2862 (s) | 2906 (s) | 2942 (s) | |

Table 7.1. Main Raman bands in the 1400-3000 $cm^{-1}$ range of the analyzed organic compounds. Spectra collected with the 532 nm laser. Relative intensities indicated by s=strong, m=medium, w=weak; vibration type indicated by ν=stretching, δ=bending, ρ=rocking, sc=scissoring (continuation)

| Organic Compound | δ($CH_2$) | δ($CH_2$) | ρ(NH) | ρ(NH) | sc($NH_2$) | ν(C=O) | ν(C=O) | ν(CH) | ν(CH) | ν(CH) | ν(CH) |
|---|---|---|---|---|---|---|---|---|---|---|---|
| Sodium pyruvate | 1411 (w) | 1448 (m) | | | | 1617 (w) | | 2855 (m) | 2921 (s) | 2960 (s) | 2960 (m) |
| Sodium L-lactate | 1421 (m) | 1457 (m) | | | | | | 2888 (s) | | 2941 (s) | 2989 (m) |
| L-Serine | 1421 (w) | 1463 (m) | | | 1600 (w) | 1629 (w) | | | 2905 (s) | 2961 (s) | 2999 (m) |
| 3-Hydroxybutyric acid | 1400 (w) | 1455 (m) | | | | | 1695 (m) | | 2889 (s) | 2939 (s) | 2986 (m) |
| L-Homoserine | 1403 (w) | 1436 (m) | | | 1588 (m) | 1637 (w) | | 2921 (s) | 2943 (s) | 2959 (s) | 2995 (s) |
| L-Allo-threonine | 1415 (m) | 1467 (m) | | 1550 (w) | 1596 (w) | 1642 (w) | | | 2905 (s) | 2946 (s) | 2985 (s) |
| Glutamine | 1418 (m) | 1450 (m) | 1498 (w) | 1550 (w) | 1605 (m) | 1624 (w) | 1688 (w) | 2883 (w) | 2933 (s) | 2960 (s) | 2990 (m) |
| L-Allo-isoleucine | 1424 (w) | 1449 (m) | 1473 (w) | 1509 (w) | 1586 (w) | 1628 (w) | | 2876 (s) | 2898 (s) | 2957 (s) | 2986 (s) |

Table 7.1. Main Raman bands in the 1400-3000 $cm^{-1}$ range of the analyzed organic compounds. Spectra collected with the 532 nm laser. Relative intensities indicated by s=strong, m=medium, w=weak; vibration type indicated by v=stretching, δ=bending, ρ=rocking, sc=scissoring (continuation)

| Organic Compound | δ($CH_2$) | δ($CH_2$) | ρ(NH) | ρ(NH) | sc($NH_2$) | ν(C=O) | ν(C=O) | ν(CH) | ν(CH) | ν(CH) | ν(CH) |
|---|---|---|---|---|---|---|---|---|---|---|---|
| Citric acid | 1418 (w) | 1443 (w) | | | | 1681 (m) | 1751 (w) | | 2949 (s) | 2965 (s) | |
| Myristic acid | 1437 (s) | 1462 (w) | | | | 1638 (w) | | 2847 (s) | 2882 (s) | 2930 (s) | 2965 (m) |
| Decanoic acid | 1436 (m) | 1462 (w) | | | | 1640 (w) | | 2848 (s) | 2883 (s) | 2920 (s) | |
| Dodecanoic acid | 1436 (m) | 1467 (w) | | | | 1634 (w) | | 2846 (s) | 2882 (s) | 2935 (s) | 2965 (m) |
| Palmitic acid | 1438 (m) | 1465 (w) | | | | 1629 (w) | | 2847 (s) | 2882 (s) | 2926 (s) | 2966 (m) |
| Tridecanoic acid | 1444 (m) | 1466 (m) | | | | 1645 (w) | | 2846 (s) | 2883 (s) | 2932 (s) | 2965 (m) |
| Stearic acid | 1441 (m) | 1463 (w) | | | | 1649 (w) | | 2849 (s) | 2882 (s) | 2928 (s) | |
| Arachidic acid | 1439 (m) | 1464 (w) | | | | 1633 (w) | | 2847 (s) | 2882 (s) | 2926 (s) | |

## 7.2. Carboxylic and Amino Acids Classification model

As was explained above, one of the main challenges for organic compound analysis using Raman spectroscopy is not the lack of spectral features or their intensity, but the characterization of the molecules once the spectra have been acquired. The Raman signals related to organic compounds change in number, position and intensity depending on different factors related to the compound, such as the different functional groups present along the carbon chain of the molecule, their position inside the chain, the length of the carbon chain, the conformation of that chain (linear or branched) or even the bond disposition of the carbon tetrahedrons (isomers) (14, 15).

As it is observed in Figure 7.1, a common Raman spectrum of an organic compound (L-aspartic acid) presents several dozens of Raman signatures. In this case, the Raman signals related to the pure L-aspartic acid appear at 138, 188, 273, 357, 418, 468, 552, 600, 662, 747, 778, 871, 902, 938, 992, 1044, 1081, 1120, 1145, 1251, 1290, 1336, 1361, 1417, 1461, 1504, 1546, 1617, 1691, 2956, 2997 and 3014 $cm^{-1}$, a total of 32 unique Raman signatures related to the different bond vibrations that the molecule has.

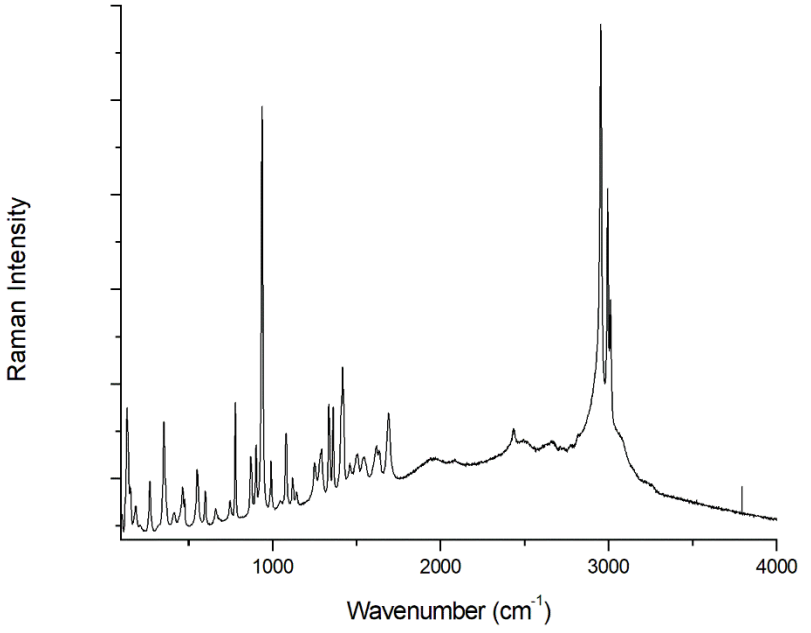


Figure 7.1. Raman spectrum of the pure organic compound L-aspartic acid, obtained with the 532 nm excitation laser. For clarity, the wavenumber positions of the signals are described in the text

Since organic compounds have many Raman signals, sometimes it is difficult to identify them analyzing the Raman spectra visually. In fact, only in some specific cases the compound presents a specific Raman band that can be used to identify it unambiguously. For instance, among the organic compounds of the database presented above, L-cysteine can be recognized unambiguously from the other compounds using its Raman spectrum, thanks to the feature at 2546 $cm^{-1}$ (Table 7.1) caused by its -SH functional group. The complexity in the visual analysis of the Raman spectra of organic compounds is the reason why chemometrics can be used to help in their identification.

In order to develop a model that could be used to classify organic compounds by Raman spectroscopy, a Principal Component Analysis (PCA) was carried out using the 100-4000 $cm^{-1}$ spectral range of the Raman spectra of the organic compounds listed in Table 7.1. The different

wavenumbers of that range were set as the variables of the model and the organic compounds as the samples. Since the results of a PCA depend on the relative variance of the variables, when developing a model with spectra it is usual to scale them using the standard deviation of the variables. In this case, different types of weighing of the variables were tested and none of them improved the model, so it was carried out without using them. In addition, the data were mean centered and a full cross validation was carried out, where all the samples of the model itself are used for the validation one by one.

Figure 7.2 shows the plot of the scores of the principal components PC 1 and PC 2. As it is observed, in this plot three clusters of samples are clearly differentiated. The green circle indicates the only organic compound of the samples set that has an -SH functional group, the L-Cysteine. It is not a cluster in itself, since it is composed only by one sample, but it is clearly differentiated from the others. The red circle of Figure 7.2 includes the saturated carboxylic acids of the analyzed set of samples that do not have any functional group. Finally, the big blue cluster groups the other organic molecules, namely, the unsaturated carboxylic acid and the saturated carboxylic acid with the functional group -OH and $-NH_2$ (amino acids). Overall, even though the developed model is not perfect, it is able to differentiate different types of organic acids depending on their nature and their functional groups. It is not able to differentiate between unsaturated carboxylic acids and saturated carboxylic acids with an -OH or $-NH_2$ functional group, but this model would be a good first step to start classifying organic acids.

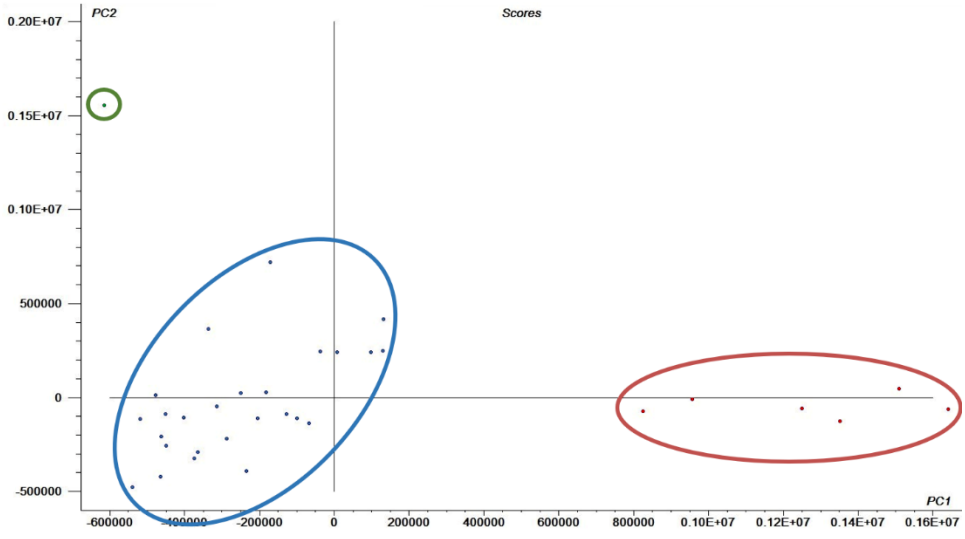


Figure 7.2. Plot of the PC 1 and PC 2 scores of the PCA model developed with the organic compounds of Table 7.1

## 7.3. Application of the model to the Northwest Africa 6148 Meteorite

The developed model for the study of organic compounds by Raman spectroscopy was used to identify the nature of the organic compounds contained in two inclusions that were found in the Martian meteorite Northwest Africa (NWA) 6148. The full study and characterization of this nakhlite can be found in Chapter 9, *Methodology Development and Testing for the Mars Returning Samples*. It was decided to use the model with a Martian meteorite to test to what extent does it work with a real sample as close to a Martian rock as possible.

The finding of organic compounds in Martian meteorites is not something new, as they have been found repeatedly in various meteorites in the past (16-18). However, the eternal debate lies in the discussion of whether those organic compounds are extraterrestrial or not. Some authors have proven with isotopic and nano-SIMS evidence that the organic compounds present in some meteorites are from an extraterrestrial origin, being able to deduce

the past presence of subsurface organic-bearing fluids on Mars (16, 17). However, the usual explanation for the presence of organic compounds in a meteorite is that they are caused by terrestrial weathering, as was the case with the amino acids observed in the Martian meteorite Elephant Moraine 79001 (18). Regardless of their origin, the finding of organic compounds in a meteorite is always relevant and can be used, in this case, to test the developed characterization methodologies.

In the case of the NWA 6148 nakhlite, two inclusions containing organic compounds were found in the meteorite while performing Raman imaging (Figure 7.3 and 7.4). Both Raman maps have more than 4000 spectra from which almost 500 have organic signatures and correspond to the highlighted red areas. The average Raman spectrum obtained from both inclusions can also be observed in Figure 7.3 and 7.4. Both inclusions were located in an olivine matrix, thus, the Raman spectra collected in the area always showed the signals of the organic molecules together with the Raman signals of olivine.

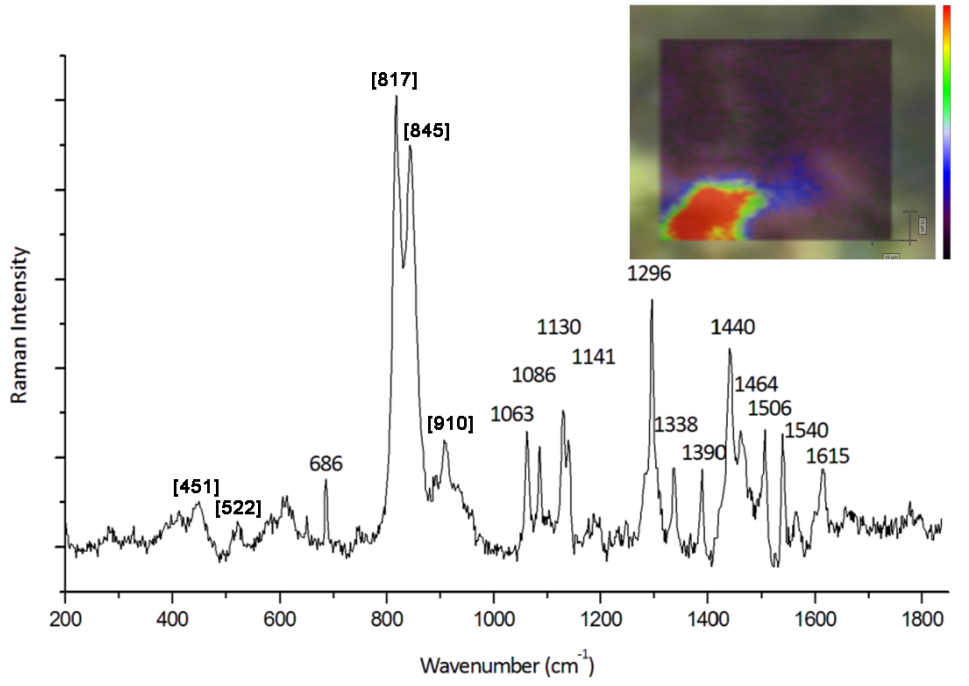


Figure 7.3. Average Raman spectrum of an inclusion present in the NWA 6148 meteorite where the presence of organic compounds is observed and the map obtained from that area using the 532 nm laser, where the red zone indicates a higher presence of organics. The olivine Raman signals related to the mineral matrix are indicated between brackets

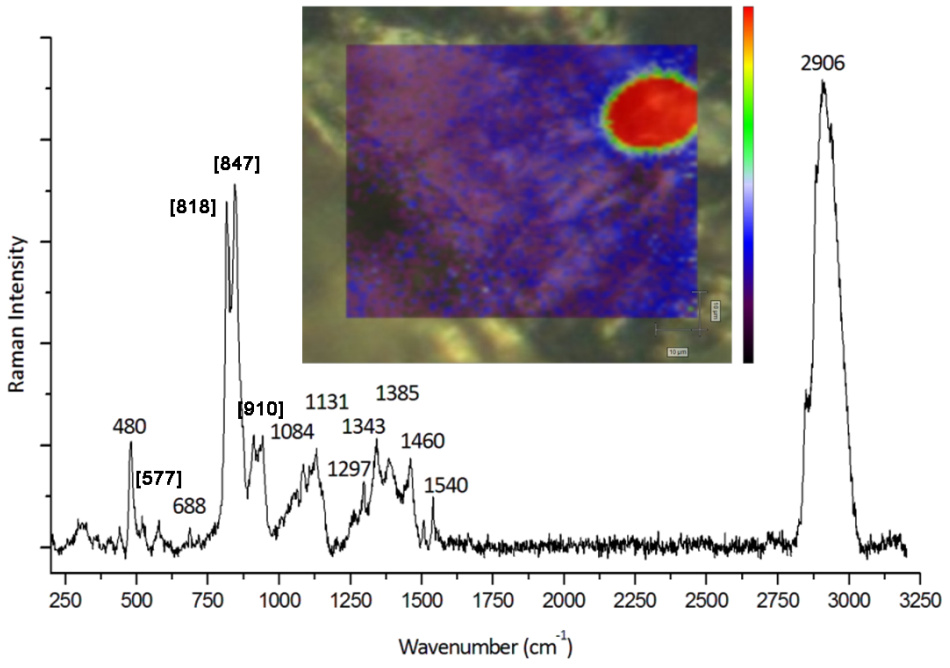


Figure 7.4. Average Raman spectrum of an inclusion present in the NWA 6148 meteorite where the presence of organic compounds is observed and the map obtained from that area using the 532 nm laser, where the red zone indicates a higher presence of organics. The olivine Raman signals related to the mineral matrix are indicated between brackets

When the developed classification model was applied to the spectra where the organic features were present, the result expressed that they fitted in the cluster of amino acids, unsaturated carboxylic acids and saturated carboxylic acids with an -OH. However, when analyzing the spectra one by one it was observed that not all the spectra were the same and that they had slight differences between them. In order to check these differences, three representative spectra were selected from the organic compounds of the inclusion of Figure 7.3. Table 7.2 shows the normalized areas, using the 1296 $cm^{-1}$ band area as a normalizing factor, of several Raman bands corresponding to those three Raman spectra from the inclusion from the NWA 6148 meteorite. The band areas were calculated by curve fitting and the area of the 1296 $cm^{-1}$ signal was selected to normalize the other signals because it is caused by the stretching vibration of the $CH_2$ and it was always present in all the spectra where organic compounds were observed in the Raman mapping. In addition, it was the, or one of the, most intense

signal related to the organic compound present in the spectra and it always appeared without additional signals nearby, which would have added uncertainty in the fitting process.

As it can be observed in Table 7.2, several areas of the different bands are not proportional from one to another. For instance, the bands at 1063 and 1130 $cm^{-1}$ (ν(C-C) stretching vibrations, correlated with the number of carbon atoms in the molecule chain), are much larger in spectrum 1 than in spectrum 2 or 3. However, in the case of the bands assigned to $\delta(CH_2)$ or $\delta(CH_3)$ deformations of linear carboxylic acids, the 1390 $cm^{-1}$ band is larger in spectrum 1, although in the case of the 1506 $cm^{-1}$ it is the smallest one. Other bands, such as the ones at 520 or 686 $cm^{-1}$ are similar from one spectrum to another. All these facts meant that the inclusions probably had a mixture of compounds of similar nature inside. More specifically, thanks to the classification model and this fact, it was possible to confirm the presence of a mixture of different carboxylic acids and amino acids in both cavities.

Table 7.2. Normalized area of some organic signature bands of three different Raman spectra collected from the analyzed inclusion of the NWA 6148 meteorite

| Raman band ($cm^{-1}$) | Normalized band area | | |
|---|---|---|---|
| | Spectrum 1 | Spectrum 2 | Spectrum 3 |
| 520 | 0.70 | 0.43 | 0.20 |
| 686 | 0.27 | 0.30 | 0.54 |
| 1063 | 5.00 | 0.49 | 0.98 |
| 1086 | 0.40 | 0.49 | 0.46 |
| 1130 | 3.83 | 0.59 | 1.20 |
| 1296 | 1.00 | 1.00 | 1.00 |
| 1338 | 2.83 | 0.56 | 1.16 |
| 1390 | 7.60 | 0.18 | 0.61 |
| 1464 | 2.65 | 0.96 | 3.63 |
| 1506 | 0.13 | 0.41 | 0.38 |

Depending on the abundance of each compound in the different areas of the inclusion, they would contribute differently to the Raman spectrum, resulting in the observed differences in the relative intensities of the spectra. Chemometrics were used in order to solve the mixture and to try to extract the spectrum of each individual organic compound that contributed to the spectra obtained in the maps. More specifically, to clarify the mixture, sparse Principal Component Analysis (sPCA) was used with all the spectra of the Raman maps that had any Raman signature related to organics. This methodology helps with the identification of individual compounds that are present in a mixture. The loadings for the sparse principal components (sPCs) 1 and 3, in the 1000–1700 $cm^{-1}$ range, and the heat map for both sPCs of the inclusion from Figure 7.4 are shown in Figure 7.5. In the case of this cavity, the method provided spectral information of the organic compounds in those two sPCs, while the sPC 2 was related with areas of the spectra where there were no bands, in other words, it was related with the noise of the spectra. However, all the different sPCs were very similar and had very similar diagnostic Raman signatures, since all of them corresponded to carboxylic acids. Even though the hypothesis of different organic compounds due to the different relative intensities in the spectra throughout the maps was correct, it was not possible to differentiate which specific molecules they were, since the developed classification method does not work properly to distinguish among different amino acids, unsaturated carboxylic acids and saturated carboxylic acids with an -OH functional group, as was explained above.

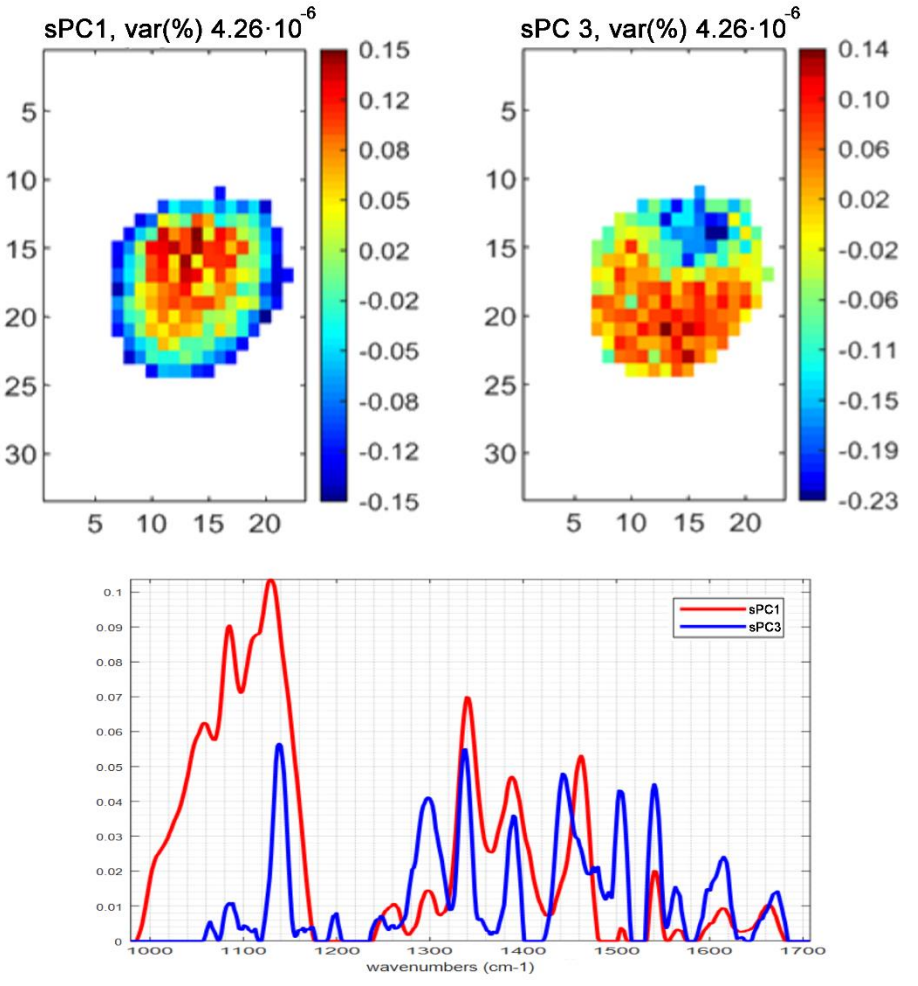


Figure 7.5. sPCA 1 and 3 loadings in the 1000–1700 cm-1 range for the organic compounds present in the inclusion of Figure 7.5 and the heat map for each sPCA

Among the different sPCs obtained with the sPCA, there was one that had spectral relevance and represented one of the organic compounds of the mixture that was labeled as a saturated carboxylic acid by the PCA classification method. This sPC was obtained from the sPCA carried out with the Raman spectra of the organic compounds of the cavity of Figure 7.4. In order to test if the applied methodologies did work, a Raman curve fitting was carried out with an experimental spectrum to detect and know precisely the position of all the Raman signals present in the spectrum (Figure 7.6).

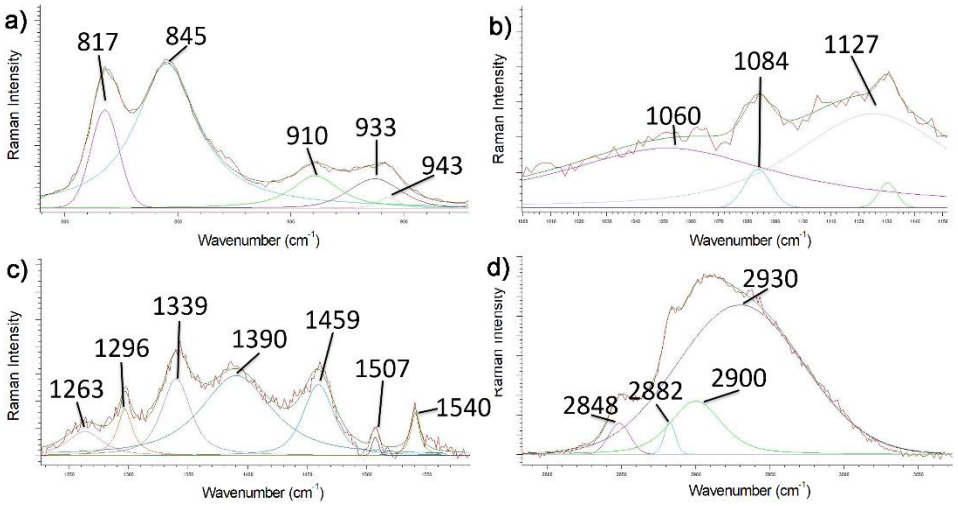


Figure 7.6. Raman band fitting of four spectral regions, a) 800-1000 $cm^{-1}$, b) 1000-1150 $cm^{-1}$, c) 1250-1550 $cm^{-1}$ and d) 2800-3050 $cm^{-1}$, of a saturated carboxylic acid spectrum of the organic compound present in the inclusion of Figure 7.4

As observed in Figure 7.6a, the bands that appeared at 817, 845, 910 and 933 $cm^{-1}$ were all associated with the matrix of the analyzed area. All of these signatures corresponded to an olivine rich in iron (higher proportion of fayalite than forsterite), which is described in Chapter 9, *Methodology Development and Testing for the Mars Returning Samples*. Regarding the signals related to the organic compound, Figure 7.6b shows signals that appeared at 1060, 1084 and 1127 $cm^{-1}$, which are typical from the ν(C-C) stretching vibrations in organic acids or carboxylates of 12 or less carbons. Regarding the Figure 7.6c, the 1296 $cm^{-1}$ band is typical of the $\delta(CH_2)$ twist vibrations of carboxylic acids and the bands at 1390, 1459 and 1507 $cm^{-1}$ were assigned to $\delta(CH_2)$ or $\delta(CH_3)$ deformations, all of them typical of linear organic acids or carboxylates. The 1339 and 1540 $cm^{-1}$ bands were assigned to the asymmetric stretching vibration of the $CO_2^-$ of carboxylates. In Figure 7.6d it is observed that there are no bands in higher wavenumbers than 3000 $cm^{-1}$ and the presence of a wide and intense band at 2930 $cm^{-1}$, assigned to the ν(CH) vibration, which reinforces the theory of this organic compound being a carboxylic acid.

In addition to this compound observed in the spectra of the map of Figure 7.4, it was detected that the same signals were present in some of the spectra of Figure 7.3, which meant that this organic compound was present in both cavities.

Using the sPCA results and the PCA classification model it was possible to confirm the presence of a saturated carboxylic acid in the inclusion of the NWA 6148. In order to identify and to provide a better characterization of this compound, a regression model was developed for saturated carboxylic acids. Similar to what happens with minerals, the position of the Raman signals of organic compounds are also related to the vibration of chemical bonds. As was observed in Chapter 5, *Forsterite and Fayalite Content in Olivines*, and 6, *Mineral Alterations Caused by High-Pressure Events* , this fact means that small changes in the surroundings of a specific bond might cause small wavenumber shifts in a spectral band, which can then be used to study the chemical-physical changes of a mineral. In the case of organic compounds, small changes in a spectrum can also be used to study other characteristics of a molecule that can help in its identification. Due to that, the spectral information of the different saturated carboxylic acids listed in Table 7.1 was used to develop a method to identify the organic compound present in the inclusions of the NWA 6148 meteorite.

Among the three v(C-C) stretching vibrations observed in saturated carboxylic acids, De Gelder et. al. (19) noticed that the one in the middle (1084 $cm^{-1}$ in Figure 7.6b) did shift to a higher wavenumber when the carbon chain length was larger. They checked this fact with lauric acid, myristic acid, palmitic acid and stearic acid. Knowing that the Raman signature in the 1075-1110 $cm^{-1}$ area did shift as the molecule had more carbons (a larger carbon chain length), a model was developed to calculate the number of carbons in a saturated carboxylic acid using that Raman signal for the compounds listed in Table 7.3.

Table 7.3. Saturated carboxylic acids used for the calibration model

| Organic molecule | Number of carbons | v (C–C) |
|---|---|---|
| Decanoic acid | 10 | 1076.4 |
| Dodecanoic acid | 12 | 1085.0 |
| Tridecanoic acid | 13 | 1087.8 |
| Myristic acid | 14 | 1093.2 |
| Palmitic acid | 16 | 1099.3 |
| Stearic acid | 18 | 1100.6 |
| Arachidic acid | 20 | 1108.1 |

When the wavenumber position of the Raman signal related to that vibration was represented against the number of carbons of the carboxylic acid, it was observed that the data followed the trend of a quadratic model (Figure 7.7), whose regression equation is presented in Equation 7.1. The variable $RB_{v(C\text{-}C)}$ is the Raman band related to that bond vibration and $C$ represents the number of carbons of the carbon chain. This regression curve had a coefficient of determination ($r^2$) of 0.9843 and a standard error of 2.14 $cm^{-1}$.

$$RB_{v(C-C)} = -0.1372 \cdot C^2 + 7.1574 \cdot C + 1018.7 \qquad \textit{Equation 7.1}$$

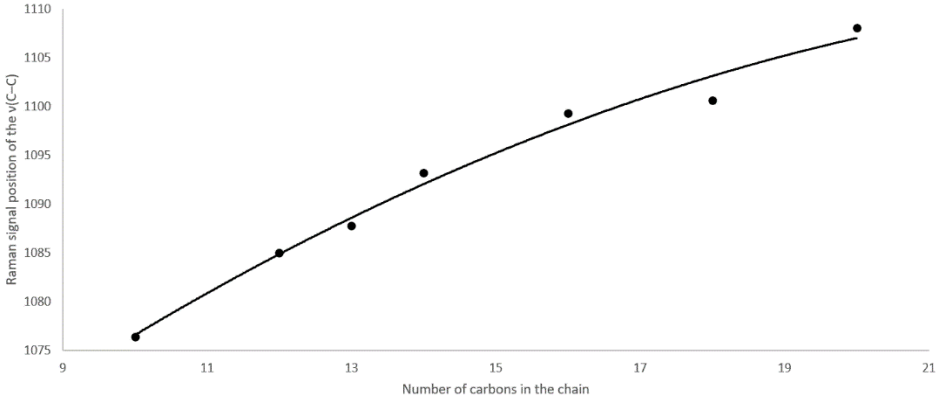


Figure 7.7. Regression model obtained from the representation of the number of carbons in the linear saturated carboxylic acid compounds versus the Raman band position related with the v(C–C) vibration

It must be pointed out that this calibration model was obtained using organic compounds that cover a specific range regarding their chain length ($10 \leq C \leq 20$). What this fact means is that if a linear saturated carboxylic acid has less than 10 carbon atoms or more than 20 in its chain, the model might not work, since they would be outside of the range of the studied compounds. Realistically, the model probably changes the regression equation at some point when adding organic compounds with less and more carbons, since the v(C–C) vibration mode cannot shift in a constant way indefinitely in the Raman spectrum, because specific bond vibrations usually appear in a particular range in the Raman spectrum. In order words, when the carbon chain tends to infinity and to zero, the Raman signal assigned to that v(C-C) stretching vibration probably would tend to a constant wavenumber. To sum it up, since the proposed model has not been tested outside the studied range, it can only be stated that it works for the estimation of the length of the carbon chain of saturated carboxylic acids with a carbon chain between 10 and 20 carbons.

Equation 7.1 was used to characterize the carboxylic acid present in the inclusions of the meteorite NWA 6148, obtaining that this organic compound had 12 saturated carbons, which matches with what was explained above in the Raman signals assignations.

As a summary, all the assigned bands of the spectrum obtained from the inclusion indicated the presence of a carboxylic acid. Besides, the number and shape of the signals in the 1350-1510 $cm^{-1}$ range suggested that the carboxylic acid was linear and did not have C=C bonds. In addition, the presence of the three bands in the 1050-1150 $cm^{-1}$ range suggested that the molecule probably had a short and saturated carbon chain, which is in agreement with the calculated carbon chain length of 12 carbons ($C_{12}$), calculated with the Equation 7.1. All these facts led to the conclusion that the studied organic compound present in the inclusions of the NWA 6148 meteorite was dodecanoic acid.

To summarize the methodology used for the characterization of the organic compounds present in the NWA 6148 meteorite (Figure 7.3 and 7.4), first the average spectra of the cavities were classified using the PCA model (Figure 7.2) as a mixture of different carboxylic acids. This fact was supported by the finding of similar representative spectra with different relative intensities (Table 7.2), which led to the conclusion that both cavities had a mixture of different carboxylic acids. In order to clarify these mixtures, a sPCA analysis was performed. For the organics present in both cavities, most of the sPCs with spectral information pointed to the presence of amino acids, unsaturated carboxylic acids or saturated carboxylic acids with an -OH functional group, which was supported by the PCA model. However, it was observed that one of the sPCs obtained from the sPCA done with the spectra of the experimental Raman maps suggested the presence of a saturated carboxylic acid, which was checked with both the PCA model and the assignation of bands of the spectrum using curve fitting (Figure 7.6). Finally, the carbon chain calibration model (Figure 7.7) was used to calculate the chain length of the organic acid. All these steps were needed to conclude the presence of dodecanoic acid in both cavities of the Martian meteorite NWA 6148. Although it was not possible to identify them as precisely as the dodecanoic acid, both cavities had presence of at least 1 more carboxylic acid, more specifically, amino acids, unsaturated acids or saturated acids with an -OH functional group.

## 7.4. Conclusions

Despite the fact that finding biosignatures and organics is one of the main objectives of the current and upcoming Martian missions, the studies about them using Raman spectroscopy that can be found in literature are scarce. More specifically, there is a lack of knowledge about what type of information can Raman spectroscopy provide about organics, besides its characterization. During this PhD thesis two models, one to classify carboxylic acids and amino acids based on their Raman spectrum and the other one to calculate the carbon chain length of saturated carboxylic acids,

have been developed. Although the models are limited in that they cover only a specific type of organics, they showed good quality parameters. They are a first step to develop more complex and complete models that would cover a wider range of compounds and would give more information about them using only their Raman spectrum. However, it must be pointed out that due to the fact that the spectra of organic compounds are more complex and the variability of compounds is much higher, the development of models is a hard task.

In order to achieve good models, an extensive and wide available database of Raman spectra of organic compounds would be needed. The main issue in this sense is that the number of organic compounds that can exist is much larger than the number of inorganic ones (minerals). It is estimated that several thousands of organic compounds are discovered and indexed each day in the Chemical Abstract Service (CAS). Of course, almost all of them are synthetic compounds not found in nature, but this fact helps to picture how bast is the number of possible organic compounds compared to the number of minerals. During this PhD thesis, a small set of carboxylic acids and amino acids has been studied using Raman spectroscopy and has been used to develop the models presented in this chapter. However, if we want to have better and more robust models regarding Raman spectroscopy and organics, a greater emphasis should be put into published organic databases.

Finally, when the developed models were tested with a real sample where organic compounds were present inside two inclusions of a Martian meteorite, it was observed that they do not always provide good results, more specifically, when analyzing a mixture of organics. The classification model did work and classified the average spectrum of the mapping of the inclusion as an amino acid, an unsaturated carboxylic acid or a saturated carboxylic acid with an -OH functional group. However, as it was observed afterwards, the inclusion had a mixture of different organic compounds and, thus, the classification model was not able to indicate that there was

presence of a saturated carboxylic acid until its particular spectrum was obtained using a sPCA. Regarding the carbon chain characterization model, it was observed that it worked properly in the studied range, as the results obtained from it matched the ones observed by curve fitting of the Raman bands. However, as it was discussed during this chapter, the model would be probably inaccurate at some point when analyzing saturated carboxylic acids outside of the studied carbon chain length. This fact cannot be completely solved, since the chains can lengthen to infinity. However, it would be sensible to expand this model with more compounds until it gets transformed into a quadratic curve that tends to a constant wavenumber when the carbon chain length tends to infinity.

## 7.5. Bibliography

1. Benzerara, K., Menguy, N., Guyot, F., Dominici, C., Gillet, P., Nanobacteria-like calcite single crystals at the surface of the Tataouine meteorite, *Proceedings of the National Academy of Sciences,* **2003**, 100, 7438-7442.

2. Formisano, V., Atreya, S., Encrenaz, T., Ignatiev, N., Giuranna, M., Detection of Methane in the Atmosphere of Mars, *Science,* **2004**, 306, 1758-1761.

3. Mumma, M. J., Villanueva, G. L., Novak, R. E., Hewagama, T., Bonev, B. P., DiSanti, M. A., Mandell, A. M., Smith, M. D., Strong Release of Methane on Mars in Northern Summer 2003, *Science,* **2009**, 323, 1041-1045.

4. DasSarma, S., Schwieterman, E. W., Early evolution of purple retinal pigments on Earth and implications for exoplanet biosignatures, *International Journal of Astrobiology,* **2018**, 1-10.

5. Berdyugina, S. V., Kuhn, J. R., Harrington, D. M., Šantl-Temkiv, T., Messersmith, E. J., Remote sensing of life: polarimetric signatures of photosynthetic pigments as sensitive biomarkers, *International Journal of Astrobiology,* **2016**, 15, 45-56.

6. Krissansen-Totton, J., Bergsman, D. S., Catling, D. C., On Detecting Biospheres from Chemical Thermodynamic Disequilibrium in Planetary Atmospheres, *Astrobiology,* **2016**, 16, 39-67.

7. Summons, R. E., Amend, J. P., Bish, D., Buick, R., Cody, G. D., Des Marais, D. J., Dromart, G., Eigenbrode, J. L., Knoll, A. H., Sumner, D. Y., Preservation of Martian Organic and Environmental Records: Final Report of the Mars Biosignature Working Group, *Astrobiology,* **2011**, 11, 157-181.

8. Bibring, J., Langevin, Y., Mustard, J. F., Poulet, F., Arvidson, R., Gendrin, A., Gondet, B., Mangold, N., Pinet, P., Forget, F., et al., Global Mineralogical and Aqueous Mars History Derived from OMEGA/Mars Express Data, *Science,* **2006**, 312, 400-404.

9. Kloprogge, J. T., Developments in Clay Science; Raman Spectroscopy of Clay Minerals (p.p. 150-99) **2017,** Elsevier Ltd, Amsterdam, the Netherlands.

10. Wiens, R. C., Maurice, S., Robinson, S. H., Nelson, A. E., Cais, P., Bernardi, P., Newell, R. T., Sharma, S. K., Deming, J., Beckman, D., et al., The SuperCam Instrument Suite on the NASA Mars 2020 Rover: Body Unit and Combined System Tests, *Space Science Reviews,* **2021**, 217, 4.

11. Maurice, S., Wiens, R. C., Bernardi, P., Caïs, P., Robinson, S., Nelson, T., Gasnault, O., Reess, J. M., Deleuze, M., Rull, F., et al., The SuperCam Instrument Suite on the Mars 2020 Rover: Science Objectives and Mast-Unit Description, *Space Science Reviews,* **2021**, 217, 47.

12. Radu, G. L., Badea, G. I., Carboxylic Acid - Key Role in Life Sciences, **2018**, IntechOpen, London, UK.

13. Jehlička, J., Edwards, H. G. M., Raman spectroscopy as a tool for the non-destructive identification of organic minerals in the geological record, *Organic Geochemistry,* **2008**, 39, 371-386.

14. Cloutis, E., Szymanski, P., Applin, D., Goltz, D., Identification and discrimination of polycyclic aromatic hydrocarbons using Raman spectroscopy, *Icarus,* **2016**, 274, 211-230.

15. Latorre, F., Guthmuller, J., Marquetand, P., A spectroscopic study of the cis/trans-isomers of penta-2,4-dienoic acid attached to gold nanoclusters, *Physical Chemistry Chemical Physics,* **2015**, 17, 7648-7658.

16. Jull, A. J. T., Beck, J. W., Burr, G. S., Isotopic evidence for extraterrestrial organic material in the Martian meteorite, Nakhla, *Geochimica Et Cosmochimica Acta,* **2000**, 64, 3763-3772.

17. Lin, Y., El Goresy, A., Hu, S., Zhang, J., Gillet, P., Xu, Y., Hao, J., Miyahara, M., Ouyang, Z., Ohtani, E., et al., NanoSIMS analysis of organic carbon from the Tissint Martian meteorite: Evidence for the past existence

of subsurface organic-bearing fluids on Mars, *Meteoritics & Planetary Science,* **2014**, 49, 2201-2218.

18. McDonald, G. D., Bada, J. L., A search for endogenous amino acids in the Martian meteorite EETA79001, *Geochimica Et Cosmochimica Acta,* **1995**, 59, 1179-1184.

19. De Gelder, J., De Gussem, K., Vandenabeele, P., Moens, L., Reference database of Raman spectra of biological molecules, *Journal of Raman Spectroscopy,* **2007**, 38, 1133-1147.

# Chapter 8
# SuperCam Raman Spectroscopy Assessment

*"Up in the sky! Look! It's a bird! It's a plane! It's SuperCam!"*

The Adventures of Superman*,* 1940*,* modified

As was explained in Chapter 1, *Introduction*, *SuperCam* is an instrument aboard NASA's *Perseverance* rover. In order to fulfill some of the different *Mars 2020* mission objectives, the instrument performs measurements of distant targets using Raman spectroscopy, laser-induced breakdown spectroscopy (LIBS), time-resolved luminescence spectroscopy (TRLS), visible and near infrared spectroscopy (VISIR), remote micro-imaging (RMI) and microphone recordings. A summary of the instrument characteristics and techniques can be found in Chapter 1, *Introduction*, as well as a more detailed description in literature (1-3). Due to the expertise in Raman spectroscopy that the IBeA research group has, proven by the new methodologies developed by the members of the group and the

numerous studies related to Mars and Martian samples (part of them presented in this PhD thesis), the IBeA research group has participated in several pre-launch activities and tasks related with the Mars 2020 mission and with *SuperCam*. These activities included (a) the analysis of some rocks as candidates to be included in the *SuperCam Calibration Target* (*SCCT*) and (b) the chemical verification of the calibration samples included in the *SCCT* (both works initiated in 2015, before the start of this PhD thesis). These activities ended in 2018 when the spare and flight models of the *SCCT* were delivered for integration.

Thanks to the collaboration of the IBeA research group with the *SuperCam* team, I participated as a PhD student of the science team of *SuperCam* in the scientific calibration process of the Flight Model (FM) of the Body Unit (BU) of *SuperCam* carried out at Los Alamos National Laboratory (LANL, USA). This calibration process was carried out prior to the delivery for its final integration in *Perseverance* at the Jet Propulsion Laboratory (JPL, Pasadena, USA).

Using the Raman spectroscopy results obtained during the scientific calibration process (see Chapter 3, *Instrumentation and Experimental Procedure*, for a description of the experimental setup), some parameters of the instrument were assessed. Regarding the spectral results, it must be pointed out that baseline correction or smoothing were not applied to any of the spectra presented in this chapter, in order to preserve the original signals and shape of the features.

## 1.1. Mineral Phases Identification

Using the setup and experimental conditions described in Chapter 3, *Instrumentation and Experimental Procedure*, 138 unique samples were analyzed to test the capabilities of the described setup of *SuperCam* to detect different mineral families by Raman spectroscopy, as well as to differentiate different minerals of the same family. Some of this samples

were prepared by the IBeA research group as a set of slabs (5x5 and 10x10 cm) from different rock samples, which were characterized by Raman spectroscopy, LIBS, ED-XRF and VISIR prior to their delivery to LANL.

Some of the Raman spectra obtained during the calibration process of *SuperCam* can be observed in Figure 8.1.

In Figure 8.1a-d the Raman spectra of apatite, $Ca_5(PO_4)_3(F, Cl, OH)$, barite, $BaSO_4$, calcite, $CaCO_3$, and nitratine, $NaNO_3$, are shown. They belong to the phosphate, sulfate, carbonate and nitrate groups of minerals, respectively. These mineral families present similar Raman spectra, where their most intense feature appears in the 950-1100 $cm^{-1}$ spectral range and their secondary bands are located at lower wavenumbers. In addition, the spectrum of a silica polymorph, quartz, $SiO_2$, was also collected (Figure 8.1e). Finally, the spectra of three relevant silicate families for the study of Mars were obtained. In Figure 8.1f and Figure 8.1g the Raman spectra of diopside, $CaMgSi_2O_6$, and olivine, $(Mg, Fe)_2SiO_4$, can be seen, respectively. They belong to two different silicate groups, inosilicates and nesosilicates, and are present in Mars, usually in igneous rocks. Talc (Figure 8.1h), $Mg_3Si_4O_{10}(OH)_2$, in contrast, is a phyllosilicate and a secondary mineral formed from magnesian primary minerals in the presence of $CO_2$ and water.

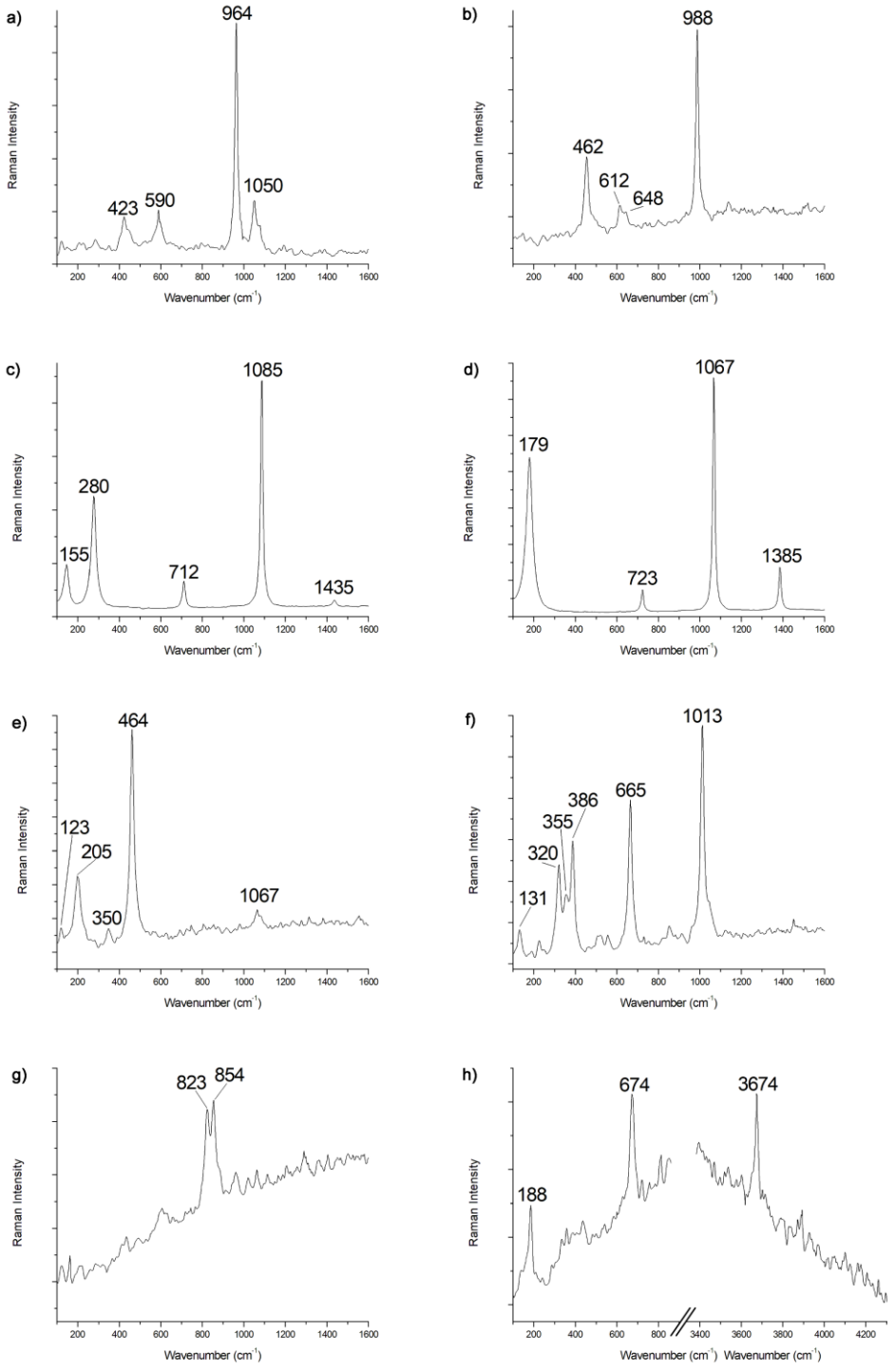


Figure 8.1. Minerals analyzed by Raman spectroscopy with *SuperCam*, a) apatite, b) barite, c) calcite, d) nitratine, e) quartz, f) diopside, g) olivine and h) talc

As observed, *SuperCam* is able to identify by Raman spectroscopy relevant minerals for the study of Mars. The obtained Raman spectra are well resolved, even their secondary signals. This fact implies that *SuperCam* is able to differentiate among phosphates, sulfates, carbonates, nitrates, silica polymorphs and silicates. In addition, *SuperCam* is also capable to differentiate between very similar minerals of the same mineral group, as was observed in the case of calcite and dolomite, $CaMg(CO_3)_2$, thanks to its spectral resolution (around 10 $cm^{-1}$ for the 150-1500 $cm^{-1}$ Raman region). They both belong to the carbonates mineral family and are differentiated by their elemental compositions, where dolomite has half the calcium of calcite substituted by magnesium. As can be observed in Figure 8.2, *SuperCam* is able to differentiate the dolomite from calcite, even though their spectra are very similar.

The fact that the instrument is able to discern between minerals with a very similar Raman spectrum is a big advantage since, for example, in the case of calcite and dolomite, the presence of one or the other has different implications for the possible presence of past life (4).

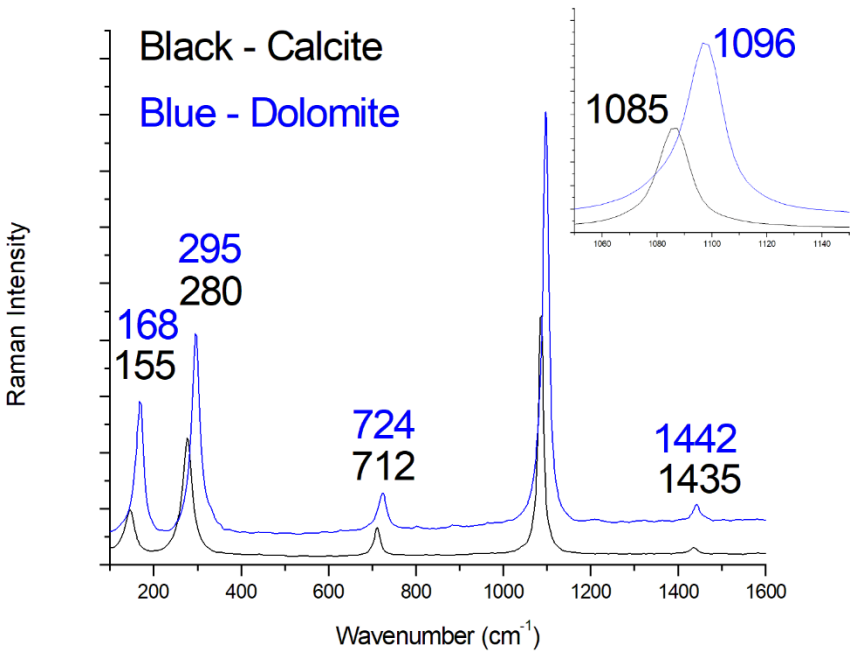


Figure 8.2. Raman spectrum of calcite (black) and dolomite (blue) obtained with *SuperCam*

In order to validate the results of *SuperCam*, the spectra obtained from the analyses of calcite, carried out at LANL, were compared with the ones obtained from the same sample using a high-end benchtop Raman spectrometer (Invia, by Renishaw), at the facilities of the IBeA research group. As can be observed in Figure 8.3, the spectrum obtained with *SuperCam* has identical Raman signal positions to the ones obtained with the benchtop spectrometer. In addition, it has almost the same quality regarding signal-to-noise ratio, which is a very positive fact taking into account that *SuperCam* is a remote instrument that uses a pulsed laser (532 nm) and the Invia uses a continuous wavelength excitation laser (532 nm) and a confocal microscope to perform the analyses.

Finally, it was observed that the width of the signals of the spectra obtained with *SuperCam* were slightly wider than the ones obtained with the Invia instrument. In order to check if the widening was constant for all the signals

or if it was affecting the relative intensities of the Raman features, a curve fitting was carried out with the signals at 280, 712 and 1085 $cm^{-1}$ for the results of both instruments. Then, the relative intensity of each signal compared to the most intense one, at 1085 $cm^{-1}$, was calculated by dividing the area of each band between the area of the main band of the spectrum. For the 280, 712 and 1085 $cm^{-1}$ signals, the relative intensities were 0.40:0.11:1 for the Invia, and 0.44:0.11:1 for the spectrum of *SuperCam*. The fact that the relative intensities of the spectra are almost identical indicates that the slight widening of the bands is constant and does not affect the relative intensities. Thus, this parameter could be used to help in the characterization of some minerals or to assess the health of the instrument through time using the on-board calibration targets, since the relative intensities should remain constant for the samples, both the ones from the calibration targets and the unknown ones from Mars.

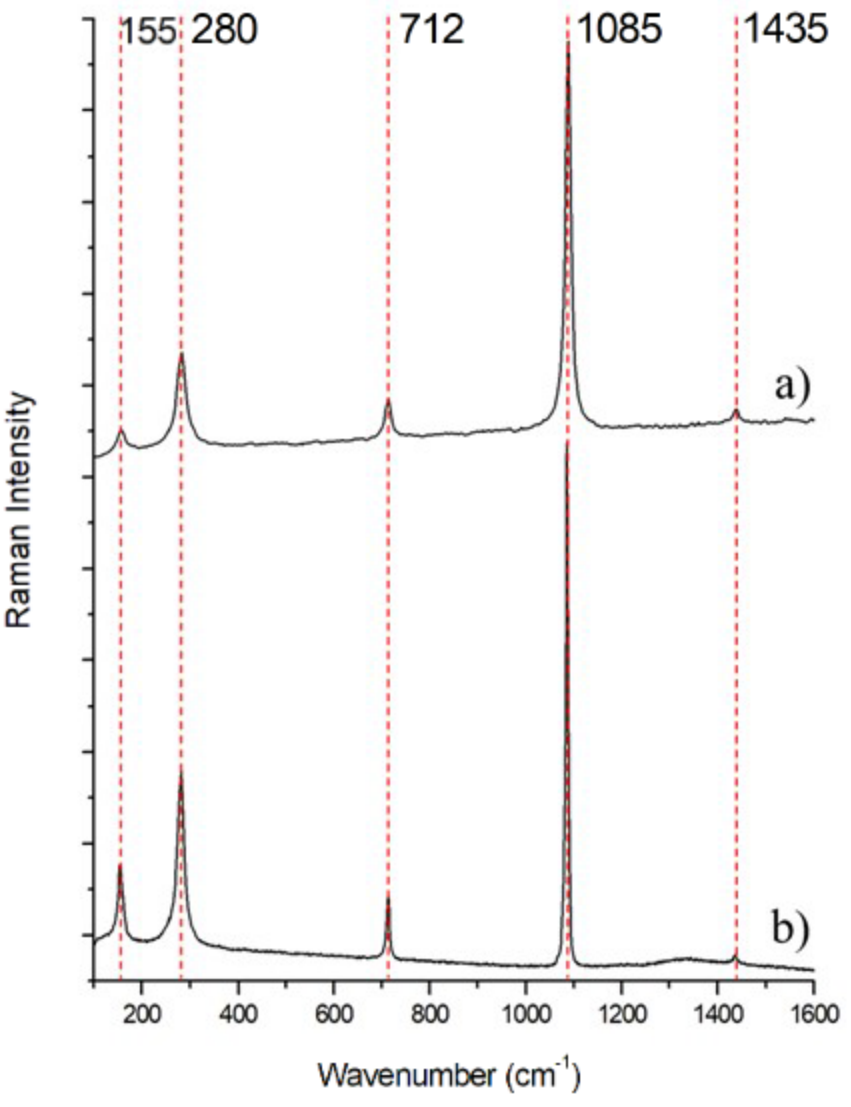


Figure 8.3. Raman spectra of the same calcite sample collected with a) *SuperCam* and b) Invia using the 532 nm excitation laser

In addition to assessing the capabilities of *SuperCam* to perform Raman spectroscopy compared to those of a high-end benchtop instrument, other quality parameters were also evaluated. In this sense, the reproducibility of the Raman results of the instrument among five different days was checked. This test was carried out with calcite (8 spectra), gypsum (9 spectra), apatite (6 spectra), quartz (6 spectra) and talc (4 spectra). The aim was to check the variability of the wavenumber position of the signals,

which is an essential parameter in order to identify and differentiate minerals of the same geological group. In Table 8.1, the average wavenumber position for the main Raman signals for each mineral, their standard deviation for the different measurements and the respective relative standard deviation (RSD) are presented.

Table 8.1. Average signal position, standard deviation and RSD of the main Raman band position of the studied minerals for the reproducibility test

| Mineral | Average signal position ($cm^{-1}$) | Standard deviation ($cm^{-1}$) | RSD (%) |
|---|---|---|---|
| Calcite | 1085 | 0.47 | 0.43 |
| Gypsum | 1008 | 0.091 | 0.0092 |
| Apatite | 964 | 1.6 | 0.17 |
| Quartz | 464 | 2.2 | 0.47 |
| Talc | 188 | 0.77 | 0.41 |

As can be observed, under the cleanroom conditions at which these analyses where performed, the RSD of the main band position was always lower than 1 %. In other words, the results from the Raman spectra of *SuperCam* presented almost no variation among several days for the tested minerals, regardless of its mineral group.

However, on Mars some parameters that were stable in the laboratory, such as the temperature of the instrument, will vary more, which could imply variations in the spectral results. This important fact means that these variations caused by the temperature of the instrument will have to be taken into account to correct the collected spectra on Mars. Fortunately, this temperature is one of the many parameters measured by *Perseverance*.

## 1.2. Organic Compounds Detection

In addition to all the measurements of minerals that were carried out with *SuperCam* during the calibration process at LANL, its capabilities to identify

and characterize possible organic compounds on Mars were also tested. In order to do that, a set of samples provided by Dr. Teresa Fornaro (Astrobiology Laboratory, Arcetri Astrophysical Observatory, Florence, Italy) was analyzed. The samples were prepared in the laboratory by adsorbing four different organic compounds separately on olivine, as a representative mineral of the surface of Mars. The four organic compounds tested were adenosine 5'-monophosphate, L-glutamic acid, L-phenylalanine and phthalic acid, which were adsorbed on the olivine in different known concentrations, 5 wt%, 1 wt% and 0.1 wt%. In addition, the olivine where the organic compounds were adsorbed was doped with 1 wt% of Mg-perchlorate to simulate the Martian aggressive conditions for organic compounds preservation, since this Mg-perchlorate is present in Mars and could cause the oxidation of organic molecules. A more detailed description of the preparation of this kind of samples can be found in literature (5).

As happened with the inorganic samples tested at LANL, the pure organic compounds analyzed with *SuperCam* had well resolved spectra. All their main and secondary bands had good intensity and the signal-to-noise ratio was even better than the observed with mineral phases. As an example, in Figure 8.4 the spectrum of the pure phthalic acid is presented, where its Raman signals at 127, 160, 211, 372, 433, 545, 642, 692, 771, 1006, 1045, 1143, 1175, 1263, 1302, 1426, 1496, 1589, 1640, 2612, 2879, 3086 and 3169 $cm^{-1}$ can be observed.

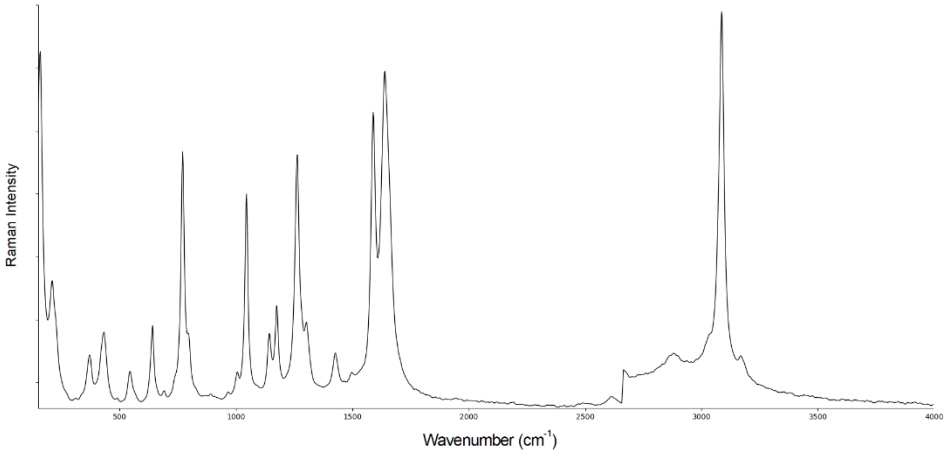


Figure 8.4. Raman spectrum of pure phthalic acid obtained with *SuperCam*. For clarity, the wavenumber positions of the signals are described in the text

Regarding the results for the different concentrations, at 5 wt% concentration the main Raman signals of the molecules were visible in the spectra. As an example, Figure 8.5 shows the Raman spectrum of Adenosine 5'-monophosphate at 5 wt%. As is observed, the Raman signals related to the C-H stretching vibrations (2884 and 2021 $cm^{-1}$) and the $-NH_2$ wagging vibration (432 $cm^{-1}$) have enough intensity to be differentiated from the noise of the spectrum. In fact, the intensity of these three bands is similar to the ones of olivine, around 830 $cm^{-1}$ (note that in this particular case the doublet of the olivine is not well resolved and the signal appears as a single wide band).

Unluckily, the four organic compounds tested were no longer detected in the Raman spectrum of the 1 wt% and 0.1 wt% samples. This fact means that if the laser of *SuperCam* hits an organic "hotspot" in a rock or in a soil from a given distance, it will be able to detect it as long as it has a concentration around 5 wt% or higher in the laser spot area, which at 2 m of distance is of around 1.5 mm, or 0.74 mrad, of diameter. Thus, organic compounds that are not uniformly distributed, forming "hotspots" in cavities of rocks, might have enough concentration in the laser spot size to be detectable by the Raman of *SuperCam*.

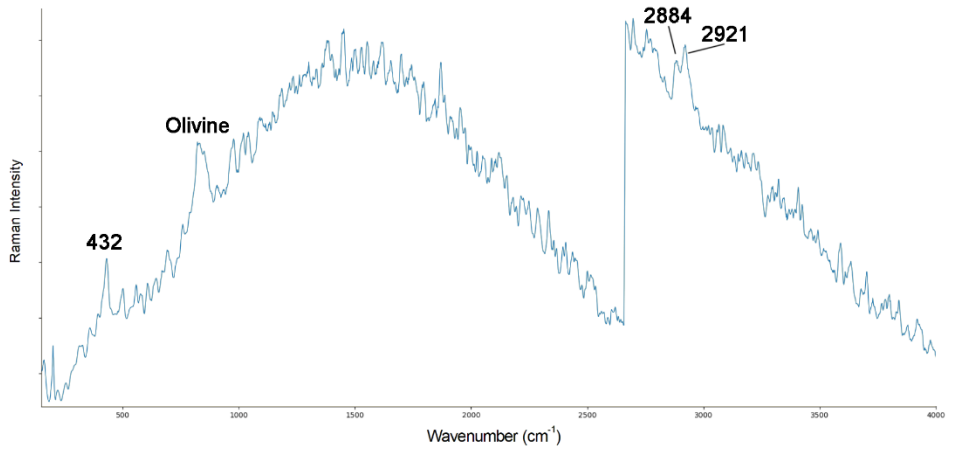


Figure 8.5. Raman spectrum obtained with *SuperCam* of Adenosine 5'-monophosphate adsorbed in an olivine matrix at a 5 wt% of concentration

## 1.3. Conclusions

In this chapter of the PhD thesis the capabilities of *SuperCam* for performing Raman spectroscopy were tested. This was done with the results obtained from the calibration process carried out at LANL (March-April 2019) before the delivery of the Flight Model (FM) to the Jet Propulsion Laboratory (JPL) for the integration of the instrument in the rover. As has been explained throughout the chapter, the Raman spectra of the most relevant mineral groups for the study of Mars had promising Raman results when analyzed with *SuperCam*. More specifically, the mineral families of phosphates, sulfates, carbonates, nitrates, silica and silicates were tested at a distance of 2 m from the instrument. The results obtained allowed to conclude that *SuperCam* is able to differentiate by Raman spectroscopy with very high reproducibility not only mineral groups with very similar Raman spectra, but polymorphs and minerals of the same family that have almost identical spectra. This fact is of great relevance for the study of Mars, since in some cases the presence of one or other mineral could imply different conclusions about the environment or formations conditions, as is the case of the presence of calcite or dolomite.

In addition to mineral phases, it was also tested the capabilities of *SuperCam* to identify organic compounds by Raman spectroscopy. Even though the organic molecules used for this test may not be relevant for Mars (e.g., finding Adenosine 5'-monophosphate on Mars is not a probable scenario), it was proven that *SuperCam* is able to detect organic compounds at a 5 wt% of concentration in a mineral matrix related to the planet in the specific conditions of this test. This fact is very significant taking into account that one of the main objectives of the *Mars 2020* mission is to find biosignatures and habitable conditions on Mars in the ancient past, more specifically, inside and in the surroundings of the Jezero crater.

## 1.4. Bibliography

1. Wiens, R. C., Maurice, S., Robinson, S. H., Nelson, A. E., Cais, P., Bernardi, P., Newell, R. T., Sharma, S. K., Deming, J., Beckman, D., et al., The SuperCam Instrument Suite on the NASA Mars 2020 Rover: Body Unit and Combined System Tests, *Space Science Reviews,* **2021**, 217, 4.

2. Maurice, S., Wiens, R. C., Bernardi, P., Caïs, P., Robinson, S., Nelson, T., Gasnault, O., Reess, J. M., Deleuze, M., Rull, F., et al., The SuperCam Instrument Suite on the Mars 2020 Rover: Science Objectives and Mast-Unit Description, *Space Science Reviews,* **2021**, 217, 47.

3. Manrique, J. A., Lopez-Reyes, G., Cousin, A., Rull, F., Maurice, S., Wiens, R. C., Madsen, M. B., SuperCam Calibration Targets: Design and Development, *Space Science Reviews,* **2020**, 216, 138.

4. Baker, P. A., Kastner, M., Constraints on the Formation of Sedimentary Dolomite, *Science,* **1981**, 213, 214-216.

5. Fornaro, T., Brucato, J. R., Poggiali, G., Corazzi, M. A., Biczysko, M., Jaber, M., Foustoukos, D. I., UV Irradiation and Near Infrared Characterization of Laboratory Mars Soil Analog Samples, *Frontiers in Astronomy and Space Sciences,* **2020**, 7.

# Chapter 9
# Methodology Development and Testing for the Mars Returning Samples

*"Mars is there, waiting to be reached"*

Buzz Aldrin, 2008

As explained in Chapter 1, *Introduction*, Perseverance carries 43 sampling tubes that will house the samples that the rover will collect from the surface of Mars. These tubes form part of the Mars Sample Return (MSR) mission efforts and they will be brought back to Earth in the future. The scientific value that these samples will have once they reach Earth is easily imaginable, as they will be the first samples we get directly from another planet. For this reason, how and in which form they are analyzed is of great relevance, as if they are consumed, altered or destroyed, it is not known

when we will get new ones again. For this reason, non-sample consuming and non-destructive analysis techniques, in which the materials do not suffer any type of alteration, should be the first techniques to be used on the returning samples. Among all the existing techniques, Raman spectroscopy is one of those that offers the most information about the sample. Proof of this is that the latest Mars missions carrying a rover to Mars have at least one instrument capable of Raman analysis. As we have seen throughout this PhD thesis, this technique is not only useful for the molecular and mineralogical characterization of the samples, which is already very relevant information in itself, but it can also provide additional information indirectly through calibration models. To test the capabilities of this technique, in combination with other non-destructive complementary techniques, 3 meteorites of different nature, to test the effects of different matrixes, have been analyzed: the Martian nakhlite Northwest Africa 6148, the meteorite from 4 Vesta Elephant Moraine 83227 and the Martian shergottite Dar al Gani 735.

## 9.1. Northwest Africa 6148

The Northwest Africa (NWA) 6148 is a Martian meteorite classified as a nakhlite. Nakhlites are igneous rocks formed from basaltic magma that are usually rich in augite. Their secondary mineral is usually olivine and it is thought that they were formed in Tharsis Elysium or Syrtis Major Planum (1). The analyses that have been carried out in nakhlites in the last years have progressively increased in number due to the information that can be deducted of Mars through them. However, one of these nakhlites, NWA 6148, has been scarcely studied. In fact, besides the study described in this PhD thesis, the only works which analyzed this meteorite were focused on the germanium dichotomy of meteorites (2) and its siderophile and chalcophile element abundances (3). Due to this fact, during the study of this meteorite not only the future analysis methodologies for the Martian returning samples were tested, but its study also clarified the geochemical composition of the NWA 6148.

As it is stated in the Meteoritical Bulletin nº 102 (4), the NWA 6148 was found in the region of Northwest Africa and its fall was not observed. This meteorite was first documented in 2009, when A. Aaronson bought two stones that fitted together from a meteorite dealer in Erfoud, Morocco. It is possibly paired with meteorite NWA 5790, although there are not studies that confirm nor deny this fact.

The analyzed sample consisted of a portion of the original NWA 6148, which weighed 270 g. The analyzed sample dimensions are about 5 x 7 x 3 mm, it weighs 0.246 g (0.09% of the original meteorite mass) and it is a fragile rock without visible impact crust, which means it was obtained from the inner part of the NWA 6148. The sample is brownish with several greenish, black and light brown areas (Figure 9.1).

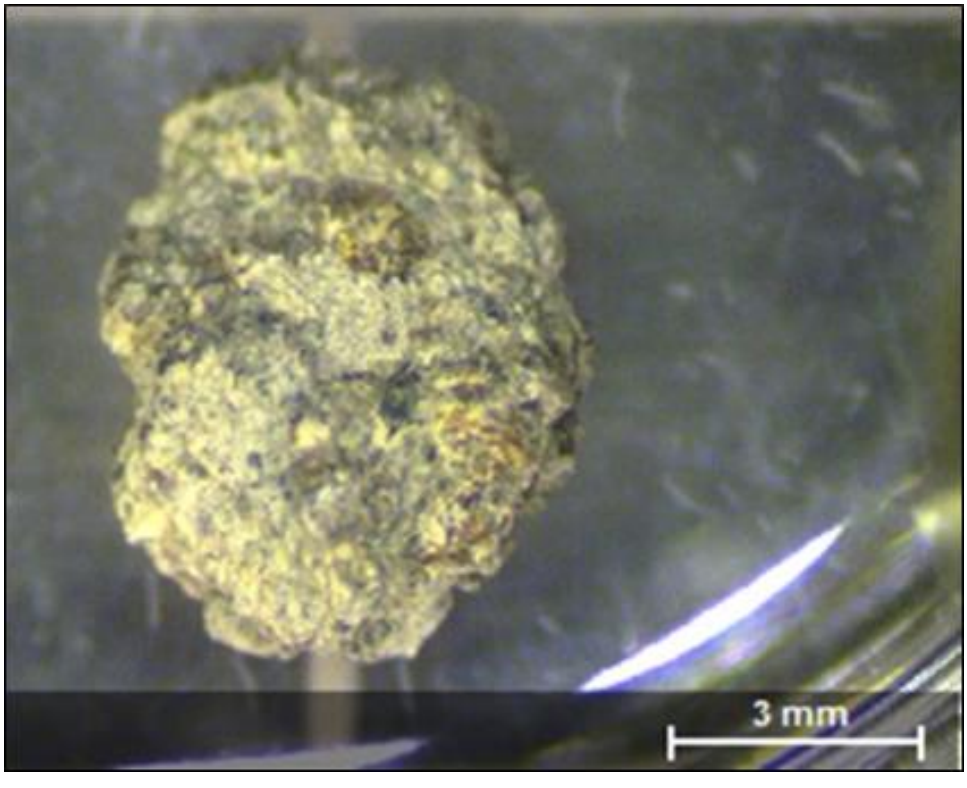


Figure 9.1. NWA 6148 picture, where different mineral grains with different colorations can be observed

In order to avoid analyzing possible contaminations of the surface of the sample previous to the handling in the laboratory, the specimen was split and only the inner parts of the sample were analyzed.

During the analysis of the NWA 6148 meteorite, by means of Raman spectroscopy it was found that the matrix of the sample was formed mainly of augite, (Ca, Na)(Mg, Fe, Al, Ti)(Si, $Al)_2O_6$, as it is usual in nakhlites (1) (Figure 9.2). Pyroxene is usually characterized by the Si-O bridging vibration mode at 1011 $cm^{-1}$, the Si-O bending mode at 665 $cm^{-1}$ and the Metal-O stretching vibration mode in the 300-400 $cm^{-1}$ range (322 $cm^{-1}$ for the Fe-O, 354 $cm^{-1}$ for the Ca-O and 390 $cm^{-1}$ for the Mg-O). This mineral is usually defined by its content of Fe, Mg and Ca, given as ferrosilite (Fs, $Fe_2Si_2O_6$), enstatite (En, $Mg_2Si_2O_6$) and wollastonite (Wo, $Ca_2Si_2O_6$), respectively. Depending on the proportions of each element in the augite, the position of the signals of the Raman spectra changes accordingly.

E. Huang et. al. (5) published a work about the different stretching and bending modes of different pyroxenes and how they affect the Raman band position. They found that some bands positions are correlated to the different proportions of the metals present in this mineral phase. Moreover, they observed that the major-element composition of the (Mg, Fe, Ca)-pyroxenes can be semi-quantitatively determined on the basis of these band position shifts. Based on this information and the different pyroxenes analyzed in that work, the Fe, Ca and Mg proportions of the augite present in the NWA 6148 meteorite were calculated by comparison with their results. Experimentally, all the Raman spectra of augite grains obtained from this meteorite had the same signals' positions, which led to think that there was only a single metal composition of augite in the analyzed NWA 6148 sample. The results obtained were $En_{34}Fs_{16}Wo_{50}$ for the Mg, Fe and Ca, respectively. The confidence intervals for this result cannot be calculated as E. Huang et al. (5) did not provide them in their work.

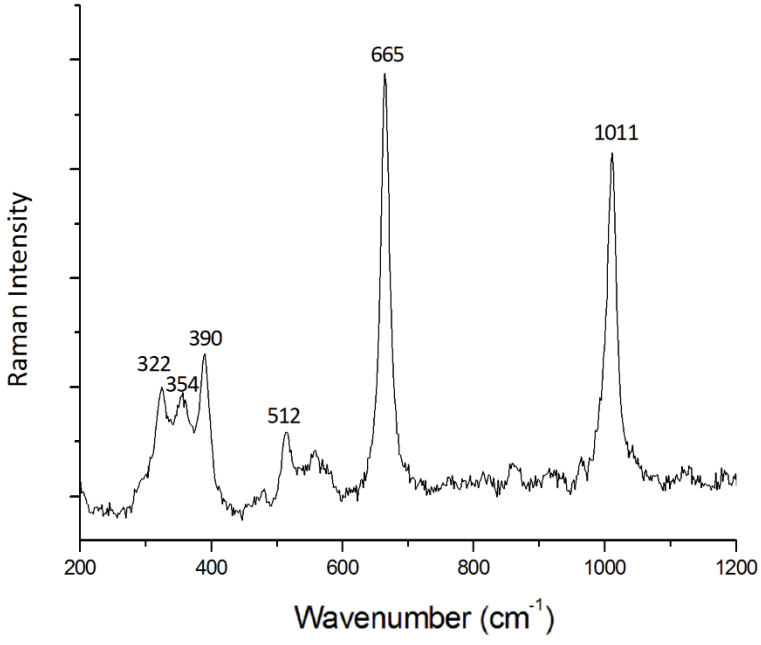


Figure 9.2. Augite Raman spectrum found in the matrix of the NWA 6148 meteorite, obtained with the 785 nm excitation laser

In order to contrast this result, the work by A. Wang et al. (6) was used. They made a multiple linear regression (MLR), which correlates $X_{Mg^{2+}}$ and $X_{Ca^{2+}}$ to the Raman band position of 665 cm$^{-1}$ ($v_2$) for Equation 9.1, and to the Raman band position of 332 cm$^{-1}$ ($v_3$) for Equation 9.2. Both Equations form a system, where $X_{Mg^{2+}}$ and $X_{Ca^{2+}}$ are the unknown quantities that must be solved. The results obtained by means of this regression using the experimental Raman spectra for the augite present in the analyzed NWA 6148 meteorite were $En_{26\pm3}Fs_{36\pm4}Wo_{38\pm4}$.

$$v_2 = (31.9 \pm 2.2)X_{Mg^{2+}} - (7.7 \pm 4.8)X_{Ca^{2+}} + 655.0 \pm 1.5 \quad \textit{Equation 9.1 (6)}$$

$$v_3 = (51.7 \pm 2.6)X_{Mg^{2+}} + (20.5 \pm 5.9)X_{Ca^{2+}} + 297.3 \pm 1.9 \quad \textit{Equation 9.2 (6)}$$

Here, $v_2$ and $v_3$ are the Raman spectrum features at 665 $cm^{-1}$ and 322 $cm^{-1}$, respectively, $X_{Mg^{2+}}$= [moles $Mg^{2+}$/ (moles $Mg^{2+}$ + moles $Fe^{2+}$ + moles $Ca^{2+}$)] and $X_{Ca^{2+}}$= [moles $Ca^{2+}$/ (moles $Mg^{2+}$ + moles $Fe^{2+}$ + moles $Ca^{2+}$)]

Besides the results obtained through these two works with the augite spectra obtained experimentally, in the Meteoritical Bulletin Database it is stated that the augite metal composition for the NWA 6148 is $En_{35}Fs_{23}Wo_{42}$ (4).

As it can be observed, the three results obtained of the augite composition (from Huang et al. work (5), $En_{34}Fs_{16}Wo_{50}$; Wang et al. work (6), $En_{26\pm3}Fs_{36\pm4}Wo_{38\pm4}$; and the Meteoritical Bulletin Database (4), $En_{35}Fs_{23}Wo_{42}$) have significant differences. To check which one of these sources was more reliable, a SEM-EDS imaging analysis was carried out in five augite grains, which were also measured by the Raman spectrometer through the SCA interface. The obtained results (Table 9.1) were compared with the ones previously mentioned (Figure 9.3).

Table 9.1. Concentrations of Mg, Fe and Ca that form the augite of the NWA 6148 observed by EDS and the ones obtained from literature

| | $X^{Mg}$ | $X^{Fe}$ | $X^{Ca}$ |
|---|---|---|---|
| **Grain 1 (EDS)** | 24.8 ± 3.2 | 35.6 ± 2.8 | 39.6 ± 2.6 |
| **Grain 2 (EDS)** | 33.5 ± 2.0 | 26.2 ± 1.4 | 40.3 ± 1.5 |
| **Grain 3 (EDS)** | 29.6 ± 0.8 | 29.2 ± 0.7 | 41.2 ± 0.7 |
| **Grain 4 (EDS)** | 24.9 ± 2.0 | 43.8 ± 1.8 | 31.3 ± 1.4 |
| **Grain 5 (EDS)** | 21.9 ± 1.1 | 39.0 ± 1.0 | 39.2 ± 0.9 |
| **Average Value (EDS)** | 26.9 ± 4.4 | 34.8 ± 3.9 | 38.3 ± 3.5 |
| **Huang et. al.** | 34 | 16 | 50 |
| **Wang et. al.** | 26 ± 3 | 36 ± 4 | 38 ± 4 |
| **M. Bulletin** | 35 | 23 | 42 |

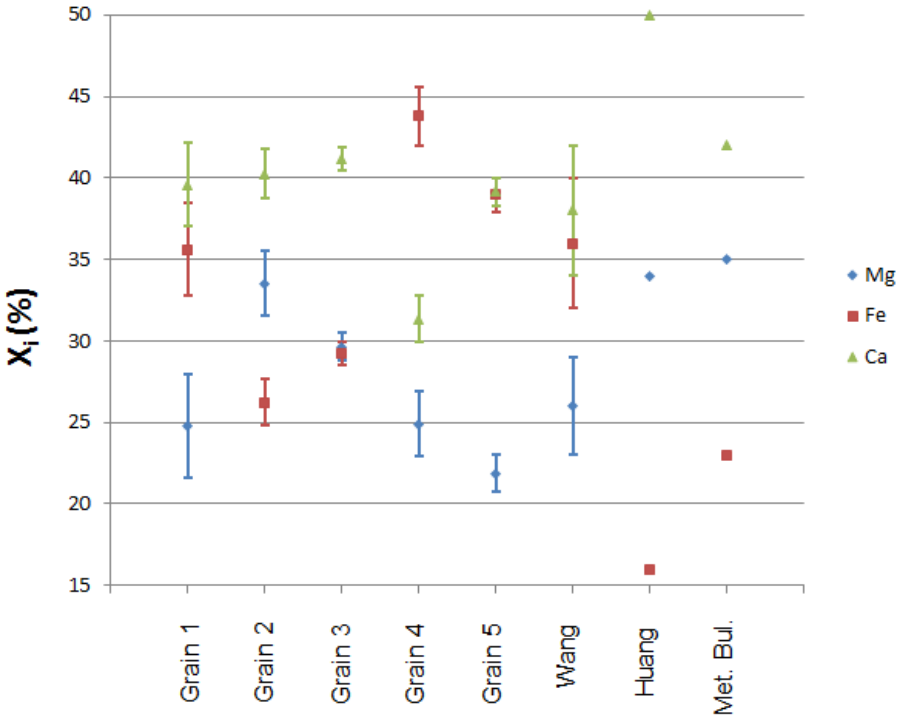


Figure 9.3. Representation of $X_i$ (where X = [moles i/ (moles Mg + moles Fe + moles Ca)] and i = Mg, Fe, Ca) for the 5 augite grains measured by EDS and for the results obtained through the works of Huang et al.(5), Wang et al. (6) and the Meteoritical Bulletin Database (4)

As it can be observed, the different augite grains measured by EDS have a high dispersion. Since all the EDS analyses were performed with a set excitation energy of 20 keV, this parameter was not the source of the variability.

This dispersion was not observed when the metal composition of the augite was calculated through Raman spectroscopy, as the Raman spectra obtained from the sample had constant band positions. However, the obtained average value of the 5 grains for each metal, $En_{60.2\pm4.4}Fs_{22.8\pm2.3}Wo_{17.0\pm1.7}$ (Table 9.1), where the confidence interval was calculated at a 95 % of confidence and using the standard deviation of the five measured areas, are equal to the ones calculated using the work by Wang et al. (6). This fact meant that this work provided the best results for the augite composition of the meteorite NWA 6148 specimen in terms of

accuracy. In addition, the uncertainties associated with the results obtained through the equation of Wang et. al. (6) are very similar for the ones obtained by SEM-EDS, which means that the augite composition variability is also correctly estimated using the Raman methodology.

Olivine, $(Mg, Fe)_2SiO_4$, was also found in the specimen as the second more relative abundant mineral. It was observed that the olivines had spectral variations from one spectrum to another (Figure 9.4). The observed range for the primary olivine Raman signatures were 817-819 $cm^{-1}$ (DB1) and 841-847 $cm^{-1}$ (DB2). These two signals correspond to the symmetric $v_1$ and asymmetric $v_3$ stretching vibrations of the $SiO_4$ tetrahedra. Some secondary bands were also recorded, such as the one at 909 $cm^{-1}$ attributed to $v_3$ derived vibrations and at 522 $cm^{-1}$, assigned to the asymmetric deformation $v_4$ of the $SiO_4$.

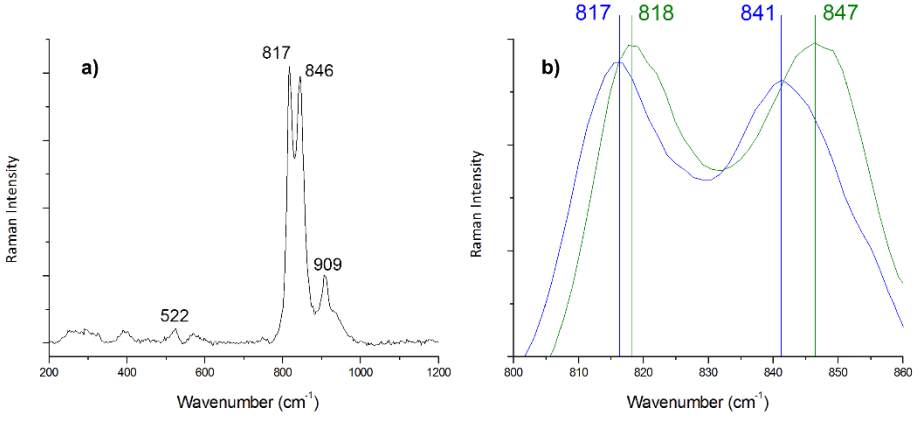


Figure 9.4. a) Olivine Raman spectrum from the NWA 6148 meteorite, obtained with the 532 nm excitation laser, and b) a zoom in of the 800-860 $cm^{-1}$ range of the spectrum, where the wavenumber shifts in two of the different olivine spectra detected in the studied sample are observed

Using the calibration curves developed in Chapter 5, *Forsterite and Fayalite Content in Olivines*, it was calculated that the metallic composition of the olivines present in the NWA 6148 meteorite had a range of $Fo_{22.6\pm3}Fa_{77.4\pm3}$ – $Fo_{51.5\pm3}Fa_{48.5\pm3}$, where the confidence interval is given as the uncertainty coming from the calibration curves. As it can be observed, the olivines

present in the sample had, for the most part of the range, a higher content of iron than magnesium, which corresponds to the usual proportions found in nakhlites (1). Furthermore, the composition that is stated in literature for the NWA 6148 is $Fo_{42.0}Fa_{58.0}$ for the core of grains of olivine and $Fo_{25.5}Fa_{74.5}$ for the rims of the grains (4). Experimentally, it was not possible to differentiate the cores and the rims of the grains of the analyzed olivine. However, olivines with the richest iron content found experimentally ($Fo_{22.6\pm3}Fa_{77.4\pm3}$) match perfectly with the composition of the olivines in the rims observed in the literature ($Fo_{25.5}Fa_{74.5}$). This high concentration of iron in the olivine usually decreases gradually over time until reaching the center of the core of the grain, which would explain the presence of different proportions of Fe and Mg found in the sample. For these olivine grain cores, where the highest amount of Mg is found in the mineral phase, the composition found experimentally ($Fo_{51.5\pm3}Fa_{48.5\pm3}$) differs significantly from the one pointed out in the literature ($Fo_{42.0}Fa_{58.0}$). This difference could be explained because the NWA 6148 nakhlite is heterogeneous in the composition of this mineral phase, thus, olivine with a higher content of Mg could have been found in the cores of the grains in the studied meteorite fragment.

Regarding other nakhlites, in the literature there is no mention of any other nakhlite olivine grains with a higher content of Mg than the ones found during the analysis of the NWA 6148 (1). In consequence, this meteorite would become the nakhlite with the highest amount of magnesium in the core of its olivine grains, with a 51.5 %. The second one would be the NWA 817, with a 43 % of magnesium in the core of its olivine grains (7). As it can be seen, there exists a notable difference between both compositions, which could lead to think that some nakhlites may have more magnesium content in olivines than what it was thought when they were first studied.

The distribution of Mg in the olivine grains is related to the element diffusion during the solidification and crystallization process of the magma from which the mineral was formed. The fact that different olivine compositions

have been found in different meteorites leads to think that the crystallization of that magma was not homogeneous. This fact would mean that the magma had different zones that crystallized faster than others, leading to different element diffusion among the formed mineral phases. In this case, the high Mg content would mean larger and sharper olivine grains (1).

In addition to the common mineral phases of nakhlites (augite and olivine), more minerals were found in the NWA 6148 analyzed fragment. By means of the SEM-EDS coupled to the Raman system though the SCA interface, the presence of cobalt was noticed in some small and isolated areas of one of the meteorite fragments (Figure 9.5). Cobalt was not distributed homogeneously through the area, something that would be observed if this element appeared as substitutional metal atoms in crystallographic defects of other mineral phases. Both facts led to think that the analyzed area was composed of at least one compound where the cobalt was the main metal, as its distribution was neither homogeneous nor large. Using the Raman spectrometer coupled to the SEM-EDS system, the Raman spectrum of the area rich in cobalt was obtained (Figure 9.5). In the collected experimental spectrum it can be observed the band attributed to the stretching vibrations of the oxygen atoms inside the octahedral unit $Co(III)O_6$ (691 $cm^{-1}$) and the bands assigned to the second $F_{2g}$ symmetry mode (482 $cm^{-1}$ and 521 $cm^{-1}$). These three signals coincide with the main and the two most intense secondary Raman-active modes of the $Co_3O_4$ (8).

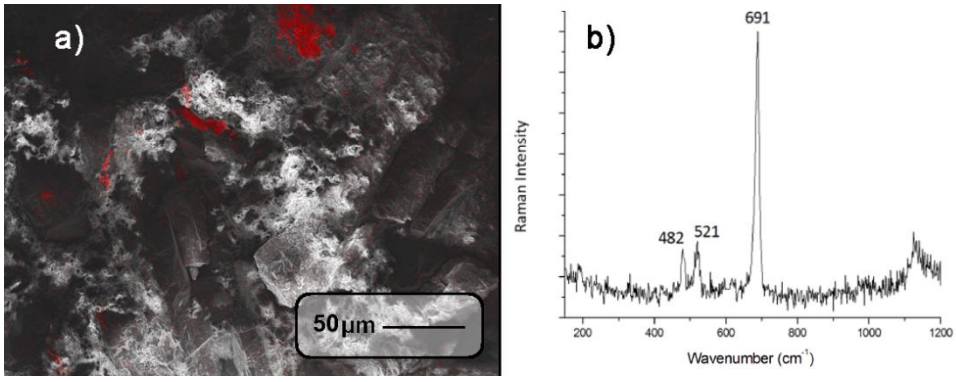


Figure 9.5. a) SEM image of the surface of a fragment of the NWA 6148 and its Co presence (EDS intensity of the Co represented in red) and b) Raman spectrum of the Co rich area obtained through the SCA interface with the 514 nm excitation laser

A larger area (200 x 150 µm) was analyzed with the Renishaw Invia micro-spectrometer doing both punctual analysis and mapping. It was found that in the same mineral grain $Co_3O_4$ and augite were present simultaneously (Figure 9.6).

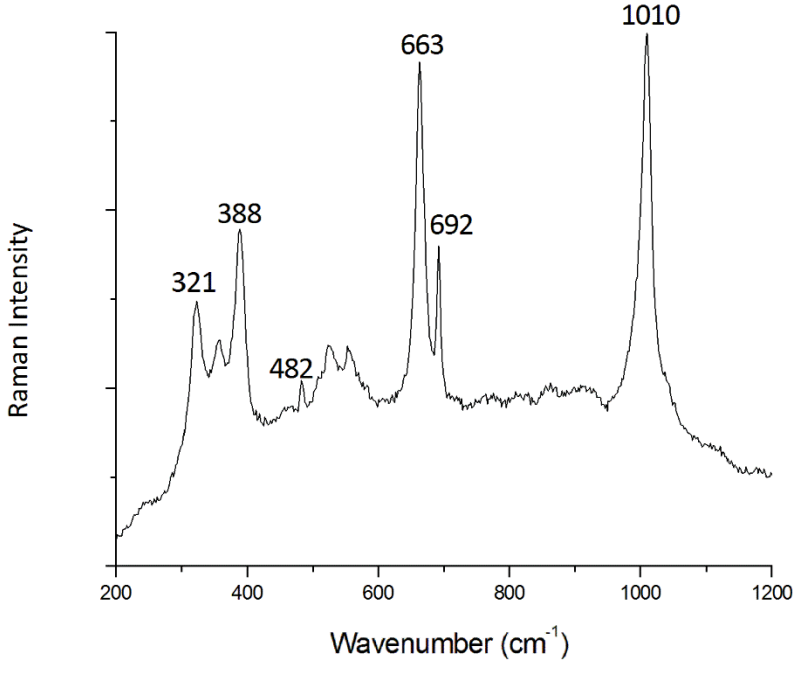


Figure 9.6. Raman spectrum of a $Co_3O_4$ rich area in which both augite and the cobalt oxide can be observed in the spectrum, obtained with the 532 nm excitation laser

In addition to the SEM-EDS and Raman analyses, TOF-SIMS was carried out to determine the origin (Martian or terrestrial) and characteristics of this compound, using for that purpose the $^{16}O/^{17}O$ and $^{16}O/^{18}O$ isotopic ratios. Once the fragment that contained the cobalt oxide detected by Raman spectroscopy was extracted (Figure 9.7), its surface was analyzed using the TOF-SIMS, obtaining the results shown in Table 9.2. Unfortunately, not all the surface was mapped properly due to its irregular topography at nanoscale.

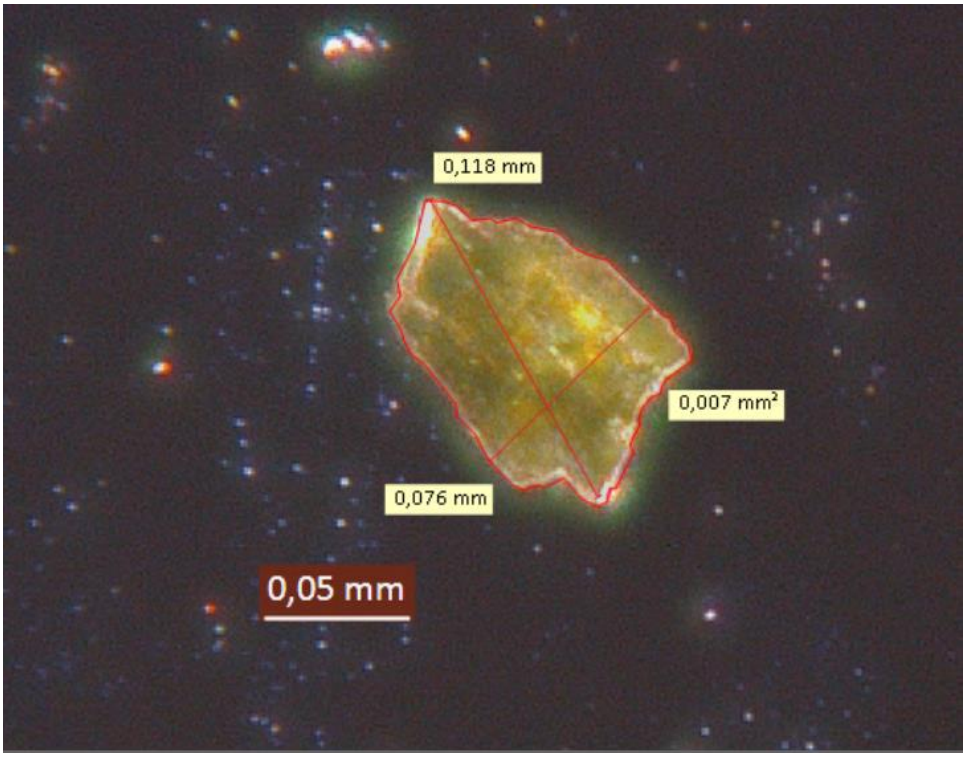


Figure 9.7. Optical image of the extracted fragment from the NWA 6148 sample, where the cobalt oxide was observed by Raman spectroscopy

Table 9.2. Abbreviated table of ions detected by TOF-SIMS in positive polarity in the meteorite fragment containing the $Co_3O_4$

| Center Mass (u) | Assignment | Resolution | Area | Norm. By Total Ion Intensity |
|---|---|---|---|---|
| 15,99 | O+ | 4527 | 1298 | $2{,}063 \cdot 10^{-4}$ |
| 22,99 | Na+ | 5197 | 199440 | $3{,}171 \cdot 10^{-2}$ |
| 23,98 | Mg+ | 5044 | 80424 | $1{,}279 \cdot 10^{-2}$ |
| 26,98 | Al+ | 5484 | 104514 | $1{,}662 \cdot 10^{-2}$ |
| 27,04 | C_2H_3+ | 7761 | 38886 | $6{,}182 \cdot 10^{-3}$ |
| 27,98 | Si+ | 4905 | 75946 | $1{,}207 \cdot 10^{-2}$ |
| 38,96 | K+ | 6429 | 309333 | $4{,}918 \cdot 10^{-2}$ |
| 39,96 | Ca+ | 5334 | 270564 | $4{,}301 \cdot 10^{-2}$ |
| 55,93 | Fe+ | 6222 | 47717 | $7{,}586 \cdot 10^{-3}$ |
| 71,93 | FeO+ | 5680 | 1958 | $3{,}112 \cdot 10^{-4}$ |
| 72,94 | CoN+ | 7137 | 3864 | $6{,}143 \cdot 10^{-4}$ |
| 74,93 | CoO+ | 5897 | 1614 | $2{,}566 \cdot 10^{-4}$ |
| 102,92 | CaPO_2+ | 5006 | 22162 | $3{,}523 \cdot 10^{-3}$ |
| 151,87 | Co_2H_2O_2+ | 5641 | 5099 | $8{,}106 \cdot 10^{-4}$ |
| 167,86 | Co_2H_2O_3+ | 6359 | 3047 | $4{,}844 \cdot 10^{-4}$ |
| 214,84 | Co_2O_6H+ | 4713 | 1778 | $2{,}826 \cdot 10^{-4}$ |

As can be observed, the typical ions of augite and pyroxenes were found in the fragment, as predicted by the Raman spectrum where both the $Co_3O_4$ and the augite were observed simultaneously. In addition to that, the existence of a cobalt oxide was confirmed thanks to the cobalt positive ions observed (see the 6 last rows in Table 9.2). The calculated dimension of that rich cobalt area inside the fragment was around 50-60 $\mu m^2$. Unfortunately, the intensities of the isotopes $^{17}O$ and $^{18}O$ obtained were under the quantification limits of the instrument. In other words, it was possible to detect the presence of these isotopes but, as they are much less intense than the main isotope $^{16}O$, it was not possible to quantify their abundance. However, the presence of $Co_3O_4$ was confirmed by TOF-SIMS.

The cobalt (II, III) oxide is a mixed valence black compound with antiferromagnetic properties (9). Regarding its presence in meteorites, it is not stated in the literature that this oxide has been observed in any kind of meteorite. Since the $^{16}O/^{17}O$ and $^{16}O/^{18}O$ isotopic ratios analysis by TOF-SIMS were inconclusive, in order to explain the presence of this compound

in the sample, two hypotheses are proposed. On the one hand, it could be an original compound that comes from Mars with the meteorite. However, this statement cannot be ensured with the available data. On the other hand, it could be an alteration product formed on Earth due to weathering processes or due to the impact of the meteorite on the Earth's surface.

This last theory could be supported by several facts found in the literature. The NWA 6148 nakhlite, as it was explained above, was first documented when it was purchased from a meteorite dealer in Erfoud, Morocco. Although its fall was not observed, it is known that it occurred in the region of Northwest Africa. According to bibliography (10), there is a geographic range in Morocco where rocks are rich in cobalt, the so-called Anti-Atlas range. In fact, in this range the Bou-Azzer mine can be found, which is the only mine in the world that extracts cobalt as a primary product. The city of Erfoud, where the meteorite was first documented, is located on the Northeast limit of the Anti-Atlas range, only 325 km far away from Bou-Azzer. Taking into account these facts, it is possible that the meteorite could have fallen in the Anti-Atlas range, impacting into an area rich in cobalt. Due to the heat and pressure generated in the impact, the cobalt would have been integrated into the structure of the NWA 6148, forming the cobalt (II, III) oxide. This would explain the presence of cobalt along with augite in different proportions in the same grains of the sample. If this hypothesis was true, the $Co_3O_4$ would not be an original compound from Mars but one formed because of the impact of the NWA 6148 with the terrestrial surface.

However, $Co_3O_4$ is formed when CoO is heated at around 600-700 ºC in the presence of oxygen (9). It is a compounds that is not found on the surface of Earth, since cobalt appears in our planet as a metallic component along with arsenic in minerals such as cobaltite (CoAsS), safflorite ($CoAs_2$), glaucodot ((Co, Fe)AsS) and skutterudite ($CoAs_3$) (11). This fact contradicts the previous theory, as $Co_3O_4$ is not naturally found on Earth and opens up another explanation, $Co_3O_4$ being an original

compound of the meteorite. If this was true, it would mean the discovery of a new compound present in Mars. Due to the formation conditions that the $Co_3O_4$ needs, it would have been formed at the same time with olivine or augite during the crystallization of the magma. Since $Co_3O_4$ is the thermodynamically stable form of cobalt oxide (12), it would have remained in that form without any chemical transformation until nowadays.

Finally, calcite was also found in the sample by means of Raman spectroscopy (Figure 9.8). In the collected experimental spectrum, it can be observed the $v_1$ symmetric $CO_3$ stretching at 1087 $cm^{-1}$ and external vibration of the $CO_3$ group that involve translatory oscillations between the anionic group and the Ca at 282 $cm^{-1}$. Contrarily to the case of the $Co_3O_4$, in this case the presence of calcite is usual in this type of samples and justified due to the terrestrial weathering processes that take place in desert areas (13, 14), since calcite crystallizes by the evaporation of water rich in carbonates and bicarbonates, which may flow through the cracks of the meteorite. This process of formation would explain the fact that calcite is scarce in the sample, as it would be only present in the cracks or pores of the NWA 6148.

Nevertheless, it must be noted that calcite is present in the surface of Mars, as it was detected by the *Phoenix* Mars lander (15). In the case of the analyzed NWA 6148 sample, this mineral was detected in a few spots of the sample and the intensity of its Raman features was in most of the cases very low, which led to think that it was present in the sample in a low relative abundance and it was the result of weathering in the cracks and pores of the meteorite.

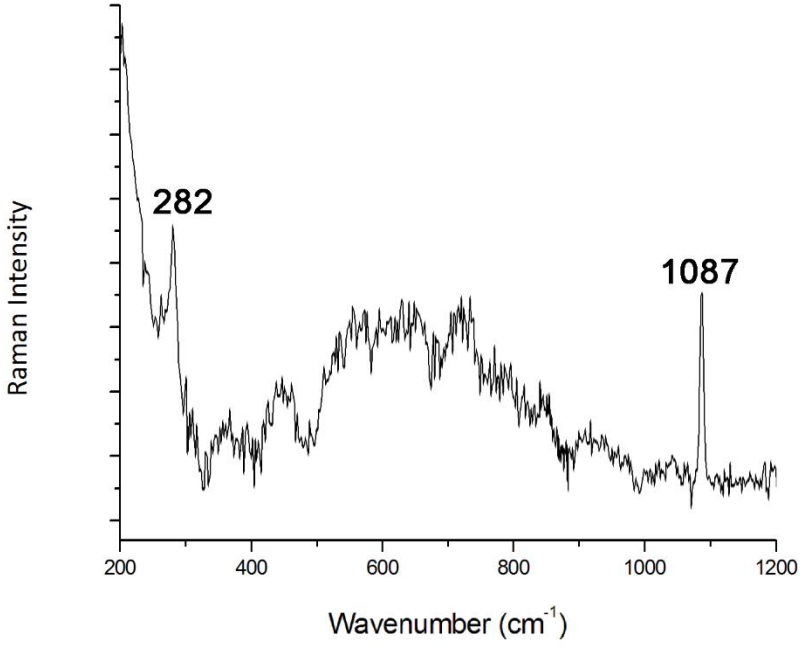


Figure 9.8. Calcite spectrum observed in the cracks of the NWA 6148 meteorite, obtained with the 785 nm excitation laser

## 9.2. Elephant Moraine 83227

The Elephant Moraine (EET) 83227 is a meteorite that was found in the Elephant Moraine icefield of Antarctica in 1983 by the US Antarctic Search for Meteorites program (ANSMET) with a weight of 1973 g. EET 83227 is one of the 268 meteorites classified as a polymict eucrite meteorite (16), belonging to the HEDs (Howardites-Eucrites-Diogenites) group of achondritic meteorites (17). Achondrites are rocks formed on a parent body that suffered a melting process, in which different phases were formed and differentiated. Based on spectroscopic data (telescopic visible and near-infrared), eucrites are rocks originated from the asteroid 4 Vesta (17-19), having a different oxygen isotopic distribution than the Earth-Moon and Mars meteorites (20).

Polymict eucrites are regolith breccias consisting of eucrite fragments and less than one part in ten of diogenite, an arbitrary dividing line from the howardites, which are related in structure. The typical polymict eucrites are characterized by (a) large medium-grained mafic clasts, containing ophitic to radial pyroxene/Ca rich plagioclase intergrowths and (b) breccias clasts with shocked pyroxene and twinned feldspar.

Regarding the particular polymict eucrite that was analyzed in this study, EET 83227, only the basic characteristics of the specimen are reported in literature (16). There, the presence of coarse-grained lithic fragments, fine-grained granular mafic clasts and rare glassy fragments is described. Moreover, three orthopyroxene grains, more magnesian than $En_{70}$, were detected by microprobe, diogenite-like clasts were said to be very rare and maskelynite was not observed (16).

Little is known about the particular mineralogy and geochemistry of the EET 83227. This meteorite is expected to be composed of the original material of 4 Vesta asteroid, although it can have varied due to the pressure and temperature conditions suffered during its travel as well as due to the entrance in the terrestrial atmosphere. Moreover, the fact that the meteorite is porous does not allow ruling out reactions among original components of the meteorite and terrestrial compounds present in the impact location, especially if we take into account the terrestrial age of this meteorite, that has been calculated with a minimum of 16.5 Ma (21). In a similar way to the NWA 6148, not only the future analysis methodologies for the Martian returning samples will be tested in a different type of matrix than the usual Martian meteorite one, but its study also serves to clarify the geochemical composition of the EET 83227.

Regarding the analyzed sample, a thin section sample of the meteorite labeled as EET 83227-9 (parent 5) was analyzed. The specimen was curated by the Department of Mineral Sciences of the Smithsonian Institution and Astromaterials Curation Office at NASA Johnson Space

Center (NASA-JSC) and provided by the US Antarctic Meteorite Program through the agreement between the University of the Basque Country (UPV/EHU) and the NASA-JSC.

An elemental map of the surface of the sample was obtained by means of ED-XRF (Figure 9.9). Besides of the semi quantitative results that this technique provides, the imaging mode of analysis can be used to discern the mineral phases present in the sample. Each mineral has a different elemental composition, so if the different element maps are compared, the mineral phases can be discerned as a first step in the geochemical characterization of the sample. In the results shown in Figure 9.9, Si was present through the entire sample, as stone meteorites are composed mainly of silicate minerals. Al substitutes Si atoms in the tetrahedral spaces of minerals in a systematic and fundamental way, depending on the mineral nature. The main minerals present in the EET 83227 meteorite, pyroxene and feldspar, suffer from this type of substitution, especially the feldspar. However, according to the Figure 9.9, there is not a direct correlation of Si and Al along the analyzed surface. This could be due to the fact that Al can also be part of the mineral in other spaces, as a cation, according to the general formula of this type of minerals, $XY(Si, Al)_2O_6$ (where X=Ca, Na, Fe(II), Mg, Zn, Mn, Li; Y=Cr, Al, Fe(III), Mg, Co, Mn, Sc, Ti, V).

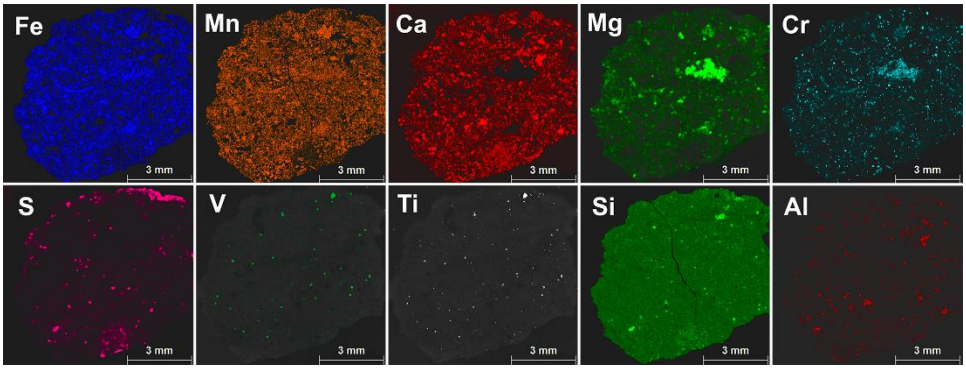


Figure 9.9. ED-XRF imaging maps for the main elements found in the EET 83227 meteorite: Fe, Mn, Ca, Mg, Cr, S, V, Ti, Si and Al. The absence of the element in their corresponding map is represented by the absence of color, while an increase of the intensity of the color means a higher relative concentration in that area

Iron, manganese, calcium and magnesium are usually found in this kind of meteorites due to the presence of pyroxene and feldspar as the main mineral phases of eucrites (16). This is the case of the EET 83227 meteorite. The ED-XRF elemental distribution maps shows a direct correlation between manganese and iron, as it is usual in silicate minerals which have iron as one of its main elements (22). Calcium might have different origins. On the one hand, eucrites have Ca rich feldspar, which can also explain the absence of potassium and sodium. On the other hand, the presence of pyroxene in this sample could explain the presence of Ca as well. The analyzed EET 83327 meteorite sample (Figure 9.9) shows the presence of magnesium through the whole sample, which might be related with the presence of pyroxene, with a hotspot of high magnesium concentration. As this hotspot is not correlated with the calcium distribution map, the presence of magnesium in this specific area is not due to the presence of pyroxene. However, the mentioned hotspot has a correlation with a hotspot of chromium in the same zone, suggesting the presence of another mineral phase besides pyroxene and feldspar.

In the case of sulfur, it was not found any correlation with any of the other elements present in the surface of the EET 83227, which might mean that it was present in its elemental state. It could also imply the presence of a sulfide or sulfate of an element present throughout the whole sample, such as iron. In this sense, an ED-XRF mapping is not always enough in order to differentiate mineral phases. Finally, the ED-XRF imaging maps for vanadium and titanium had an extremely high correlation, which led to think that a mineral phase composed mainly of V and Ti was present in those hotspots.

Regarding the Raman spectroscopy results, it was found that one of the main mineral phases of the sample was pyroxene, usually mixed with other compounds (Figure 9.10). In literature, pyroxene is characterized by the Si-O bridging mode at around 1010 $cm^{-1}$, the Si-O bending mode at 666 $cm^{-1}$ and the Metal-O stretching at the 300-400 $cm^{-1}$ range (323 $cm^{-1}$ for the Fe-

O stretching in ferrosilite (Fs, $Fe_2Si_2O_6$), 356 $cm^{-1}$ for the Ca-O in wollastonite (Wo, $Ca_2Si_2O_6$) and 390 $cm^{-1}$ for the Mg-O in enstatite (En, $Mg_2Si_2O_6$)). As seen, well resolved stretching bands of the three metals are shown in Figure 9.10, indicating the presence of calcium, magnesium and iron in the pyroxene.

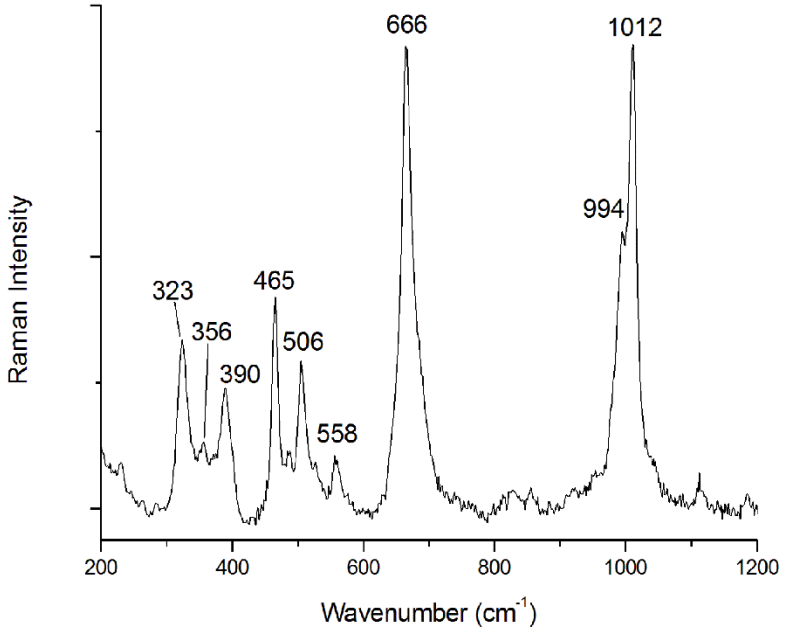


Figure 9.10. Raman spectrum of pyroxene mixed with quartz in the EET 83227 meteorite, the spectrum was acquired with the 532 nm excitation laser

As it is known, there are different types of pyroxenes depending both on their crystalline structure and their calcium, iron and magnesium content in the cation positions (23). In the Raman spectra (Figure 9.10), these structural and chemical differences among pyroxenes can be observed by shifts in the wavenumber of the bands and also in the number or shape of some bands. For example, quadrilateral pyroxenes, $(Mg, Fe, Ca)_2Si_2O_6$, present a single strong band near 1000 $cm^{-1}$, a strong doublet or single band in the range of 600-800 $cm^{-1}$ and two groups of overlapping bands with moderate intensities in the ranges of 300-450 $cm^{-1}$ and 450-600 $cm^{-1}$

(6). A. Wang et al. provided accurate results for the content of Fe, Mg and Ca for the quadrilateral pyroxenes by means of Raman spectroscopy (6). Unfortunately, in the EET 83227 meteorite sample none of the pyroxene Raman spectra collected corresponded to quadrilateral pyroxene, as all of them had a doublet in the 990-1020 $cm^{-1}$ spectral range, instead of a single intense band. This fact meant that the works developed by A. Wang et al. (24) and E. Huang (25) could not be used to quantify the metallic content of the pyroxenes of the EET 83227, as it was done with the NWA 6148.

In order to clarify the pyroxene metallic composition, in other words, the abundance of Fs, En and Wo, the SEM-EDS coupled to a Raman spectrometer through the SCA interface was used to characterize the metal proportions of this mineral phase, as was explained previously during this chapter. Four different pyroxene areas were analyzed and the mean value of the concentrations for each area was obtained. The averaged metal composition observed in the sample was $En_{60.2\pm4.4}Fs_{22.8\pm2.3}Wo_{17.0\pm1.7}$, where the confidence interval was calculated at a 95 % of confidence and using the standard deviation of the four measured areas. The metallic concentration of the pyroxene present in the EET 83227 meteorite is rich in magnesium and poor in iron and calcium, with calcium being the lowest of them. This ratio of metals in pyroxene is the one that is supposed to have the eucritic crust in 4 Vesta, where pyroxenes are rich in Mg and especially poor in Ca (19). Despite being very similar, the pyroxene composition for the EET 83227 found in this study has lower concentration of Mg than the one stated in literature ($En_{70}$) (16).

Besides pyroxene, feldspar was also observed as the other main mineral phase in the meteorite sample by means of Raman spectroscopy (Figures 11, 12). The two strongest bands in feldspar Raman spectra appear in the range of 450-520 $cm^{-1}$ and correspond to the ring-breathing modes of the four-membered rings of silicate tetrahedron. The bands in the range of 200-300 $cm^{-1}$ are related to rotation-translation modes of the four-membered rings, while the bands in the 150-200 $cm^{-1}$ correspond to rotation-

translation modes of cage-shear modes. The Raman bands observed in the range of 900-1200 $cm^{-1}$ are assigned to the vibrational stretching modes of the silicate tetrahedron. Finally, the bands in the 700-900 $cm^{-1}$ range are related to the deformation modes of the tetrahedron (26).

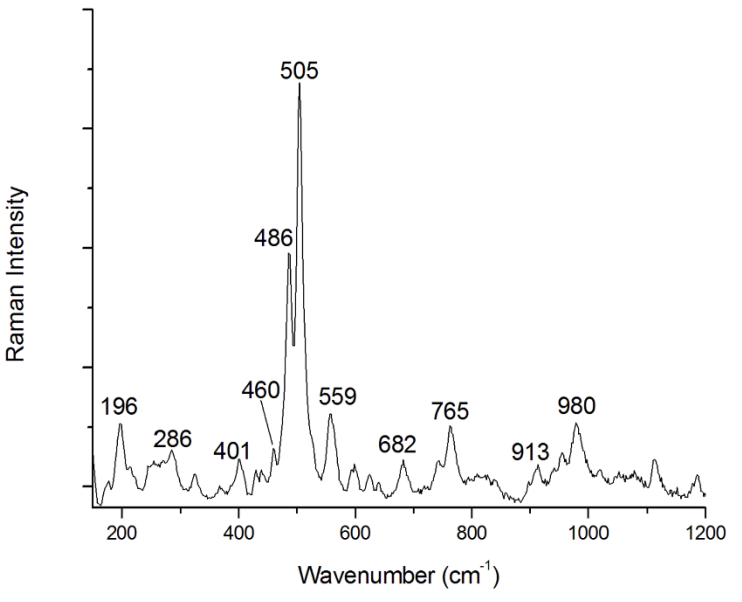


Figure 9.11. Raman spectrum of the low temperature Ca rich feldspar found in the EET 83227 meteorite using the 532 nm excitation laser

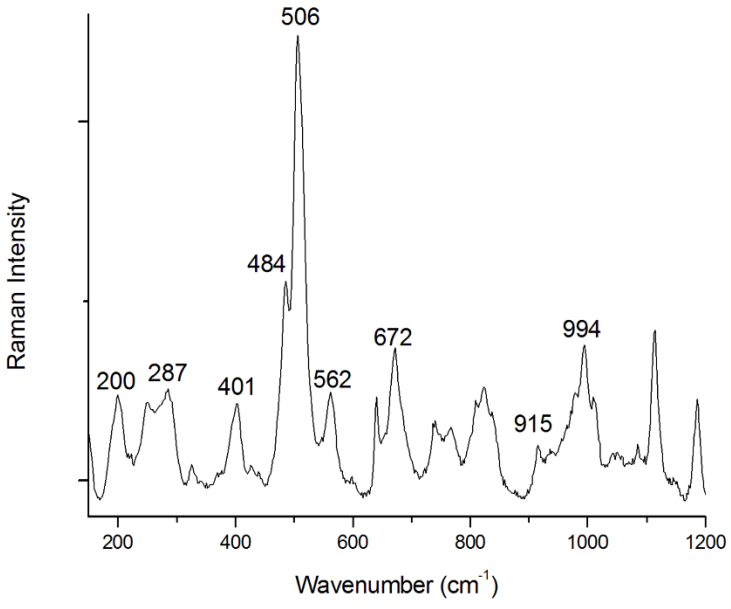


Figure 9.12. Raman spectrum of the high temperature Ca rich feldspar found in the EET 83227 meteorite using the 532 nm excitation laser

In the case of the feldspar present in the EET 83227 meteorite sample, the determination of its crystalline structure was carried out based on the work by J. J. Freeman et al. (27). First of all, it was observed that the feldspar present in the EET 83227 meteorite corresponded to a calcium rich feldspar. This fact was deduced due to the band that appears at 505 $cm^{-1}$, which is observed at a lower wavenumber than the Na and K rich feldspar, and the low relative Raman intensity and position for the band at 460 $cm^{-1}$, which appears with higher relative intensity and at higher wavenumbers for the Na and K rich feldspar. Among Ca rich feldspar, two structurally different feldspars can be differentiated, the low temperature ones, with a primitive unit cell, and the high temperature ones, with a body-centered unit cell (27). Both types of mineral phases are distinguished by the small band that appears at 460 $cm^{-1}$. In the case of a Ca rich feldspar with a low temperature formation, the band can be observed and visually distinguished from the doublet at 486 $cm^{-1}$ and 505 $cm^{-1}$ (Figure 9.11). When the band at 460 $cm^{-1}$ cannot be distinguished without a

decomposition of the bands, the Ca rich feldspar belongs to the high temperature type, with a body centered unit cell (Figure 9.12) (27).

Both kinds of feldspar were observed in the EET 83227 meteorite, which led to think that at some point one of the two crystalline types transformed partially into the other one. It is a known fact that low temperature (primitive unit cell) can be transformed into the high temperature one (body-centered unit cell) with high temperatures (around 237 ºC) or with the increase in sodium content (28). Although the increase in sodium content cannot be discarded, the most likely explanation for this alteration is the temperature increase caused by the heat generated when the meteorite entered Earth's atmosphere. A temperature of at least 237±1 ºC is needed to begin the transformation in the crystallographic system of the feldspar (29). High temperatures are reached in the atmospheric entry of celestial bodies. However, in order to assess the temperature that a meteorite reached when it travelled through the atmosphere, several parameters must be known, such as the shock layer thickness, the mass and the volume or the angle at which the meteorite entered the Earth (30). On the one hand, some of these are well known for this specific meteorite, such as the mass (1973.0 g) or the volume (13 x 10 x 9 cm) (16). On the other hand, the angle at which the meteorite entered the atmosphere is not known and, although it is stated in the Meteoritical Bulletin that the EET 83227 had a few millimeter-sized patches of fusion crust (16), the exact measurements of the shock layer are not provided. Nevertheless, even though the temperature that the meteorite suffered in the atmospheric entry is unknown, this type of bodies usually suffers higher temperatures than 237±1 ºC (30). This fact means that the meteorite's feldspar probably suffered a partial transformation from a primitive unit cell crystalline structure into a body-centered unit cell one.

Silica in two different forms, quartz and tridymite, was also observed by means of Raman spectroscopy. Quartz (465 $cm^{-1}$ as the main band, and 128 and 204 $cm^{-1}$ as the secondary bands, Figure 9.13) was formed in 4

Vesta after a crystallization process in liquid water which, probably, came from outside the asteroid (31). Regardless of the origin of this water, the quartz is an original compound from the meteorite, and not a product of a possible weathering process on Earth. Together with quartz, tridymite was also observed in the EET 83227 sample by means of Raman spectroscopy (212, 307, 355 and 435 $cm^{-1}$ as the main bands and 793 $cm^{-1}$ as a secondary band, Figure 9.14). This mineral phase is a polymorph of quartz which is formed at low pressure (around 1 bar) and high temperature (>870 ºC) conditions (32).

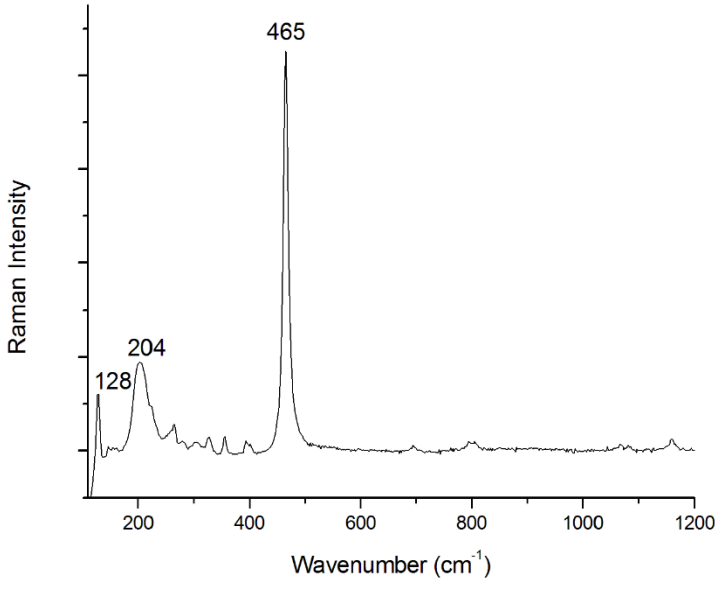


Figure 9.13. Raman spectrum of quartz found in the EET 83227 meteorite using the 532 nm excitation laser

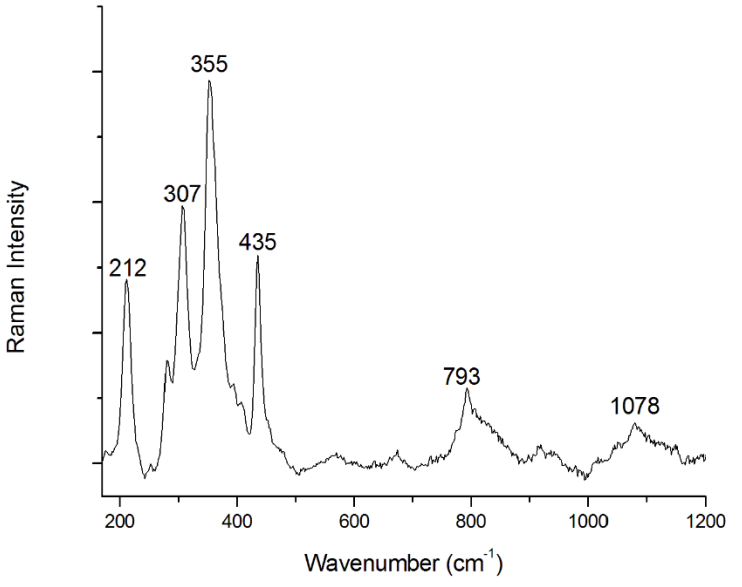


Figure 9.14. Raman spectrum of tridymite found in the EET 83227 meteorite using the 532 nm excitation laser

Although quartz is a known compound present in 4 Vesta, tridymite has never been observed previously neither in the asteroid itself nor in a meteorite coming from it, so this is the first time that this mineral is observed in 4 Vesta. Tridymite could have been formed through different ways. It could have been formed in the impact or atmospheric entry of the meteorite on Earth. As it has been already explained above, this event can achieve the necessary temperatures for a mineral phase alteration. In fact, literature states that the impact can generate a temperature up to 2000 ºC (33). Another hypothesis is that this polymorph could have been formed in 4 Vesta. As it is known, the asteroid has received through the years, and keeps receiving in the present, numerous impacts of different celestial bodies (34, 35). These impacts can also produce pressure transformations of the quartz present in 4 Vesta. However, these two hypotheses have an issue, which is the pressure that the quartz had to suffer. As it has been stated previously, a meteorite impact can generate enough temperature for the transformation, but it also generates pressure up to 25 GPa (33). This

high-pressure would not transform the quartz into tridymite, but into β-quartz or coesite (36). Due to this fact, the transformation of quartz into tridymite had to occur at less pressure than 1 GPa, regardless if it was formed in 4 Vesta or in the entrance and impact in the Earth, because otherwise coesite would be also present. This fact opens a third possible origin for the tridymite observed in the EET 83227 meteorite. Even though this mineral is an uncommon material in Earth, it has been found in Mars by the rover Curiosity (32), thus, it could have been formed in 4 Vesta through the same process as in Mars, which is still unknown nowadays, or as in Earth.

As stated above, the formation of the tridymite mineral phase in 4 Vesta during the geological active period of the asteroid could be the third possible hypothesis. As it is known, 4 Vesta had once a magma ocean which, gradually, solidified in the asteroid's core and in different geological layers (37). During this period, tridymite could have formed in a similar way as it is formed on the Earth, appearing in cavities and vesicles of igneous rocks (38). During that time, there was enough temperature for the formation of this mineral phase, whilst the pressure in its surface was less than 1GPa, due to the small size and therefore very low gravity of 4 Vesta (37).

Besides these mineral phases, several minor compounds belonging to 4 Vesta were found by means of Raman spectroscopy: chromite, (Fe, Mg)$Cr_2O_4$ (685 $cm^{-1}$ as the main band), apatite, $Ca_5(PO_4)_3$(F, Cl, OH) (963 $cm^{-1}$ as the main band), and sulfur, $S_8$ (153, 221 and 472 $cm^{-1}$ as the main bands and 247 and 439 $cm^{-1}$ as the secondary bands). Chromite is, along with ilmenite ($FeTiO_3$), a known mineral phase that is present in the eucritic materials of 4 Vesta at low concentration (0.3 % for both minerals) (39). The presence of chromite would explain the chromium hotspot observed previously in the ED-XRF analysis (Figure 9.9). This hotspot matched perfectly with the presence of Mg and the absence of Ca. In addition, the

area also had iron presence. These facts led to the confirmation of a grain of chromite in the sample.

In addition to these mineral phases, Raman spectroscopy detected in the sample of the EET 83227 meteorite the presence of calcite ($CaCO_3$, Raman bands at 1086 $cm^{-1}$ as the main band and 155, 282 and 713 $cm^{-1}$ as secondary bands). Calcite was found along with pyroxene, which appeared in all the spectra where $CaCO_3$ was determined (Figure 9.15).

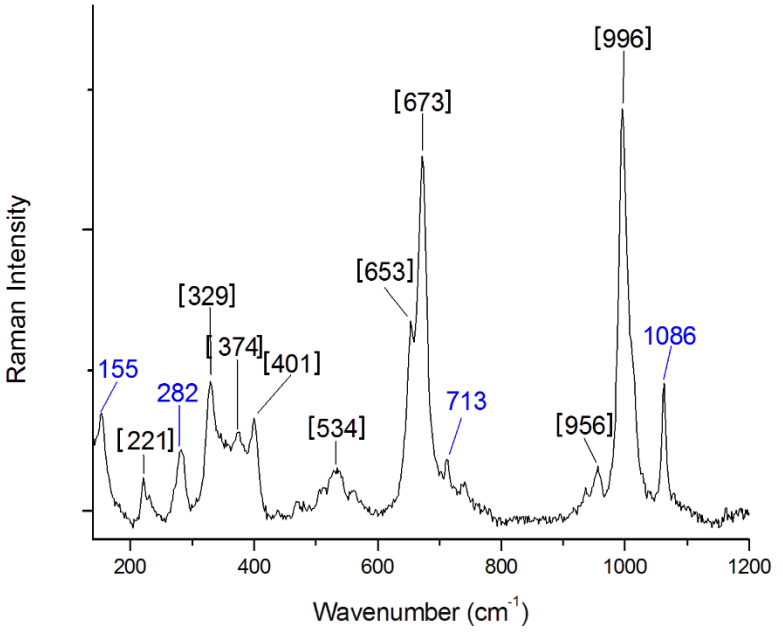


Figure 9.15. Calcite (blue labels) and pyroxene (black labels with brackets) Raman spectrum observed in the EET 83227 meteorite using the 532 nm excitation laser

In order to carry out a deeper study of the area where calcite appeared, a Raman chemical image was acquired using the main band of this mineral phase (Figure 9.16). As it can be observed, this mineral is present only in an area that is significantly different from the pyroxene/feldspar matrix. This area does clearly not belong to the original matrix of the meteorite sample, from a visual point of view, and appears as an addition to the surface of the sample. The calcite terrestrial weathering processes can lead to formations

of this mineral phase with a similar shape to nanobacteria colonies (40), similar to the formation observed in the EET 83227. The formation of calcite with this shape is explained by a process that involves water, atmospheric $CO_2$ and the original minerals from the meteorite. In addition to those components, biological activity must take place in these original minerals in order for the calcite to acquire these unusual formations and shapes (40). Bacteria and other microorganisms usually produce weathering processes in minerals to transform their chemical composition (41). This alteration of the minerals caused by biological activity could lead to the precursors that, with water and atmospheric $CO_2$, ended forming calcite with the unusual nanobacteria-like forms observed in the EET 83227.

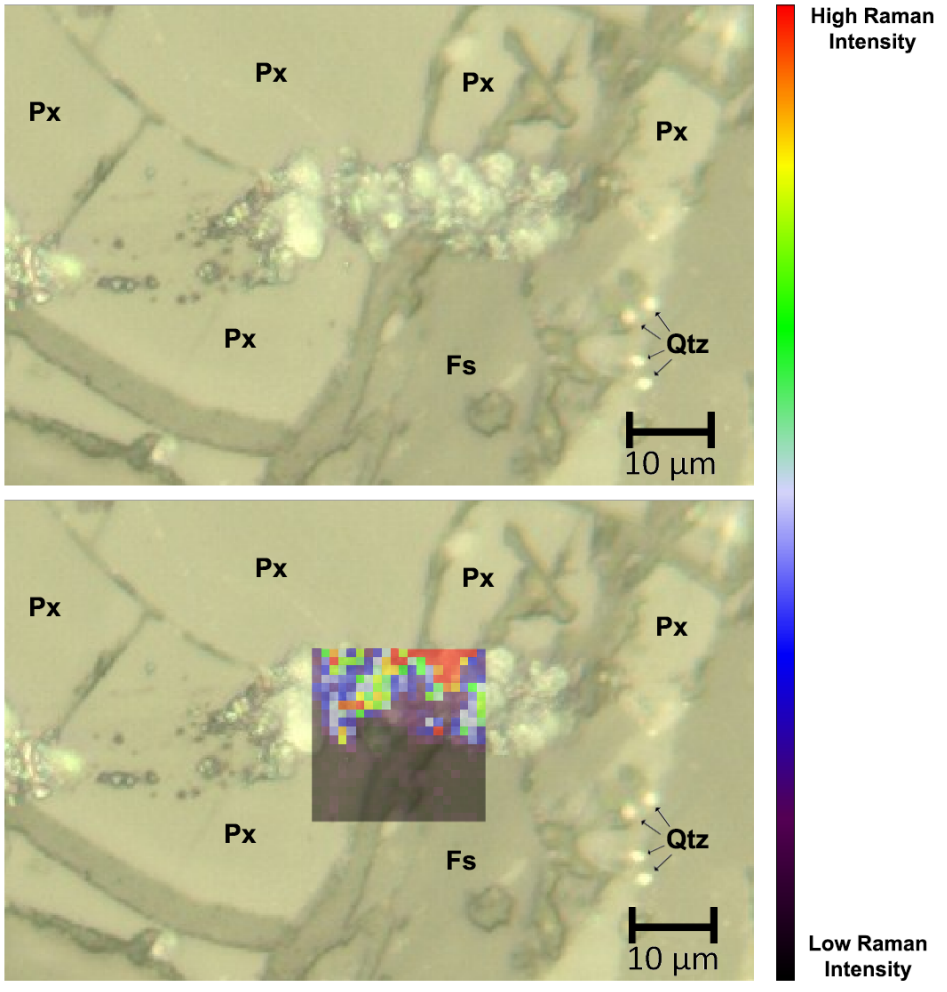


Figure 9.16. Raman imaging performed with the 532 nm excitation laser. The morphology of the area analyzed (left) together with the calcite Raman image, where the calcite main band was used for the mapping (right) can be observed

## 9.3. Dar al Gani 735

The Dar al Gani (DaG) 735 Martian meteorite was found in 1997 in the Dar al Gani strewn field (Al Jufrah, Libya) as a complete stone, covered by desert varnish, with a total mass of 588 g (42). As described in literature, DaG 735 is part of a meteorite shower, along its paired meteorites, DaG 476, DaG 489, DaG 670, DaG 876, DaG 975 and DaG 1037, which was composed of large and small fragments with a total mass higher than 10

kg. The surfaces of these fragments have no fusion crust, and some of them show fractures containing calcite due to desert weathering (42).

As mentioned above, all these paired meteorites were found in the strewn fields in the Dar al Gani site, which are located on a plateau of marine carbonate rocks with marly components. The preservation of meteorites is guaranteed through the absence of quartz sand on the plateau, strongly reducing wind erosion, and a basic environment emerging from the carbonate ground rusting of metallic meteorite components. A supposed soil cover has probably protected meteorites during pluvial times (43). These aspects must be taken into account when trying to identify the secondary mineral phases due to terrestrial chemical weathering.

The DaG meteorites are classified as olivine-phyric shergottites. They are basaltic rocks composed of olivine megacrysts up to 5 mm set in a fine-grained groundmass of pyroxene, maskelynitized plagioclase and mesostasis (42). Large pockets of brownish-colored recrystallized impact glass are found associated with pyroxene and olivine (44). Regarding the olivine present in these meteorites, it is stated in literature that the grains of this mineral are typically present as large subhedral crystals, zoned from $Fo_{76}$ (core) to $Fo_{58}$ (rim) (45). The pyroxene is present in the form of low- and high-Ca pyroxenes. The low-Ca pyroxenes are zoned from $En_{76}Fs_{21}Wo_{3}$ to $En_{58}Fs_{30}Wo_{12}$, being Mg-rich (44, 45). The high-Ca pyroxenes, present mainly as augite, do have a metallic composition of $En_{50}Fs_{18}Wo_{32}$, having a higher content of wollastonite than the other specimens of this mineral family. The third most important group of minerals in the DaG collection of meteorites is plagioclases. In this case, plagioclase glass (mainly present as maskelynite) is reported to be $An_{50-70}$ (An: anorthite, $CaAl_2Si_2O_8$). The next most important group of minerals are phosphates.

Other minor mineral phases have been observed in the DaG collection of meteorites, such as merrillite, $Ca_{8.85}(Mg,Fe)_{1.05}Na_{0.27}(PO_4)_7$), calcite,

$CaCO_3$, whitlockite, $Ca_9Mg(PO_3OH)(PO_4)_6$, Cl-apatite, $Ca_5(PO_4)_3(Cl)$, pyrrhotite, $Fe_{(1-x)}S$ (x=0 to 0.2) ,with Ni-rich exsolutions, euhedral chromite, $FeCr_2O_4$, Ti-chromite, iddingsite, $MgFe_2Si_3O_{10}{\cdot}4(H_2O)$, and ilmenite, $FeTiO_3$ (44-47). It must be taken into account that these secondary mineral phases could be the product of terrestrial weathering due to the conditions that the DaG collection of meteorites have suffered after they arrived to Earth.

During this PhD thesis a fragment of the DaG 735 was studied, which weighed 0.558g and had 1.3 x 0.7 cm of dimensions with both faces polished. Both surfaces looked similar to the naked eye and they were mainly composed by a light-colored matrix with black big crystals inside of it.

An elemental map of the surface of the sample was obtained by means of ED-XRF (Figure 9.17). As can be observed, the surface of the meteorite was composed mainly of Ca, Fe, Mg, Si and Al, which is consistent with the DaG meteorites elemental abundances.

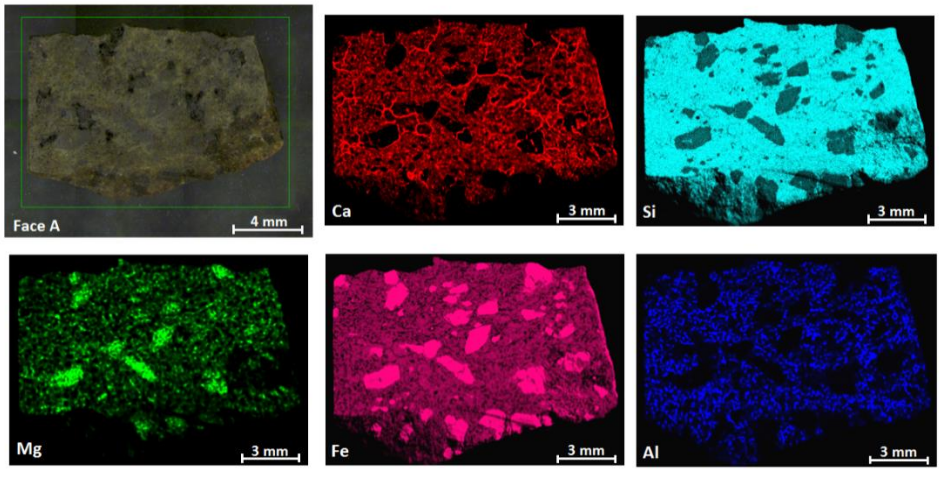


Figure 9.17. ED-XRF imaging maps for the main elements found in the DaG 735 meteorite: Ca, Si, Mg, Fe and Al. The absence of the element in their corresponding map is represented by the absence of color, while an increase of the intensity of the color means a higher relative concentration in that area

The crystals where no Ca nor Al are found in the elemental distribution correspond to the big olivine crystals, which in some cases were bigger than 1 mm in length. Mg and Fe distributions are the elemental distributions that better show the shape of the visually black crystals of the olivine. As it can be observed in Figure 9.17, Mg and Fe are irregularly distributed in the olivine crystals (different color shades can be seen in their distribution maps), suggesting different proportions of forsterite and fayalite in the olivines as previously reported in the analyses of its paired meteorites DaG 476 and DaG 489 (44). This fact is probably related with the olivine characterization of the DaG 476, where the forsterite content decreased from $Fo_{76}$ in the core to $Fo_{58}$ in the rim (44). Moreover, some of the crystals observed in the ED-XRF maps according to the intensity of the Fe $K_\alpha$ line do not present clear Mg $K_\alpha$ signal, suggesting the only presence of fayalite for such olivine crystals. In addition, the analysis of the $K_\alpha$ Mg line in the ED-XRF map shows a lighter Mg matrix, which corresponds to the Mg content of the pyroxenes with more intense areas of Mg, suggesting the presence of olivines more or less rich in forsterite. Since olivines and pyroxenes are the main minerals present in this meteorite, the Si map shows the presence of this element throughout the entire surface of the sample.

Regarding the Ca, it can be observed in Figure 9.15 that this element is distributed throughout the entire sample. On the one hand, this fact could be explained with the presence of pyroxene in the meteorite, since this mineral family has Ca in its elemental composition. On the other hand, it is important to highlight more intense Ca signal drawing cracks on the analyzed surface, which suggests the presence of calcite inside the meteorite cracks. This mineral was probably formed by weathering processes in the basic environment emerging from the carbonate ground in the plateau of marine carbonate rocks where the meteorite was found. The presence of calcite as weathering compound has also been reported for DaG 476, DaG 670 and DaG 489 (48).

By means of Raman spectroscopy, pyroxene was the main mineral phase found in the sample (Figure 9.18, 19). According to Huang et al. (25) the Raman bands shown in Figure 9.18 can be related to clinopyroxenes, $CaMgSi_2O_6$ (cpx, diopside-hedenbergite series). However, these bands may also be due to the presence of augite, $CaMgFe)_2Si_2O_6$, a subcalcic clinopyroxene or due to a mixture of both types of clinopyroxenes. In Figure 9.19, the Raman spectrum shows clearly the presence of an ortopyroxene (opx, eg. enstatite, $MgSiO_3$) (25). Similarly to the pyroxenes of the EET 83227, the metallic content of the pyroxenes found in the DaG 735 cannot be assessed using the woks by A. Wang et al. (24) and E. Huang (25), since they are not quadrilateral pyroxenes.

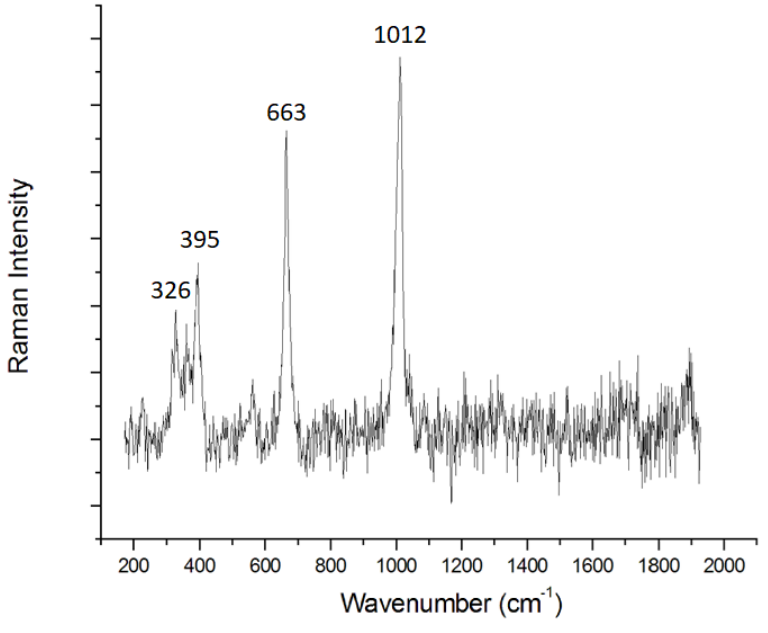


Figure 9.18. Raman spectrum of a clinopyroxene found in the DaG 735 meteorite, the spectrum was acquired with the 532 nm excitation laser

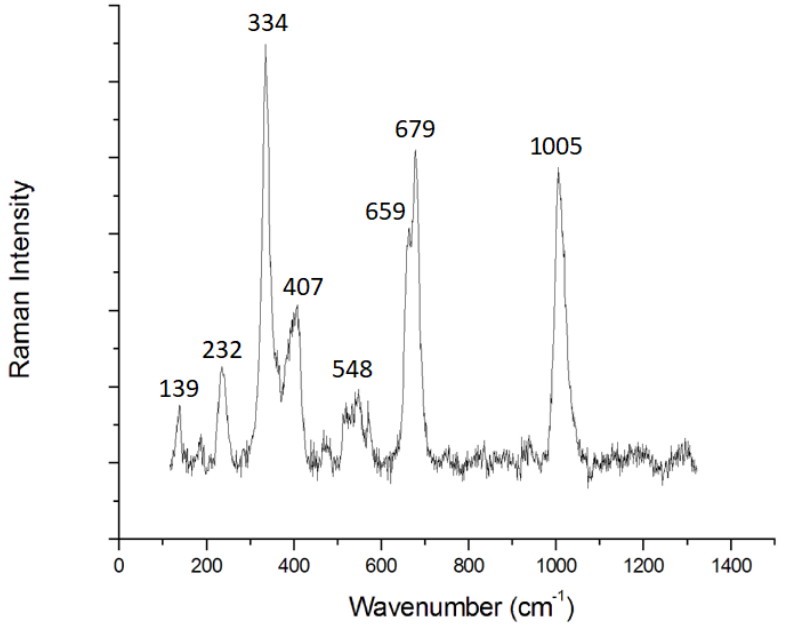


Figure 9.19. Raman spectrum of an ortopyroxene (enstatite) found in the DaG 735 meteorite, the spectrum was acquired with the 785 nm excitation laser

In addition to pyroxene, olivine was also observed as the second most abundant mineral phase present in the DaG 735 meteorite (Figure 9.20). Most of the olivine main signals observed were located at 820 and 850 $cm^{-1}$. Using the calibration models developed in Chapter 5, *Forsterite and Fayalite Content in Olivines*, it was calculated that the metallic composition of the olivine present in the DaG 735 meteorite had a composition of $Fo_{64.6\pm3}Fa_{35.4\pm3}$, where the confidence interval is given at a 95 % of confidence and as the uncertainty coming from the calibration curves.

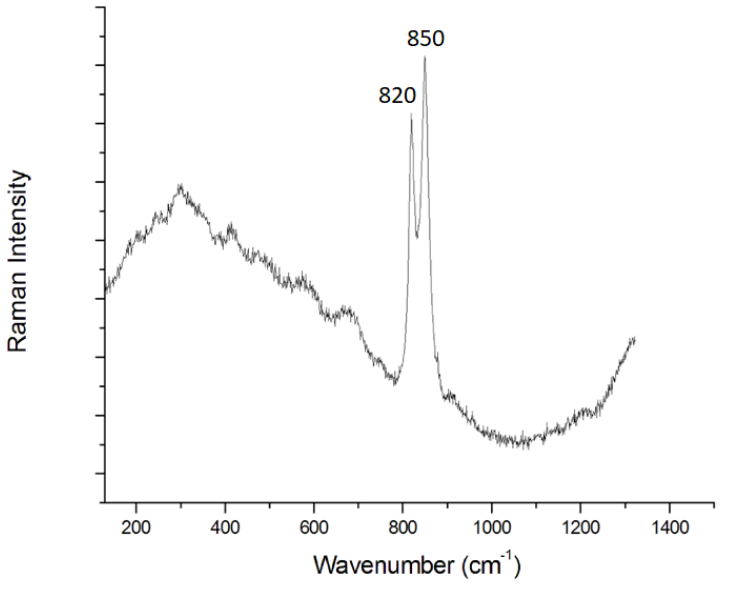


Figure 9.20. Raman spectrum of olivine found in the DaG 735 meteorite, the spectrum was acquired with the 785 nm excitation laser

Chromite, $FeCr_2O_4$, crystals were also found in the surface of the analyzed sample (Figure 9.21), whose presence is consistent with the studies performed on the DaG paired meteorites (44-46). Its main Raman signal was at 687 $cm^{-1}$, related to the symmetric stretching vibrational mode A1g($v_1$), and a secondary broad band of lower intensity at 500 $cm^{-1}$ was also observed in the spectrum, related to the vibrational mode F2g($v_4$) (49).

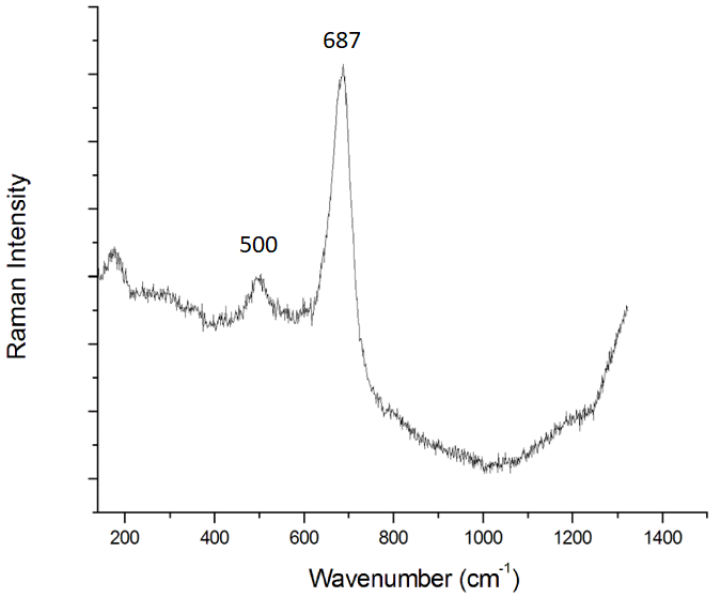


Figure 9.21. Raman spectrum of chromite found in the DaG 735 meteorite, the spectrum was acquired with the 785 nm excitation laser

Raman spectroscopy in mapping mode was used in order to study the fractures and cracks of the DaG 735 meteorite. Figure 9.22 shows an area where one of these maps was carried out. As observed, the area was mainly composed of pyroxene (Figure 9.22b, the 642-711 $cm^{-1}$ range was used for the abundance mapping) crossed by a fracture and some cracks and cavities on the sides.

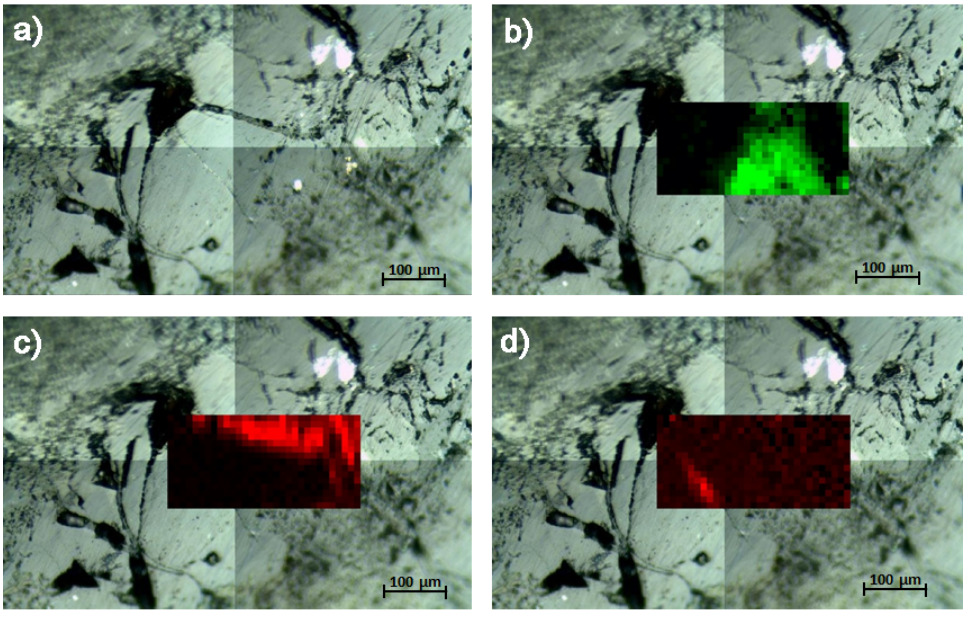


Figure 9.22. Raman imaging performed with the 785 nm excitation laser on the surface of the DaG 735 meteorite. They are showed a) the optical image of the analyzed area, b) the pyroxene distribution, c) the calcite distribution and d) the hematite distribution

The Raman analysis performed on this area showed that the largest fractures were filled with calcite (Figure 9.22c, the 1082-1095 $cm^{-1}$ range was used for the abundance mapping). This is in agreement with the calcium distribution in the ED-XRF measurements shown in Figure 9.17 for fractures and cracks, where the most intense colors depict the forms of such fractures. The most probably explanation for the calcite found in the DaG 735 meteorite is the terrestrial weathering, since the mineral appears in the fractures and cracks of the sample. In addition, it has already been stated in literature the finding of calcite in two paired DaG meteorites caused by terrestrial weathering, the DaG 476 and the DaG 489 (50).

As can be observed in Figure 9.22a, d, another thinner and brighter fracture is filled with hematite, $Fe_2O_3$ (the 277- 320 $cm^{-1}$ range was used for the abundance mapping). The presence of this mineral in the DaG 735 meteorite can be explained by the terrestrial weathering of Fe-bearing minerals that are progressively altered into clays and iron oxides and hydroxides, which often fill cracks and mineral fractures, together with

terrestrial quartz grains and carbonates (51). It must be pointed out that hematite has not been previously reported filling fractures in any of the paired fragments of DaG 735.

## 9.4. Conclusions

As has been observed throughout this chapter, Raman spectroscopy can be a very useful tool for the non-destructive characterization of major and minor mineral phases in geological samples. In addition, if it is accompanied by other complementary techniques, it is possible to obtain much information beyond the mineralogical characterization, both of primary and secondary minerals, of a sample. This makes Raman spectroscopy an ideal technique for the non-destructive analysis of the Mars return samples.

For instance, despite of being a molecular technique, it is possible to characterize in a semi-quantitative way the metal content of certain minerals, such as from augite or olivine, as already demonstrated in Chapter 5, *Forsterite and Fayalite Content in Olivines,* and in the analyses of the three meteorites presented in this chapter.

In addition to the estimation of the metallic content of certain minerals, Raman spectroscopy was used to determine the formation conditions of some minerals. In the case of the EET 83227 meteorite, Raman spectra were enough to determine the formation temperature conditions of feldspar and to make a rough approximation of the pressure and temperature of the magmas that formed this meteorite, thanks to the presence of tridymite.

Even so, the return samples from Mars will not only be able to undergo punctual analysis, but also Raman mapping, since they can be performed at micrometric level without the need of a polished surface, avoiding the physical alteration of the samples. Thanks to this methodology, it is possible to differentiate the grains present in a sample and, thus, trace their surface distribution. This is of particular importance for the study of cracks,

since both optical and mineralogical images can be observed in the same analysis. In this way, for instance, it is possible to study how the forsterite/fayalite ratio varies in an olivine grain (rim versus core part) without the need of destructive techniques. It would also be possible to study secondary minerals to determine how they were formed or where they come from using their spatial distribution, as has been done in the case of the different analyses of calcites in cracks in the studied meteorites.

In addition, Raman spectroscopy can be accompanied by other support techniques to further increase its performance in terms of results. The ED-XRF mapping is very useful as an initial analysis of a sample. This technique visually represents the elemental distribution of a sample without altering it. This fact is of great relevance, as this information can be used to discern all the grains of a sample or the presence of cracks. This elemental distribution can help to decide where or how to focus the more time-consuming analyses.

Finally, the SEM-EDS coupled to a Raman spectrometer through the SCA interface combines all the advantages of the elemental and molecular techniques. With this setup, it is possible to obtain in a non-destructive way the elemental maps from the surface of a sample and point the Raman laser in the SEM chamber. This was used for instance to assess the elemental characterization pyroxene in the studied meteorites, or to locate and measure the $Co_3O_4$ present in the NWA 6148 meteorite.

Using the described analytical techniques for the analyses of the three meteorites, the advantages of the proposed methodologies aimed for the analysis of the Martian return samples were demonstrated. These methodologies are able to detect critical compounds at a micrometric scale without altering the sample, which will be of great relevance once the samples collected by Perseverance come back to Earth.

## 9.5. Bibliography

1. Treiman, A. H., The nakhlite meteorites: Augite-rich igneous rocks from Mars, *Chemie Der Erde,* **2005**, 65, 203-270.

2. Humayun, M., Yang, S., Righter, K., Zanda, B., Hewins, R. H., The Germanium Dichotomy in Martian Meteorites, *47th Lunar and Planetary Science Conference,* **March 21, 2016,** The Woodlands, Texas, USA.

3. Yang, S., Humayun, M., Righter, K., Jefferson, G., Fields, D., Irving, A. J., Siderophile and chalcophile element abundances in shergottites: Implications for Martian core formation, *Meteoritics & Planetary Science,* **2015**, 50, 691-714.

4. Ruzicka, A., Grossman, J., Bouvier, A., Herd, C. D. K., Agee, C. B., The Meteoritical Bulletin, No. 102, *Meteoritics & Planetary Science,* **2015**, 50, 1662.

5. Huang, E., Chen, C. H., Huang, T., Lin, E. H., Xu, J., Raman spectroscopic characteristics of Mg-Fe-Ca pyroxenes, *The American Mineralogist,* **2000**, 85, 473-479.

6. Wang, A., Jolliff, B. L., Haskin, L. A., Kuebler, K. E., Viskupic, K. M., Characterization and comparison of structural and compositional features of planetary quadrilateral pyroxenes by Raman spectroscopy, *The American Mineralogist,* **2001**, 86, 790-806.

7. Sautter, V., Barrat, J. A., Jambon, A., Lorand, J. P., Gillet, P., Javoy, M., Joron, J. L., Lesourd, M., A new Martian meteorite from Morocco: the nakhlite North West Africa 817, *Earth and Planetary Science Letters,* **2002**, 195, 223-238.

8. Hadjiev, V. G., Iliev, M. N., Vergilov, I. V., The Raman spectra of $Co_3O_4$, *Journal of Physics. C, Solid State Physics,* **1988**, 21, L199-L201.

9. Greenwood, N. N., Earnshaw, A., Chemistry of the Elements, 2nd ed. **1997**, Butterworth- Heinemann, Oxford, UK.

10. U. S. Department of Interior, U. S. Geological Survey, Minerals Yearbook, Area Reports: International 2011, Africa and the Middle East: Volume III, **2013**, USGS, Washington DC, USA.

11. Wiberg, N., Wiberg, E., Holleman, A. F., Lehrbuch der anorganischen Chemie, **2007**, de Gruyter, Berlin.

12. Petitto, S. C., Marsh, E. M., Carson, G. A., Langell, M. A., Cobalt oxide surface chemistry: The interaction of CoO(1 0 0), $Co_3O_4$(1 1 0) and $Co_3O_4$(1 1 1) with oxygen and water, *Journal of Molecular Catalysis. A, Chemical,* **2008**, 281, 49-58.

13. Rull, F., Martinez-Frias, J., Sansano, A., Medina, J., Edwards, H. G. M., Comparative micro-Raman study of the Nakhla and Vaca Muerta meteorites, *Journal of Raman Spectroscopy,* **2004**, 35, 497-503.

14. Tomkinson, T., Lee, M. R., Mark, D. F., Dobson, K. J., Franchi, I. A., The Northwest Africa (NWA) 5790 meteorite: A mesostasis-rich nakhlite with little or no Martian aqueous alteration, *Meteoritics & Planetary Science,* **2015**, 50, 287-304.

15. Boynton, W. V., Ming, D. W., Kounaves, S. P., Young, S. M. M., Arvidson, R. E., Hecht, M. H., Hoffman, J., Niles, P. B., Hamara, D. K., Quinn, R. C., et al., Evidence for Calcium Carbonate at the Mars Phoenix Landing Site, *Science,* **2009**, 325, 61-64.

16. Grossman, J. N., The Meteoritical Bulletin, No. 76, 1994 January: The U.S. Antarctic Meteorite Collection, *Meteoritics,* **1994**, 29, 100-143.

17. Binzel, R. P., Xu, S., Chips off of Asteroid 4 Vesta: Evidence for the Parent Body of Basaltic Achondrite Meteorites, *Science,* **1993**, 260, 186-191.

18. Magna, T., Šimčíková, M., Moynier, F., Lithium systematics in howardite–eucrite–diogenite meteorites: Implications for crust–mantle evolution of planetary embryos, *Geochimica Et Cosmochimica Acta,* **2014**, 125, 131-145.

19. De Sanctis, M. C., Ammannito, E., Capria, M. T., Tosi, F., Capaccioni, F., Zambon, F., Carraro, F., Fonte, S., Frigeri, A., Jaumann, R., et al., Spectroscopic Characterization of Mineralogy and Its Diversity Across Vesta, *Science,* **2012**, 336, 697-700.

20. Scott, E. R. D., Greenwood, R. C., Franchi, I. A., Sanders, I. S., Oxygen isotopic constraints on the origin and parent bodies of eucrites, diogenites, and howardites, *Geochimica Et Cosmochimica Acta,* **2009**, 73, 5835-5853.

21. Herpers, U., Vogt, S., Bremer, K., Hofmann, H. J., Suter, M., Wieler, R., Lange, H. J., Michel, R., Cosmogenic nuclides in differentiated antarctic meteorites: measurements and model calculations, *Planetary and Space Science,* **1995**, 43, 545-556.

22. Sarbas, B., Töpper, W., Ditz, R., Mn Manganese, 8th ed. **1993**, Springer, Heidelberg, Germany.

23. Morimoto, N., Fabries, J., Ferguson, A. K., Ginzburg, I. V., Ross, M., Seifert, F. A., Zussman, J., Aoki, K., Gottardi, G., Nomenclature of Pyroxenes, *Mineralogy and Petrology,* **1988**, 39, 55-76.

24. Wang, A., Jolliff, B. L., Haskin, L. A., Kuebler, K. E., Viskupic, K. M., Characterization and comparison of structural and compositional features of planetary quadrilateral pyroxenes by Raman spectroscopy, *The American Mineralogist,* **2001**, 86, 790-806.

25. Huang, E., Chen, C. H., Huang, T., Lin, E. H., Xu, J., Raman spectroscopic characteristics of Mg-Fe-Ca pyroxenes, *The American Mineralogist,* **2000**, 85, 473-479.

26. McKeown, D. A., Raman spectroscopy and vibrational analyses of albite: from 25°C through the melting temperature, *The American Mineralogist,* **2005**, 90, 1506-1517.

27. Freeman, J. J., Wang, A., Kuebler, K. E., Jolliff, B. L., Haskin, L. A., Characterization of natural feldspars by Raman spectroscopy for future planetary exploration, *Canadian Mineralogist,* **2008**, 46, 1477-1500.

28. Gay, P., Taylor, W. H., The structures of the plagioclase felspars. IV. Variations in the anorthite structure, *Acta Crystallographica,* **1953**, 6, 647-650.

29. Frey, F., Jagodzinski, H., Prandl, W., Yelon, W. B., Dynamic character of the primitive to body-centered phase transition in anorthite, *Physics and Chemistry of Minerals,* **1977**, 1, 227-231.

30. Lyne, J. E., Tauber, M., Fought, R., An analytical model of the atmospheric entry of large meteors and its application to the Tunguska Event, *Journal of Geophysical Research: Planets,* **1996**, 101, 23207-23212.

31. Treiman, A. H., Lanzirotti, A., Xirouchakis, D., Ancient water on asteroid 4 Vesta: evidence from a quartz veinlet in the Serra de Magé eucrite meteorite, *Earth and Planetary Science Letters,* **2004**, 219, 189-199.

32. Morris, R. V., Vaniman, D. T., Blake, D. F., Gellert, R., Chipera, S. J., Rampe, E. B., Ming, D. W., Morrison, S. M., Downs, R. T., Treiman, A. H., et al., Silicic volcanism on Mars evidenced by tridymite in high-$SiO_2$ sedimentary rock at Gale crater, *Proceedings of the National Academy of Sciences,* **2016**, 113, 7071-7076.

33. Baziotis, I. P., Liu, Y., DeCarli, P. S., Melosh, H. J., McSween, H. Y., Bodnar, R. J., Taylor, L. A., The Tissint martian meteorite as evidence for the largest impact excavation, *Nature Communications,* **2013**, 4, 1404.

34. Stephan, K., Jaumann, R., De Sanctis, M. C., Tosi, F., Ammannito, E., Krohn, K., Zambon, F., Marchi, S., Ruesch, O., Matz, K. D., et al., Small fresh impact craters on asteroid 4 Vesta: A compositional and geological fingerprint, *Journal of Geophysical Research. Planets,* **2014**, 119, 771-797.

35. Clenet, H., Jutzi, M., Barrat, J., Asphaug, E. I., Benz, W., Gillet, P., A deep crust-mantle boundary in the asteroid 4 Vesta, *Nature,* **2014**, 511, 303-306.

36. Ford, M. H., Auerbach, S. M., Monson, P. A., On the mechanical properties and phase behavior of silica: a simple model based on low coordination and strong association, *The Journal of Chemical Physics,* **2004**, 121, 8415-8422.

37. Righter, K., Drake, M. J., A magma ocean on Vesta: Core formation and petrogenesis of eucrites and diogenites, *Meteoritics & Planetary Science,* **1997**, 32, 929-944.

38. Klein, C., Philpotts, A. R., Earth materials, 2nd ed. **2017**, Cambridge University Press, Cambridge.

39. Zuber, M. T., Mcsween, H. Y., Binzel, R. P., Eelkins-Tanton, L. T., Konopliv, A. S., Pieters, C. M., Smith, D. E., Origin, Internal Structure and Evolution of 4 Vesta, *Space Science Reviews,* **2011**, 163, 77-93.

40. Benzerara, K., Menguy, N., Guyot, F., Dominici, C., Gillet, P., Nanobacteria-like calcite single crystals at the surface of the Tataouine meteorite, *Proceedings of the National Academy of Sciences,* **2003**, 100, 7438-7442.

41. Uroz, S., Calvaruso, C., Turpault, M., Frey-Klett, P., Mineral weathering by bacteria: ecology, actors and mechanisms, *Trends in Microbiology,* **2009**, 17, 378-387.

42. Grossman, J. N., The Meteoritical Bulletin, No. 84, 2000 August, *Meteoritics & Planetary Science,* **2000**, 35, A199-A225.

43. Schlüter, J., Schultz, L., Thiedig, F., Al-Mahdi, B. O., Aghreb, A. E. A., The Dar al Gani meteorite field (Libyan Sahara): Geological setting, pairing of meteorites, and recovery density, *Meteoritics & Planetary Science,* **2002**, 37, 1079-1093.

44. Zipfel, J., Scherer, P., Spettel, B., Dreibus, G., Schultz, L., Petrology and chemistry of the new shergottite Dar al Gani 476, *Meteoritics & Planetary Science,* **2000**, 35, 95-106.

45. Mikouchi, T., Miyamoto, M., McKay, G. A., Mineralogy and petrology of the Dar al Gani 476 martian meteorite: Implications for its cooling history and relationship to other shergottites, *Meteoritics & Planetary Science,* **2001**, 36, 531-548.

46. Wadhwa, M., Lentz, R. C. F., McSween, H. Y., Crozaz, G., A petrologic and trace element study of Dar al Gani 476 and Dar al Gani 489: Twin meteorites with affinities to basaltic and lherzolitic shergottites, *Meteoritics & Planetary Science,* **2001**, 36, 195-208.

47. Herd, C. D. K., Papike, J. J., Brearley, A. J., Oxygen fugacity of Martian basalts from electron microprobe oxygen and TEM-EELS analyses of Fe-Ti oxides, *The American Mineralogist,* **2001**, 86, 1015-1024.

48. Borg, L. E., Nyquist, L. E., Wiesmann, H., Shih, C., Reese, Y., The age of Dar al Gani 476 and the differentiation history of the Martian meteorites inferred from their radiogenic isotopic systematics, *Geochimica Et Cosmochimica Acta,* **2003**, 67, 3519-3536.

49. Reddy, B. J., Frost, R. L., Spectroscopic characterization of chromite from the Moa-Baracoa Ophiolitic Massif, Cuba, *Spectrochimica Acta. Part A, Molecular and Biomolecular Spectroscopy,* **2005**, 61, 1721-1728.

50. Crozaz, G., Wadhwa, M., The terrestrial alteration of Saharan shergottites Dar al Gani 476 and 489: a case study of weathering in a hot desert environment, *Geochimica Et Cosmochimica Acta,* **2001**, 65, 971-977.

51. Gillet, P., Biellmann, C., Reynard, B., McMillan, P., Raman spectroscopic studies of carbonates part I: High-pressure and high-temperature behaviour of calcite, magnesite, dolomite and aragonite, *Physics and Chemistry of Minerals,* **1993**, 20.

# Chapter 10
# General Conclusions

*"There is no real ending. It's just the place where you stop the story"*

Frank Herbert, 1969

According to the results summarized throughout this PhD thesis, the main objective proposed was achieved. Several tools and protocols were developed and tested to provide useful knowledge about Mars related samples using Raman spectroscopy.

In order to accomplish the main objective, the different partial objectives have also been achieved. First, more than 100 individual samples of minerals relevant to the study of Mars were analyzed and used to create part of the IMPAT database described in Chapter 4, *IMPAT Database*. This database will be of great aid in the interpretation of the Raman results coming from Mars, since it has minerals whose Raman spectra have not been published in the literature yet, had poor quality in the published spectra, or had scarce literature references. As observed in Chapter 4,

IMPAT Database, the Raman spectra of the IMPAT database obtained with a continuous excitation laser had clear and well defined diagnostic signals of the analyzed minerals.

With regard to future work, additional minerals that are not so well characterized in the literature should be collected and analyzed. In addition, the minerals that form part of the IMPAT database could be measured by 246.8 nm deep-UV excitation laser too, since that is type of laser that SHERLOC uses A good database should always be in constant development and growth.

In addition to the creation of the IMPAT database, different models for the study of certain characteristics of minerals were developed based on Raman spectroscopy. In this sense, a model to quantify the forsterite and fayalite ratio of olivines, a way to assess past high-pressure events in carbonate and silica based minerals and a methodology capable of classifying and identifying carboxylic acids were developed.

Regarding the forsterite and fayalite ratio of olivines, a new model was developed to quantify it and was described in Chapter 5, *Forsterite and Fayalite Content in Olivines*. Three different regression curves were first tested, using the two main Raman signals of olivine and the difference between them. The three models were developed in a way to avoid any possible bias that the instrumentation could introduce, using 64 different data points from 14 different research works. After the validation process of the models, which involved a standard commercial olivine, from which the mineralogical and metallic characterization was carried out by XRD and WD-XRF, it was stablished that the best way to quantify the forsterite and fayalite ratio of olivines was to do it through the two models obtained directly from the main signals position of olivine, and then average their results.

Overall, the proposed final method to quantify the metallic content of olivines had an uncertainty associated to the result of around ± 2-3 %,

which is a great improvement compared to the uncertainties of the models that can be found currently in literature, which is of around ± 10 %.

This method was tested with some samples collected in Reykjanes (Iceland), since they are considered analogs to Mars. The results obtained pointed out that, even though the samples were formed form the same parent magma and were collected in the same area, they were heterogeneous among them, and presented different olivine compositions. This fact means that two rocks can be very different at a micrometric scale even thought they might seem similar visually.

With regard to future work, it was not possible to test the proposed calibration models for the quantification of the content of magnesium and iron in olivine with other commercial olivine (reagent grade) than the one used during this PhD thesis. However, in the case that other standard olivines with a different concentration were commercialized, they should be used to test and further validate the proposed models.

In addition, it might be possible to calibrate the metallic content of other minerals in an accurate and precise way, since some of the Raman signals are sometimes related to the cations present in the crystal lattice of minerals. In this sense, families of minerals composed of endmembers with different cations should be tested as possible candidates to develop additional models such as the one proposed for olivine. For instance, feldspars are composed of different ratios of potassium, sodium and calcite, and their endmembers are orthoclase, $KAlSi_3O_8$, albite, $NaAlSi_3O_8$ and anorthite, $CaAl_2Si_2O_8$. They do have similar Raman spectra and some of their spectral features are related with the cations present in their crystal lattice, so it might be possible to calibrate their metallic content in order to characterize them. A similar thing occurs with pyroxene and its three endmembers, enstatite, $MgSiO_3$, ferrosilite, $FeSiO_3$ and wollastonite, $CaSiO_3$, where previous works in literature were only able to propose models for the quadrilateral pyroxenes.

In order to propose possible new calibration models for other minerals, first, a wide variety of the given mineral, in terms of its metallic composition, should be collected and analyzed. Then, different calibration models should be tested and validated as was done with the olivine during this PhD thesis.

Regarding the high-pressure events and how they affect the Raman spectra, the capabilities of Raman spectroscopy to detect said events was assessed and described in Chapter 6, *Mineral Alterations Caused by High-Pressure Events*. A model was developed to estimate the residual stress remaining in a calcite after it is subjected to a high-pressure event. Moreover, the calibration model was tested with the NWA 6148 meteorite, leading to the identification of calcite II inside of it. After doing a literature review of the different emplacements where carbonates had been found on Mars, and knowing that the NWA 6148 nakhlite had calcite original from Mars inside of it, their most probable Martian geographic origin, based on this finding, was suggested, Syrtis Major Planum.

In this sense, it was noticed how the determination of the geographical origin of a collection of meteorites, beyond knowing which celestial body they came from, is usually a hard task, since many factors and characteristics of the meteorites should be taken into account. However, any additional piece of information that helps in this matter, like the finding of calcite in this meteorite, is always useful, and it was proven that Raman spectroscopy can contribute to that discussion.

Raman spectroscopy was also used to identify past high-pressure events that affected quartz and feldspar. The latter was found in a sample collected from the Chesapeake Bay Crater, a wet-target analog. The former was identified in the EET 83227 meteorite.

Thanks to the study carried out, it was checked that high-pressure plays an important role in the space exploration field, especially in Mars, where past volcanic activity and the constant impact of external celestial bodies

generate enough high-pressure events to alter the composition of the minerals of its surface. Due to this fact, it was concluded that high-pressure, its implications for minerals and how can it be analyzed should be considered in further studies. Regarding Raman spectroscopy, it can provide valuable information regarding alterations of minerals caused by high-pressure, which could help in the understanding of the surrounding area of the analyzed sample.

With regard to future work, it was observed in this PhD thesis that a calibration to obtain the residual stress of calcite by Raman spectroscopy can be developed. In this sense, as was observed with quartz and feldspar, other minerals also suffer alterations with pressure, which might be able to be observed by Raman spectroscopy. Thus, an in-depth literature revision should be carried out looking for other minerals present in Mars that suffer changes in the spectral features when they are subjected to pressure. Afterwards, it should be checked if the pressure that they suffer is calibratable using the Raman spectra. This would help in the study of Mars since, as was discussed during the PhD thesis, its surface has been, and still is, subjected to high-pressure events.

Regarding the third task proposed for this partial objective, two models, one to classify carboxylic acids and amino acids based on their Raman spectrum and the other one to calculate the carbon chain length of saturated carboxylic acids, were developed and described in Chapter 7, *Development of Classification and Characterization Models for Organics Analysis*.

The models were tested with two inclusions of the NWA 6148 Martian meteorite, which contained a mixture of different organic compounds. The classification model predicted that the average spectrum of the mapping of the inclusion could be an amino acid, an unsaturated carboxylic acid or a saturated carboxylic acid with an -OH functional group. However, as it was observed afterwards, the inclusion had a mixture of different organic

compounds and, thus, the classification model was not able to indicate that there was a saturated carboxylic acid until its particular spectrum was obtained using a sPCA approach.

The other model developed for the characterization of organic compounds was to determine the carbon chain length of linear saturated carboxylic acids. Even though the model worked properly in the studied range (10-20 carbons), it would probably be inaccurate at some point when analyzing saturated carboxylic acids outside the range of the studied carbon chain length, especially when increasing it.

Using both models and chemometrics it was possible to characterize the content of the studied inclusions of the meteorite, which were a mixture of carboxylic acids. Among them, it was possible to identify the dodecanoic acid. However, regarding its future uses and improvements, currently the models only cover a specific type of organic compounds. In that sense, they could be considered as a first step to develop more complex and complete models that were able to identify and characterize a wider range of organic molecules using their Raman spectra. In order to achieve that, first, a wide, good and reliable database of Raman spectra of organic compounds would be needed. The focus should be put on any organic compound, or family of compounds, that might be still preserved on Mars. With that database, it would be possible to improve and expand on the classification model proposed in this PhD thesis. In addition, other characterization models, such as the one to estimate the carbon chain length, could be developed.

The third proposed partial objective was accomplished by assessing the capabilities of *SuperCam* to analyze the surface of Mars, described in Chapter 8, *SuperCam Raman Spectroscopy Assessment*. It was observed that the instrument is able to differentiate mineral phases with very similar characteristics and Raman spectrum. In addition, some organic compounds adsorbed in olivine along Mg-perchlorate to simulate Martian

conditions were analyzed with *SuperCam*. These analyses allowed to establish the detection limit of this specific test at 5 wt%. All these results proved that Raman spectroscopy is a good technique to study the surface of Mars and that the spectra obtained with *SuperCam* have enough quality to obtain valuable information of the Red Planet.

Finally, the fourth proposed partial objective was achieved by analyzing three different meteorites and testing the different developed models throughout this PhD thesis on them. The analyses of the NWA 6148, EET 83227 and DaG 735 meteorites were described in Chapter 9, *Methodology Development and Testing for the Mars Returning Samples*. In addition to Raman spectroscopy, it was observed that the use of complementary techniques, especially techniques that provide elemental information of the sample and can do chemical maps, such as the ED-XRF, are very useful when they are combined with Raman spectroscopy.

Besides the mineralogical characterization of the samples by Raman spectroscopy, the technique was also used to assess the metallic content of some minerals present in the meteorites, such as in the case of olivines and pyroxenes. It was also used to determine the formation conditions of some minerals. As an example, the formation temperature conditions of feldspar were assessed by Raman spectroscopy, as well as a rough estimation magma conditions for the formation of tridymite.

In addition, the Raman mapping capabilities were tested for the characterization of meteorites. By doing so, it was possible to differentiate the mineral grains present in the samples and, thus, trace their surface distribution. This fact is very relevant for the study of cracks and veins, since both optical and mineralogical images can be observed in the same analysis.

Regarding other complementary techniques, the ED-XRF mapping was very useful as an initial approach to the analysis of the samples. Using this technique, it was possible to visualize the elemental distribution of the

surface of the meteorite, greatly easing the Raman spectroscopy punctual analysis locations and, thus, saving time.

Finally, the SCA interface, which couples a Raman spectrometer with a SEM-EDS system, was proven as a very useful setup. It combines the advantages of the SEM image and the EDS elemental analysis with the mineralogical and molecular characterization of the sample by Raman spectroscopy. With this setup, it is possible to obtain in a non-destructive way the elemental maps from the surface of a sample and point the Raman laser in the SEM chamber. As an example, this setup was used for the assessment of the elemental characterization of pyroxenes or to locate and analyze the $Co_3O_4$ present in the NWA 6148 meteorite.

As a summary, ED-XRF elemental maps were used to provide an elemental distribution of the studied samples. Then, Raman spectroscopy was used taking into account the elemental information to perform both punctual and mapping analyses. In order to get additional information by other techniques to support the results found, the SCA interface, which allows to perform Raman analyses inside the SEM-EDS chamber, was of great use. These techniques provided great advantages and synergies between them and were proven as very good complementary techniques. In conclusion, the described procedure could be of great interest for the analysis of the Martian return samples.

Overall, the work carried out during this PhD thesis could be a useful source of information regarding the Raman study of Martian samples, using both the IMPAT database and the developed models and methodology, as has been proven with the geochemical characterization of the meteorites. A wider collection of Raman spectral data for the calibration models (e.g., more spectra of high-pressure calcite polymorphs, organic compounds or other commercial standard olivines) would have helped to further improve their quality, refinement and/or validation. Nevertheless, these novel models could provide relevant information related to the area where

analyses are carried out on Mars. In this sense, this PhD thesis has contributed to the capabilities of characterizing the surface of Mars, and any sample of the same nature, by Raman spectroscopy.

# Chapter 11
# Bibliography

Allwood, A. C., Hurowitz, J. A., Clark, B. C., Cinquini, L., Davidoff, S., Denise, R. W., Elam, W. T., Foote, M. C., Flannery, D. T., Gerhard, J. H., et al., The PIXL Instrument on the Mars 2020 Perseverance Rover, **2021**.

Altheide, T. S., Chevrier, V. F., Noe Dobrea, E., Mineralogical characterization of acid weathered phyllosilicates with implications for secondary martian deposits, *Geochimica Et Cosmochimica Acta,* **2010**, 74, 6232-6248.

Artemieva, N., Ivanov, B., Launch of martian meteorites in oblique impacts, *Icarus,* **2004**, 171, 84-101.

Arvidson, R. E., DeGrosse, P., Grotzinger, J. P., Heverly, M. C., Shechet, J., Moreland, S. J., Newby, M. A., Stein, N., Steffy, A. C., Zhou, F., et al., Relating geologic units and mobility system kinematics contributing to Curiosity wheel damage at Gale Crater, Mars, *Journal of Terramechanics,* **2017**, 73, 73-93.

Ashwal, L. D., Wood, C. A., SNC meteorites - Igneous rocks from Mars, *13th Lunar and Planetary Science Conference,* **March 15, 1982,** Houston, Texas, USA.

Baker, P. A., Kastner, M., Constraints on the Formation of Sedimentary Dolomite, *Science,* **1981**, 213, 214-216.

Baldridge, A. M., Hook, S. J., Crowley, J. K., Marion, G. M., Kargel, J. S., Michalski, J. L., Thomson, B. J., de Souza Filho, C. R, Bridges, N. T., Brown, A. J., Contemporaneous deposition of phyllosilicates and sulfates: Using Australian acidic saline lake deposits to describe geochemical variability on Mars, *Geophysical Research Letters,* **2009**, 36, L19201-n/a.

Bandfield, J. L., Hamilton, V. E., Christensen, P. R., A Global View of Martian Surface Compositions from MGS-TES, *Science,* **2000**, 287, 1626-1630.

Barlow, N., Mars: An Introduction to its Interior, Surface and Atmosphere, 1st ed. **2008**, Cambridge University Press, Cambridge, UK.

Bayer, J., Uranometria, omnium asterismorum continens schemata, nova methodo delineata aereis laminis expressa, **1603**, Christoph Mangle, Augsburg, Germany.

Baziotis, I. P., Liu, Y., DeCarli, P. S., Melosh, H. J., McSween, H. Y., Bodnar, R. J., Taylor, L. A., The Tissint martian meteorite as evidence for the largest impact excavation, *Nature Communications,* **2013**, 4, 1404.

Becker, L., Glavin, D. P., Bada, J. L., Polycyclic aromatic hydrocarbons (PAHs) in Antarctic Martian meteorites, carbonaceous chondrites, and polar ice, *Geochimica Et Cosmochimica Acta,* **1997**, 61, 475-481.

Befus, K. S., Lin, J., Cisneros, M., Fu, S., Feldspar Raman shift and application as a magmatic thermobarometer, *The American Mineralogist,* **2018**, 103, 600-609.

Bell, J. F., Maki, J. N., Mehall, G. L., Ravine, M. A., Caplinger, M. A., Bailey, Z. J., Brylow, S., Schaffner, J. A., Kinch, K. M., Madsen, M. B., et al., The Mars 2020 Perseverance Rover Mast Camera Zoom (Mastcam-Z) Multispectral, Stereoscopic Imaging Investigation, *Space Science Reviews,* **2021**, 217, 24.

Bell, J., The Martian Surface: Composition, Mineralogy and Physical Properties, Edited by Bell, J., **2008**, Cambridge University Press, Cambridge, UK.

Benzerara, K., Menguy, N., Guyot, F., Dominici, C., Gillet, P., Nanobacteria-like calcite single crystals at the surface of the Tataouine meteorite, *Proceedings of the National Academy of Sciences,* **2003**, 100, 7438-7442.

Berdyugina, S. V., Kuhn, J. R., Harrington, D. M., Šantl-Temkiv, T., Messersmith, E. J., Remote sensing of life: polarimetric signatures of

photosynthetic pigments as sensitive biomarkers, *International Journal of Astrobiology,* **2016**, 15, 45-56.

Bertelsen, P., Goetz, W., Madsen, M. B., Kinch, K. M., Hviid, S. F., Knudsen, J. M., Gunnlaugsson, H. P., Merrison, J., Nornberg, P., Squyres, S. W., et al., Magnetic Properties Experiments on the Mars Exploration Rover Spirit at Gusev Crater, *Science,* **2004**, 305, 827-829.

Besson, J. M., Pinceaux, J. P., Anastopoulos, C., Velde, B., Raman spectra of olivine up to 65 kilobars, *Journal of Geophysical Research: Solid Earth,* **1982**, 87, 10773-10775.

Bibring, J., Langevin, Y., Mustard, J. F., Poulet, F., Arvidson, R., Gendrin, A., Gondet, B., Mangold, N., Pinet, P., Forget, F., et al., Global Mineralogical and Aqueous Mars History Derived from OMEGA/Mars Express Data, *Science,* **2006**, 312, 400-404.

Binzel, R. P., Xu, S., Chips off of Asteroid 4 Vesta: Evidence for the Parent Body of Basaltic Achondrite Meteorites, *Science,* **1993**, 260, 186-191.

Black, S. R., Hynek, B. M., Mchenry, L. J., Mccollom, T., Cameron, B., Ludyan, J., Alteration Mineralogy and the Effect of Parent Lithology at Hydrothermal Mars Analog Sites: Initial Results from Hengill and Krafla Volcanoes, Iceland, *48th Lunar and Planetary Science Conference,* **March 20, 2017,** The Woodlands, Texas, USA.

Bloise, A., Dattola, L., Allegretta, I., Terzano, R., Miriello, D., Linarite and connellite dataset from Calabria region (Southern Italy): First evidence, *Data in Brief,* **2019**, 27, 104597.

Borg, L. E., Nyquist, L. E., Wiesmann, H., Shih, C., Reese, Y., The age of Dar al Gani 476 and the differentiation history of the Martian meteorites inferred from their radiogenic isotopic systematics, *Geochimica Et Cosmochimica Acta,* **2003**, 67, 3519-3536.

Bost, N., Westall, F., Gaillard, F., Ramboz, C., Foucher, F., New Synthetic Martian Basalts from Spirit data, Gusev crater, *European Planetary Science Congress,* **October 2, 2011,** Nantes, France.

Boynton, W. V., Ming, D. W., Kounaves, S. P., Young, S. M. M., Arvidson, R. E., Hecht, M. H., Hoffman, J., Niles, P. B., Hamara, D. K., Quinn, R. C., et al., Evidence for Calcium Carbonate at the Mars Phoenix Landing Site, *Science,* **2009**, 325, 61-64.

Breitenfeld, L. B., Dyar, M. D., Carey, C. J., Tague, T. J., Wang, P., Mullen, T., Parente, M., Predicting olivine composition using Raman spectroscopy

through band shift and multivariate analyses, *The American Mineralogist,* **2018**, 103, 1827-1836.

Bridges, J. C., Warren, P. H., The SNC meteorites; basaltic igneous processes on Mars, *Journal of the Geological Society,* **2006**, 163, 229-251.

Brown, A. J., Viviano, C. E., Goudge, T. A., Olivine-Carbonate Mineralogy of the Jezero Crater Region, *Journal of Geophysical Research. Planets,* **2020**, 125, 1-30.

Bunch, T. E., Cohen, A. J., Coesite and Shocked Quartz from Holleford Crater, Ontario, Canada, *Science,* **1963**, 142, 379-381.

Carr, M. H., Head, J. W., Geologic history of Mars, *Earth and Planetary Science Letters,* **2010**, 294, 185-203.

Carrasco-Busturia, D., The temperature - pressure phase diagram of the calcite I - calcite II phase transition: A first-principles investigation, *The Journal of Physics and Chemistry of Solids,* **2021**, 154, 110045.

Catalano, J. G., Thermodynamic and mass balance constraints on iron-bearing phyllosilicate formation and alteration pathways on early Mars, *Journal of Geophysical Research. Planets,* **2013**, 118, 2124-2136.

Chaikin, A., Hanks, T., A Man on the Moon: The Voyages of the Apollo Astronauts, 1st ed. **2007**, Penguin Books Limited, London, UK.

Chen, M., Xiao, W., Xie, X., Coesite and quartz characteristic of crystallization from shock-produced silica melt in the Xiuyan crater, *Earth and Planetary Science Letters,* **2010**, 297, 306-314.

Chide, B., Maurice, S., Murdoch, N., Lasue, J., Bousquet, B., Jacob, X., Cousin, A., Forni, O., Gasnault, O., Meslin, P., et al., Listening to laser sparks: a link between Laser-Induced Breakdown Spectroscopy, acoustic measurements and crater morphology, *Spectrochimica Acta. Part B: Atomic Spectroscopy,* **2019**, 153, 50-60.

Chopelas, A., Single crystal Raman spectra of forsterite, fayalite, and monticellite, *The American Mineralogist,* **1991**, 76, 1101-1109.

Christensen, P. R., Bandfield, J. L., Rogers, A. D., Glotch, T. D. R., Hamilton, V. E., Ruff, S. W., Wyatt, M. B., The Martian Surface; Global mineralogy mapped from the Mars Global Surveyor Thermal Emission Spectrometer (p.p. 193-220) **2008,** Cambridge University Press, Cambridge, UK.

Clenet, H., Jutzi, M., Barrat, J., Asphaug, E. I., Benz, W., Gillet, P., A deep crust-mantle boundary in the asteroid 4 Vesta, *Nature,* **2014**, 511, 303-306.

Cloutis, E., Szymanski, P., Applin, D., Goltz, D., Identification and discrimination of polycyclic aromatic hydrocarbons using Raman spectroscopy, *Icarus,* **2016**, 274, 211-230.

Collins, G. S., Wünnemann, K., How big was the Chesapeake Bay impact? Insight from numerical modeling, *Geology,* **2005**, 33, 925-928.

Craig, P. I., Ming, D. W., Rampe, E. B., Morris, R. V., Sulfate Mineral Formation from Acid-Weathered Phyllosilicates: Implications for the Aqueous History of Mars, .

Crozaz, G., Wadhwa, M., The terrestrial alteration of Saharan shergottites Dar al Gani 476 and 489: a case study of weathering in a hot desert environment, *Geochimica Et Cosmochimica Acta,* **2001**, 65, 971-977.

DasSarma, S., Schwieterman, E. W., Early evolution of purple retinal pigments on Earth and implications for exoplanet biosignatures, *International Journal of Astrobiology,* **2018**, 1-10.

Davis, A. M., Meteorites, comets and planets, 1st ed. **2005**, Elsevier, Amsterdam, the Netherlands.

De Gelder, J., De Gussem, K., Vandenabeele, P., Moens, L., Reference database of Raman spectra of biological molecules, *Journal of Raman Spectroscopy,* **2007**, 38, 1133-1147.

De Sanctis, M. C., Ammannito, E., Capria, M. T., Tosi, F., Capaccioni, F., Zambon, F., Carraro, F., Fonte, S., Frigeri, A., Jaumann, R., et al., Spectroscopic Characterization of Mineralogy and Its Diversity Across Vesta, *Science,* **2012**, 336, 697-700.

Decremps, F., Pellicer-Porres, J., Saitta, A. M., Chervin, J., Polian, A., High-pressure Raman spectroscopy study of wurtzite ZnO, *Physical Review. B, Condensed Matter,* **2002**, 65.

Dodony, I., Posfai, M., Buseck, P. R., Revised structure models for antigorite; an HRTEM study, *The American Mineralogist,* **2002**, 87, 1443-1457.

Edwards, H. G. M., Farwell, D. W., Grady, M. M., Wynn-Williams, D. D., Wright, I. P., Comparative Raman microscopy of a Martian meteorite and Antarctic lithic analogues, *Planetary and Space Science,* **1999**, 47, 353-362.

Edwards, H. G. M., Villar, S. E. J., Parnell, J., Cockell, C. S., Lee, P., Raman spectroscopic analysis of cyanobacterial gypsum halotrophs and relevance for sulfate deposits on Mars, *Analyst,* **2005**, 13, 917-923.

Edwards, H. G. M., Vandenabeele, P., Jorge-Villar, S. E., Carter, E. A., Perez, F. R., Hargreaves, M. D., The Rio Tinto Mars Analogue site: An extremophilic Raman spectroscopic study, *Spectrochimica Acta. Part A, Molecular and Biomolecular Spectroscopy,* **2007**, 68, 1133-1137.

Eggleton, R. A., Tilley, D. B., Hisingerite: a ferric kaolin mineral with curved morphology, *Clays and Clay Minerals,* **1998**, 46, 400-413.

Ehlmann, B. L., Bish, D. L., Ruff, S. W., Mustard, J. F., Mineralogy and chemistry of altered Icelandic basalts: Application to clay mineral detection and understanding aqueous environments on Mars, *Journal of Geophysical Research: Planets,* **2012**, 117, 1-27.

Ehlmann, B. L., Mustard, J. F., Murchie, S. L., Poulet, F., Bishop, J. L., Brown, A. J., Calvin, W. M., Clark, R. N., Marais, D. J. D., Milliken, R. E., et al., Orbital Identification of Carbonate-Bearing Rocks on Mars, *Science,* **2008**, 322, 1828-1832.

Elkins-Tanton, L. T., hess, P. C., Parmentier, E. M., Possible formation of ancient crust on Mars through magma ocean processes, *Journal of Geophysical Research - Planets,* **2005**, 110, 1-11.

English, P. M., Formation of analcime and moganite at Lake Lewis, central Australia: significance of groundwater evolution in diagenesis, *Sedimentary Geology,* **2001**, 143, 219-244.

Farley, K. A., Williford, K. H., Stack, K. M., Bhartia, R., Chen, A., de la Torre, M., Hand, K., Mars 2020 Mission Overview, *Space Science Reviews,* **2020**, 216.

Farquhar, J., Kim, S., Masterson, A., Implications from sulfur isotopes of the Nakhla meteorite for the origin of sulfate on Mars, *Earth and Planetary Science Letters,* **2007**, 264, 1-8.

Farrell-Turner, S., Reimold, W. U., Nieuwoudt, M., Erasmus, R. M., Raman spectroscopy of olivine in dunite experimentally shocked to pressures between 5 and 59 GPa, *Meteoritics & Planetary Science,* **2005**, 40, 1311-1327.

Fernández-Remolar, D. C., Sánchez-Román, M., Amils, R., The case of the lacking carbonates and the emergence of early life on mars, *Sustainability (Basel, Switzerland),* **2010**, 2, 2541-2554.

Filiberto, J., Schwenzer, S. P., Volatiles in the Martian Crust, **2018**, Elsevier, Saint Louis, Missouri, USA.

Fong, M. Y., Nicol, M., Raman spectrum of calcium carbonate at high pressures, *The Journal of Chemical Physics,* **1971**, 54, 579-585.

Ford, M. H., Auerbach, S. M., Monson, P. A., On the mechanical properties and phase behavior of silica: a simple model based on low coordination and strong association, *The Journal of Chemical Physics,* **2004**, 121, 8415-8422.

Formisano, V., Atreya, S., Encrenaz, T., Ignatiev, N., Giuranna, M., Detection of Methane in the Atmosphere of Mars, *Science,* **2004**, 306, 1758-1761.

Fornaro, T., Brucato, J. R., Poggiali, G., Corazzi, M. A., Biczysko, M., Jaber, M., Foustoukos, D. I., UV Irradiation and Near Infrared Characterization of Laboratory Mars Soil Analog Samples, *Frontiers in Astronomy and Space Sciences,* **2020**, 7.

Freeman, J. J., Wang, A., Kuebler, K. E., Jolliff, B. L., Haskin, L. A., Characterization of natural feldspars by Raman spectroscopy for future planetary exploration, *Canadian Mineralogist,* **2008**, 46, 1477-1500.

Frey, F., Jagodzinski, H., Prandl, W., Yelon, W. B., Dynamic character of the primitive to body-centered phase transition in anorthite, *Physics and Chemistry of Minerals,* **1977**, 1, 227-231.

Fritz, J., Wünnemann, K., Reimold, W. U., Meyer, C., Hornemann, U., Shock experiments on quartz targets pre-cooled to 77 K, *International Journal of Impact Engineering,* **2011**, 38, 440-445.

Fritz, J., Artemieva, N., Greshake, A., Ejection of Martian meteorites, *Meteoritics & Planetary Science,* **2005**, 40, 1393-1411.

Fritz, J., Greshake, A., High-pressure phases in an ultramafic rock from Mars, *Earth and Planetary Science Letters,* **2009**, 288, 619-623.

Fritz, J., Greshake, A., Stoffler, D., Micro-Raman spectroscopy of plagioclase and maskelynite in Martian meteorites: Evidence of progressive shock metamorphism, *Antarctic Meteorite Research,* **2005**, 18, 96-116.

Frost, R. L., Xi, Y., Raman spectroscopic study of the minerals apophyllite-(KF) $KCa_4Si_8O_{20}F{\cdot}8H_2O$ and apophyllite-(KOH) $KCa_4Si_8O_{20}(F,OH){\cdot}8H_2O$, *Journal of Molecular Structure,* **2012**, 1028, 200-207.

Gaft, M., Reisfeld, R., Panczer, G., Modern Luminescence Spectroscopy of Minerals and Materials, **2015**, Springer International Publishing AG, Cham, Germany.

García-Florentino, C., Gomez-Nubla, L., Huidobro, J., Torre-Fdez, I., Ruíz-Galende, P., Aramendia, J., Hausrath, E. M., Castro, K., Arana, G., Madariaga, J. M., Interrelationships in the Gypsum–Syngenite–Görgeyite System and Their Possible Formation on Mars, *Astrobiology,* **2021**, 21, 332-344.

Garvin, J. B., Frawley, J. J., Sakimoto, S. E. H., Craters on Mars: Global Geometric Properties from Gridded MOLA Topography, *6th International Conference on Mars,* **July 20, 2003,** Pasadena, California, USA.

Gasda, P. J., Haldeman, E. B., Wiens, R. C., Rapin, W., Bristow, T. F., Bridges, J. C., Schwenzer, S. P., Clark, B., Herkenhoff, K., Frydenvang, J., et al., In situ detection of boron by ChemCam on Mars, *Geophysical Research Letters,* **2017**, 44, 8739-8748.

Gaudin, A., Dehouck, E., Grauby, O., Mangold, N., Formation of clay minerals on Mars: Insights from long-term experimental weathering of olivine, *Icarus,* **2018**, 311, 210-223.

Gay, P., Taylor, W. H., The structures of the plagioclase felspars. IV. Variations in the anorthite structure, *Acta Crystallographica,* **1953**, 6, 647-650.

Geyh, M. A., Schleicher, H., Absolute Age Determination: Physical and Chemical Dating Methods and Their Application, **1990**, Springer-Verlag, Berlin Heidelberg.

Gillet, P., Biellmann, C., Reynard, B., McMillan, P., Raman spectroscopic studies of carbonates part I: High-pressure and high-temperature behaviour of calcite, magnesite, dolomite and aragonite, *Physics and Chemistry of Minerals,* **1993**, 20.

Gilmore, M. S., Golder, K. B., Korn, L., Aaron, L. M., Carbonate Associated with Gullies in the Eridania Region of Mars, *Eighth International Conference on Mars,* **July 14, 2014,** Pasadena, California, USA.

Goncharov, A. F., Raman Spectroscopy at High Pressures, *International Journal of Spectroscopy,* **2012**, 2012, 1-16.

Goudge, T. A., Mustard, J. F., Head, J. W., Fassett, C. I., Wiseman, S. M., Assessing the mineralogy of the watershed and fan deposits of the Jezero crater paleolake system, Mars, *Journal of Geophysical Research. Planets,* **2015**, 120, 775-808.

Greenwood, N. N., Earnshaw, A., Chemistry of the Elements, 2nd ed. **1997**, Butterworth- Heinemann, Oxford, UK.

Grossman, J. N., The Meteoritical Bulletin, No. 84, 2000 August, *Meteoritics & Planetary Science,* **2000**, 35, A199-A225.

Grossman, J. N., The Meteoritical Bulletin, No. 76, 1994 January: The U.S. Antarctic Meteorite Collection, *Meteoritics,* **1994**, 29, 100-143.

Guyot, F., Boyer, H., Madon, M., Velde, B., Poirier, J. P., Comparison of the Raman microprobe spectra of $(Mg,Fe)_2SiO_4$ and $Mg_2GeO_4$ with olivine and spinel structures, *Physics and Chemistry of Minerals,* **1986**, 13, 91-95.

Haberle, R. M., Clancy, R. T., Forget, F., Smith, M. D., Zurek, R. W., The atmosphere and climate of Mars, **2017**, Cambridge University Press, Cambridge, United Kingdom.

Hadjiev, V. G., Iliev, M. N., Vergilov, I. V., The Raman spectra of $Co_3O_4$, *Journal of Physics. C, Solid State Physics,* **1988**, 21, L199-L201.

Halliday, A. N., Wänke, H., Birck, J. L., Clayton, R. N., Chronology and Evolution of Mars; The Accretion, Composition and Early Differentiation of Mars (p.p. 197-230) **2001,** Springer, the Netherlands, Dordrecht.

Hamran, S., Paige, D. A., Amundsen, H. E. F., Berger, T., Brovoll, S., Carter, L., Hanssen, L., Dypvik, H., Eide, J., Eide, S., et al., Radar imager for Mars' subsurface experiment—RIMFAX, *Space Science Reviews,* **2020**, 216.

Hartmann, W. K., Martian cratering 9: Toward resolution of the controversy about small craters, *Icarus,* **2007**, 189, 274-278.

Hartmann, W. K., Martian cratering 8: Isochron refinement and the chronology of Mars, *Icarus,* **2005**, 174, 294-320.

Hartmann, W., Neukum, G., Cratering Chronology and the Evolution of Mars, *Space Science Reviews,* **2001**, 96, 165-194.

Haskin, L. A., Korotev, R. L., Jolliff, B. L., Wang, A., Viskupic, K. M., Rockow, K. M., Raman Spectroscopy for Mineral Identification and Quantification for in situ Planetary Surface Analysis: A Point Count Method, *Journal of Geophysical Research,* **1997**, 102, 19293-19306.

Hecht, M., Hoffman, J., Rapp, D., McClean, J., SooHoo, J., Schaefer, R., Aboobaker, A., Mellstrom, J., Hartvigsen, J., Meyen, F., et al., Mars Oxygen ISRU Experiment (MOXIE), *Space Science Reviews,* **2021**, 217.

Hemley, R. J., Effects of high pressure on molecules, *Annual Review of Physical Chemistry,* **2000**, 51, 763-800.

Henderson, C. M. B., Taylor, D., Structural behaviour of chkalovite, Na2BeSi2O6: a member of the cristobalite family, *Mineralogical Magazine,* **1989**, 53, 117-119.

Herd, C. D. K., Papike, J. J., Brearley, A. J., Oxygen fugacity of Martian basalts from electron microprobe oxygen and TEM-EELS analyses of Fe-Ti oxides, *The American Mineralogist,* **2001**, 86, 1015-1024.

Herpers, U., Vogt, S., Bremer, K., Hofmann, H. J., Suter, M., Wieler, R., Lange, H. J., Michel, R., Cosmogenic nuclides in differentiated antarctic meteorites: measurements and model calculations, *Planetary and Space Science,* **1995**, 43, 545-556.

Hoefen, T. M., Clark, R. N., Bandfield, J. L., Smith, M. D., Pearl, J. C., Christensen, P. R., Discovery of Olivine in the Nili Fossae Region of Mars, *Science,* **2003**, 302, 627-630.

Hoffmann, G. G., Raman spectroscopy, **2019**, Momentum Press, New York, New York, USA.

Holzhausen, G. R., Johnson, A. M., The concept of residual stress in rock, *Tectonophysics,* **1979**, 58, 237-267.

Huang, E., Chen, C. H., Huang, T., Lin, E. H., Xu, J., Raman spectroscopic characteristics of Mg-Fe-Ca pyroxenes, *The American Mineralogist,* **2000**, 85, 473-479.

Humayun, M., Yang, S., Righter, K., Zanda, B., Hewins, R. H., The Germanium Dichotomy in Martian Meteorites, *47th Lunar and Planetary Science Conference,* **March 21, 2016,** The Woodlands, Texas, USA.

Hutchinson, I. B., Ingley, R., Edwards, H. G. M., Harris, L., McHugh, M., Malherbe, C., Parnell, J., Raman spectroscopy on Mars: identification of geological and bio-geological signatures in Martian analogues using miniaturized Raman spectrometers, *Philosophical Transactions of the Royal Society of London. Series A: Mathematical, Physical, and Engineering Sciences,* **2014**, 372, 20140204.

Iishi, K., Lattice dynamics of forsterite, *The American Mineralogist,* **1978**, 63, 1198-1208.

Ishibashi, H., Arakawa, M., Yamamoto, J., Kagi, H., Precise determination of Mg/Fe ratios applicable to terrestrial olivine samples using Raman spectroscopy, *Journal of Raman Spectroscopy,* **2012**, 43, 331-337.

J. Wright Horton, J., Michael J. Kunk, Harvey E. Belkin, John N. Aleinikoff, John C. Jackson, I-Ming Chou, Evolution of crystalline target rocks and impactites in the Chesapeake Bay impact structure, ICDP-USGS Eyreville B core, *Special Papers (Geological Society of America),* **2009**, 458, 277.

Jakobsson, S. P., Jónsson, J., Shido, F., Petrology of the Western Reykjanes Peninsula, Iceland, *Journal of Petrology,* **1978**, 19, 669-705.

James, E., The History and Practice of Ancient Astronomy, 1st ed. **1998**, Oxford University Press, Oxford, UK.

Jehlička, J., Edwards, H. G. M., Raman spectroscopy as a tool for the non-destructive identification of organic minerals in the geological record, *Organic Geochemistry,* **2008**, 39, 371-386.

Jull, A. J. T., Courtney, C., Jeffrey, D. A., Beck, J. W., Isotopic Evidence for a Terrestrial Source of Organic Compounds Found in Martian Meteorites Allan Hills 84001 and Elephant Moraine 79001, *Science,* **1998**, 279, 366-369.

Jull, A. J. T., Beck, J. W., Burr, G. S., Isotopic evidence for extraterrestrial organic material in the Martian meteorite, Nakhla, *Geochimica Et Cosmochimica Acta,* **2000**, 64, 3763-3772.

Kenji Hiraga, Eiji Ohtani, Toshiro Nagase, Henry J. Melosh, Masaaki Miyahara, Shin Ozawa, Naohisa Hirao, Ahmed El Goresy, Makoto Kimura, Takeshi Sakai, et al., Natural dissociation of olivine to (Mg,Fe) $SiO_3$ perovskite and magnesiowüstite in a shocked Martian meteorite, *Proceedings of the National Academy of Sciences - PNAS,* **2011**, 108, 5999-6003.

Kereszturi, A., Chatzitheodoridis, E., Searching for the Source Crater of Nakhlite Meteorites, *Origins of Life and Evolution of Biospheres,* **2016**, 46, 455-471.

King, R. J., Olivine Group, *Geology Today,* **2009**, 25, 193-197.

Kirkland, B. L., Lynch, F. L., Rahnis, M. A., Folk, R. L., Molineux, I. J., McLean, R. J. C., Alternative origins for nannobacteria-like objects in calcite, *Geology,* **1999**, 27, 347-350.

Klein, C., Hurlbut, C. S., Dana, J. D., Manual of mineralogy, 21st ed. **1999**, Wiley, New York, New York, USA.

Klein, C., Philpotts, A. R., Earth materials, 2nd ed. **2017**, Cambridge University Press, Cambridge.

Kloprogge, J. T., Developments in Clay Science; Raman Spectroscopy of Clay Minerals (p.p. 150-99) **2017,** Elsevier Ltd, Amsterdam, the Netherlands.

Kolesov, B. A., Geiger, C. A., A Raman spectroscopic study of Fe–Mg olivines, *Physics and Chemistry of Minerals,* **2004**, 31, 142-154.

Kolesov, B. A., Tanskaya, J. V., Raman spectra and cation distribution in the lattice of olivines, *Materials Research Bulletin,* **1996**, 31, 1035-1044.

Krissansen-Totton, J., Bergsman, D. S., Catling, D. C., On Detecting Biospheres from Chemical Thermodynamic Disequilibrium in Planetary Atmospheres, *Astrobiology,* **2016**, 16, 39-67.

Kuebler, K. E., Jolliff, B. L., Wang, A., Haskin, L. A., Extracting olivine (Fo–Fa) compositions from Raman spectral peak positions, *Geochimica Et Cosmochimica Acta,* **2006**, 70, 6201-6222.

Kurokawa, H., Sato, M., Ushioda, M., Matsuyama, T., Moriwaki, R., Dohm, J. M., Usui, T., Evolution of water reservoirs on Mars: Constraints from hydrogen isotopes in martian meteorites, *Earth and Planetary Science Letters,* **2014**, 394, 179-185.

Lafuente, B., Downs, R. T., Yang, H., Stone, N., Highlights in Mineralogical Crystallography; The power of databases: The RRUFF project (p.p. 1-30) **2015,** de Gruyter, Berlin, München, Boston.

Lane, M. D., Christensen, P. R., Determining olivine composition of basaltic dunes in Gale Crater, Mars, from orbit: Awaiting ground truth from Curiosity, *Geophysical Research Letters,* **2013**, 40, 3517-3521.

Latorre, F., Guthmuller, J., Marquetand, P., A spectroscopic study of the cis/trans-isomers of penta-2,4-dienoic acid attached to gold nanoclusters, *Physical Chemistry Chemical Physics,* **2015**, 17, 7648-7658.

Leshin, L. A., Vicenzi, E., Aqueous processes recorded by Martian meteorites; analyzing Martian water on Earth, *Elements,* **2006**, 2, 157-162.

Lin, Y., El Goresy, A., Hu, S., Zhang, J., Gillet, P., Xu, Y., Hao, J., Miyahara, M., Ouyang, Z., Ohtani, E., et al., NanoSIMS analysis of organic carbon from the Tissint Martian meteorite: Evidence for the past existence of subsurface organic-bearing fluids on Mars, *Meteoritics & Planetary Science,* **2014**, 49, 2201-2218.

Liu, C., Zheng, H., Wang, D., Raman spectroscopic study of calcite III to aragonite transformation under high pressure and high temperature, *High Pressure Research,* **2017**, 37, 545-557.

Liu, L., Mernagh, T. P., Raman spectra of forsterite and fayalite at high pressures and room temperature, *High Pressure Research,* **1993**, 11, 241-256.

Liu, L., Mernagh, T. P., Phase transitions and Raman spectra of calcite at high pressures and room temperature, *The American Mineralogist,* **1990**, 75, 801-806.

Lowell, P., Mars and its Canals (reproduction of the original), **2020**, Outlook Verlag GmbH, Frankfurt, Germany.

Lowell, P., Lockyer, J. N., First photographs of the canals of Mars, *Proceedings of the Royal Society A: Mathematical, Physical and Engineering Sciences,* **1906**, 77, 132-135.

Lunar and Planetary Institute, Meteoritical Bulletin Database [Internet]. Available from: https://www.lpi.usra.edu/meteor/ [accessed May 18, 2021].

Lunar and Planetary Lab, University of Arizona, Gamma Ray Spectrometer (GRS), Mars Odyssey [Internet]. Available from: https://grs.lpl.arizona.edu/home.jsp [accessed May 18, 2021].

Lyne, J. E., Tauber, M., Fought, R., An analytical model of the atmospheric entry of large meteors and its application to the Tunguska Event, *Journal of Geophysical Research: Planets,* **1996**, 101, 23207-23212.

M. Akaogi, Phase transitions of minerals in the transition zone and upper part of the lower mantle, *Special Papers (Geological Society of America),* **2007**, 421, 1.

Magna, T., Šimčíková, M., Moynier, F., Lithium systematics in howardite–eucrite–diogenite meteorites: Implications for crust–mantle evolution of planetary embryos, *Geochimica Et Cosmochimica Acta,* **2014**, 125, 131-145.

Malin, M. C., Edgett, K. S., Posiolova, L. V., McColley, S. M., Dobrea, E. Z. N., Present-Day Impact Cratering Rate and Contemporary Gully Activity on Mars, *Science,* **2006**, 314, 1573-1577.

Mangold, N., Poulet, F., Mustard, J. F., Bibring, J. P., Gondet, B., Langevin, Y., Ansan, V., Masson, P. H., Fassett, C., Head, J. W., et al., Mineralogy of the Nili Fossae region with OMEGA/Mars Express data: 2. Aqueous alteration of the crust, *Journal of Geophysical Research. Planets,* **2007**, 112, 1-25.

Manrique, J. A., Lopez-Reyes, G., Cousin, A., Rull, F., Maurice, S., Wiens, R. C., Madsen, M. B., SuperCam Calibration Targets: Design and Development, *Space Science Reviews,* **2020**, 216, 138.

Martín-Torres, F. J., Zorzano, M., Valentín-Serrano, P., Harri, A., Genzer, M., Kemppinen, O., Rivera-Valentin, E. G., Jun, I., Wray, J., Bo Madsen, M., et al., Transient liquid water and water activity at Gale Crater on Mars, *Nature Geoscience,* **2015**, 8, 357-361.

Maurice, S., Wiens, R. C., Bernardi, P., Caïs, P., Robinson, S., Nelson, T., Gasnault, O., Reess, J. M., Deleuze, M., Rull, F., et al., The SuperCam Instrument Suite on the Mars 2020 Rover: Science Objectives and Mast-Unit Description, *Space Science Reviews,* **2021**, 217, 47.

McDonald, G. D., Bada, J. L., A search for endogenous amino acids in the Martian meteorite EETA79001, *Geochimica Et Cosmochimica Acta,* **1995**, 59, 1179-1184.

McKeown, D. A., Raman spectroscopy and vibrational analyses of albite: from 25°C through the melting temperature, *The American Mineralogist,* **2005**, 90, 1506-1517.

McLennan, S. M., Sedimentary silica on Mars, *Geology,* **2003**, 31, 315-318.

Mcmillan, P. F., Wolf, G. H., Lambert, P., A Raman spectroscopic study of shocked single crystalline quartz, *Physics and Chemistry of Minerals,* **1992**, 19, 71-79.

McSween, H. Y., Harvey, R. P., A possible high-temperature origin for the carbonates in the martian meteorite ALH84001, *Nature,* **1996**, 382, 49-51.

Melosh, H. J., Impact ejection, spallation, and the origin of meteorites, *Icarus,* **1984**, 59, 234-260.

MEPAG Special Regions-Science Analysis Group, Findings of the Mars Special Regions Science Analysis Group, *Astrobiology,* **2006**, 6, 677-732.

Mer'kov, A. N., Bussen, I. V., Goyko, Y. A., Kul'chitskaya, Y. A., Men'shikov, Y. P., Nedorezova, A. P., Raite and zorite, new minerals from the Lovozero Tundra, *International Geology Review,* **1973**, 15, 1087-1094.

Michalski, J. R., Kraft, M. D., Diedrich, T., Sharp, T. G., Christensen, P. R., Thermal emission spectroscopy of the silica polymorphs and considerations for remote sensing of Mars, *Geophysical Research Letters,* **2003**, 30, 1-4.

Michalski, J. R., Niles, P. B., Deep crustal carbonate rocks exposed by meteor impact on Mars, *Nature Geoscience,* **2010**, 3, 751-755.

Mikouchi, T., Miyamoto, M., Micro Raman spectroscopy of amphiboles and pyroxenes in the Martian meteorites Zagami and Lewis Cliff 88516, *Meteoritics & Planetary Science,* **2000**, 35, 155-159.

Mikouchi, T., Miyamoto, M., McKay, G. A., Mineralogy and petrology of the Dar al Gani 476 martian meteorite: Implications for its cooling history and relationship to other shergottites, *Meteoritics & Planetary Science,* **2001**, 36, 531-548.

Miller, C. F., Stoddard, E. F., Bradfish, L. J., Dollase, W. A., Composition of plutonic muscovite: genetic implications, *Canadian Mineralogist,* **1981**, 19, 25-34.

Morimoto, N., Fabries, J., Ferguson, A. K., Ginzburg, I. V., Ross, M., Seifert, F. A., Zussman, J., Aoki, K., Gottardi, G., Nomenclature of Pyroxenes, *Mineralogy and Petrology,* **1988**, 39, 55-76.

Morris, R. V., Vaniman, D. T., Blake, D. F., Gellert, R., Chipera, S. J., Rampe, E. B., Ming, D. W., Morrison, S. M., Downs, R. T., Treiman, A. H., et al., Silicic volcanism on Mars evidenced by tridymite in high-$SiO_2$ sedimentary rock at Gale crater, *Proceedings of the National Academy of Sciences,* **2016**, 113, 7071-7076.

Morris, R. V., Ruff, S. W., Gellert, R., Ming, D. W., Arvidson, R. E., Clark, B. C., Golden, D. C., Siebach, K., Klingelhöfer, G., Schröder, C., et al., Identification of Carbonate-Rich Outcrops on Mars by the Spirit Rover, *Science,* **2010**, 329, 421-424.

Mouri, T., Enami, M., Raman spectroscopic study of olivine-group minerals, *Journal of Mineralogical and Petrological Sciences,* **2008**, 103, 100-104.

Muirhead, B. K., Nicholas, A. K., Umland, J., Sutherland, O., Vijendran, S., Mars Sample Return Campaign Concept Status, *Acta Astronautica,* **2020**, 176, 131-138.

Mumma, M. J., Villanueva, G. L., Novak, R. E., Hewagama, T., Bonev, B. P., DiSanti, M. A., Mandell, A. M., Smith, M. D., Strong Release of Methane on Mars in Northern Summer 2003, *Science,* **2009**, 323, 1041-1045.

Murchie, S. L., Mustard, J. F., Ehlmann, B. L., Milliken, R. E., Bishop, J. L., McKeown, N. K., Noe Dobrea, E. Z., Seelos, F. P., Buczkowski, D. L., Wiseman, S. M., et al., A synthesis of Martian aqueous mineralogy after 1 Mars year of observations from the Mars Reconnaissance Orbiter, *Journal of Geophysical Research. Planets,* **2009**, 114, 1-30.

Mustard, J. F., Murchie, S. L., Pelkey, S. M., Ehlmann, B. L., Milliken, R. E., Grant, J. A., Bibring, J. P., Poulet, F., Bishop, J., Dobrea, E. N., et al., Hydrated silicate minerals on Mars observed by the Mars Reconnaissance Orbiter CRISM instrument, *Nature,* **2008**, 454, 305-309.

Nachon, M., Clegg, S. M., Mangold, N., Schröder, S., Kah, L. C., Dromart, G., Ollila, A., Johnson, J. R., Oehler, D. Z., Bridges, J. C., et al., Calcium sulfate veins characterized by ChemCam/Curiosity at Gale crater, Mars, *Journal of Geophysical Research. Planets,* **2014**, 119, 1991-2016.

National Aeronautics and Space Administration, The Mars Orbiter Laser Altimeter [Internet]. Available from: https://attic.gsfc.nasa.gov/mola/images.html [accessed May 18, 2021].

Nelson, M., Mars water discoveries - implications for finding ancient and current life, *Life Sciences in Space Research,* **2015**, 7, 1-5.

Neukum, G., Hiller, K., Martian ages, *Journal of Geophysical Research: Solid Earth,* **1981**, 86, 3097-3121.

Neukum, G., Wise, D. U., Mars: A Standard Crater Curve and Possible New Time Scale, *Science,* **1976**, 194, 1381-1387.

Neukum, G., Basilevsky, A. T., Kneissl, T., Chapman, M. G., van Gasselt, S., Michael, G., Jaumann, R., Hoffmann, H., Lanz, J. K., The geologic evolution of Mars: Episodicity of resurfacing events and ages from cratering analysis of image data and correlation with radiometric ages of Martian meteorites, *Earth and Planetary Science Letters,* **2010**, 294, 204-222.

Neumann, G. A., Zuber, M. T., Wieczorek, M. A., McGovern, P. J., Lemoine, F. G., Smith, D. E., Crustal structure of Mars from gravity and topography, *Journal of Geophysical Research: Planets,* **2004**, 109.

Nikiforov, S. Y., Mitrofanov, I. G., Litvak, M. L., Lisov, D. I., Djachkova, M. V., Jun, I., Tate, C. G., Sanin, A. B., Assessment of water content in martian subsurface along the traverse of the Curiosity rover based on passive measurements of the DAN instrument, *Icarus,* **2020**, 346, 113818.

Nimmo, F., Tanaka, K., Early crustal evolution of mars, *Annual Review of Earth and Planetary Sciences,* **2005**, 33, 133-161.

Oberti, R., Hawthorne, F. C., Cannillo, E., Camara, F., Long-range order in amphiboles, *Reviews in Mineralogy and Geochemistry,* **2007**, 67, 125-171.

Ody, A., Poulet, F., Bibring, J. P., Loizeau, D., Carter, J., Gondet, B., Langevin, Y., Global investigation of olivine on Mars: Insights into crust and

mantle compositions, *Journal of Geophysical Research. Planets,* **2013**, 118, 234-262.

Osinski, G. R., Pierazzo, E., Impact Cratering, 1st ed. **2012**, Wiley-Blackwell, Chicester, UK.

Papike, J. J., Chemistry of the rock-forming silicates: Ortho, ring, and single-chain structures, *Reviews of Geophysics,* **1987**, 25, 1483-1526.

Papike, J. J., Karner, J. M., Shearer, C. K., Burger, P. V., Silicate mineralogy of Martian meteorites, *Geochimica Et Cosmochimica Acta,* **2009**, 73, 7443-7485.

Peplow, M., How Mars got its rust, *Nature news,* **2004** May 3,.

Petitto, S. C., Marsh, E. M., Carson, G. A., Langell, M. A., Cobalt oxide surface chemistry: The interaction of CoO(1 0 0), $Co_3O_4$(1 1 0) and $Co_3O_4$(1 1 1) with oxygen and water, *Journal of Molecular Catalysis. A, Chemical,* **2008**, 281, 49-58.

Pettit, E., Nicholson, S. B., Radiation measures on the planet Mars, *Publications of the Astronomical Society of the Pacific,* **1924**, 36, 269-272.

Pla-García, J., Rafkin, S. C. R., Martinez, G. M., Vicente-Retortillo, Á, Newman, C. E., Savijärvi, H., de la Torre, M., Rodriguez-Manfredi, J. A., Gómez, F., Molina, A., et al., Meteorological Predictions for Mars 2020 Perseverance Rover Landing Site at Jezero Crater, *Space Science Reviews,* **2020**, 216.

Poulet, F., Mangold, N., Loizeau, D., Bibring, J. -., Langevin, Y., Michalski, J., Gondet, B., Abundance of minerals in the phyllosilicate-rich units on Mars, *Astronomy and Astrophysics (Berlin),* **2008**, 487, L41-L44.

Powell, J., From cave art to Hubble; Cave Paintings That Recorded the Night Sky (p.p. 9-16) **2019,** Springer, New York, USA.

Radu, G. L., Badea, G. I., Carboxylic Acid - Key Role in Life Sciences, **2018**, IntechOpen, London, UK.

Rampe, E. B., Blake, D. F., Bristow, T. F., Ming, D. W., Vaniman, D. T., Morris, R. V., Achilles, C. N., Chipera, S. J., Morrison, S. M., Tu, V. M., et al., Mineralogy and geochemistry of sedimentary rocks and eolian sediments in Gale crater, Mars: A review after six Earth years of exploration with Curiosity, *Geochemistry,* **2020**, 80, 1-31.

Reddy, B. J., Frost, R. L., Spectroscopic characterization of chromite from the Moa-Baracoa Ophiolitic Massif, Cuba, *Spectrochimica Acta. Part A, Molecular and Biomolecular Spectroscopy,* **2005**, 61, 1721-1728.

Righter, K., Drake, M. J., A magma ocean on Vesta: Core formation and petrogenesis of eucrites and diogenites, *Meteoritics & Planetary Science,* **1997**, 32, 929-944.

Rogers, A. D., Arvidson, R. E., Glotch, T. D., Wyatt, M. B., Bandfield, J. L., Blaney, D. L., Budney, C., Christensen, P. R., Anwar, S., Calvin, W. M., Mineral Composition and Abundance of the Rocks and Soils at Gusev and Meridiani from the Mars Exploration Rover Mini-TES Instruments, **2005**.

Rubin, A. E., Grossman, J. N., Meteorite and meteoroid: New comprehensive definitions, *Meteoritics & Planetary Science,* **2010**, 45, 114-122.

Ruggles, C. L. N., Ancient Astronomy: An Encyclopedia of Cosmologies and Myth, 1st ed. **2005**, ABC-CLIO, Santa Barbara, California, USA.

Ruiz-Galende, P., Torre-Fdez, I., Aramendia, J., Gómez-Nubla, L., Castro, K., Arana, G., Madariaga, J. M., Study of a terrestrial Martian analogue: Geochemical characterization of the Meñakoz outcrops (Biscay, Spain), *Journal of Raman Spectroscopy,* **2020**, 51, 1603-1612.

Ruiz-Galende, P., Fernández, G., Torre-Fdez, I., Aramendia, J., Gomez-Nubla, L., García-Florentino, C., Castro, K., Arana, G., Madariaga, J. M., Characterization of sedimentary and volcanic rocks in Armintza outcrop (Biscay, Spain) and its implication for Oxia Planum (Mars) exploration, *Spectrochimica Acta. Part A, Molecular and Biomolecular Spectroscopy,* **2021**, 251, 119443.

Rull, F., Martinez-Frias, J., Sansano, A., Medina, J., Edwards, H. G. M., Comparative micro-Raman study of the Nakhla and Vaca Muerta meteorites, *Journal of Raman Spectroscopy,* **2004**, 35, 497-503.

Ruzicka, A., Grossman, J., Bouvier, A., Herd, C. D. K., Agee, C. B., The Meteoritical Bulletin, No. 102, *Meteoritics & Planetary Science,* **2015**, 50, 1662.

Sarbas, B., Töpper, W., Ditz, R., Mn Manganese, 8th ed. **1993**, Springer, Heidelberg, Germany.

Sautter, V., Barrat, J. A., Jambon, A., Lorand, J. P., Gillet, P., Javoy, M., Joron, J. L., Lesourd, M., A new Martian meteorite from Morocco: the nakhlite North West Africa 817, *Earth and Planetary Science Letters,* **2002**, 195, 223-238.

Sautter, V., Jambon, A., Boudouma, O., Cl-amphibole in the nakhlite MIL 03346: Evidence for sediment contamination in a Martian meteorite, *Earth and Planetary Science Letters,* **2006**, 252, 45-55.

Sautter, V., Toplis, M. J., Beck, P., Mangold, N., Wiens, R., Pinet, P., Cousin, A., Maurice, S., LeDeit, L., Hewins, R., et al., Magmatic complexity on early Mars as seen through a combination of orbital, in-situ and meteorite data, *Lithos,* **2016**, 254-255, 36-52.

Schlüter, J., Schultz, L., Thiedig, F., Al-Mahdi, B. O., Aghreb, A. E. A., The Dar al Gani meteorite field (Libyan Sahara): Geological setting, pairing of meteorites, and recovery density, *Meteoritics & Planetary Science,* **2002**, 37, 1079-1093.

Schon, S. C., Head, J. W., Fassett, C. I., An overfilled lacustrine system and progradational delta in Jezero crater, Mars: Implications for Noachian climate, *Planetary and Space Science,* **2012**, 67, 28-45.

Schroeder, G., NASA's Ingenuity Mars Helicopter: The first attempt at powered flight on another world, *American Scientist,* **2020**, 108, 330.

Scott, E. R. D., Greenwood, R. C., Franchi, I. A., Sanders, I. S., Oxygen isotopic constraints on the origin and parent bodies of eucrites, diogenites, and howardites, *Geochimica Et Cosmochimica Acta,* **2009**, 73, 5835-5853.

Segura, A., Navarro-González, R., Nitrogen fixation on early Mars by volcanic lightning and other sources, *Geophysical Research Letters,* **2005**, 32, 1-4.

Sekiya, T., Ohta, S., Kamei, S., Hanakawa, M., Kurita, S., Raman spectroscopy and phase transition of anatase TiO2 under high pressure, *The Journal of Physics and Chemistry of Solids,* **2001**, 62, 717-721.

Semenov, E. I., Sorensenite, a new sodium-beryllium-tin-silicate from the Ilimaussaq intrusion, South Greenland, **1965**, Reitzel, Kobenhavn.

Servoin, J. L., Piriou, B., Infrared Reflectivity and Raman Scattering of $Mg_2SiO_4$ Single Crystal, *Physica Status Solidi (B),* **1973**, 55, 677-686.

Sheehan, W., Bell, J., The Planet Mars: A History of Observation and Discovery, 1st ed. **1997**, The University of Arizona Press, Arizona, USA.

Siauciunas, R., Baltakys, K., Formation of gyrolite during hydrothermal synthesis in the mixtures of CaO and amorphous SiO2 or quartz, *Cement and Concrete Research,* **2004**, 34, 2029-2036.

Sims, M., Jaret, S. J., Johnson, J. R., Whitaker, M. L., Glotch, T. D., Unconventional high-pressure Raman spectroscopy study of kinetic and peak pressure effects in plagioclase feldspars, *Physics and Chemistry of Minerals,* **2020**, 47.

Smith, M. R., Bandfield, J. L., Geology of quartz and hydrated silica-bearing deposits near Antoniadi Crater, Mars, *Journal of Geophysical Research. Planets,* **2012**, 117, 1-24.

Smyth, J. R., Ahrens, T. J., The crystal structure of calcite III, *Geophysical Research Letters,* **1997**, 24, 1595-1598.

Squyres, S. W., Arvidson, R. E., Ruff, S., Gellert, R., Morris, R. V., Ming, D. W., Crumpler, L., Farmer, J. D., Des Marais, D. J., Yen, A., et al., Detection of Silica-Rich Deposits on Mars, *Science,* **2008**, 320, 1063-1067.

Squyres, S. W., Grotzinger, J. P., Arvidson, R. E., Bell, J. F., Calvin, W., Christensen, P. R., Clark, B. C., Crisp, J. A., Farrand, W. H., Herkenhoff, K. E., et al., In Situ Evidence for an Ancient Aqueous Environment at Meridiani Planum, Mars, *Science,* **2004**, 306, 1709-1714.

Stephan, K., Jaumann, R., De Sanctis, M. C., Tosi, F., Ammannito, E., Krohn, K., Zambon, F., Marchi, S., Ruesch, O., Matz, K. D., et al., Small fresh impact craters on asteroid 4 Vesta: A compositional and geological fingerprint, *Journal of Geophysical Research. Planets,* **2014**, 119, 771-797.

Stephanie C. Werner, Anouck Ody, François Poulet, The Source Crater of Martian Shergottite Meteorites, *Science,* **2014**, 343, 1343-1346.

Stern, J. C., Sutter, B., Freissinet, C., Navarro-González, R., McKay, C. P., Archer, P. D., Buch, A., Brunner, A. E., Coll, P., Eigenbrode, J. L., et al., Evidence for indigenous nitrogen in sedimentary and aeolian deposits from the Curiosity rover investigations at Gale crater, Mars, *Proceedings of the National Academy of Sciences,* **2015**, 112, 4245-4250.

Strachan, C. J., Rades, T., Gordon, K. C., Rantanen, J., Raman spectroscopy for quantitative analysis of pharmaceutical solids, *Journal of Pharmacy and Pharmacology,* **2007**, 59, 179-192.

Suito, K., Namba, J., Horikawa, T., Taniguchi, Y., Sakurai, N., Kobayashi, M., Onodera, A., Shimomura, O., Kikegawa, T., Phase relations of $CaCO_3$ at high pressure and high temperature, *The American Mineralogist,* **2001**, 86, 997-1002.

Summons, R. E., Amend, J. P., Bish, D., Buick, R., Cody, G. D., Des Marais, D. J., Dromart, G., Eigenbrode, J. L., Knoll, A. H., Sumner, D. Y.,

Preservation of Martian Organic and Environmental Records: Final Report of the Mars Biosignature Working Group, *Astrobiology,* **2011**, 11, 157-181.

Sutter, B., Heil, E., Navarro-Gonzalez, R., Niles, P. B., Mahaffy, P. R., Stern, J. C., Mertzman, S., Rampe, E. B., Morris, R. V., Ming, D. W., et al., Iron-Rich Carbonates as the Potential Source of Evolved CO2 Detected by the Sample Analysis at Mars (SAM) Instrument in Gale Crater, *American Geophysical Union,* **December 14, 2015,** San Francisco, California, USA.

Svensson, U., Dreybrodt, W., Dissolution kinetics of natural calcite minerals in $CO^{2-}$ water systems approaching calcite equilibrium, *Chemical Geology,* **1992**, 100, 129-145.

Talboys, D. L., Barber, S., Bridges, J. C., Kelley, S. P., Pullan, D., Verchovsky, A. B., Butcher, G., Fazel, A., Fraser, G. W., Pillinger, C. T., et al., In situ radiometric dating on Mars: Investigation of the feasibility of K-Ar dating using flight-type mass and X-ray spectrometers, *Planetary and Space Science,* **2009**, 57, 1237-1245.

Tarnas, J. D., Mustard, J. F., Lin, H., Goudge, T. A., Amador, E. S., Bramble, M. S., Kremer, C. H., Zhang, X., Itoh, Y., Parente, M., Orbital Identification of Hydrated Silica in Jezero Crater, Mars, *Geophysical Research Letters,* **2019**, 46, 12771-12782.

Taylor, S. R., McLennan, S., Planetary Crusts: Their Composition, Origin and Evolution, **2008**, Cambridge University Press, Cambridge, UK.

Thompson, J. E. S., Maya astronomy, *Philosophical Transactions of the Royal Society of London. Series A, Mathematical and Physical Sciences,* **1974**, 276, 83-98.

Tischendorf, G., Förster, H. J., Gottesmann, B., Rieder, M., True and brittle micas: composition and solid-solution series, *Mineralogical Magazine,* **2007**, 71, 285-320.

Tokano, T., Water on Mars and Life, **2004**, Springer, Berlin.

Tomkinson, T., Lee, M. R., Mark, D. F., Dobson, K. J., Franchi, I. A., The Northwest Africa (NWA) 5790 meteorite: A mesostasis-rich nakhlite with little or no Martian aqueous alteration, *Meteoritics & Planetary Science,* **2015**, 50, 287-304.

Treiman, A. H., The nakhlite meteorites: Augite-rich igneous rocks from Mars, *Chemie Der Erde,* **2005**, 65, 203-270.

Treiman, A. H., Drake, M. J., Janssens, M., Wolf, R., Ebihara, M., Core formation in the Earth and Shergottite Parent Body (SPB): Chemical

evidence from basalts, *Geochimica Et Cosmochimica Acta,* **1986**, 50, 1071-1091.

Treiman, A. H., Lanzirotti, A., Xirouchakis, D., Ancient water on asteroid 4 Vesta: evidence from a quartz veinlet in the Serra de Magé eucrite meteorite, *Earth and Planetary Science Letters,* **2004**, 219, 189-199.

Tribaudino, M., Mantovani, L., Bersani, D., Lottici, P. P., Raman spectroscopy of (Ca, Mg)$MgSi_2O_6$ clinopyroxenes, *The American Mineralogist,* **2012**, 97, 1339-1347.

Turner, S. M. R., Bridges, J. C., Grebby, S., Ehlmann, B. L., Hydrothermal activity recorded in post Noachian-aged impact craters on Mars, *Journal of Geophysical Research. Planets,* **2016**, 121, 608-625.

U. S. Department of Interior, U. S. Geological Survey, Minerals Yearbook, Area Reports: International 2011, Africa and the Middle East: Volume III, **2013**, USGS, Washington DC, USA.

Ulmer, P., Trommsdorff, V., Serpentine Stability to Mantle Depths and Subduction-Related Magmatism, *Science,* **1995**, 268, 858-861.

Uroz, S., Calvaruso, C., Turpault, M., Frey-Klett, P., Mineral weathering by bacteria: ecology, actors and mechanisms, *Trends in Microbiology,* **2009**, 17, 378-387.

Velbel, M. A., Aqueous corrosion of olivine in the Mars meteorite Miller Range (MIL) 03346 during Antarctic weathering: Implications for water on Mars, *Geochimica Et Cosmochimica Acta,* **2016**, 180, 126-145.

Veneranda, M., Lopez-Reyes, G., Manrique, J. A., Medina, J., Ruiz-Galende, P., Torre-Fdez, I., Castro, K., Lantz, C., Poulet, F., Dypvik, H., et al., ExoMars Raman Laser Spectrometer: A Tool for the Potential Recognition of Wet-Target Craters on Mars, *Astrobiology,* **2020**, 20, 349-363.

Veneranda, M., Manrique-Martinez, J. A., Lopez-Reyes, G., Medina, J., Torre-Fdez, I., Castro, K., Madariaga, J. M., Lantz, C., Poulet, F., Krzesińska, A. M., et al., Spectroscopic study of olivine-bearing rocks and its relevance to the ExoMars rover mission, *Spectrochimica Acta. Part A, Molecular and Biomolecular Spectroscopy,* **2019**, 223, 117360.

Voosen, P., NASA Curiosity rover hits organic pay dirt on Mars, *Science,* **2018**, 360, 1054-1055.

Wadhwa, M., Lentz, R. C. F., McSween, H. Y., Crozaz, G., A petrologic and trace element study of Dar al Gani 476 and Dar al Gani 489: Twin

meteorites with affinities to basaltic and lherzolitic shergottites, *Meteoritics & Planetary Science,* **2001**, 36, 195-208.

Wang, A., Freeman, J. J., Jolliff, B. L., Chou, I., Sulfates on Mars: A systematic Raman spectroscopic study of hydration states of magnesium sulfates, *Geochimica Et Cosmochimica Acta,* **2006**, 70, 6118-6135.

Wang, A., Han, J., Guo, L., Yu, J., Zeng, P., Database of Standard Raman Spectra of Minerals and Related Inorganic Crystals, *Applied Spectroscopy,* **1994**, 48, 959-968.

Wang, A., Jolliff, B. L., Haskin, L. A., Kuebler, K. E., Viskupic, K. M., Characterization and comparison of structural and compositional features of planetary quadrilateral pyroxenes by Raman spectroscopy, *The American Mineralogist,* **2001**, 86, 790-806.

Wang, A., Kuebler, K. E., Jolliff, B. L., Haskin, L. A., Raman spectroscopy of Fe-Ti-Cr-oxides, case study: Martian meteorite EETA79001, *The American Mineralogist,* **2004**, 89, 665-680.

Wang, A., Kuebler, K., Jolliff, B., Haskin, L. A., Mineralogy of a Martian meteorite as determined by Raman spectroscopy, *Journal of Raman Spectroscopy,* **2004**, 35, 504-514.

Watters, T. R., McGovern, P. J., Irwin, R. P., Hemispheres Apart: The Crustal Dichotomy on Mars, *Annual Review of Earth and Planetary Sciences,* **2007**, 35, 621-652.

Weisberg, M. K., McCoy, T. J., Krot, A. N., Meteorites and the Early Solar System II; Systematics and evaluation of meteorite classification (p.p. 19-52) **2006,** Univ. of Arizona Press, Arizona, USA.

Weitz, C. M., Milliken, R. E., Grant, J. A., McEwen, A. S., Williams, R. M. E., Bishop, J. L., Thomson, B. J., Mars Reconnaissance Orbiter observations of light-toned layered deposits and associated fluvial landforms on the plateaus adjacent to Valles Marineris, *Icarus,* **2010**, 205, 73-102.

Whitley, S., Halama, R., Gertisser, R., Preece, K., Deegan, F. M., Troll, V. R., Magmatic and Metasomatic Effects of Magma–Carbonate Interaction Recorded in Calc-silicate Xenoliths from Merapi Volcano (Indonesia), *Journal of Petrology,* **2020**, 61.

Wiberg, N., Wiberg, E., Holleman, A. F., Lehrbuch der anorganischen Chemie, **2007**, de Gruyter, Berlin.

Wiens, R. C., Maurice, S., Rull, F., The SuperCam remote sensing instrument suite for the mars 2020 rover: A preview, *Spectroscopy,* **2017**, 32, 50-55.

Wiens, R. C., Maurice, S., Robinson, S. H., Nelson, A. E., Cais, P., Bernardi, P., Newell, R. T., Sharma, S. K., Deming, J., Beckman, D., et al., The SuperCam Instrument Suite on the NASA Mars 2020 Rover: Body Unit and Combined System Tests, *Space Science Reviews,* **2021**, 217, 4.

Williams, K. B., Sonzogni, Y., Amphibole in the Tissint Martian Meteorite: Composition and Implication for Volatile Content of Parental Magma, *45th Lunar and Planetary Science Conference,* **March 17, 2014,** The Woodlands, Texas, USA.

Williford, K. H., Farley, K. A., Stack, K. M., Allwood, A. C., Beaty, D., Beegle, L. W., Bhartia, R., Brown, A. J., de la Torre Juarez, M., Hamran, S., et al., From Habitability to Life on Mars; The NASA Mars 2020 Rover Mission and the Search for Extraterrestrial Life (p.p. 275-308) Edited by Cabrol, N. A., Grin, E. A., **2018,** Elsevier, Amsterdam, the Netherlands.

Wray, J. J., Murchie, S. L., Bishop, J. L., Ehlmann, B. L., Milliken, R. E., Wilhelm, M. B., Seelos, K. D., Chojnacki, M., Orbital evidence for more widespread carbonate-bearing rocks on Mars, *Journal of Geophysical Research. Planets,* **2016**, 121, 652-677.

Xie, X., Minitti, M. E., Chen, M., Mao, H. o., Wang, D., Shu, J., Fei, Y., Natural high-pressure polymorph of merrillite in the shock veins of the Suizhou meteorite, *Geochimica Et Cosmochimica Acta,* **2002**, 66, 2439-2444.

Yang, S., Humayun, M., Righter, K., Jefferson, G., Fields, D., Irving, A. J., Siderophile and chalcophile element abundances in shergottites: Implications for Martian core formation, *Meteoritics & Planetary Science,* **2015**, 50, 691-714.

Yasuzuka, T., Ishibashi, H., Arakawa, M., Yamamoto, J., Kagi, H., Simultaneous determination of Mg# and residual pressure in olivine using micro-Raman spectroscopy, *Journal of Mineralogical and Petrological Sciences,* **2009**, 104, 395-400.

Yen, A. S., Morris, R. V., Ming, D. W., Schwenzer, S. P., Sutter, B., Vaniman, D. T., Treiman, A. H., Gellert, R., Achilles, C. N., Berger, J. A., et al., Formation of Tridymite and Evidence for a Hydrothermal History at Gale Crater, Mars, *Journal of Geophysical Research. Planets,* **2021**, 126, 1-16.

Zhang, L., Meng, Y., Yang, W., Wang, L., Mao, W. L., Zeng, Q., Jeong, J. S., Wagner, A. J., Mkhoyan, K. A., Liu, W., et al., Disproportionation of

(Mg,Fe)$SiO_3$ perovskite in Earth's deep lower mantle, *Science,* **2014**, 344, 877-882.

Zipfel, J., Scherer, P., Spettel, B., Dreibus, G., Schultz, L., Petrology and chemistry of the new shergottite Dar al Gani 476, *Meteoritics & Planetary Science,* **2000**, 35, 95-106.

Zuber, M. T., Banerdt, W. B., Andrews-Hanna, J. C., The Borealis basin and the origin of the Martian crustal dichotomy, *Nature (London),* **2008**, 453, 1212-1215.

Zuber, M. T., Mcsween, H. Y., Binzel, R. P., Eelkins-Tanton, L. T., Konopliv, A. S., Pieters, C. M., Smith, D. E., Origin, Internal Structure and Evolution of 4 Vesta, *Space Science Reviews,* **2011**, 163, 77-93.

Zuber, M. T., Solomon, S. C., Phillips, R. J., Smith, D. E., Tyler, G. L., Aharonson, O., Balmino, G., Banerdt, W. B., Head, J. W., Johnson, C. L., et al., Internal Structure and Early Thermal Evolution of Mars from Mars Global Surveyor Topography and Gravity, *Science,* **2000**, 287, 1788-1793.

# Chapter 12
# Appendices

**Appendix I.** Glossary of Acronyms

**Appendix II.** Mineral Formulation

**Appendix III.** Scientific Publications

## 12.1. Appendix I. Glossary of Acronyms

ANSMET – Antarctic Search for Meteorites program

BU – Body Unit

CACTI – Scientific-Technological Support Center for Research

CAS – Chemical Abstract Service

CaSSIS – Colour and Stereo Surface Imaging System

CCD – Charge Couple Device

ChemCam – Chemistry and Camera complex

CNES – Centre National d'Etudes Spatiales

CRISM – Compact Reconnaissance Imaging Spectrometer for Mars

DaG – Dar al Gani

DAN – Dynamic Albedo of Neutrons

EDS – Energy Dispersive X-Ray Spectroscopy

ED-XRF – Energy Dispersive X-Ray Fluorescence

EET – Elephant Moraine

EQM – Engineering Qualification Model

ESA – European Space Agency

FM – Flight Model

FWHM – Full Width at Half Maximum

GAP – Gas Analysis Package

GRS – Gamma Ray Spectrometer

HED – Howardites-Eucrites-Diogenites

IGME – Spanish Geological and Miner Institute

IMPAT database – Inorganic and Mineralogical Planetary And Terrestrial compounds database

JPL – Jet Propulsion Laboratory

JSC – Johnson Space Center

LANL – Los Alamos National Laboratory

Laspea – Coupled Multispectroscopy Singular Laboratory

LIBS – Laser-Induced Breakdown Spectroscopy

MarCO A/B – Mars Cube One A/B

MAVEN – Mars Atmosphere and Volatile EvolutioN

MEDA – Mars Environmental Dynamics Analyzer

MEP – Mars Exploration Program

MGS – Mars Global Surveyor

MLR – Multiple Linear Regression

MOC – Mars Orbiter Camera

MOLA – Mars Orbiter Laser Altimeter

MOXIE – Mars Oxygen In-Situ Resource Utilization Experiment

MRO – Mars Reconnaissance Orbiter

MSR – Mars Sample Return

MU – Mast Unit

N.A. – Numerical Aperture

NASA – National Aeronautics and Space Administration

NWA – Northwest Africa

OB – Olivine Bands

OMEGA – Visible and Infrared Mineralogical Mapping Spectrometer

PC – principal component

PCA – Principal Component Analysis

PIXL – Planetary Instrument for X-Ray Lithochemistry

RB – Raman Band

RIMFAX – Radar Imager for Mars' Subsurface Experiment

RMI – Remote Micro-Imaging

SAM – Sample Analysis at Mars

SCA – Chemical Analyzer interface

SCCT – SuperCam Calibration Target

SE – Secondary Electron

SEM – Scanning Electron Microscope

SGIker – UPV/EHU Advanced Research Facilities

SHERLOC – Scanning Habitable Environments with Raman and Luminescence for Organics and Chemicals

SIMS – Secondary Ion Mass Spectrometry

SNC – Shergottites-Nakhlites-Chassignites

sPC – sparse Principal Component

sPCA – sparse Principal Component Analysis

sPUL – science Payload Uplink Lead

TES – Thermal Emission Spectrometer

TGO – Trace Gas Orbiter

THEMIS – Thermal Emission Imaging System

ToF – Time-of-Flight

TRLS – Time-Resolved Luminescence Spectroscopy

UPV/EHU – University of the Basque Country

VISIR – Visible and Near Infrared Spectroscopy

WD-XRF – Wavelength Dispersive X-Ray Fluorescence

XRD – X-Ray Diffraction

XRS – X-ray Spectrometer

## 12.2. Appendix II. Mineral Formulation

Aegirine – $NaFe(Si_2O_6)$

Albite – $NaAlSi_3O_8$

Analcime – $NaAlSi_2O_6 \cdot H2O$

Anatase – $TiO_2$

Anorthite – $CaAl_2Si_2O_8$

Antigorite – $(Mg, Fe)_3Si_2O_5OH_4$

Apatite – $Ca_5(PO_4)_3(F, Cl, OH)$

Aragonite – $CaCO_3$

Augite – $(Ca, Mg, Fe)_2(Si, Al)_2O_6$

Barite – $BaSO_4$

Calcite – $CaCO_3$

Chkalovite – $Na_2BeSi_2O_6$

Chromite – $(Fe, Mg)Cr_2O_4$

Clinochlore – $Mg_5Al(AlSi_3O_{10})(OH)_8$

Clintonite – $Ca(Mg, Al)_3(Al_3Si)O_{10}(OH)_2$

Cobaltite – CoAsS

Coesite – $SiO_2$

Diaphorite – $Ag_3Pb_2Sb_3S_8$

Diopside – $CaMgSi_2O_6$

Dolomite – $CaMg(CO_3)_2$

Edenite – $NaCa_2Mg_5(Si_7Al)O_{22}(OH)_2$

Enstatite – $MgSiO_3$

Epidote – $Ca_2FeAl_2(Si_2O_7)(SiO_4)O(OH)$

Fayalite – $Fe_2SiO_4$

Ferrosilite – $FeSiO_3$

Fluorapophyllite-(K) – $KCa_4(Si_8O_{22})F \cdot 8H_2O$

Forsterite – $MgSiO_4$

Glaucodot – (Co, Fe)AsS

Goethite – α-FeO(OH)

Görgeyite – $K_2Ca_5(SO_4)_6 \cdot H_2O$

Gypsum – $CaSO_4 \cdot 2H_2O$

Gyrolite – $NaCa_{16}(Si_{23}Al)O_{60}(OH)_8 \cdot 14H_2O$

Hedenbergite – $CaFeSi_2O_6$

Hematite – $Fe_2O_3$

Hillebrandite – $Ca_2(SiO_3)(OH)_2$

Hisingerite – $Fe_2Si_2O_5(OH)_4 \cdot 2H_2O$

Iddingsite – $MgFe_2Si_3O_{10} \cdot 4(H_2O)$

Ilimaussite – $(Na, K)_{7\text{-}8}(Ba, K)_{10}Ce_5(Nb, Ti)_6(Si_3O_9)_4(Si_9O_{18})O_6(O,OH)_{24}$

Ilmenite – $FeTiO_2$

Kirschsteinite – $CaFeSiO_4$

Lepidolite – $K(Li, Al)_3(Al, Si, Rb)_4O_{10}(F, OH)_2$

Linarite – $PbCu(OH)_2SO_2$

Lizardite – $Mg_3(Si_2O_5)(OH)_4$

Magnesiumwüstite – (Mg, Fe)O

Magnetite – $Fe_2O_4$

Merrillite – $Ca_9NaMg(PO_4)_7$

Monticellite – $CaMgSiO_4$.

Muscovite – $KAl_2(AlSi_3O_{10})(F,OH)_2$

Nepheline – $NaAlSiO_4$

Nitratine – $NaNO_3$

Opaline – $SiO_2 \cdot nH_2O$

Orthoclase – $KAlSi_3O_8$

Pectolite – $NaCa_2Si_3O_8(OH)$

Perovskite – $(Mg, Fe)SiO_3$

Polylithionite – $KLi_2Al(Si_4O_{10})(F,OH)_2$

Pyrrhotite – $Fe_{(1-x)}S$, x=0-0.2

Quartz – $SiO_2$

Raite – $Na_4Mn_3Ti_{0.25}Si_8O_{20}(OH)_2 \cdot 10H_2O$

Safflorite – $CoAs_2$

Serandite – $NaMn_2Si_3O_8(OH)$

Skutterudite – $CoAs_3$

Sorensenite – $Na_4SnBe_2Si_6O_{16}(OH)_4$

Syngenite – $K_2Ca(SO_4)_2 \cdot H_2O$

Talc – $Mg_3Si_4O_{10}(OH)_2$

Tremolite – $Ca_2Mg_5Si_8O_{22}(OH)_2$

Tridymite – $SiO_2$

Trilithionite – $K(Li_{1.5}Al_{1.5})(AlSi_3O_{10})(F,OH)_2$

Ussingite – $Na_2AlSi_3O_8(OH)$

Varite – $BaSO_4$

Vesuvianite – $Ca_{10}(Mg, Fe)_2Al_4(SiO_4)_5(Si_2O_7)_2(OH ,F)_4$

Whitlockite – $Ca_9Mg(PO_3OH)(PO_4)_6$

Wollastonite – $CaSiO_3$,

Wurtzite – ZnS

## 12.3. Appendix III. Scientific Publications

- **Scientific articles in research journals:**

**–** Maurice, S., Wiens, R. C., Bernardi, P., Caïs, P., Robinson, S., Nelson, T., Gasnault, O., Reess, J. M., Deleuze, M., Rull, F., Manrique, J. A., Abbaki, S., Anderson, R. B., André, Y., Angel, S. M., Arana, G., Battault, T., Beck, P., Benzerara, K., Bernard, S., Berthias, J. P., Beyssac, O., Bonafous, M., Bousquet, B., Boutillier, M., Cadu, A., Castro, K., Chapron, F., Chide, B., Clark, K., Clavé, E., Clegg, S., Cloutis, E., Collin, C., Cordoba, E. C., Cousin, A., Dameury, J. C., D'Anna, W., Daydou, Y., Debus, A., Deflores, L., Dehouck, E., Delapp, D., De Los Santos, G., Donny, C., Doressoundiram, A., Dromart, G., Dubois, B., Dufour, A., Dupieux, M., Egan, M., Ervin, J., Fabre, C., Fau, A., Fischer, W., Forni, O., Fouchet, T., Frydenvang, J., Gauffre, S., Gauthier, M., Gharakanian, V., Gilard, O., Gontijo, I., Gonzalez, R., Granena, D., Grotzinger, J., Hassen-Khodja, R., Heim, M., Hello, Y., Hervet, G., Humeau, O., Jacob, X., Jacquinod, S., Johnson, J. R., Kouach, D., Lacombe, G., Lanza, N., Lapauw, L., Laserna, J., Lasue, J., Le Deit, L., Le Mouélic, S., Le Comte, E., Lee, Q. M., Legett, C., Leveille, R., Lewin, E., Leyrat, C., Lopez-Reyes, G., Lorenz, R., Lucero, B., Madariaga, J. M., Madsen, S., Madsen, M., Mangold, N., Manni, F., Mariscal, J. F., Martinez-Frias, J., Mathieu, K., Mathon, R., McCabe, K. P., McConnochie, T., McLennan, S. M., Mekki, J., Melikechi, N., Meslin, P. Y., Micheau, Y., Michel, Y., Michel, J. M., Mimoun, D., Misra, A., Montagnac, G., Montaron, C., Montmessin, F., Moros, J., Mousset, V., Morizet, Y., Murdoch, N., Newell, R. T., Newsom, H., Nguyen Tuong, N., Ollila, A. M., Orttner, G., Oudda, L., Pares, L., Parisot, J., Parot, Y., Pérez, R., Pheav, D., Picot, L., Pilleri, P., Pilorget, C., Pinet, P., Pont, G., Poulet, F., Quantin-Nataf, C., Quertier, B., Rambaud, D., Rapin, W., Romano, P., Roucayrol, L., Royer, C., Ruellan, M., Sandoval, B. F., Sautter, V., Schoppers, M. J., Schröder, S., Seran, H. -., Sharma, S. K., Sobron, P., Sodki, M., Sournac, A., Sridhar, V., Standarovsky, D., Storms, S., Striebig, N., Tatat, M., Toplis, M., **Torre-Fdez, I.**, Toulemont, N., Velasco, C., Veneranda, M., Venhaus, D., Virmontois, C., Viso, M., Willis, P., Wong, K. W., The SuperCam Instrument Suite on the Mars 2020 Rover: Science Objectives and Mast-Unit Description, Space Science Reviews, 2021, 217, 47

**–** Garcia-Florentino, C., **Torre-Fdez, I.**, Ruiz-Galende, P., Aramendia, J., Castro, K., Arana, G., Maguregui, M., Fdez-Ortiz de Vallejuelo, S., Madariaga, J. M., Development of innovative non-destructive analytical

strategies for Mars Sample Return tested on Dar al Gani 735 Martian Meteorite, *Talanta*, **2021**, 224, 121863

**–** Wiens, R. C., Maurice, S., Robinson, S. H., Nelson, A. E., Cais, P., Bernardi, P., Newell, R. T., Sharma, S. K., Deming, J., Beckman, D., Gasnault, O., André, Y., Michael Angel, S., Arana, G., Auden, E., Beck, P., Benzerara, K., Bernard, S., Beyssac, O., Borges, L., Bousquet, B., Boyd, K., Caffrey, M., Carlson, J., Castro, K., Clark, K., Cloutis, E., Cordoba, E. C., Cousin, A., Dale, M., Deflores, L., Delapp, D., Deleuze, M., Donny, C., Dromart, G., George Duran, M., Egan, M., Ervin, J., Fabre, C., Fau, A., Fischer, W., Forni, O., Frydenvang, J., Gasway, D., Gontijo, I., Grotzinger, J., Johnson, J. R., Klisiewicz, R. A., Lake, J., Lanza, N., Laserna, J., Le Mouélic, S., Legett, 4., Carey, Leveille, R., Lewin, E., Lorenz, R., Lorigny, E., Lucero, B., Madariaga, J. M., Madsen, M., Martinez, J. P., McConnochie, T. H., McGlown, J. M., McLennan, S. M., Melikechi, N., Meslin, P., Michel, J. M., Mimoun, D., Misra, A., Montmessin, F., Mousset, V., Newsom, H., Ott, L. A., Ousnamer, Z. R., Pares, L., Parot, Y., Pilleri, P., Pinet, P., Poulet, F., Provost, C., Quinn, H., Rapin, W., Reess, J., Romano, P. J., Royer, C., Sarrao, J. H., Sautter, V., Schoppers, M. J., Schröder, S., Seitz, D., Shepherd, T., Sobron, P., Sridhar, V., Toplis, M. J., **Torre-Fdez, I.**, Trettel, I. A., Underwood, M., Valdez, A., Venhaus, D., Willis, P., The SuperCam Instrument Suite on the NASA Mars 2020 Rover: Body Unit and Combined System Tests, Space Science Reviews, 2021, 217, 4

**–** Veneranda, M., Lopez-Reyes, G., Manrique, J. A., Medina, J., Ruiz-Galende, P., **Torre-Fdez, I.**, Castro, K., Lantz, C., Poulet, F., Dypvik, H., Werner, S., Rull, F., ExoMars Raman Laser Spectrometer: A Tool for the Potential Recognition of Wet-Target Craters on Mars, *Astrobiology*, **2020**, 20, 349-363

**–** Veneranda, M., Manrique, J. A., Lopez-Reyes, G., Medina, J., **Torre-Fdez, I.**, Castro, K., Madariaga, J. M., Lantz, C., Poulet, F., Krzesińska, A., Hellevang, H., Werner, S., Rull, F, Spectroscopic study of olivine-bearing rocks and its relevance to the ExoMars rover mission, *Spectrochimica Acta Part A: Molecular and Biomolecular Spectroscopy*, **2019**, 223, 1386-1425

**–** Ruiz-Galende, P., **Torre-Fdez, I.**, Aramendia, J., Gomez-Nubla, L., C., Castro, K., Arana, G., Fdez-Ortiz de Vallejuelo, S., Maguregui, M., Medina, J., Baonza, V. G., Rull, F., Madariaga, J. M., New Raman–visible near-

infrared database of inorganic and mineralogical planetary and terrestrial compounds and its implications for Mars: Phyllosilicates, *Journal of Raman Spectroscopy*, **2019**, 51, 1750-1760

**– Torre-Fdez, I.**, Aramendia, J., Gomez-Nubla, L., C., Castro, K., Maguregui, M., Fdez-Ortiz de Vallejuelo, Arana, G., Madariaga, J. M., Non-destructive characterisation of the Elephant Moraine 83227 meteorite using confocal Raman, micro-energy-dispersive X-ray fluorescence and Raman-scanning electron microscope-energy-dispersive X-ray microscopies, *Analytical and Bioanalytical Chemistry*, **2018**, 410, 7477-7488

**– Torre-Fdez, I.**, Aramendia, J., Gomez-Nubla, L., C., Castro, K., Madariaga, J. M., Geochemical study of the Northwest Africa 6148 Martian meteorite and its terrestrial weathering processes, *Journal of Raman Spectroscopy*, 48, 1536-1543

- **Contributions to scientific conferences:**

**– Torre-Fdez, I.**, Garcia-Florentino, C., Huidobro, J., Coloma, L., Ruiz-Galende, P., Aramendia, J., Castro, K., Arana, G., Madariaga, J. M., Characterization of olivines and their metallic composition: Raman spectroscopy could provide an accurate solution for the active and future Mars missions, *EPSC 2021*, **September 13, 2021**, virtual meeting

**– Torre-Fdez, I.**, Fornaro, T., Aramendia, J., Ollila, A.M., Castro, K., Madariaga, J.M., Clegg, S., Delap, D., Angel, S.M., Benzerara, K., Bernard, S., Bernardi, P., Beyssac, O., Bonal, L., Bousquet, B., Chide, B., Clavé, E., Fabre, C., Forni, O., Garcia-Baonza, V., Gasnault, O., Legett, C., Lopez-Reyes, G., Manrique, J. A., Maurice, S., Meslin, P. Y., Misra, A. K., Montagnac, G., Nelson, T., Newell, R., Perez, R., Pilleri, P., Rull, F., Schröder, S., Sharma, S., Veneranda, M., Wiens, R., Willis, P. A., Analysis of organic compounds in Mars soil analog samples using SuperCam-Raman of Mars2020, *EGU 2021*, **April 19, 2021**, virtual meeting

**–** Wiens, R., Maurice, S., Gasnault, O., Anderson, R., Beyssac, O., Bonal, L., Clegg, S., Deflores, L., Dromart, G., Fischer, W., Forni, O., Grotzinger, J., Johnson, J., Martinez-Frias, J., Mangold, N., Mclennan, S., Montmessin, F., Rull, F., Sharma, S., Cousin, A., Pilleri, P., Sautter, V., Lewin, E., Cloutis, E., Poulet, F., Bernard, S., McConnochie, T., Lanza, N., Newsom,

H., Ollila, A., Leveille, R., Le Mouelic, S., LASUE, J., Melikechi, N., Meslin, P. -., Grasset, O., Angel, S., Fouchet, T., Beck, P., Bousquet, B., Fabre, C., Pinet, P., Benzerara, K., Montagnac, G., Arana, G., Castro, K., Laserna, J., Madariaga, J. -., Manrique, J. -., Lopez, G., Lorenz, R., Mimoun, D., Acosta-Maeda, T., Alvarez, C., Dehouck, E., Delory, G., Doressoundiram, A., Francis, R., Frydenvang, J., Gabriel, T., Jacob, X., Madsen, M., Moros, J., Murdoch, N., Newell, R., Porter, J., Quantin-Nataf, C., Rapin, W., Schröder, S., Sobron, P., Toplis, M., Brown, A., Veneranda, M., Chide, B., Legett, C., Royer, C., Stott, A., Vogt, D., Robinson, S., Delapp, D., Clavé, E., Connell, S., Essunfeld, A., Gallegos, Z., Garcia-Florentino, C., Gibbons, E., Huidobro, J., Kelly, E., Kalucha, H., Ruiz, P., **Torre- Fdez, I.**, Shkolyar, S., SuperCam on the Perseverance Rover for Exploration of Jezero Crater: Remote LIBS, VISIR, Raman, and Time-Resolved Luminescence Spectroscopies Plus Micro-Imaging and Acoustics, *52nd LPSC*, **March 15, 2021**, The Woodlands, USA

**–** Beyssac, O., Ollila, A.M., Arana, G., Angel, S.M., Benzerara, K., Bernard, S., Bernardi, P., Bousquet, B., Castro, K., Clavé, E., Clegg, S., Cousin, A., Dehouck, E., Delap, D., Egan, M., Forni, O., Gasnault, O., Legett, C., Lopez-Reyes, G., Madariaga, J.M., Manrique, J. A., Maurice, S., Meslin, P. Y., Montagnac, G., Nelson, T., Newell, R., Pilleri, P., Robinson, S., Rull, F., Schröder, S., Sharma, S., **Torre-Fdez, I.**, Wiens, R., Willis, P. A., SuperCam's time-resolved Raman and luminescence spectroscopy onboard the Perseverance rover, *52nd LPSC*, **March 15, 2021**, The Woodlands, USA

**–** Huidobro, J., **Torre-Fdez, I.**, Amigo, J. M., Ruiz-Galende, P., Aramendia, J., Garcia-Florentino, C., Arana, G., Castro, K., Madariaga, J. M., Chemical Analysis of an Organic Bubble in the North West Africa 6148 Meteorite Using Raman Spectroscopy Imaging and Chemometrics, *AGU Fall Meeting* 2020, **December 1, 2020**, virtual meeting

**– Torre-Fdez, I.**, Aramendia, J., Garcia-Florentino, C., Ollila, A.M., Ruiz-Galende, P., Arana, G., Bernard, S., Beyssac, O., Castro, K., Clegg, S., Cousin, A., Egan, M., Forni, O., Gasnault, O., Lopez-Reyes, G., Madariaga, J.M., Manrique, J. A., Maurice, S., Misra, A. K., Montagnac, G., Nelson, T., Newell, R., Pilleri, P., Robinson, S., Rull, F., Sharma, S., Veneranda, M., Wiens, R., Willis, P. A., Perseverance's SuperCam-Raman: a Quality

Assurance of Analytical Spectral Variables, *AGU Fall Meeting 2020*, **December 1, 2020**, virtual meeting

**– Torre-Fdez, I.**, Ruiz-Galende, P., Aramendia, J., Garcia-Florentino, C., Ollila, A.M., Arana, G., Bernard, S., Bernardi, P., Beyssac, O., Caïs, P., Castro, K., Clegg, S., Egan, M., Forni, O., Gasnault, O., Gontijo, I., Madariaga, J.M., Manrique, J. A., Maurice, S., Misra, A. K., Montagnac, G., Nelson, T., Newell, R., Pilleri, P., Robinson, S., Rull, F., Sharma, S., Wiens, R., Willis, P. A., Validation of the SuperCam-Raman for NASA's Mars2020 mission: Tests and comparison with laboratory results, *GeoRaman 2020*, **November 2, 2020**, virtual meeting

**–** Madariaga, J. M., Garcia-Florentino, C., **Torre-Fdez, I.**, Ruiz-Galende, P., Huidobro, J., Aramendia, J., Castro, K., Arana, G., Fdez-Ortiz de Vallejuelo, S., Maguregui, M., Study of Alterations in the Dar al Gani 735 Martian Meteorite studied by Exomars2022 RLS-like Instrument and HR Raman, *EPSC 2020*, **September 21, 2020**, virtual meeting

**– Torre-Fdez, I.**, Castro, K., Beyssac, O., Ollila, A.M., Madariaga, J.M., Arana, G., Bernard, S., Bernardi, P., Clegg, S., Egan, M., Forni, O., Gasnault, O., Gontijo, I., Manrique, J. A., Maurice, S., Misra, A. K., Montagnac, G., Nelson, T., Newell, R., Pilleri, P., Robinson, S., Rull, F., Sharma, S., Wiens, R., Willis, P. A., SuperCam Raman onboard Mars 2020 rover: comparison with laboratory results, *51st LPSC*, **March 16, 2020**, virtual meeting

**–** Beyssac, O., Ollila, A.M., Arana, G., Bernard, S., Bernardi, P., Caïs, P., Castro, K., Clegg, S., Cousin, A., Egan, M., Forni, O., Gasnault, O., Gontijo, I., Madariaga, J.M., Manrique, J. A., Maurice, S., Meslin, P. Y., Misra, A. K., Montagnac, G., Nelson, T., Newell, R., Pilleri, P., Robinson, S., Rull, F., Sharma, S., **Torre-Fdez, I.**, Wiens, R., Willis, P. A., SuperCam Raman onboard Mars 2020 rover: overview and test data, *51st LPSC*, **March 16, 2020**, virtual meeting

**–** Garcia-Florentino, C., Huidobro, J., Gomez-Nubla, L., **Torre-Fdez, I.**, Ruiz-Galende, P., Aramendia, J., Castro, K., Arana, G., Madariaga, J. M., Raman spectroscopy to detect alterations in volcanic mineral phases due to shock and environmental impacts, *Ninth International Conference On Mars*, **July 22, 2019**, Pasadena, California, USA

**–** Ollila, A.M., Wiens, R., Maurice, S., Cousin, A., Anderson, O., Beyssac, O., Bonal, L., Beck, P., Clegg, S., Chide, B., DeFlores, L., Dromart, G., Fischer, W., Forni, O., Fouchet, T., Gasnault, O., Grotzinger, J., Johnson, J., Lasue, J., Laserna, J., Madariaga, J.M., Madsen, M., Mangold, N., Nelson, T., Newell, Martinez-Frias, J., McLennan, S., Montmessin, F., Robinson, S., Sharma, S., Misra, A., Rull, F., Venhaus, D., Bernardi, P., Reess, J. M., Reyes-Newell, A., Poulet, F., Lanza, N., **Torre-Fdez, I.**, Aramendia, J., Perez, R., Cloutis, E., Angel, S., Dimoun, D., Lorenz, R., Rapin, W., Meslin, P. Y., Frydenvang, J., McConnochie, T., Bernard, S., Preparing SuperCam for Jezero crater, mars: LIBS, Raman, VISIR, luminescence, imaging, and acoustic analyses, *Ninth International Conference On Mars*, **July 22, 2019**, Pasadena, California, USA

**–** Madariaga, J. M., Ruiz-Galende, P., **Torre-Fdez, I.**, Huidobro, J., Garcia-Florentino, C., Gomez-Nubla, L., Aramendia, J., Fdez-Ortiz de Vallejuelo, S., Maguregui, M.,Castro, K., Arana, G., Raman microspectroscopy coupled to SEM/EDS to detect and identify organic matter in Impact Glasses, Meteorites and Terrestrial Analogs, *VI Reunion CPESS*, **May 27, 2019**, Torrejón de Ardoz, Madrid, Spain

**–** Castro, K., Ruiz-Galende, P., **Torre-Fdez, I.**, Huidobro, J., Garcia-Florentino, C., Gomez-Nubla, L., Aramendia, J., Fdez-Ortiz de Vallejuelo, S., Maguregui, M., Arana, G., Madariaga, J. M., Raman microspectroscopy to detect high temperature and high pressure minerals in meteorites: clues about their formation, *VI Reunion CPESS*, **May 27, 2019**, Torrejón de Ardoz, Madrid, Spain

**– Torre-Fdez, I.**, Ruiz-Galende, P., Aramendia, J., Gomez-Nubla, L., Castro, K., Arana, G., Madariaga, J. M., New quantitative model to determine fayalite-forsterite content in olivine minerals by Raman spectroscopy, *50$^{th}$ LPSC*, **March 18, 2019**, The Woodlands, USA

**– Torre-Fdez, I.**, Ruiz-Galende, P., Aramendia, J., Gomez-Nubla, L., Castro, K., Fdez-Ortiz de Vallejuelo, S., Arana, G., Madariaga, J. M., Study of organic compounds present in the NorthWest Africa 6148 nakhlite by means of Raman spectroscopy, *EPSC 2018*, **September 16, 2018**, Berlin, Germany

**– Torre-Fdez, I.**, Ruiz-Galende, P., Aramendia, J., Gomez-Nubla, L., Fdez-Ortiz de Vallejuelo, S., Castro, K, Arana, G., Baonza, V. G., Medina, J., Rull, F., Madariaga, J. M., Discrimination between original calcite and calcite from terrestrial weathering in NWA 6148 Martian meteorite by Raman spectroscopy, *GeoRaman 2018*, **June 10, 2018**, Catania, Sicily, Italy

**– Torre-Fdez, I.**, Aramendia, J., Castro, K., Madariaga, J. M., In-depth study of the Elephant Moraine 83227 meteorite: new discoveries of the 4 Vesta asteroid, *GeoRaman 2018*, **June 10, 2018**, Catania, Sicily, Italy

**–** Ruiz-Galende, P., **Torre-Fdez, I.**, Aramendia, J., Gomez-Nubla, L., Fdez-Ortiz de Vallejuelo, S., Medina, J., Castro, K, Maguregui, M., Arana, G., Baonza, V. G., Rull, F., Madariaga, J. M., New Raman-NIR Database of Inorganic and Mineralogical Planetary and Terrestrial compounds (IMPAT-Dat): Phyllosilicates, *GeoRaman 2018*, **June 10, 2018**, Catania, Sicily, Italy

**–** Madariaga, J. M., **Torre-Fdez, I.**, Ruiz-Galende, P., Aramendia, J., Gomez-Nubla, L., Fdez-Ortiz de Vallejuelo, S., Maguregui, M., Castro, K., Arana, G., Advanced analytical methodologies based on Raman spectroscopy to detect prebiotic and biotic molecules: applicability in the study of the Martian nakhlite NWA 6148 meteorite, *2nd International Mars Sample Return 2018*, **April 25, 2018**, Berlin, Germany

**– Torre-Fdez, I.**, Ruiz-Galende, P., Madariaga, J. M., Aramendia, J., Gomez-Nubla, L., Castro, K, Fdez-Ortiz de Vallejuelo, S., Arana, G., In-depth study of the calcite present in the Martian nakhlite NorthWest Africa 6148 meteorite, *49$^{th}$ LPSC*, **March 19, 2018**, The Woodlands, USA

**– Torre-Fdez, I.**, Ruiz-Galende, P., Madariaga, J. M., Aramendia, J., Gomez-Nubla, L., Fdez-Ortiz de Vallejuelo, S., Castro, K, Maguregui, M., Arana, G., Baonza, V. G., Rull, F., The relevance of the creation of a Raman and NIR spectroscopic database for the upcoming Mars missions, *49$^{th}$ LPSC*, **March 19, 2018**, The Woodlands, USA

**– Torre-Fdez, I.**, Ruiz-Galende, P., Castro, K, Gomez-Nubla, L., Aramendia, J., Maguregui, M., Baonza, V. G., Medina, J., Rull, F., Madariaga, J. M., Novel calibration functions to quantify forsterite and

fayalite in olivine minerals by Raman spectroscopy, *XXXVI Reunión Bienal de la RSEQ*, **June 25, 2017**, Sietges, Catalonia, Spain

**– Torre-Fdez, I.**, Aramendia, J., Gomez-Nubla, L., Castro, K, Madariaga, J. M., Raman analysis of the NWA 6148 Martian meteorite: olivine characterization and its differences with other nakhlites, *GeoRaman 2016*, **June 9, 2016**, Novosibirsk, Russia